



**HAL**  
open science

# Probing the Quark-Gluon Plasma from bottomonium production at forward rapidity with ALICE at the LHC

Massimiliano Marchisone

► **To cite this version:**

Massimiliano Marchisone. Probing the Quark-Gluon Plasma from bottomonium production at forward rapidity with ALICE at the LHC. Other [cond-mat.other]. Université Blaise Pascal - Clermont-Ferrand II, 2013. English. NNT : 2013CLF22406 . tel-00925826v2

**HAL Id: tel-00925826**

**<https://theses.hal.science/tel-00925826v2>**

Submitted on 16 Jan 2014

**HAL** is a multi-disciplinary open access archive for the deposit and dissemination of scientific research documents, whether they are published or not. The documents may come from teaching and research institutions in France or abroad, or from public or private research centers.

L'archive ouverte pluridisciplinaire **HAL**, est destinée au dépôt et à la diffusion de documents scientifiques de niveau recherche, publiés ou non, émanant des établissements d'enseignement et de recherche français ou étrangers, des laboratoires publics ou privés.

N° d'ordre : D.U. 2406

PCCF T 1306

**Université Blaise Pascal de Clermont-Ferrand**  
U.F.R. Sciences et Technologies  
École Doctorale des Sciences Fondamentales N° 774

**Università degli Studi di Torino**  
Scuola di Dottorato in Scienza ed Alta Tecnologia  
Indirizzo di Fisica ed Astrofisica – XXVI ciclo

## **THESE**

présentée pour obtenir le grade de  
**Docteur d'Université**

*Spécialité : Physique Corpusculaire*

par

**Massimiliano Marchisone**

# **Probing the Quark-Gluon Plasma from bottomonium production at forward rapidity with ALICE at the LHC**

Soutenue publiquement le 6 décembre 2013 à Clermont-Ferrand,  
devant la commission d'examen composée de :

Directeurs de thèse :	P. Dupieux	LPC, Clermont-Ferrand
	E. Vercellin	Università di Torino e INFN
Rapporteurs :	G. Iaselli	Università di Bari, Politecnico di Bari e INFN
	I. Laktineh	IPN, Lyon
Examineurs :	R. Arnaldi	INFN di Torino
	X. Lopez	LPC, Clermont-Ferrand

**Università degli Studi di Torino**  
Scuola di Dottorato in Scienza ed Alta Tecnologia  
Indirizzo di Fisica ed Astrofisica – XXVI ciclo

**Université Blaise Pascal de Clermont-Ferrand**  
École Doctorale des Sciences Fondamentales N° 774  
Spécialité : Physique Corpusculaire

---

Tesi di Dottorato di Ricerca in Scienza ed Alta Tecnologia

# **Probing the Quark-Gluon Plasma from bottomonium production at forward rapidity with ALICE at the LHC**

Clermont-Ferrand, 06/12/2013

**Massimiliano Marchisone**

Tutors:	P. Dupieux	LPC, Clermont-Ferrand
	E. Vercellin	Università di Torino e INFN
Controrelatori:	I. Laktineh	IPN, Lyon
	G. Iaselli	Università di Bari, Politecnico di Bari e INFN
Esaminatori:	R. Arnaldi	INFN di Torino
	X. Lopez	LPC, Clermont-Ferrand

# Contents

<b>Introduction</b>	<b>v</b>
<b>1 The Quark-Gluon Plasma in heavy-ion collisions</b>	<b>1</b>
1.1 QCD and asymptotic freedom . . . . .	1
1.2 The Quark-Gluon Plasma . . . . .	3
1.3 Heavy-ion collisions . . . . .	5
1.4 QGP effects: experimental signatures . . . . .	7
<b>2 Quarkonium in medium</b>	<b>9</b>
2.1 Discovery of quarkonium states . . . . .	9
2.2 Decay and feed-down of quarkonium . . . . .	10
2.3 Quarkonium production mechanisms . . . . .	11
2.3.1 Color Singlet Model . . . . .	12
2.3.2 Color Evaporation Model . . . . .	12
2.3.3 Non-Relativistic QCD . . . . .	13
2.4 Quarkonium as a probe of the QGP . . . . .	14
2.5 Cold nuclear matter effects . . . . .	16
2.5.1 Initial-state effects . . . . .	16
2.5.2 Final-state effects . . . . .	18
2.6 Quarkonium measurements in heavy-ion collisions . . . . .	18
2.6.1 Before the LHC era . . . . .	19
2.6.2 Charmonium measurements at the LHC . . . . .	21
<b>3 <math>\Upsilon</math> production</b>	<b>23</b>
3.1 The $\Upsilon$ family . . . . .	23
3.2 $\Upsilon$ production in pp and p $\bar{p}$ collisions . . . . .	25
3.2.1 Introduction to the quarkonium polarization . . . . .	25
3.2.2 Experimental results . . . . .	26
3.3 $\Upsilon$ production in pA and dA collisions . . . . .	35
3.3.1 Experimental results . . . . .	35
3.4 $\Upsilon$ production in heavy-ion collisions . . . . .	39
3.4.1 Introduction to theoretical models . . . . .	40
3.4.2 Experimental results . . . . .	41

3.5	Summary of the results . . . . .	43
<b>4</b>	<b>ALICE at the LHC</b>	<b>45</b>
4.1	The Large Hadron Collider . . . . .	45
4.2	A Large Ion Collider Experiment . . . . .	47
4.2.1	The ALICE coordinate system . . . . .	47
4.2.2	Central barrel detectors . . . . .	48
4.2.3	Forward detectors . . . . .	55
4.2.4	The Muon Spectrometer . . . . .	58
4.3	Online Control System . . . . .	59
4.3.1	Detector Control System . . . . .	59
4.3.2	Central Trigger Processor . . . . .	59
4.3.3	Data AcQuisition System . . . . .	60
4.3.4	High Level Trigger . . . . .	60
4.3.5	Data Quality Monitoring . . . . .	60
4.3.6	Detector Algorithms . . . . .	61
4.4	ALICE offline framework . . . . .	61
4.4.1	AliRoot . . . . .	61
4.4.2	The GRID . . . . .	63
4.5	ALICE upgrade program . . . . .	64
<b>5</b>	<b>The forward Muon Spectrometer and its trigger system</b>	<b>66</b>
5.1	Physics with the Muon Spectrometer . . . . .	66
5.2	The Muon Spectrometer setup . . . . .	67
5.2.1	Front absorber . . . . .	67
5.2.2	Muon filter . . . . .	68
5.2.3	Dipole magnet . . . . .	68
5.2.4	Beam shield . . . . .	69
5.2.5	Muon Tracking . . . . .	69
5.2.6	Trigger system . . . . .	72
5.3	The Muon Trigger system . . . . .	72
5.3.1	Detector geometry . . . . .	73
5.3.2	Resistive Plate Chambers . . . . .	74
5.3.3	Trigger principle . . . . .	76
5.3.4	Electronics . . . . .	78
<b>6</b>	<b>Cluster size of the Muon Trigger</b>	<b>82</b>
6.1	Cluster size: definition and dependences . . . . .	82
6.2	Estimate of the cluster size . . . . .	83
6.2.1	Analysis conditions . . . . .	83
6.2.2	Cluster size distribution and average values . . . . .	84
6.3	Cluster size in Pb–Pb collisions . . . . .	85
6.3.1	Dependence on the geometry of the detector . . . . .	85
6.3.2	Time dependence of the cluster size . . . . .	87

6.3.3	Comparison with results in pp collisions . . . . .	87
6.4	Simulation of the cluster size . . . . .	88
6.4.1	State of the art before 2012 . . . . .	88
6.4.2	New simulation procedure . . . . .	89
6.4.3	Results with the new class . . . . .	91
<b>7</b>	<b>Muon Trigger performance in Pb–Pb collisions</b>	<b>93</b>
7.1	Muon Trigger configurations . . . . .	93
7.2	Analysis conditions . . . . .	94
7.3	Multiplicities . . . . .	94
7.3.1	Muon multiplicity . . . . .	95
7.3.2	Strip multiplicity . . . . .	96
7.4	Trigger response as a function of $p_T$ . . . . .	97
7.4.1	Effects of the cluster size . . . . .	97
7.5	Global triggers . . . . .	100
7.6	Trigger-tracking matching probability . . . . .	101
<b>8</b>	<b>Analysis of <math>\Upsilon</math> production in Pb–Pb collisions</b>	<b>103</b>
8.1	$\Upsilon$ analysis framework . . . . .	103
8.1.1	The Correction Framework . . . . .	103
8.1.2	Dedicated classes for $\Upsilon$ analysis . . . . .	104
8.2	Data processing . . . . .	106
8.2.1	Pass1 . . . . .	106
8.2.2	Pass2 . . . . .	106
8.2.3	Pass2 after refit . . . . .	107
8.3	Data selection . . . . .	108
8.3.1	Triggers . . . . .	108
8.3.2	Centrality . . . . .	108
8.3.3	Number of minimum bias events . . . . .	109
8.3.4	Track selection . . . . .	110
8.4	Signal extraction . . . . .	111
8.4.1	Fit procedure . . . . .	111
8.4.2	Fit results . . . . .	113
8.4.3	Systematic uncertainties . . . . .	115
8.5	MC simulation . . . . .	122
8.5.1	Embedding production . . . . .	122
8.5.2	Systematic uncertainties on MC parametrizations . . . . .	126
8.6	Systematic uncertainties on detector response . . . . .	128
8.7	pp reference cross section . . . . .	129
8.7.1	Interpolation of the $\Upsilon(1S)$ cross section at midrapidity . . . . .	130
8.7.2	Extrapolation to forward rapidity . . . . .	131
8.8	Summary of the uncertainties . . . . .	135
8.9	Nuclear modification factor . . . . .	136
8.9.1	Method . . . . .	136

8.9.2	Results . . . . .	137
8.10	Central-to-peripheral ratio . . . . .	139
<b>9</b>	<b>Discussion and comparison of the results</b>	<b>140</b>
9.1	Comparison to the $J/\psi$ $R_{AA}$ measured at forward rapidity by ALICE . . . . .	140
9.2	Comparison to the CMS results . . . . .	142
9.3	Comparison to theoretical predictions . . . . .	144
<b>10</b>	<b>Conclusions and outlook</b>	<b>147</b>
10.1	Muon Trigger cluster size . . . . .	147
10.2	Muon Trigger performance . . . . .	147
10.3	$\Upsilon$ production . . . . .	148
<b>A</b>	<b>Fitting functions</b>	<b>149</b>
A.1	Crystal Ball function . . . . .	149
A.2	Extended Crystal Ball function . . . . .	149
A.3	Double exponential function . . . . .	151
A.4	Double power-law function . . . . .	151
	<b>Résumé</b>	<b>152</b>
	<b>Abstract</b>	<b>154</b>
	<b>List of Figures</b>	<b>156</b>
	<b>List of Tables</b>	<b>164</b>
	<b>Bibliography</b>	<b>166</b>
	<b>Acknowledgements</b>	<b>179</b>

# Introduction

Ultrarelativistic heavy-ion collisions are the unique tool to produce in laboratory nuclear matter at very high temperature and energy density. Under these extreme conditions, the created system undergoes a phase transition, from the ordinary hadronic phase constituted by uncoloured baryons and mesons, to a new state of deconfined quarks and gluons, called Quark-Gluon Plasma (QGP).

Amongst the possible probes of the QGP, heavy quarks are of particular interest since they are expected to be produced in the primary partonic scatterings and to coexist with the surrounding medium. Therefore, the measurement of the quarkonium production is expected to provide the essential information on the properties of the strongly-interacting system formed in the early stages of heavy-ion collisions. Furthermore, according to the colour screening model, measurement of the in-medium dissociation of the different quarkonium states should provide an estimate of the initial temperature of the system.

A Large Ion Collider Experiment (ALICE) is specifically designed to study the characteristics of this matter created by colliding Pb nuclei accelerated in the Large Hadron Collider (LHC) of CERN at a center-of-mass energy of 2.76 TeV per nucleon.

Beside the ALICE detectors, the Muon Spectrometer is dedicated to the study of quarkonium, open heavy-flavours and low-mass mesons via the (di)muon decay channel at forward rapidity ( $2.5 < y < 4$ ) and down to  $p_T = 0$ .

The work here presented was carried out from 2011 to 2013 during the first years of data taking of ALICE. It is mainly focused on the analysis of the  $\Upsilon$  production in Pb–Pb collisions, but important detector performance are also studied<sup>1</sup>. This Ph.D. thesis is divided in the following chapters:

- in **Chap. 1** a short introduction to the Quark-Gluon Plasma (QGP) in heavy-ion collisions is given and the most important experimental

---

<sup>1</sup>Warning: all figures obtained from my data analysis without the ALICE logo are not officially approved by the ALICE Collaboration (except Fig. 8.19, 8.20 and all those contained in Chap. 9). Therefore, they must be considered as results of my personal work under my own responsibility.

signatures are described;

- **Chap. 2** contains an overview of the quarkonium production with a particular regard to the role played by the hot and dense medium;
- **Chap. 3** is a review of the most important results obtained so far on the  $\Upsilon$  production in different colliding systems with a comparison to theoretical models;
- in **Chap. 4** the LHC facility and the ALICE apparatus are briefly described, focusing the attention on the performance of those detectors directly involved in the following analyses;
- the Muon Spectrometer is described in **Chap. 5** with particular attention to the trigger system: the hardware and software components and their behaviour are summarized;
- **Chap. 6** is dedicated to the analysis of the Muon Trigger cluster size: after an introduction of the topic, its simulation procedure is described and the results are compared to real data;
- **Chap. 7** contains a description of some Muon Trigger performance in Pb–Pb collisions in order to demonstrate the good stability of the detector and its effectiveness in view of the analysis contained in next chapter;
- the analysis of  $\Upsilon$  production in Pb–Pb at  $\sqrt{s_{NN}} = 2.76$  TeV is presented in **Chap. 8** in order to extract the nuclear modification factor and the central-to-peripheral ratio used to quantify the QGP formation;
- in **Chap. 9** the results obtained in the previous chapter are compared to other experimental measurements and to the prediction of models described in Chap. 3;
- finally, **Chap. 10** contains a summary of the most important results achieved in this thesis and the future perspectives.

# Chapter 1

## The Quark-Gluon Plasma in heavy-ion collisions

The main purpose of ultrarelativistic heavy-ion collisions is the investigation of a complex and evolving system in extreme conditions of energy density and temperature, called Quark-Gluon Plasma (QGP). In this chapter the QGP and its most important signatures will be described after a brief introduction to the quantum chromodynamics.

### 1.1 QCD and asymptotic freedom

The Standard Model of particle physics was formulated in its present form in the 1970s after a variety of experimental discoveries and theoretical predictions. To the present knowledge, all matter is built up by 12 elementary fermions (6 leptons and 6 quarks) and their interactions are mediated by 5 bosons, as depicted in Fig. 1.1.

Quantum chromodynamics (QCD), the gauge field theory that describes the strong interactions of coloured quarks and gluons, is the SU(3) component of the SU(3)×SU(2)×U(1) unitary groups of the Standard Model. One of its fundamental properties is the running coupling constant, i.e. the dependence of the coupling constant  $\alpha_s$  on the scale of the momentum transfer  $Q$ , according to the following equation for 1-loop corrections [1]:

$$\alpha_s(Q) = \frac{12\pi}{(11n_c - 2n_f) \ln\left(\frac{Q^2}{\Lambda_{QCD}^2}\right)} \quad (1.1)$$

where  $n_c$  and  $n_f$  are the number of colours and the number of quark flavours respectively.

When  $Q$  is high (i.e. the scale of the interaction is very small) the coupling constant is small as shown in Fig. 1.2. This is the *asymptotic*

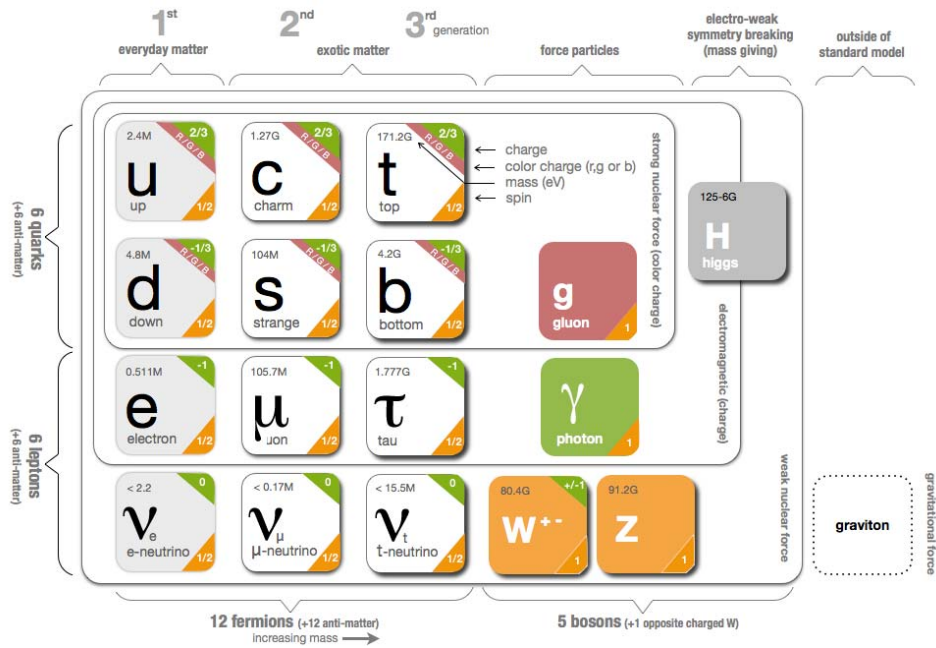


Figure 1.1: The fundamental particles predicted by the Standard Model.

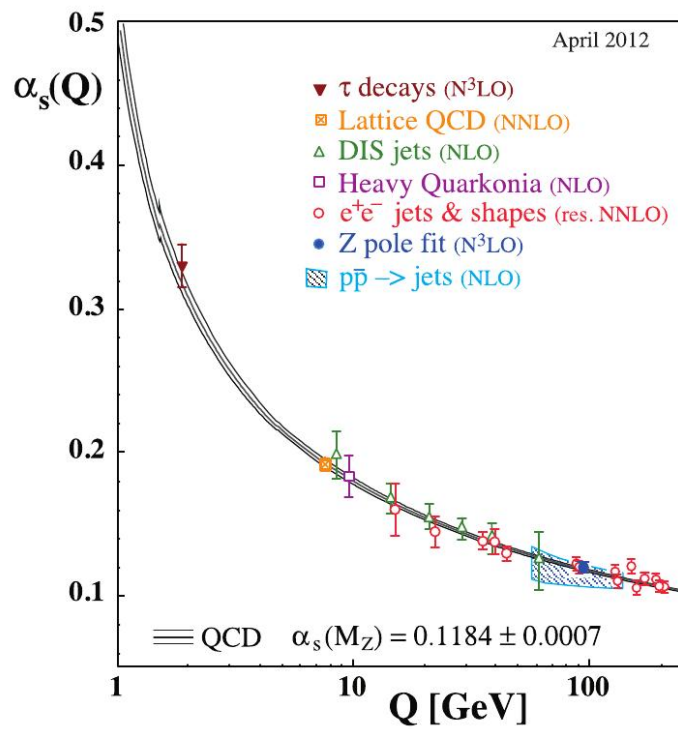


Figure 1.2: Summary of  $\alpha_s$  measurements as a function of the energy scale  $Q$  [2].

*freedom* regime which means that in very high-energy reactions, quarks and gluons interact weakly. In the framework of  $\alpha_s \ll 1$ , perturbative QCD (pQCD) approach can be used to make predictions for observables expressed in terms of powers of coupling constant  $\alpha_s$  [3].

On the other hand, when the distance scale is large the constituent quarks are subject to confining forces and the colour degree of freedom is confined into hadrons. This condition called *confinement* is the situation observed at the energy densities and temperatures typical of standard nuclear matter. In this regime  $\alpha_s$  is not small enough to use pQCD.

The QCD scale  $\Lambda_{QCD} \sim 200$  MeV delimits the two conditions [2].

## 1.2 The Quark-Gluon Plasma

Several models, using the quantum chromodynamics theory as input, predict that hadronic matter, in conditions of extreme energy density and temperature, could undergo a phase transition to a state of matter where quarks and gluons are deconfined. This new state is called *Quark-Gluon Plasma* [4, 5] and is described as matter which no longer consists of hadrons (baryons and mesons), but is made up of their fundamental constituents: quarks and gluons.

Three different approaches based on QCD are developed in order to study the QGP.

- pQCD: it can be used only to describe those processes such as heavy-flavour production in hadron collisions which guarantee the  $\alpha_s \ll 1$  condition.
- Effective models: they provide a phenomenological and qualitative description of the physical processes. This approach is extremely useful to predict some of the fundamental properties of the hadronic matter. The MIT bag model [6] and the parton models are widely used for practical calculations.
- Lattice QCD: it is a non-perturbative treatment of QCD formulated on a discrete lattice of space-time coordinates and provides a quantitative understanding of the new phase of matter [7]. Nevertheless, these calculations show uncertainties related to limitations on the lattice spacing and size mainly due to the big amount of computing power needed.

The asymptotic freedom suggests two possibilities to vanishing coupling constant and to create the QGP: either the energy must be increased or the distances decreased. The former can be achieved by increasing the tempe-

perature ( $T$ ), the latter by increasing the baryonic chemical potential ( $\mu_B^1$ ), i.e. the baryon density for a certain volume.

Fig. 1.3 presents the  $(T, \mu_B)$  phase diagram of strongly interacting matter. Analogous to that for ordinary matter, it presents a first order phase transition (blue line) between the hadronic phase and the QGP. A critical endpoint separates the transition from a crossover region<sup>2</sup> also predicted by lattice QCD [8, 9].

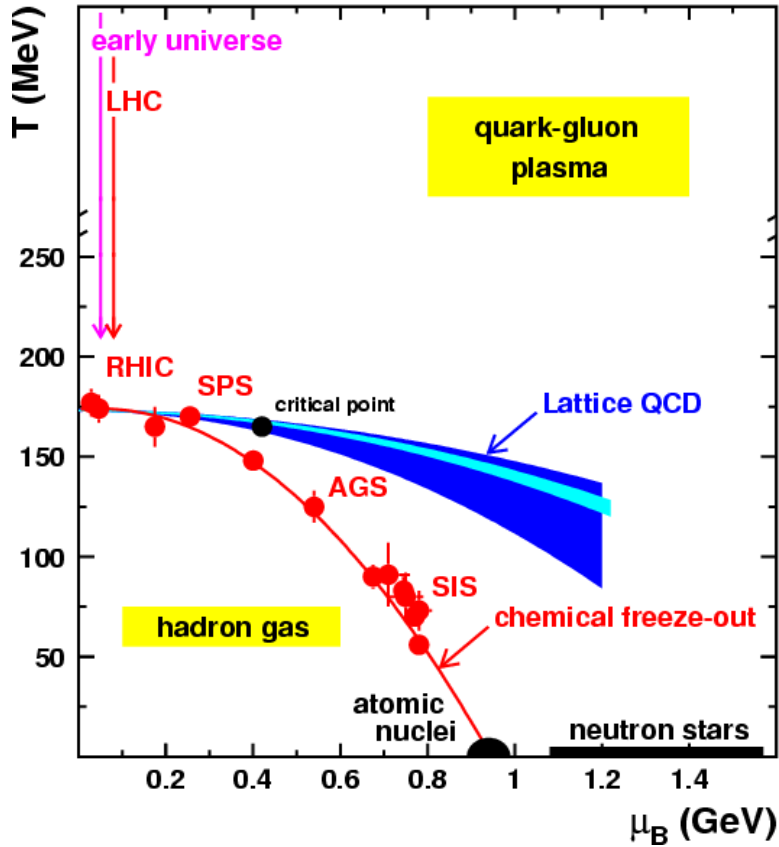


Figure 1.3: QCD phase diagram as predicted by lattice QCD calculations and with experimental points, adapted from [9, 10].

The red line corresponds to the chemical freeze-out edge (see later): it is a fit of statistical model to the data in heavy-ion collisions at different center-of-mass energies [11, 12].

<sup>1</sup>In thermodynamics the baryonic chemical potential is defined as the partial derivative of the internal energy with respect to the number of baryons at volume and entropy fixed:  $\mu_B = \left( \frac{\partial E}{\partial N_B} \right)_{S,V}$ .

<sup>2</sup>A first order phase transition exhibits a discontinuity in the first derivative of the free energy with respect to a given thermodynamic variable. In a crossover the transition happens without any discontinuity.

Depending on the details of the calculations, the critical temperature  $T_c$  at  $\mu_B = 0$  should be around 170 MeV [8, 13, 14, 15, 16], while the critical potential  $\mu_{B,c}$  at  $T = 0$  is around  $1.1 \div 1.2$  GeV, according to the rough estimate provided by the MIT bag model [6].

The QGP is expected to be created in the following processes.

- The universe is assumed to be created after a big bang expanding from a singularity. Measurements of the cosmic microwave background provide the current temperature of the universe of  $2.725 \text{ K} \cong 2.3 \cdot 10^{-13} \text{ GeV}$  [17]. It is expected that the QCD critical temperature was passed in the early universe roughly some  $\mu\text{s}$  after the big bang. In the phase diagram in Fig. 1.3 this evolution corresponds to a path at low  $\mu_B$  values, close to the  $y$ -axis, from high to low temperatures.
- In the core of neutron stars the gravitational pressure and the baryonic chemical potential are supposed to exceed the critical value of  $\mu_B$ , pushing the nucleons so tightly into each other that the constituting quarks cannot be assigned to one or another nucleon [18].
- Finally, QGP can be produced in high-energy collisions of heavy cosmic rays with other heavy particles or in controlled heavy-ion collisions<sup>3</sup> in accelerator experiments.

### 1.3 Heavy-ion collisions

The region of high  $T$  and low  $\mu_B$  of the QCD phase diagram is experimentally investigated with ultrarelativistic heavy-ion collisions in various laboratories, such as the Brookhaven National Laboratory in the USA and at CERN in Switzerland.

At low energies, up to a few tens of GeV per nucleon, the colliding nuclei tend to stop each other reaching moderately high temperatures and high baryonic densities. Increasing the energy above 100 GeV per nucleon, the nuclei pass through each other leaving extremely high temperatures but very low baryonic densities: this regime is called *transparency*.

Before the collision, the ions travel along the beam axis with a velocity close to the speed of light and can be depicted as thin disks due to the Lorentz contraction. After the collision, a large amount of inelastic scatterings of the nucleons of the two nuclei take place.

The energy density generated can be estimated by means of the Bjorken formula measuring the average charged particle multiplicity produced per rapidity unit:

$$\varepsilon = \frac{1}{\tau_f A} \langle m_T \rangle \frac{dN}{dy} \quad (1.2)$$

---

<sup>3</sup>Usually indicated as AA collisions.

where  $\tau_f$  is formation time of the particles,  $A$  is the section of the nuclei and  $\langle m_T \rangle$  is the average transverse mass ( $\sqrt{E^2 - p_z^2}$ ). According to the MIT Bag Model, an energy density around  $1 \text{ GeV}/\text{fm}^3$  is needed to create the Quark-Gluon Plasma [6].

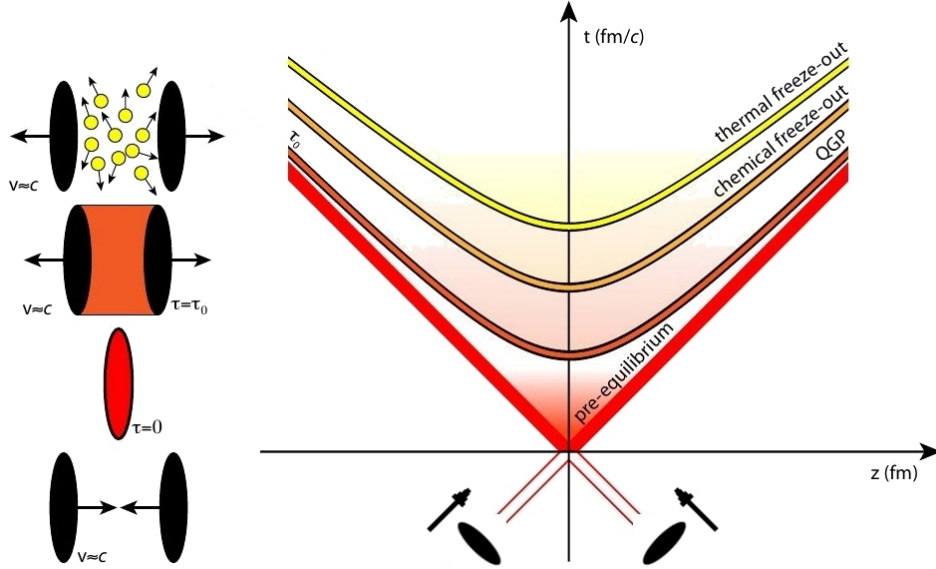


Figure 1.4: Space-time evolution of an heavy-ion collision [19].

The time evolution of the collision is shown in Fig. 1.4. On the left side of the figure, from bottom to top, the colliding nuclei are shown right before the collision, when the collision takes place at  $\tau = 0$ , at  $\tau = \tau_0$  (when the QGP is created) and after the phase transition back to hadronic matter. Each stage is delimited by an hyperbola  $\tau = \sqrt{c^2 t^2 - z^2}$  ( $\tau$  is the proper time) on the right side. Here the two incident nuclei are drawn as the two red lines in a space-time diagram. At the origin of the diagram the nuclei hit and start passing through each other. In this initial stage called *pre-equilibrium* very hard processes with high momentum transfer occur within partons. As an example, the creation of heavy  $q\bar{q}$  pairs predominantly happens for gluon fusion in this phase. After a fraction of fm/c, multiple scattering processes among the nucleons and their constituents lead to a thermal equilibration of the medium, a fireball of strongly interacting matter, the Quark-Gluon Plasma. The maximum energy density reached can be estimated using Eq. 1.2: it is around  $3 \text{ GeV}/\text{fm}^3$  at Super Proton Synchrotron (SPS), between 5 and  $10 \text{ GeV}/\text{fm}^3$  at the Relativistic Heavy-Ion Collider (RHIC) and it is expected to be some tens of  $\text{GeV}/\text{fm}^3$  at the LHC [20], as reported in Fig. 1.5 along with the maximum temperature reached expressed in terms of  $T_c$ . Being surrounded by the vacuum, the QGP expands and cools down. The fireball dimension at the LHC energy is around  $300 \text{ fm}^3$  [21]. Hydro-

dynamic models describe successfully the evolution of the medium [22] with the thermodynamic equations using the grand canonical ensemble.

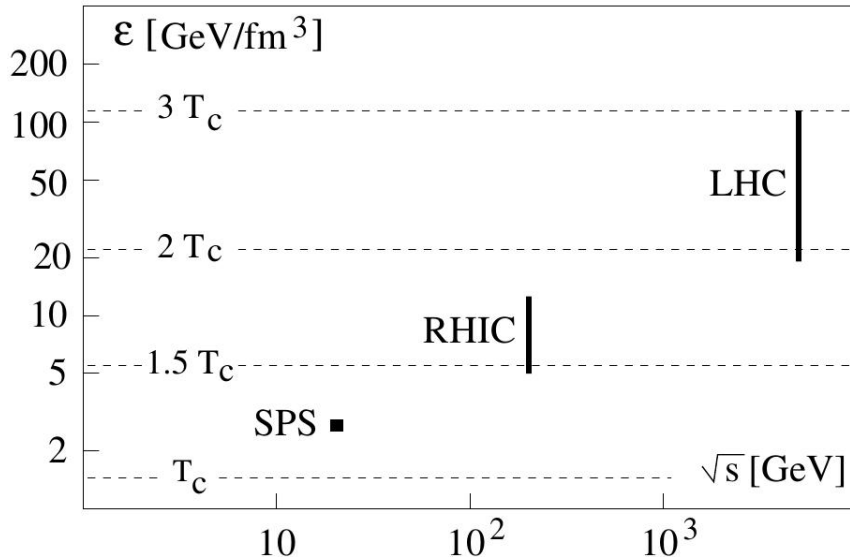


Figure 1.5: Energy densities and temperatures expressed in units of  $T_c$  for different collision energies [20].

When the temperature drops, the phase boundary is crossed and the medium begins to hadronize. The lifetime of the plasma depends on the energy density reached in the collision. It approximately ranges from 1 fm/c at the SPS to some fm/c at the LHC. At the *chemical freeze-out* the kinetic energy of the produced particles is too low to allow for further inelastic collisions: from this moment on, all abundances and particle ratios are fixed. Finally, after the *thermal freeze-out*, also elastic collisions cease and the kinematic distributions of the particles are fixed.

## 1.4 QGP effects: experimental signatures

The very short lifetime of the QGP (only a few  $10^{-23}$  s) does not allow to measure directly its characteristics. For this reason, only indirect signals are able to probe the properties of the medium. The most relevant signatures are now briefly summarized.

- Two quarks or two gluons can be produced at the early stage of the collision back-to-back with high  $p_T$ . If it happens near the surface of the fireball, one of them can hadronize and form a jet without interacting with the medium, while the other, passing through a big part of the plasma, loses energy mainly by gluon radiation proportional to

the square of the in-medium path length [23, 24]. The visible effect is the away-side jet quenching.

- High- $p_T$  particles (such as heavy-flavour mesons) produced in primordial  $q\bar{q}$ ,  $gg$  or  $qq$  reactions with high momentum transfer are attenuated by gluonic bremsstrahlung in the medium [25, 26]. This phenomenon is similar to the jet quenching.
- The partonic pressure gradients (typical of an expanding system) create hydrodynamic collective motions called flows taking place at the beginning of the thermal equilibrium. The radial flow is a collective global expansion [27, 28, 29] of all the particles composing the system. The elliptic flow happens in non-central collision when the overlap region of the two nuclei has an almond shape leading to a spatial and momentum anisotropy of the particles produced due to pressure gradients [30, 31].
- The hadronic chemical freeze-out fixes the abundance ratios of the hadronic species. Occurring close to the hadronization phase, it reveals the dynamical evolution path in the QCD phase diagrams.
- According to the Standard Model Lagrangian, the QCD chiral symmetry is spontaneously broken, but it is supposed to be restored in a deconfined medium with very high density energy like QGP [32]. Measurements of low-mass vector meson yield (as  $\rho$ ,  $\omega$  and  $\phi$ ) could give hints about this possible restoration [33].
- The quarkonium production plays a key role in the study of the hot and interacting medium. Due to its importance for this thesis, it will be widely discussed in the next chapter.

## Chapter 2

# Quarkonium in medium

The following chapter is dedicated to the quarkonium bound states (charmonium,  $c\bar{c}$ , and bottomonium,  $b\bar{b}$ ) which represent a very important testing ground for the QCD theory and are a fundamental probe for the QGP. The most important properties are briefly discussed and the effects on those particles of the hot medium are described.

### 2.1 Discovery of quarkonium states

The  $J/\psi$  meson (a  $c\bar{c}$  bound state) with a mass of  $3.1 \text{ GeV}/c^2$  was discovered in 1974 by two different laboratories almost at the same time. S. Ting observed a sharp peak in the electron-positron invariant mass spectrum studying 30 GeV protons accelerated by the AGS at Brookhaven National Laboratory (BNL) colliding on a fixed target [34], while B. Richter found the same structure in  $e^+e^-$  annihilation at the electron-positron storage ring SPEAR at the Stanford Linear Accelerator Center (SLAC) [35]. In the following weeks the Frascati group confirmed the presence of this new particle [36]. The first excited state of  $J/\psi$ , the  $\psi(2S)$  or  $\psi'$  was discovered by the same group at SLAC.

Afterwards a new resonance called  $\Upsilon$  ( $b\bar{b}$ ) was discovered at the Fermi National Accelerator Laboratory (FNAL) and in a short delay the excited states were found as well (for more details see Sec. 3.1).

In addition, many efforts were done to discover particles with total *charm* or total *beauty* flavours  $\neq 0$ . The first open charm meson named  $D^0$  was found in 1976 [37], the first charged charmed meson, the  $D^+$ , was discovered right after [38] and the first charmed baryon,  $\Lambda_c^+$ , was also discovered in the same year [39].

The CLEO Collaboration in 1980 found evidence of the the first open beauty meson ( $B$ ) [40] and one year later, the first baryon with a  $b$  quark (the  $\Lambda_b^0$ ) was seen at CERN [41].

---

<sup>1</sup>Due to the very short lifetime of the  $t$  quark, no  $t\bar{t}$  bound state can be formed.

Thanks to more and more recent generations of experiments, a large amount of heavier  $c\bar{c}$  and  $b\bar{b}$  resonances was found as  $\psi(3770)$ ,  $\psi(4040)$ ,  $\psi(4160)$ ,  $\psi(4415)$  and  $\Upsilon(10860)$ ,  $\Upsilon(11020)$  (all above open heavy-flavours threshold). The analysis of the radiative decays of the  $\psi$  and  $\Upsilon$  families led to the discovery of the  $1P$  states ( $\chi_c$  and  $\chi_b$  families) and of the lightest  $c\bar{c}$  resonance (the  $\eta_c(1S)$ ).

In 2012 the ATLAS Collaboration reported on the observation of a new conventional quarkonium state: the  $\chi_b(3P)$  [42]. This is, for the moment, the latest quarkonium state found.

## 2.2 Decay and feed-down of quarkonium

Vector quarkonia, like  $\psi$  and  $\Upsilon$  resonances, have a relatively high probability to decay into two leptons: the branching ratio of  $J/\psi \rightarrow e^+e^-$  or  $\mu^+\mu^-$  is 5.9%, while that for  $\Upsilon(1S) \rightarrow e^+e^-$  or  $\mu^+\mu^-$  is around 2.4% [2]. First, because these states are below the mass threshold for decaying into open heavy-flavour hadrons ( $m_{J/\psi, \psi(2S)} < 2m_D$  and  $m_{\Upsilon(1S, 2S, 3S)} < 2m_B$ ). Secondly, the characteristics of colour interaction prevent these states to decay into single gluon and quantum numbers conservation rules forbid the decay into two gluons: as a consequence the hadronic decay has to pass through a three gluons emission that is therefore suppressed. This is also the reason for having very narrow peaks: only 93 keV/c<sup>2</sup> for the  $J/\psi$  and even less (54 keV/c<sup>2</sup>) for the  $\Upsilon(1S)$  [2]. The aptitude to decay into leptons is widely exploited by the experiments. For instance, muons are not stopped by the detectors they pass through and can be detected by dedicated spectrometers. In this way the signal is not complicated by the large amount of hadron background which is characteristic of high-energy experiments.

Another important issue to be discussed is the feed-down from higher states and from open heavy-flavours. A  $J/\psi$  can come from the direct hadronization of a  $c\bar{c}$  (*direct*  $J/\psi$ ) or can be produced by the radiative transitions from excited and  $1P$  states ( $\psi(2S)$  or  $\chi_c(1P)$ ): they are usually called *prompt*  $J/\psi$ . The same happens for the  $\Upsilon(1S)$ , but in this case many more particles can decay into it. For the  $c\bar{c}$  family another contribution has to be considered. Open bottom mesons ( $B^\pm$ ,  $B^0$ ,  $B_s^0$  and  $B_c^\pm$ ) can weakly decay into *non-prompt*  $J/\psi$  or  $\psi(2S)$  with the formation of one or more hadrons. Prompt and non-prompt  $J/\psi$  or  $\psi(2S)$  form the inclusive sample. In Fig. 2.1 all the states of the charmonium family below the open heavy-flavour pair production threshold are shown along with their radiative transitions into lower mass states.

From the experimental point of view it is rather important to be able to disentangle the different creation processes, otherwise in case of a non negligible feed-down the comparison data-theory could be less meaningful (even if certain models can make inclusive predictions). Usually the non-

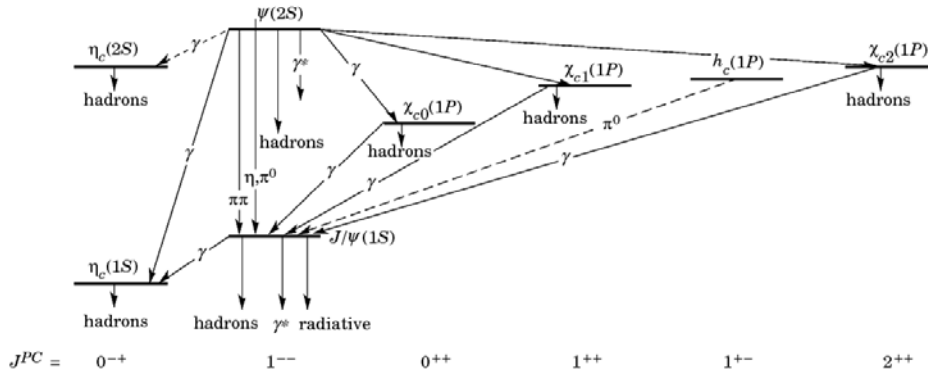


Figure 2.1: Charmonium decay modes with spectroscopy notation [43].

prompt component can be recognized exploiting the fact that the open-flavour decay into a quarkonium state is a weak process and occurs in a long time scale<sup>2</sup>: the daughter particles of the quarkonium (e.g. two muons) will then point back to a vertex different to the primary one. It is therefore sufficient to have a good vertex resolution for being able to subtract the non-prompt component. In the case of the radiative decays the situation is more complicated since the transition occurs at the scale of the electromagnetic interaction and no proper time cut can be applied. The common way to proceed is to measure the cross section for the production of the higher mass states and, through the branching ratio, to calculate the amount of lower states coming from radiative decay. This is much more difficult with respect to the non-prompt component determination, because higher mass states are in general more difficult to be detected.

## 2.3 Quarkonium production mechanisms

The processes involved in the quark pair creation and in the subsequent formation of the bound state strongly depend on the colliding particles [44]. In hadron collisions the dominant processes are gluon fusion and gluon fragmentation. Past experiments ruled out the hypothesis of electromagnetic production via  $q\bar{q}$  annihilation (the production rate of  $J/\psi$  in  $\pi^+N$  should be suppressed by a factor 4 with respect to that in  $\pi^-N$ , but it is not the case [45]). Similarly, the hypothesis of  $q\bar{q}$  annihilation into gluon as the main process was rejected after the comparison between the production rate in  $pp$  and in  $p\bar{p}$  (the difference in anti-quarks between  $p$  and  $\bar{p}$  should lead to a suppression in  $pp$  by a factor  $5 \div 10$ , not observed [45]).

The creation of a  $q\bar{q}$  pair occurs at short distance scale and can be calculated in perturbative approach. The leading-order QCD (LO QCD)

<sup>2</sup>Long if compared to hard or electromagnetic processes.

processes are quark and anti-quark pair annihilation in a virtual gluon and gluon-gluon fusion as shown in Fig. 2.2. Then, at long-distance scale a non-perturbative transition to the quarkonium state happens.

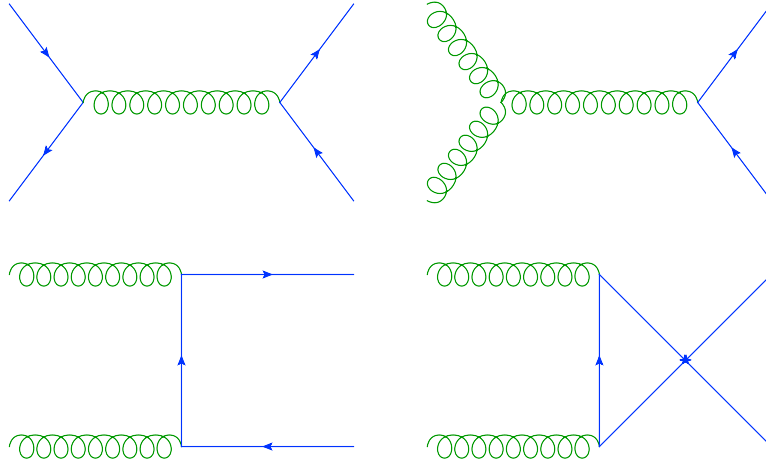


Figure 2.2: The LO QCD processes for quarkonium production.

The different treatments of the non-perturbative evolution of the  $q\bar{q}$  pair into a quarkonium lead to various theoretical models: Color Singlet Model, Color Evaporation Model and Non-Relativistic QCD are the most complete.

### 2.3.1 Color Singlet Model

The Color Singlet Model (CSM), proposed right after the discovery of the  $J/\psi$ , assumes that the  $q\bar{q}$  pair evolving in a quarkonium state is in a colour singlet state and the quantum numbers such as spin and angular momentum are conserved after the formation of the meson. The only inputs required in the model are the absolute value of the colour singlet  $q\bar{q}$  wave function and its derivatives that can be determined from data of decay processes. Once these quantities are provided, the CSM has no free parameters [46].

The CSM at leading-order predicts well the quarkonium production rates at relatively low energy [47], but fails to describe the data for charmonium measured by CDF experiment in  $p\bar{p}$  collisions [48] as shown in Fig. 2.3 probably because it ignores the fragmentation processes from higher states or  $B$  mesons, dominant at Tevatron energies [49].

### 2.3.2 Color Evaporation Model

The Color Evaporation Model (CEM) is a phenomenological model, initially introduced in 1977 [50, 51] and then revived in 1996 [52] due to the unsatisfactory performance of CSM.

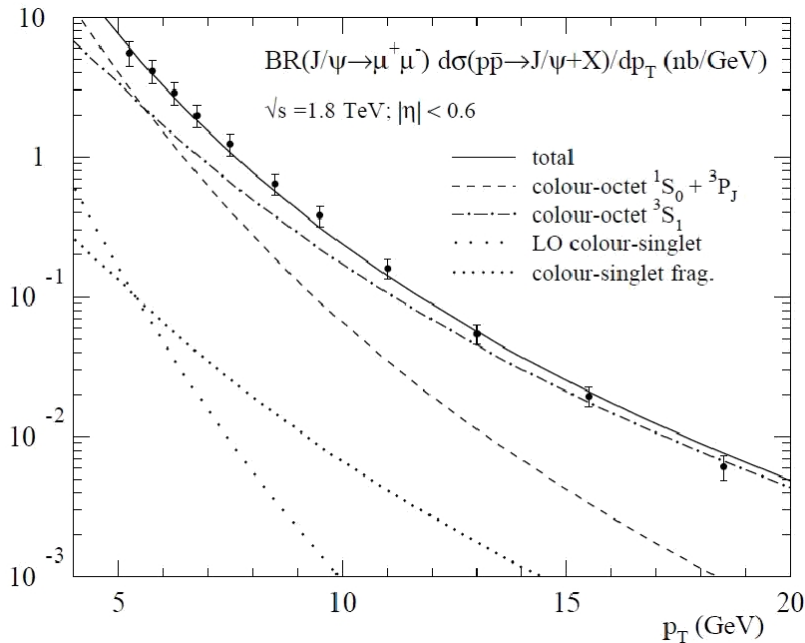


Figure 2.3: Comparison between CDF  $J/\psi$  measurements (full circles) and CSM (dotted lines), CEM (dashed and dashed dotted lines) and NRQCD (solid line) predictions [45].

In this approach, the production rate for the quarkonium state is a certain fraction of the cross section for producing  $q\bar{q}$  pairs with invariant mass below the lowest mass meson containing the heavy quark  $q$ . This cross section has an upper limit on the  $q\bar{q}$  pair mass, but no constraints on the colour or spin of the final state. The  $q\bar{q}$  pair is supposed to neutralize its colour by interaction with the collision-induced colour field by “colour evaporation” randomizing the spin of the pair. This assumption leads to the prediction that the quarkonium production rate is independent of the quarkonium spin of the quarkonium states. An important feature is that the fractions are assumed to be universal, so that, once they are determined by data, they can be used to predict the cross sections of other processes and in other kinematic regions.

The CDF measurements fitted with CEM predictions for charmonium states production also including  $\chi_c$  ( $P$  states) are shown in Fig. 2.3.

### 2.3.3 Non-Relativistic QCD

Within the framework of Non-Relativistic QCD (NRQCD) [53], the production cross section of a quarkonium state  $H$  can be written as a sum of terms taking into account a short distance partonic cross section and a long distance matrix element:

$$d\sigma(H) = \sum_n d\hat{\sigma}(q\bar{q}_n) \langle 0 | \mathcal{O}_n^H | 0 \rangle \quad (2.1)$$

The sum includes all possible colours and angular momenta of the  $q\bar{q}$  pair denoted by  $n$ . The short distance terms  $d\hat{\sigma}$  are proportional to the cross sections for production of a  $q\bar{q}$  pair in the state  $n$  and with small relative momentum that can be calculated in perturbative theory. The transition probabilities from the  $q\bar{q}$  state  $n$  into the quarkonium  $H$  are given by the vacuum expectation values of NRQCD operators.

NRQCD is the only model able to reproduce the cross section of charmonium production in  $p\bar{p}$  collisions at Tevatron energies (Fig. 2.3), but it fails to describe the polarization of quarkonium<sup>3</sup> as shown in Fig. 2.4 [54].

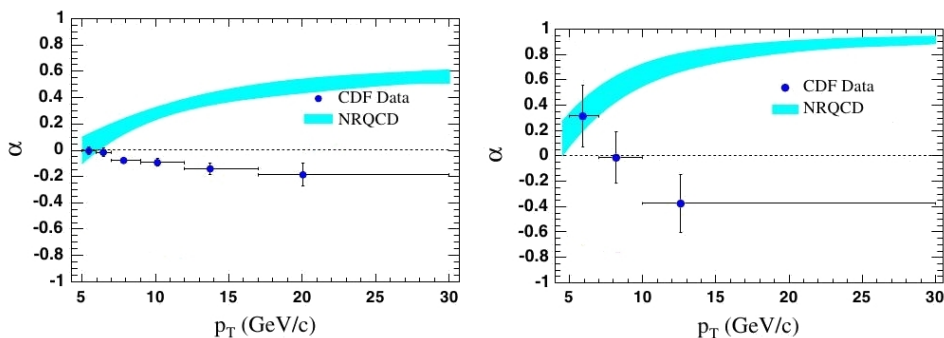


Figure 2.4: Prompt polarization of  $J/\psi$  (left) and  $\psi(2S)$  (right) as a function of  $p_T$  measured by CDF experiment compared to NRQCD predictions [54].

To conclude, the mechanism of quarkonium production is still an open question. The efforts for establishing the theory are still ongoing and its completion will help to understand the phenomena expected in the medium created in heavy-ion collisions.

## 2.4 Quarkonium as a probe of the QGP

The bound state of heavy quarks can be described by the Schrödinger equation justified by the non-relativistic quark motion:

$$\left( -\frac{\nabla^2}{2\mu} + V(r) \right) \psi(r) = E \psi(r) \quad (2.2)$$

where  $\mu = m_q/2$  is the reduced mass,  $E$  is the binding energy and  $V(r)$  is the static Cornell  $q\bar{q}$  potential composed of two parts [55]:

$$V(r) = -\frac{4}{3} \frac{\alpha_s}{r} + \sigma r \quad (2.3)$$

<sup>3</sup>The polarization measures the degree of spin alignment of a particle with respect to a chosen axis. See Sec. 3.2.1 for more details.

The Coulomb-like term describes the single-gluon exchange between quark and anti-quark and is the result of first-order pQCD calculation, while the second part is a confinement term which parametrizes the non-perturbative effects. The parameter  $\sigma$  represents the strength confinement force.

When the quarkonium is immersed in the QGP, the surrounding matter alters the confinement term potential which vanishes. The high density of partons around the heavy quark pair modifies as well the remaining Coulomb-like component into a short-range Yukawa-like potential (Eq. 2.4):

$$V(r) = -\frac{4}{3} \frac{\alpha_s}{r} \cdot e^{-\frac{r}{\lambda_D}} \quad (2.4)$$

The effect is similar to the electromagnetic screening due to the atomic plasma made of positive and negative charges.  $\lambda_D$  is the Debye length: if two quarks are closer than this parameter they can be considered as interacting and tied, otherwise resonance can not be formed. Basing on pQCD calculations, it is possible to demonstrate that  $\lambda_D \propto \frac{1}{\sqrt{T}}$ , i.e. it decreases with increasing temperature of the medium. At high temperatures, the range of the attractive interaction becomes so small to make impossible the formation of a  $q\bar{q}$  bound state. When it happens, the pair dissociates into separate quarks in the plasma [56].

Since resonances have different dimensions and binding energies, it is expected that the less tightly bound states melt at lower temperatures: this effect is known as *sequential suppression* [57]. While the excited states are dissociated just above the critical temperature  $T_c$  needed to form the QGP, the fundamental states melt far above that value, as shown in Tab. 2.1.

It is important to note that the uncertainties are large and old calculations predict lower values than those reported here. The dissociation of specific resonances can thus be used as a thermometer of the QGP.

State	J/ $\psi$	$\chi_c$	$\psi(2S)$	$\Upsilon(1S)$	$\chi_b(1P)$	$\Upsilon(2S)$	$\Upsilon(3S)$
$\Delta E$ (GeV)	0.64	0.20	0.05	1.10	0.67	0.54	0.20
$r_0$ (fm)	0.50	0.72	0.90	0.28	0.44	0.56	0.78
$T_d/T_c$	2.10	1.16	1.12	> 4	1.76	1.60	1.17

Table 2.1: Quarkonium binding energies ( $\Delta E$ ), quark distance ( $r_0$ ) and dissociation temperatures in units of  $T_c = 173$  MeV [58].

An opposite mechanism to the suppression taking place in AA collisions is the statistical hadronization of the heavy quarks emerging from the medium leading to a quarkonium regeneration, more and more important when the center-of-mass energy of the collision increases since more and more heavy quarks are produced. Seen the number of  $q\bar{q}$  reported in Tab. 2.2, this contribution is expected to be important for the charmonium yield and negligible or very small for the  $\Upsilon$  yield, even at the LHC energy.

Accelerator and center-of-mass energy	SPS 20 GeV	RHIC 200 GeV	LHC 2.76 TeV
$N_{c\bar{c}}/\text{event}$	$\sim 0.2$	$\sim 10$	$\sim 60$
$N_{b\bar{b}}/\text{event}$	–	$\sim 0.05$	$\sim 4$

Table 2.2: Number of heavy quark pairs produced in central heavy-ion collisions at different energies.

## 2.5 Cold nuclear matter effects

The quarkonium suppression in the hot and dense medium described before relies on rather solid theoretical basis, but the direct comparison of theory with data is complicated by concurrent mechanisms named cold nuclear matter (CNM) effects. The name cold matter arises because these effects are observed in proton-nucleus or deuteron-nucleus<sup>4</sup> interactions where no hot or dense matter effects are expected. They can either suppress or enhance the quarkonium production.

### 2.5.1 Initial-state effects

Shadowing, parton energy loss and Cronin effect are classified as initial-state effects, as they affect the partons before the hard scattering.

#### Shadowing

The parton distribution function (PDF) of a free nucleon differs from that of a nucleon bound in a nucleus. Fig. 2.5 shows the prediction of the EPS09 model of the ratio  $R_G^A(x, Q^2)$  between the gluon PDF in a nucleon of a Pb nucleus and in a free proton as a function of the Bjorken- $x$ <sup>5</sup>. Four regions can be distinguished: *shadowing* at very small  $x$  values ( $x \lesssim 10^{-2}$ ); *anti-shadowing* for  $10^{-2} \lesssim x \lesssim 0.5$ ; *EMC effect* at  $0.5 \lesssim x \lesssim 0.7$  (named after the European Muon Collaboration and due to the nucleon-nucleon interaction with pions exchange); *Fermi motion* where  $x$  is very close to 1 [59].

Since the quarkonium cross sections directly depend on these partonic distribution functions, the modifications have to be accounted for when comparing different collision systems such as pp, pA or AA. At the LHC energies the region of very small  $x$  is accessible [60] and therefore an important shadowing effect is expected.

<sup>4</sup>Also indicated as pA or dA collisions.

<sup>5</sup>The Bjorken- $x$  is the momentum fraction carried by a parton in the nucleon.

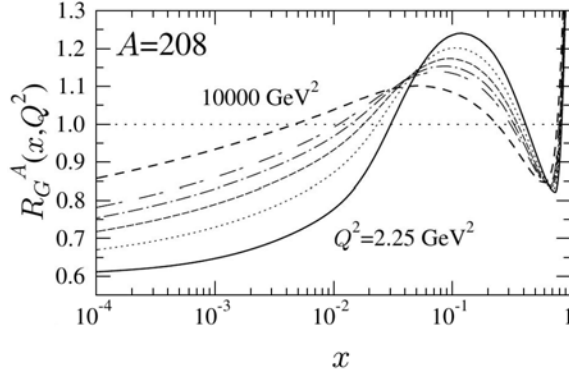


Figure 2.5: Scale evolution of the ratios  $R_G^A(x, Q^2)$  for a Pb nucleus and different values of  $Q^2$  [59].

### Coherent parton energy loss

When a parton (quark or gluon) moves through the nucleus, it can scatter elastically and lose energy before the hard scattering. This initial state energy loss that essentially depletes the projectile parton is responsible of a suppression of the hadrons in pA collisions [61].

### Cronin effect

In pA collisions a parton can undergo a multiple scattering process in the nucleus before to hadronize. Contrary to the parton energy loss effect, in this case the parton survives to the medium and in his random walk it acquires an extra transverse momentum which will modify the  $p_T$  differential spectrum of the hadrons with respect to pp collisions. This effect is responsible of an enhanced hadron production in pA collisions as measured by the STAR Collaboration at RHIC (Fig. 2.6) [62].

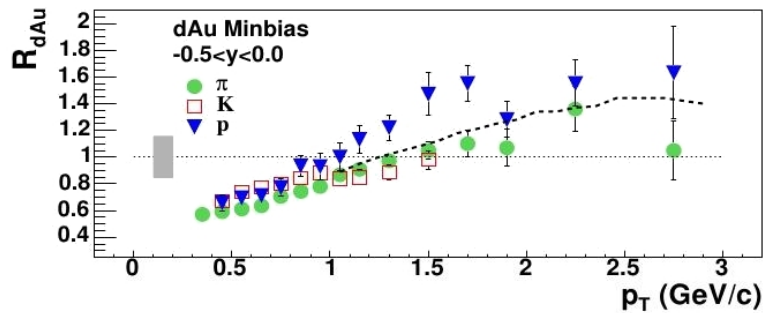


Figure 2.6: Hadron yields in dAu collisions at  $\sqrt{s_{NN}} = 200$  GeV normalized to pp collisions. Dashed line is the  $R_{dAu}$  of inclusive charged hadrons [62].

### 2.5.2 Final-state effects

Final-state cold nuclear matter effects taking place after the hadronization include nuclear and comovers absorption.

#### Nuclear absorption

Nuclear absorption occurs when the  $q\bar{q}$  pair is formed and passes through the nucleus. The effect is responsible of the break-up of the quarkonium state. It is parametrized using a phenomenological production cross section [61]:

$$\sigma(AB \rightarrow J/\psi) \propto AB e^{-\rho_0 \sigma_{abs} L} \quad (2.5)$$

where  $A$  and  $B$  are the mass numbers of the two colliding nuclei,  $\rho_0$  is the ordinary nuclear density,  $L$  is the path length of the  $q\bar{q}$  pair through the nuclear matter and  $\sigma_{abs}$  is the absorption cross section determined in pA or dA collisions. The probability to survive from the absorption depends on  $\sigma_{abs}$  of the quarkonium which decreases increasing the collision energy [63, 64].

#### Comovers absorption

In a dense gas system formed by conventional hadrons like pions and kaons, the quarkonium could be suppressed by processes like  $J/\psi + \pi \rightarrow D + \bar{D} + X$ , called suppression by hadronic comovers. This process can be described by a cross section analogue to Eq. 2.5, but in this case the density  $\rho$  evolves with the time due to the expansion of the system [61].

## 2.6 Quarkonium measurements in heavy-ion collisions

The quarkonium suppression can be quantified experimentally analysing the yields as a function of the collision centrality: the production is in fact expected to drop in central collisions where the number of interacting nucleons is high enough to reach temperatures above the deconfinement threshold. The information is estimated via the nuclear modification factor  $R_{AA}$ , defined as the yield in nucleus-nucleus collisions normalized to a reference obtained in absence of QGP (usually pp or pA collisions). Another indicator used is the  $R_{CP}$  (central-to-peripheral ratio), similar to the previous observable, but normalized to the yield measured in peripheral collisions where the deconfinement is not expected.

What follows is a short review of the main results on charmonium in heavy-ion collisions. An exhaustive description of  $\Upsilon$  mesons production will be given in Chap. 3.

### 2.6.1 Before the LHC era

The fixed target experiment NA50 at the SPS studied  $J/\psi$  suppression in Pb–Pb collisions at 158 GeV/nucleon. An anomalous suppression, stronger than the expected one in case of only cold nuclear matter effects, is observed in central Pb–Pb collisions [65].

The CNM effects are extracted by extrapolating the  $J/\psi$  production data collected in various pA collisions at 450 GeV and in a slightly different rapidity domain. The suppression pattern is shown in Fig. 2.7 as a function of the path length of the particle in the nuclear matter. The observed maximum suppression of  $\sim 40\%$  is compatible with the suppression of the  $\chi_c$  and  $\psi(2S)$  mesons, since the feed-down of the  $J/\psi$  from higher resonances is around 35%.

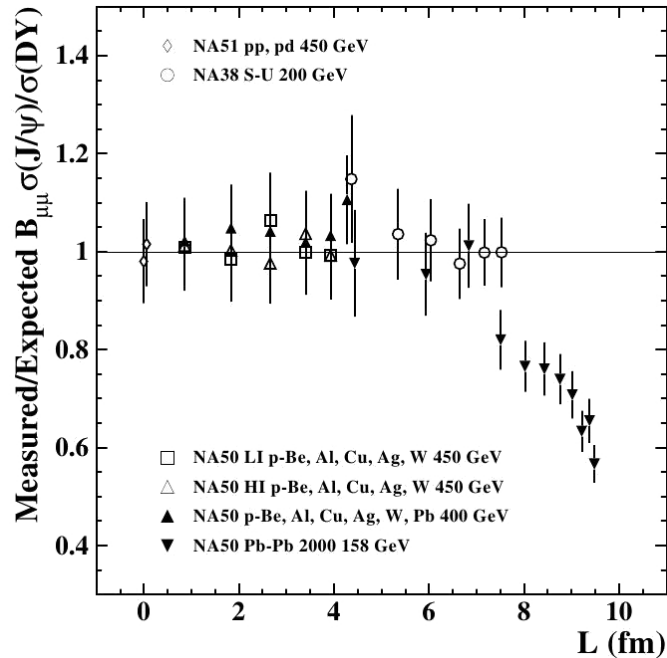


Figure 2.7: The  $J/\psi$  and Drell-Yan cross section ratio vs the path length in nucleus ( $L$ ) divided by the normal nuclear absorption pattern for several collision systems [65].

The NA60 Collaboration measured the  $J/\psi$  production in In–In and different pA collisions at the same energy than NA50 [66]. The trend in Fig. 2.8 as a function of the participants confirms the stronger suppression in the most central collisions seen by the previous experiment.

The PHENIX experiment at RHIC measured the  $J/\psi$  suppression in Au–Au collisions at  $\sqrt{s_{NN}} = 200$  GeV [67] in two rapidity bins, as reported in Fig. 2.9. The stronger suppression at forward rapidity than at midrapidity

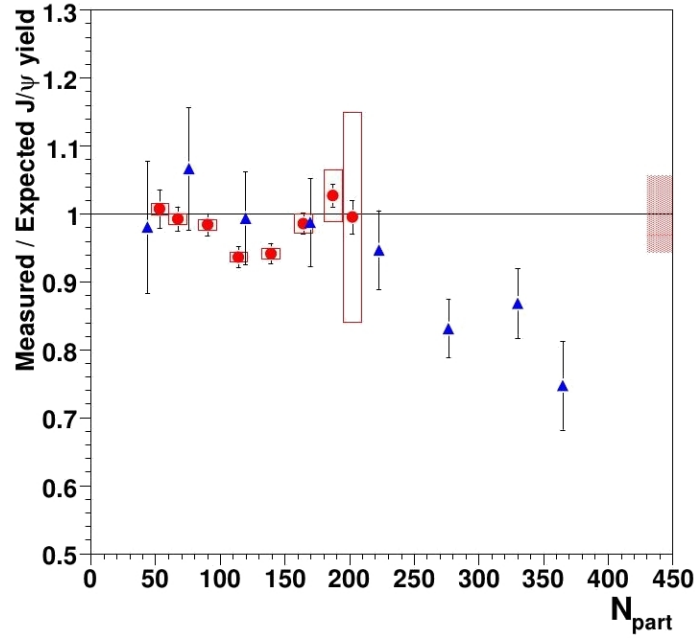


Figure 2.8:  $J/\psi$  suppression pattern in In-In (circles) and Pb-Pb (triangles) from NA60 experiment [66].

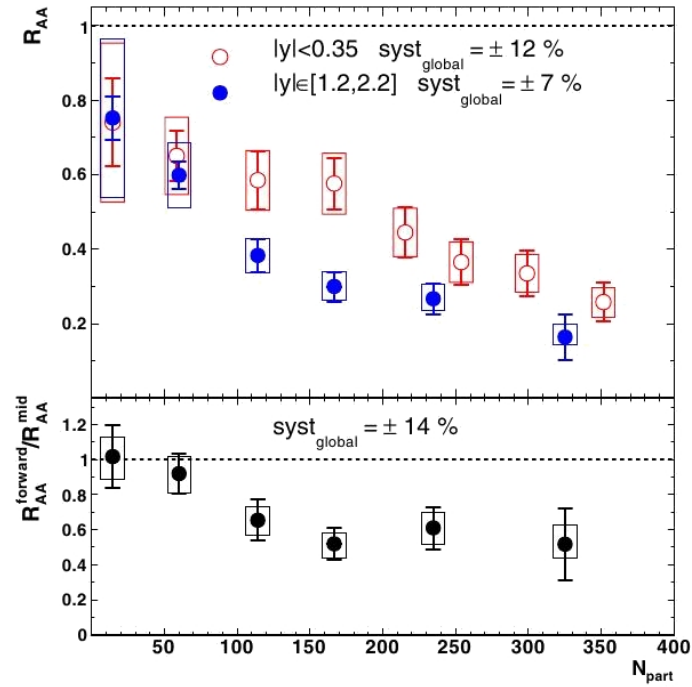


Figure 2.9:  $J/\psi$   $R_{AA}$  at forward and midrapidity in Au–Au collisions measured by PHENIX as a function of the number of participants [67].

might be explained by the recombination mechanism (at midrapidity the number of  $c\bar{c}$  pairs is higher) or by CNM effects like gluon shadowing, but it still remains unclear.

Study at the LHC may clarify the previous results on  $J/\psi$  suppression.

## 2.6.2 Charmonium measurements at the LHC

ALICE, ATLAS and CMS showed their first results obtained during 2010 and 2011 data taking in Pb–Pb collisions at  $\sqrt{s_{NN}} = 2.76$  TeV [68, 69, 70]. The  $J/\psi$  suppression is less important at the LHC than at RHIC at forward rapidity (Fig. 2.10, left), while at midrapidity the situation seems to be the opposite (Fig. 2.10, right). In this second case it is important to underline that the sample collected by CMS has a  $p_T > 6.5$  GeV/c, so a direct comparison of the two results is not straightforward.

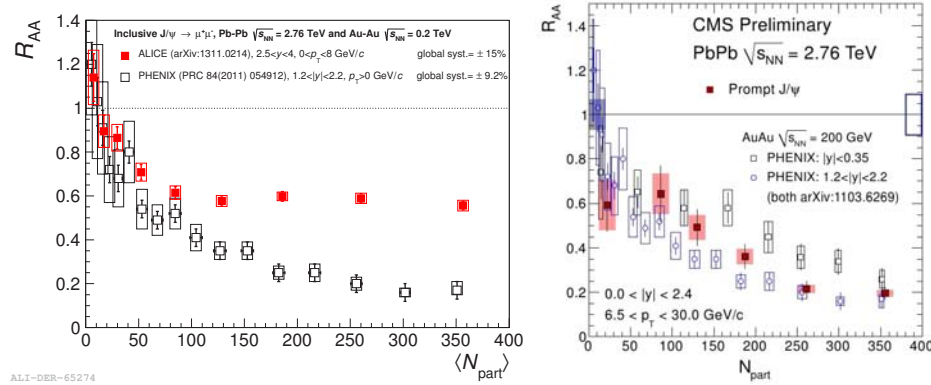


Figure 2.10: Inclusive  $J/\psi$   $R_{AA}$  measured by ALICE and PHENIX (left) and by CMS and PHENIX (right) [68, 70].

ALICE pointed out a stronger inclusive  $J/\psi$  suppression at forward rapidity than at midrapidity and at high  $p_T$  than at low  $p_T$  (Fig. 2.11). The comparison of these data with theoretical models [71] suggests an important  $c\bar{c}$  recombination for low- $p_T$   $J/\psi$  mostly in central collisions, as Fig. 2.12 indicates.

After the first runs of heavy-ion collisions at the LHC, the overall picture of quarkonium suppression is even more complicated, due to the different results obtained at forward and at midrapidity, difficult to explain. More data in AA and pA are needed to achieve better measurements and to estimate the cold nuclear matter effects.

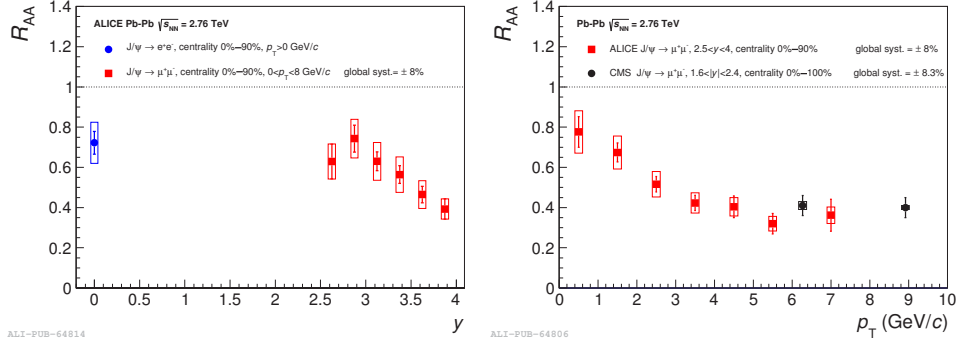


Figure 2.11: Inclusive  $J/\psi$   $R_{AA}$  measured by ALICE vs rapidity (left) and vs  $p_T$  (right, with CMS points).

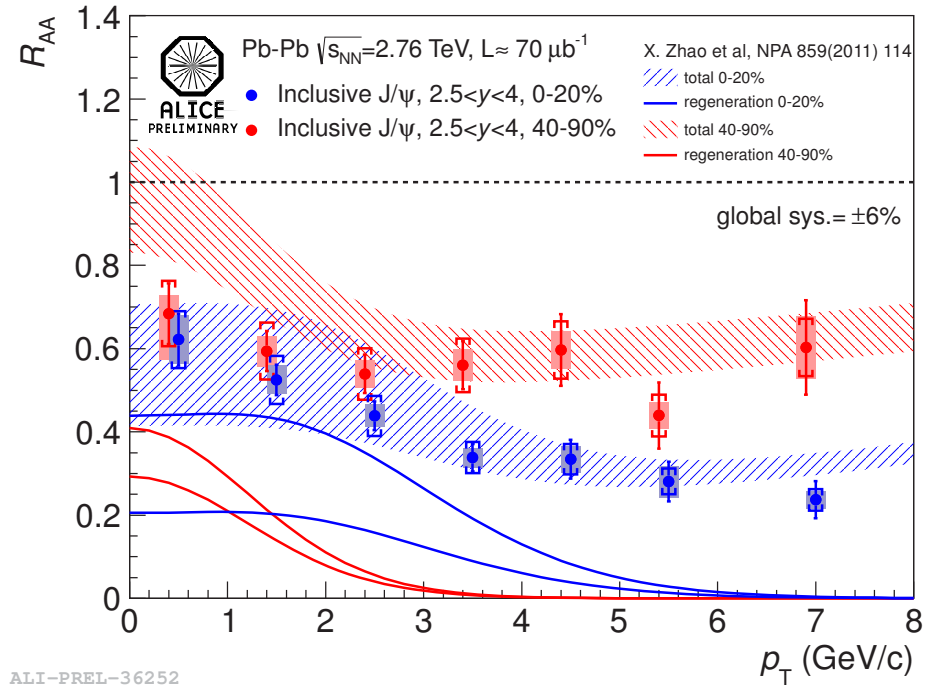


Figure 2.12: Inclusive  $J/\psi$   $R_{AA}$  vs  $p_T$  for two centrality bins.

## Chapter 3

# $\Upsilon$ production

In this chapter a review of the most important results achieved on the  $\Upsilon$  measurements in pp, p $\bar{p}$ , pA, dA and AA collisions and in different rapidity intervals will be presented. This summary is useful for better understanding the importance of the analysis presented in Chap. 8.

### 3.1 The $\Upsilon$ family

The bottom quark was theorized in 1973 by M. Kobayashi and T. Maskawa to explain the CP violation<sup>1</sup>. Four years later, in 1977, a new resonance called  $\Upsilon$  and similar to the J/ $\psi$  appeared in the dimuon mass spectrum (Fig. 3.1) at around 9.5 GeV/c<sup>2</sup> in 400 GeV proton-nucleus collisions at FNAL. This particle was interpreted as the lightest  $b\bar{b}$  vector meson [72].

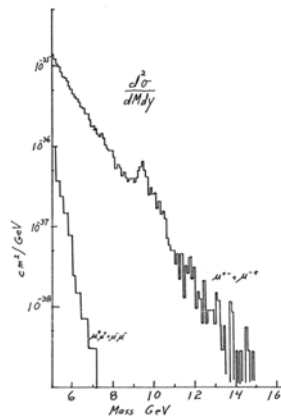


Figure 3.1: Measured dimuon production cross sections as a function of the dimuon invariant mass. The peak of the  $\Upsilon$  resonances is well visible at around 9.5 GeV/c<sup>2</sup> [72].

<sup>1</sup>In particle physics the CP violation is a violation of the postulated CP-symmetry, i.e. the combination of charge conjugation symmetry and parity symmetry.

Few months later, physicists claimed the observation of a new  $b\bar{b}$  bound state, the  $\Upsilon(2S)$ , very close to the fundamental resonance [73] and after two years also the  $\Upsilon(3S)$  was observed at DORIS [74].

Tab. 3.1 contains the latest and most accurate measurements of mass ( $m$ ), full width ( $\Gamma$ ), relevant quantum numbers and symmetries and the most important decay modes of the three  $\Upsilon$  states [2]. It is important to note the large feed-down of the  $\Upsilon(1S)$  from heavier states. In fact, the  $\Upsilon(2S)$  has a quite high probability to decay into the fundamental state plus two pions and the  $\chi_b(1P)$  produced with a photon in the radiative decays can themselves decay into  $\Upsilon(1S)$  plus another photon with a branching ratio ranging from  $< 6\%$  up to  $35\%$ . The  $\Upsilon(3S)$  has the same behaviour: it can decay into  $\Upsilon(2S)$  plus  $\pi\pi$  or  $\gamma\gamma$  or into  $\Upsilon(1S)\pi\pi$ . The various  $\chi_b(2P)$  usually decay as well into  $\gamma\Upsilon(2S)$  (branching ratio from  $5\%$  to  $21\%$ ) or, more rarely, into  $\Upsilon(1S)$  plus a photon [2]. From CDF measurements in  $p\bar{p}$  collisions at 1.8 GeV, 27% of all the  $\Upsilon(1S)$  with  $p_T > 8$  GeV/c are originated from  $\chi_b(1P)$ , almost 11% come from  $\chi_b(2P)$  and only 51% are directly produced [75]. The  $\Upsilon$  decays are also summarized in Fig. 3.2.

State	$\Upsilon(1S)$	$\Upsilon(2S)$	$\Upsilon(3S)$
$m$ (MeV/c <sup>2</sup> )	$9460.30 \pm 0.26$	$10023.26 \pm 0.31$	$10355.2 \pm 0.5$
$\Gamma$ (keV/c <sup>2</sup> )	$54.02 \pm 1.25$	$31.98 \pm 2.63$	$20.32 \pm 1.85$
$I^G(J^{PC})^2$	$0^-(1^{--})$	$0^-(1^{--})$	$0^-(1^{--})$
<b>Principal hadronic decays</b>	$ggg$ 81.7%	$ggg$ 58.8%	$ggg$ 35.7%
	$\gamma gg$ 2.2%	$\gamma gg$ 8.8%	$\Upsilon(2S)\pi^+\pi^-$ 2.8%
	$\eta'X$ 2.9%	$\Upsilon(1S)\pi^+\pi^-$ 17.9%	$\Upsilon(2S)\pi^0\pi^0$ 1.9%
	$D^{*\pm}X$ 2.5%	$\Upsilon(1S)\pi^0\pi^0$ 8.6%	$\Upsilon(2S)\gamma\gamma$ 5.0%
<b>Principal leptonic decays</b>	$e^+e^-$ 2.4%	$e^+e^-$ 1.9%	$\Upsilon(1S)\pi^+\pi^-$ 4.4%
	$\mu^+\mu^-$ 2.5%	$\mu^+\mu^-$ 1.9%	$\Upsilon(1S)\pi^0\pi^0$ 2.2%
	$\tau^+\tau^-$ 2.6%	$\tau^+\tau^-$ 2.0%	$\mu^+\mu^-$ 2.2%
<b>Principal radiative decays</b>	Negligible	$\gamma\chi_{b0}(1P)$ 3.8%	$\tau^+\tau^-$ 2.3%
		$\gamma\chi_{b1}(1P)$ 6.9%	$\gamma\chi_{b0}(2P)$ 5.9%
		$\gamma\chi_{b2}(1P)$ 7.2%	$\gamma\chi_{b1}(2P)$ 12.6%
		$\gamma\chi_{b2}(2P)$ 13.1%	

Table 3.1: Summary of the most important characteristics of the three  $\Upsilon$  states. The percentages near the decay modes are the branching ratios [2].

Other  $b\bar{b}$  bound states were discovered after the  $3S$  state such as the  $\Upsilon(4S)$  (also called  $\Upsilon(10580)$ ) [40], the  $\Upsilon(10860)$  and the  $\Upsilon(11020)$ , all of them with a mass above the  $B\bar{B}$  production threshold which constitutes their main decay channel. Being quite new and rare states, not many other

<sup>2</sup> $I$  is the isospin,  $G$  the G-parity,  $J$  the angular momentum,  $P$  the parity symmetry and  $C$  the charge conjugation symmetry.

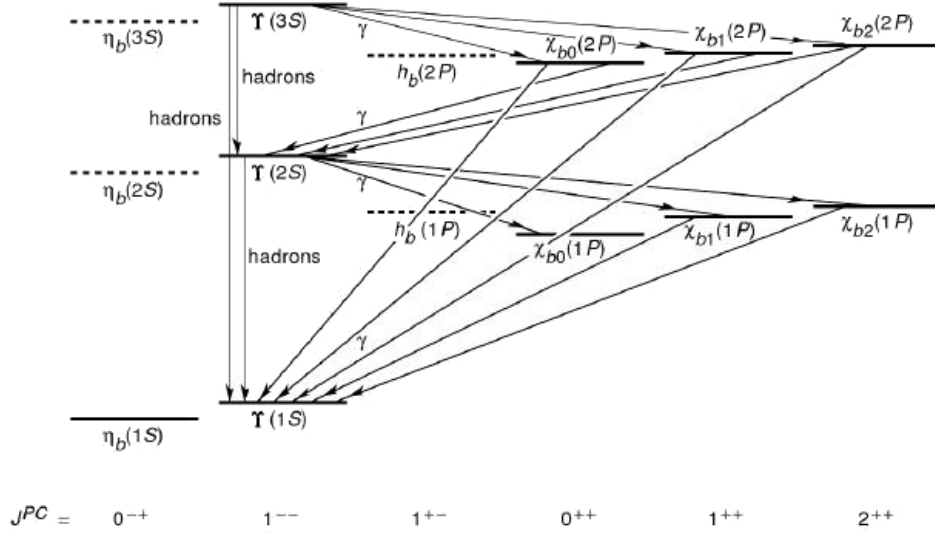


Figure 3.2: Bottomonium decay modes with spectroscopy notation [43].

information are known.

## 3.2 Υ production in pp and p $\bar{p}$ collisions

The Υ production is measured since long time, but the underlying formation mechanism is still not well understood. Several models exist, but they reproduce the cross section and the polarization measurements with difficulty [76, 77]. Although the disagreement of the theory with the data is less pronounced for bottomonium than for charmonium, the measurement of Υ production is important as the theoretical calculations are more robust due to the heavier bottom quark. Before to summarize the results in pp and p $\bar{p}$  collisions, an introduction to the polarization concept is given, since it plays an important role in the cross section determination.

### 3.2.1 Introduction to the quarkonium polarization

The information on the polarization of charmonium and bottomonium states is encoded in the angular distribution  $\frac{dN}{d\theta}$  of the leptons coming from their decays, described in the quarkonium rest frame (labelled  $\Lambda$  in Fig. 3.3) with respect to a particular axis. Usually this axis is taken along the direction of the quarkonium momentum  $\vec{P}_\Lambda$  in the laboratory frame (in this case  $\Omega$ ), choice named *helicity frame*.

In hadron-hadron collisions, polarization analyses are often restricted to the measurement of the distribution as a function of the polar angle with

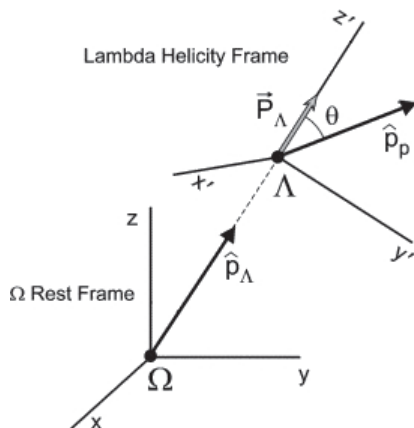


Figure 3.3: Schema of the helicity frame.

respect to the chosen axis, parametrized as:

$$1 + \alpha \cdot \cos \theta_{\ell\ell} \quad (3.1)$$

The parameter  $\alpha$  in Eq. 3.1 is directly related to the fraction of the cross section longitudinal or transverse with respect to the axis:  $\alpha = +1$  corresponds to 100% transverse polarization, while  $\alpha = -1$  corresponds to 100% longitudinal polarization. In experimental analyses, knowledge of the angular distribution of dileptons is important because for kinematic reasons it affects the detector acceptance. This effect is always corrected, but it leads to important systematic uncertainties.

The measurement of  $\Upsilon$  polarization may give information about the production mechanisms not available from the study of unpolarized cross sections alone.

### 3.2.2 Experimental results

#### Measurements at Tevatron

##### CDF

The CDF Collaboration measured the inclusive  $\Upsilon(1S)$  cross section in  $p\bar{p}$  collisions at 1.8 TeV at Fermilab Tevatron collider. The results as a function of  $p_T$  reported in Fig 3.4 on the left are compared to CSM, CEM and NRQCD, all at leading-order (see Sec. 2.3 for more details on the models). Only the latter lead to a satisfactory agreement from 8 GeV/ $c$  onwards, while at lower transverse momenta all the theoretical curves do not reproduce the data [44].

Recently, the CSM with corrections at next-to-leading order (NLO) and next-to-next-to-leading order (NNLO) showed a better agreement to the  $\Upsilon(1S)$  production cross section (Fig. 3.4, right) [78].

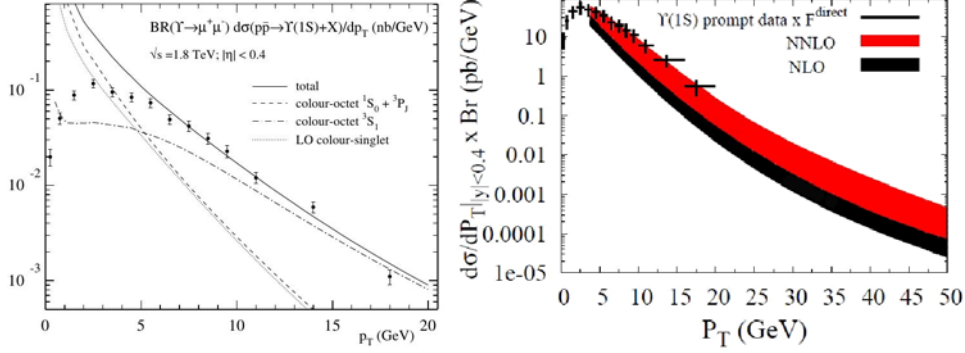


Figure 3.4:  $\Upsilon(1S)$  cross section as a function of the transverse momentum compared to LO NRQCD, CSM, CEM (left) and to NLO and NNLO CSM (right) [44, 78].

## DØ

The DØ experiment determined the differential  $\Upsilon(1S)$  production cross sections in  $p\bar{p}$  collisions at  $\sqrt{s} = 1.96$  TeV at Tevatron as a function of the transverse momentum [79]. Left plot of Fig. 3.5 shows the results normalized to the unity and compared to theoretical predictions described in [80]. On the right plot the same results are compared to the CDF [76] ones.

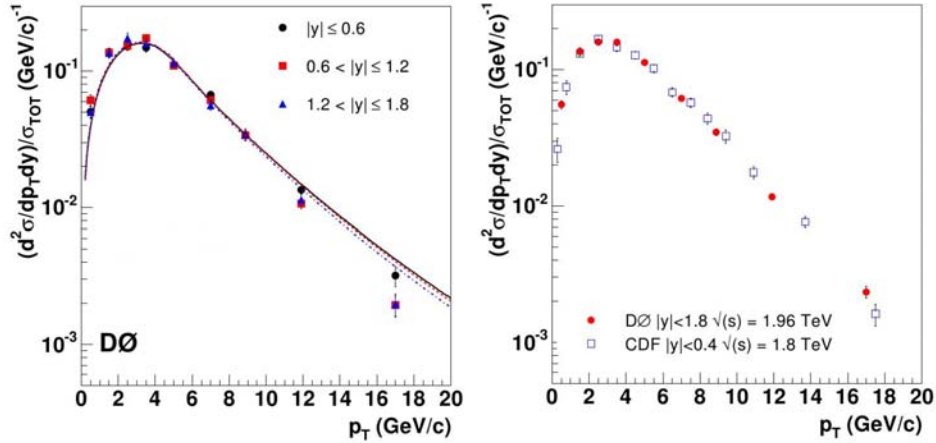


Figure 3.5: Normalized differential cross sections for  $\Upsilon(1S)$  production in different rapidity bins compared with theory predictions (left) and with CDF results (right) [76, 80].

DØ studied as well the polarization of the inclusive  $\Upsilon(1S)$  production at midrapidity ( $|y| < 0.4$ ) [77]. The results are shown in Fig. 3.6 (left) along with the NRQCD factorization prediction at LO in  $\alpha$  and compared to CDF measurements [76]. The origin of the large discrepancy between the

two experiments is still unclear. However, the CDF measurements are made over the rapidity interval  $|y| < 0.6$ , while those of DØ are made in the range  $|y| < 1.8$ . The LO NRQCD prediction is marginally compatible with the CDF data only in a narrow  $p_T$  range and with the DØ data only at large  $p_T$ .

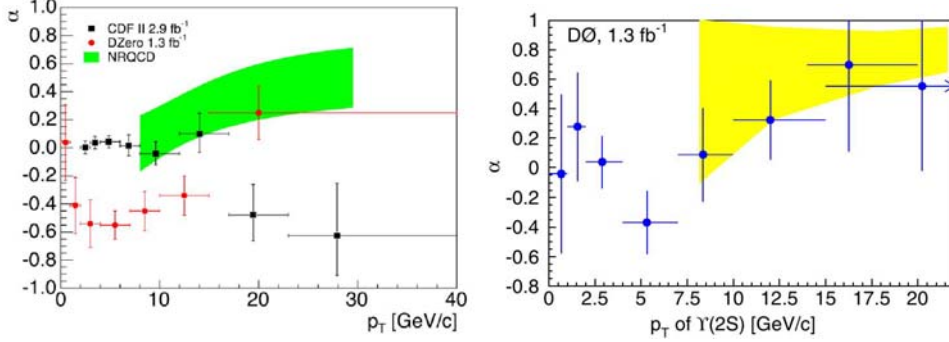


Figure 3.6: Left: polarization parameter  $\alpha$  measured by DØ and CDF for  $\Upsilon(1S)$  production compared with LO NRQCD. Right: polarization parameter  $\alpha$  measured by DØ for  $\Upsilon(2S)$  production [77].

The DØ Collaboration measured the  $\Upsilon(2S)$  polarization too, but the error bars are so large that it is impossible to make any conclusion (Fig. 3.6, right) [77].

### Measurements at RHIC: PHENIX and STAR

PHENIX and STAR measured the production cross section of the unresolved  $\Upsilon$  states in the dielectron channel in pp collisions at 200 GeV at RHIC [81, 82]:

$$\text{PHENIX: } BR \cdot \frac{d\sigma_{\Upsilon}}{dy} \Big|_{|y| < 0.35} = 114^{+46}_{-45} \text{ pb}$$

$$\text{STAR: } BR \cdot \frac{d\sigma_{\Upsilon}}{dy} \Big|_{|y| < 0.5} = 91 \pm 28 \pm 22 \text{ pb}$$

The two results, in agreement within uncertainties, follow the world trend and the estimates based on CEM (Fig. 3.7).

### Measurements at the LHC

#### LHCb

The measurements of the  $\Upsilon \rightarrow \mu^+ \mu^-$  production cross sections in pp collisions at 7 TeV made by LHCb are given in the rapidity range  $2 < y < 4.5$  and transverse momentum range up to 15 GeV/c. The integrated values are:

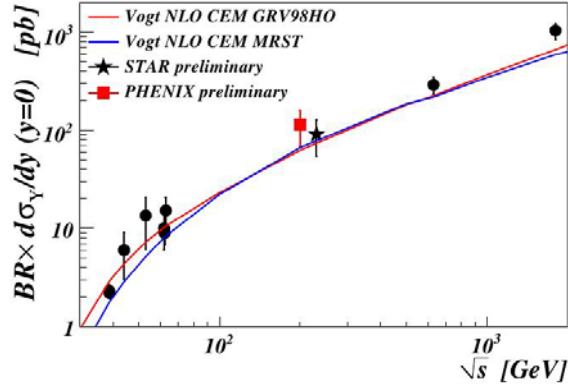


Figure 3.7: Collision energy dependence of the  $\Upsilon$  cross section [81].

$$BR_{\mu\mu} \cdot \sigma(pp \rightarrow \Upsilon(1S)X) = 2.29 \pm 0.01 \pm 0.10_{-0.37}^{+0.19} \text{ nb}$$

$$BR_{\mu\mu} \cdot \sigma(pp \rightarrow \Upsilon(2S)X) = 0.562 \pm 0.007 \pm 0.023_{-0.092}^{+0.048} \text{ nb}$$

$$BR_{\mu\mu} \cdot \sigma(pp \rightarrow \Upsilon(3S)X) = 0.283 \pm 0.005 \pm 0.012_{-0.048}^{+0.025} \text{ nb}$$

where the first uncertainties are statistical, the second systematic (they include the luminosity contribution) and the third are due to the unknown polarization of the three states [83]. The  $p_T$  and  $y$  differential trends are shown in Fig. 3.8.

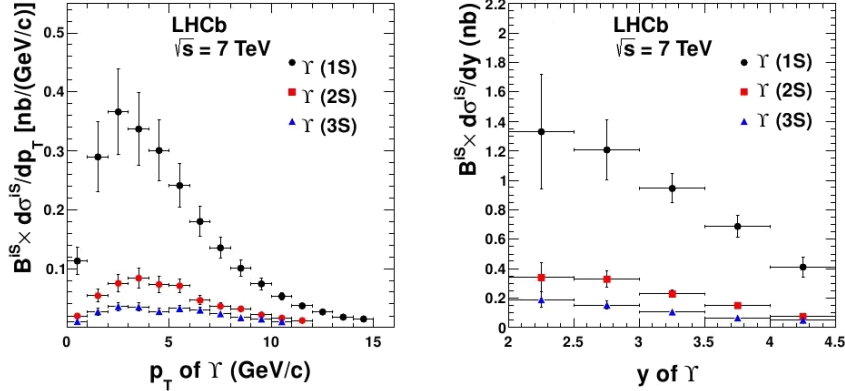


Figure 3.8: Differential cross sections multiplied by the dimuon branching ratio as a function of  $p_T$  (left) and  $y$  (right) in pp collisions at 7 TeV [83].

On the left plot of Fig. 3.9 the data are compared to the  $\Upsilon(1S)$  direct production as calculated with the NLO and NNLO CSM approach, while on the right they are compared to NRQCD and CEM calculations, both at NLO and including contributions from  $\chi_b$  and higher  $\Upsilon$  states decays.

Excluding NLO CSM, a quite satisfactory agreement is found between data and models.

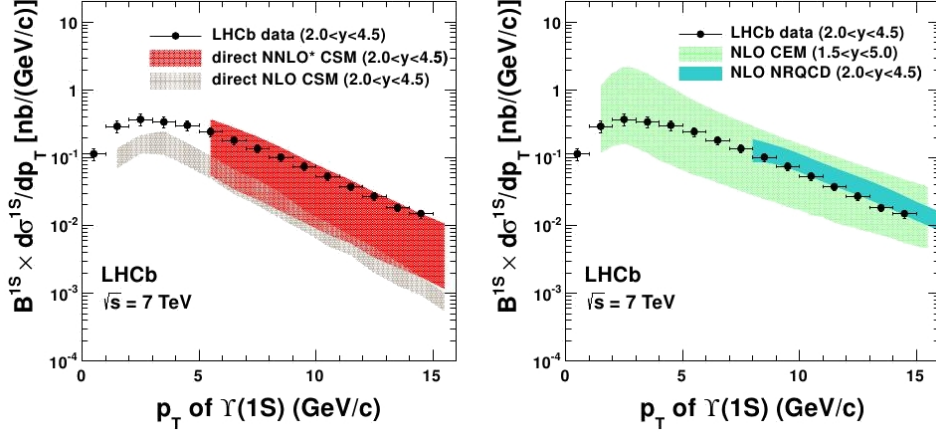


Figure 3.9: Differential  $\Upsilon(1S)$  cross section times the dimuon branching ratio as a function of  $p_T$  compared to NLO and NNLO CSM (left) and NLO NRQCD and CEM (right) [83].

LHCb studied as well the  $\Upsilon$  production at  $\sqrt{s} = 8$  TeV. The differential cross section are displayed in Fig. 3.10, with the assumption of zero polarization [84].

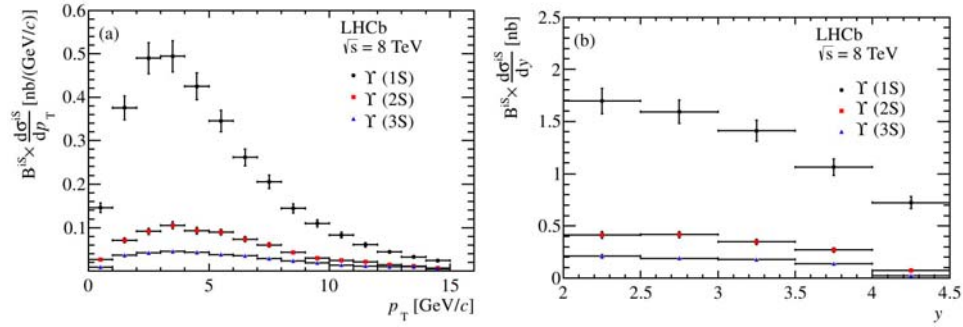


Figure 3.10: Differential cross sections multiplied by the dimuon branching ratio as a function of  $p_T$  (left) and  $y$  (right) in pp collisions at 8 TeV [84].

## ALICE

ALICE measured the inclusive production cross sections of  $\Upsilon(1S)$  and  $\Upsilon(2S)$  in pp collisions at  $\sqrt{s} = 7$  TeV with the Muon Spectrometer [85]. The  $\Upsilon$  yields are determined from a fit to the reconstructed dimuon invariant mass of selected candidates corrected by the acceptance and efficiency of the detector. The distribution in Fig. 3.11 is described by the sum of three

extended Crystal Ball functions<sup>3</sup> (green lines, one for each resonance) and a double exponential function for the underlying continuum (dashed red line).

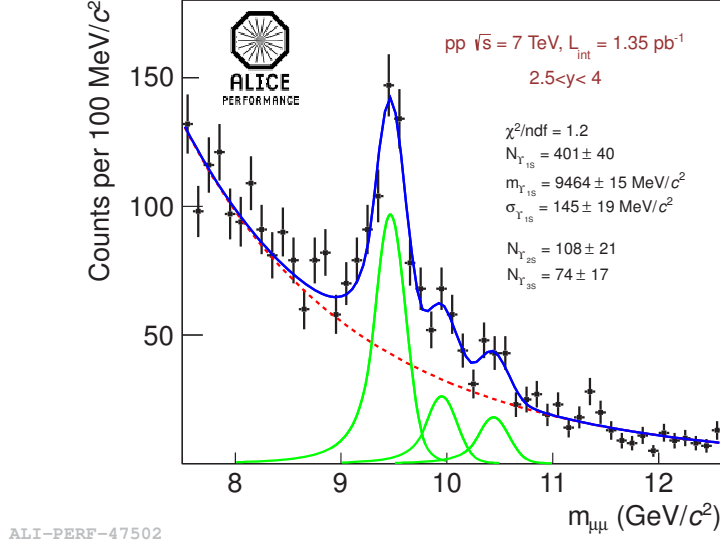


Figure 3.11: Dimuon invariant mass distribution with fit functions (see text for more details).

The cross sections times branching ratio, integrated over the rapidity range  $2.5 < y < 4$  and for  $p_T > 0$  are:

$$BR_{\mu\mu} \cdot \sigma(pp \rightarrow \Upsilon(1S)X) = 1.35 \pm 0.13 \pm 0.16_{-0.26}^{+0.49} \text{ nb}$$

$$BR_{\mu\mu} \cdot \sigma(pp \rightarrow \Upsilon(2S)X) = 0.36 \pm 0.07 \pm 0.04_{-0.07}^{+0.13} \text{ nb}$$

where the first uncertainty is statistical, the second systematic and the third is due to the unknown polarization of the two states. The luminosity uncertainty is considered in the systematic error.

The differential cross sections measured as a function of the transverse momentum and rapidity are shown in Fig. 3.12. The comparison with the analogous LHCb results shows a good agreement.

## CMS

CMS measured the  $\Upsilon$  production cross sections for the three resonances in the dimuon decay channel in pp collisions at  $\sqrt{s} = 7 \text{ TeV}$ , for  $0 < p_T < 50 \text{ GeV}/c$  and  $|y| < 2.4$ . The results are:

$$BR_{\mu\mu} \cdot \sigma(pp \rightarrow \Upsilon(1S)X) = 8.55 \pm 0.05_{-0.50}^{+0.56} \pm 0.34 \text{ nb}$$

<sup>3</sup>See Eq. A.2.

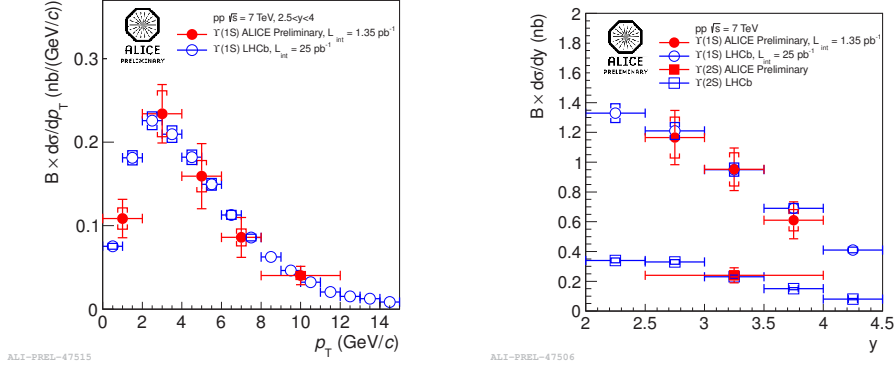


Figure 3.12:  $\Upsilon$  differential cross sections multiplied by the dimuon branching ratio as a function of  $p_T$  (left) and rapidity (right) measured by ALICE and LHCb.

$$BR_{\mu\mu} \cdot \sigma(pp \rightarrow \Upsilon(2S)X) = 2.21 \pm 0.03_{-0.14}^{+0.16} \pm 0.09 \text{ nb}$$

$$BR_{\mu\mu} \cdot \sigma(pp \rightarrow \Upsilon(3S)X) = 1.11 \pm 0.02_{-0.08}^{+0.10} \pm 0.04 \text{ nb}$$

The first uncertainty is statistical, the second one is systematic and the last comes from luminosity uncertainty [86]. Recently, the CMS Collaboration found the polarizations of the  $\Upsilon$  states in pp collisions to be compatible with zero [87]. For this reason, no net polarization is assumed in the calculations.

The  $p_T$  and  $y$  differential cross sections along with the theoretical predictions are shown in Fig. 3.13 assuming an unpolarized  $\Upsilon$  production. Comparisons are made to the CASCADE Monte Carlo generator, to the normalized PYTHIA, to CEM without feed-down, NLO NRQCD including feed-down and to CSM at NLO and NNLO with feed-down. The  $\Upsilon(1S)$  cross section is smaller than the CEM prediction at low  $p_T$ . The data agree with NRQCD at  $p_T > 10$  GeV/c and with CASCADE for the  $1S$  state, but the agreement is not satisfactory for the other resonances. The NLO CSM does not describe at all the data, while the NNLO CSM shows a better agreement within the large uncertainties. The  $p_T$  dependence of the cross section predicted by PYTHIA agrees with the data for the  $\Upsilon(1S)$  and  $\Upsilon(3S)$ , but it fails for the  $2S$  state. PYTHIA also describes better than the CASCADE Monte Carlo the rapidity dependence over the range of the measurement, as shown in the bottom right plot of Fig. 3.13.

## ATLAS

The total production cross sections measured by ATLAS for a transverse momentum  $< 70$  GeV/c in the rapidity interval  $|y| < 2.25$  are found to be:

$$BR_{\mu\mu} \cdot \sigma(pp \rightarrow \Upsilon(1S)X) = 8.01 \pm 0.02 \pm 0.36 \pm 0.31 \text{ nb}$$

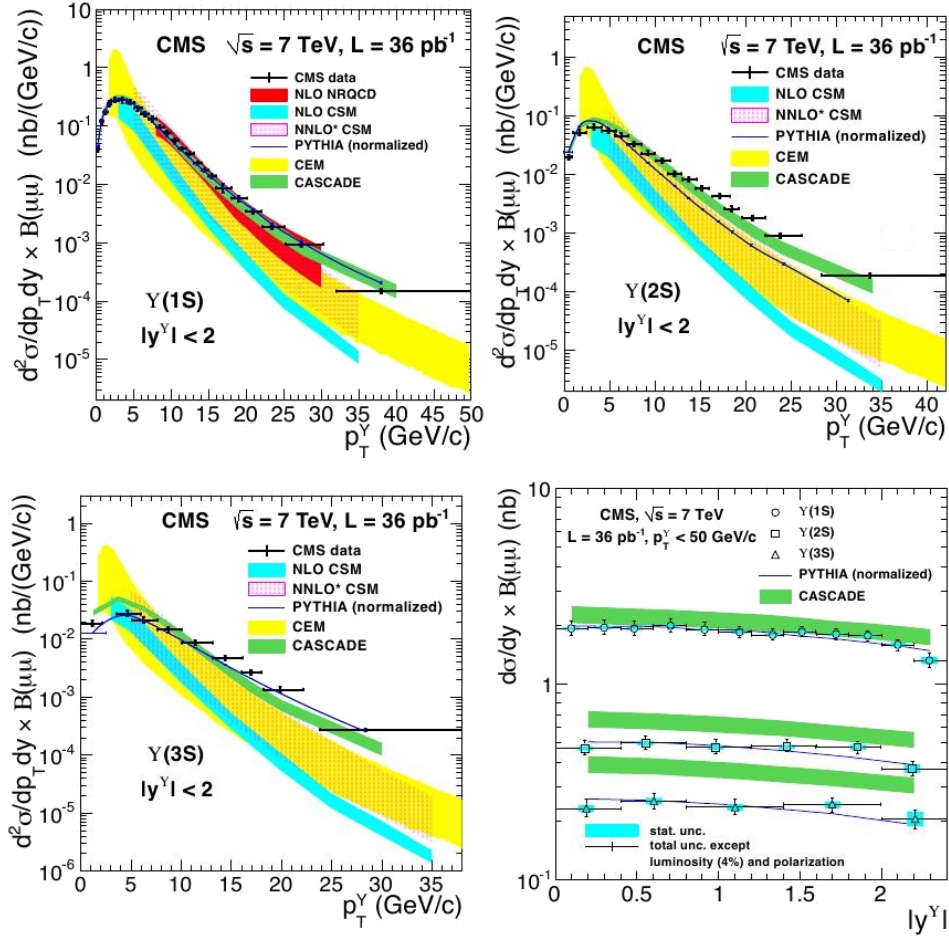


Figure 3.13: Double-differential cross sections of the  $\Upsilon$  states as a function of  $p_T$  (top plots and bottom left plot) and  $y$  differential cross section (bottom right plot) compared to different theoretical predictions [86] (see text for more details).

$$BR_{\mu\mu} \cdot \sigma(pp \rightarrow \Upsilon(2S)X) = 2.05 \pm 0.01 \pm 0.12 \pm 0.08 \text{ nb}$$

$$BR_{\mu\mu} \cdot \sigma(pp \rightarrow \Upsilon(3S)X) = 0.92 \pm 0.01 \pm 0.07 \pm 0.04 \text{ nb}$$

with uncertainties separated into statistical, systematic, and luminosity measurement effects. In addition, differential cross section times dimuon branching ratio for the three states as a function of transverse momentum and rapidity are presented in Fig. 3.14 assuming an unpolarized production [88].

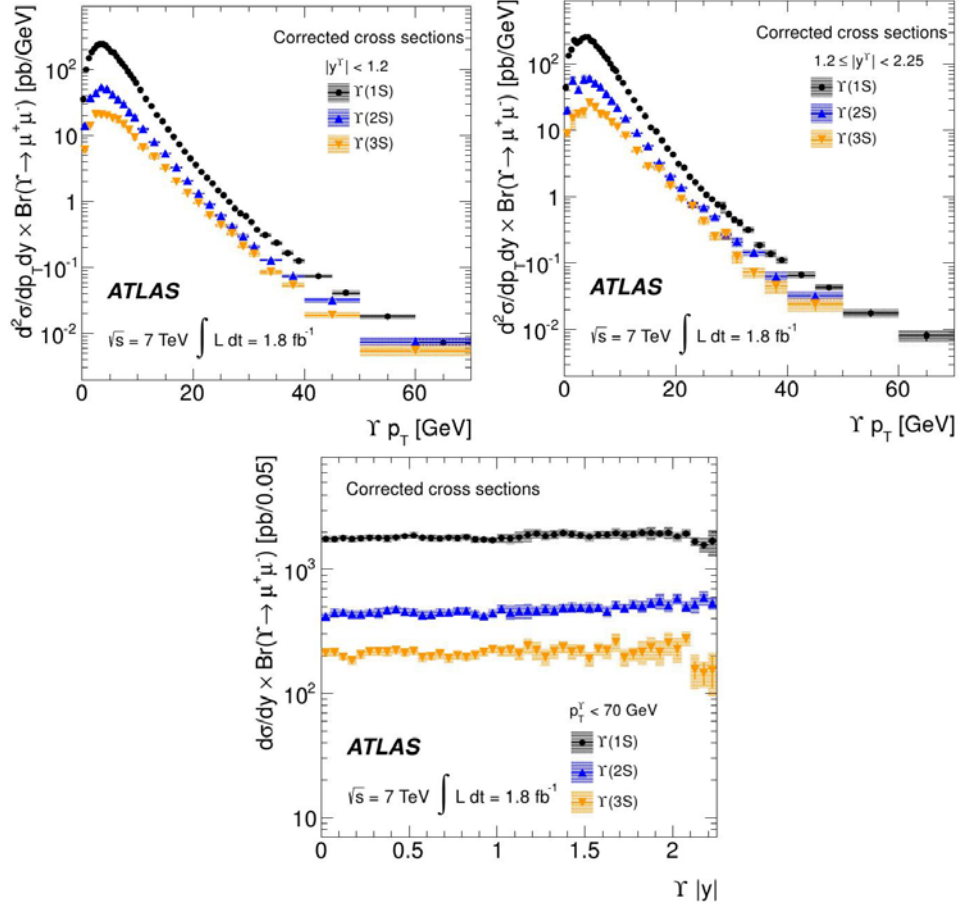


Figure 3.14: Double-differential  $\Upsilon$  cross sections vs  $p_T$  in two bins of rapidity (top) and differential  $\Upsilon$  cross sections vs rapidity (bottom) [88].

The results are consistent with measurements by CMS [89] and by LHCb in the small region of rapidity overlap from 2.0 to 2.25 [83] and allow to test phenomenological models of  $\Upsilon$  production at high  $p_T$  where higher-order contributions become particularly important. Fig. 3.15 shows the differential  $\Upsilon(1S)$  cross section in comparison with theoretical predictions as a function of the transverse momentum. The effects of different spin-alignment assumptions, larger at low  $p_T$ , are indicated by the cyan band. Despite CDF

and CMS suggest an unpolarized production [76, 87], results under a variety of scenarios are provided in the lower panels of each plot. NNLO CSM approach for direct  $\Upsilon(1S)$  production predicts a largely longitudinal polarization mostly at high  $p_T$  (although the effect of feed-down introduces large uncertainties to this prediction). Inclusive calculations from CEM offers no explicit prediction of the spin-alignment evolution of  $\Upsilon$ , but the nature of the model suggests that no strong polarization should be observed as no single production mechanism dominates. The two models provide quite different descriptions of the production.

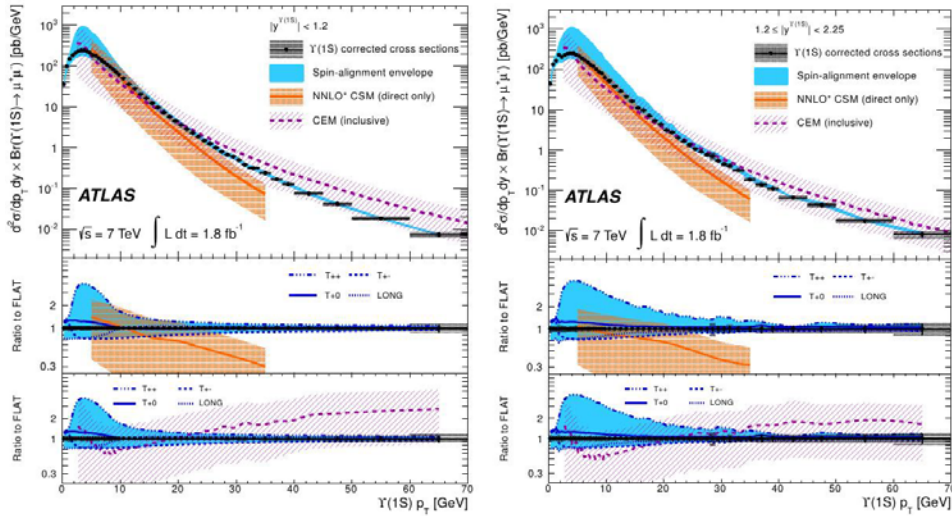


Figure 3.15: Double-differential  $\Upsilon(1S)$  cross sections in two rapidity bins. The solid band indicates the variation of the result due to spin-alignment uncertainty. In the lower panels NNLO CSM prediction of direct production and inclusive prediction from CEM are presented as the ratio to the data along with cross section measurements under four possible spin-alignment scenarios [88].

### 3.3 $\Upsilon$ production in pA and dA collisions

Data in proton-nucleus collisions, where no hot and dense matter effects are expected, are an essential reference for well understanding the quarkonium suppression predicted to occur in ultrarelativistic heavy-ion collisions.

#### 3.3.1 Experimental results

##### Measurements at Tevatron: E772

E772 at Fermilab reported on the  $\Upsilon$  family production in a fixed target collision experiment with protons at 800 GeV on liquid deuterium and solid

nuclear targets of C, Ca, Fe, and W. The experiment had sufficient mass resolution to resolve the  $\Upsilon(1S)$  and partially resolve the  $2S$  and  $3S$  states [90].

Left plot in Fig. 3.16 shows for each target the yield of  $\Upsilon(1S)$  and  $\Upsilon(2S + 3S)$  relative to deuterium. Describing the  $A$  dependence by the parametrization:

$$\sigma_{pA} = \sigma_{pp} \cdot A^\alpha \quad (3.2)$$

one finds  $\alpha_{1S} = 0.962 \pm 0.006$  and  $\alpha_{2S+3S} = 0.948 \pm 0.012$ , both quite below  $\alpha = 1$  found in the Drell-Yan process, but still significantly larger than those of the  $J/\psi$  and  $\psi(2S)$  resonances (around 0.92).

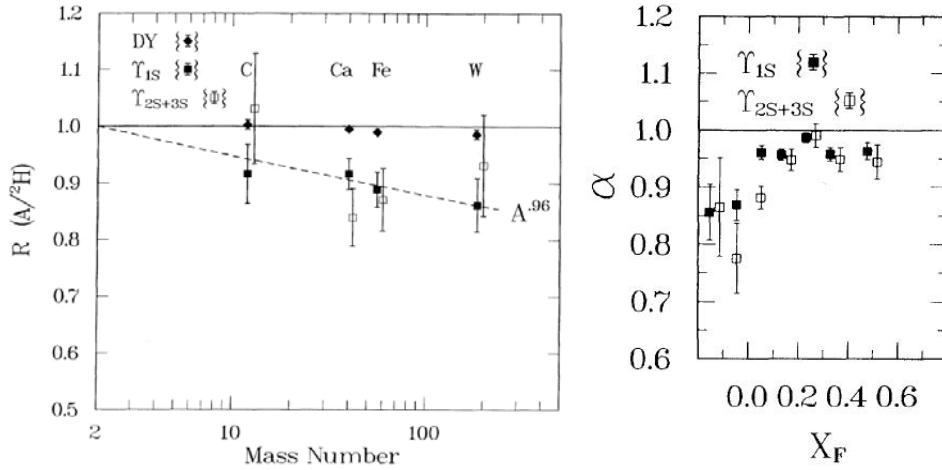


Figure 3.16: Left: ratio of yields per nucleon vs  $A$  for  $\Upsilon(1S)$  and  $\Upsilon(2S+3S)$ . Right:  $\alpha$  dependence on  $x_F$  [90].

The  $\alpha$  dependence on Feynman- $x^4$  (right plot) is particularly interesting as it shows a significant change over the kinematic range. Data at negative  $x_F$  are rare in fixed-target experiments and never observed before. Such a large decrease in  $\alpha$  for  $x_F < 0$  and the integrated value of  $\alpha = 0.96$  probably reflect physics including comover interactions [90].

### Measurements at the SPS: NA50

The NA50 Collaboration measured the  $\Upsilon(1S+2S+3S)$  production with protons of 450 GeV incident on Be, Al, Cu, Ag and W fixed targets [91].

The left plot in Fig. 3.17 shows, as a function of the mass number  $A$ , the Drell-Yan cross sections divided by the nucleon number  $A$  of each target (i.e. the cross section per nucleon-nucleon collision). In absence of final

<sup>4</sup>The Feynman- $x$  ( $x_F$ ) is a kinematic variable defined as  $\frac{p_z}{p}$ , where  $p_z$  is the particle momentum along the beam axis and  $p$  is the total momentum. It is an alternative to the rapidity defined as  $y = \frac{1}{2} \ln \left( \frac{E+p_z}{E-p_z} \right)$ .

state interactions and if nuclear effects on the PDF are negligible, a flat behaviour is expected. By fitting the points with the function in Eq. 3.2 one gets  $\alpha = 0.98 \pm 0.02$ , a value not very far from the E772 result, but in this case, compatible with 1, i.e. with the scaling of the cross section with the number of elementary collisions.

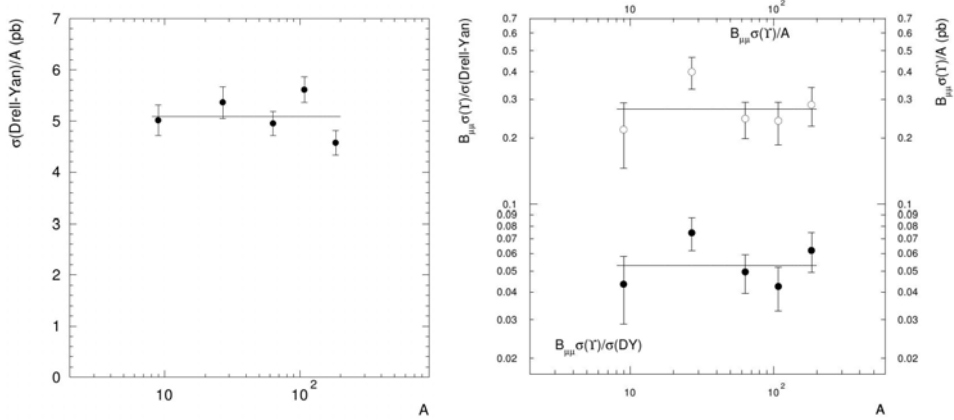


Figure 3.17: Left: Drell-Yan  $\Upsilon$  cross section divided by the mass number  $A$ . Right: ratio  $BR_{\mu\mu} \cdot \sigma_{\Upsilon}/\sigma_{DY}$  (full circles) and the cross section per nucleon  $BR_{\mu\mu} \cdot \sigma_{\Upsilon}/A$  (open circles), always as a function of  $A$  [91].

In the right plot the  $A$  dependence of bottomonium production is presented through the ratios  $BR_{\mu\mu} \cdot \sigma_{\Upsilon}/\sigma_{DY}$  and  $BR_{\mu\mu} \cdot \sigma_{\Upsilon}/A$ . The fits of the two sets of points give in both cases an  $\alpha$  compatible with 1 which means that the  $\Upsilon$  is not strongly absorbed in the nuclear medium. This result is in slight contradiction with the previous direct determination of the  $A$  dependence carried out by E772 [90] at higher incident energy.

## Measurements at RHIC

### STAR

The  $\Upsilon(1S + 2S + 3S)$  cross section measured by STAR in dAu collisions at  $\sqrt{s_{dAu}} = 200$  GeV at midrapidity via the dielectron decay mode is found to be:

$$BR \cdot \frac{d\sigma}{dy}|_{y=0} = 35 \pm 4 \pm 5 \text{ nb}$$

In Fig. 3.18 the measurement is successfully compared with NLO CEM calculations which include the anti-shadowing effect obtained from EKS98 parametrization, but they do not include absorption effects.

The nuclear modification factor was extracted as well:

$$R_{dAu} = 0.98 \pm 0.32 \pm 0.28$$

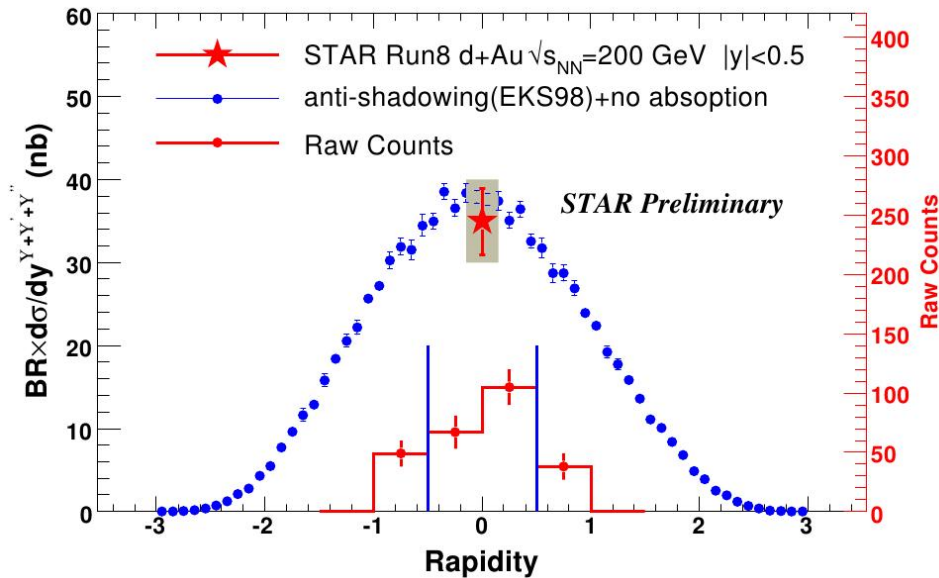


Figure 3.18:  $\Upsilon$  cross section at midrapidity compared with the NLO CEM model prediction. The raw yield vs rapidity is shown by the red histogram [92].

which seems to suggest the  $\Upsilon(1S + 2S + 3S)$  production in dAu collision at these energies and at midrapidity follows the binary collisions scaling, but it is not possible to quantify the cold nuclear matter effects seen the big uncertainty of the  $R_{dAu}$  [92].

## PHENIX

To separate CNM effects from those due to the presence of the QGP PHENIX measured the  $\Upsilon$  yield in dAu collisions at  $\sqrt{s_{dAu}} = 200$  GeV. At forward rapidity the  $\Upsilon$  production shows no significant suppression with an  $R_{dAu} = 0.91 \pm 0.33 \pm 0.16$ , while at backward rapidity the suppression is more important with an  $R_{dAu} = 0.62 \pm 0.26 \pm 0.13$  (but still consistent within the errors with the forward measurement). Fig. 3.19 (top) shows the comparison with the results of  $J/\psi$  for which a larger suppression at forward than at backward rapidity is seen. A NLO calculation with EPS09 shadowing predicts modest suppression at backward rapidity, but no shadowing at forward rapidity. The rapidity dependence of this calculation appears to be consistent with the trend between backward and forward rapidity measurements, but the large uncertainties do not give a significant constraint on the cross section value used in the model [93].

It is also possible to parametrize the nuclear dependence of  $\Upsilon$  production with the formula in Eq. 3.2. At PHENIX's backward rapidity ( $\langle x_F \rangle \sim -0.2$ )

the  $\alpha_{\Upsilon(1S+2S+3S)}$  is found to be  $0.925 \pm 0.070 \pm 0.035$  and at forward rapidity ( $\langle x_F \rangle \sim 0.2$ )  $0.990 \pm 0.060 \pm 0.029$ . The  $\alpha$  trend shown in the bottom plot of Fig. 3.19 together with E772 data [90] demonstrates that the suppression levels of the two experiments are consistent within uncertainties [93].

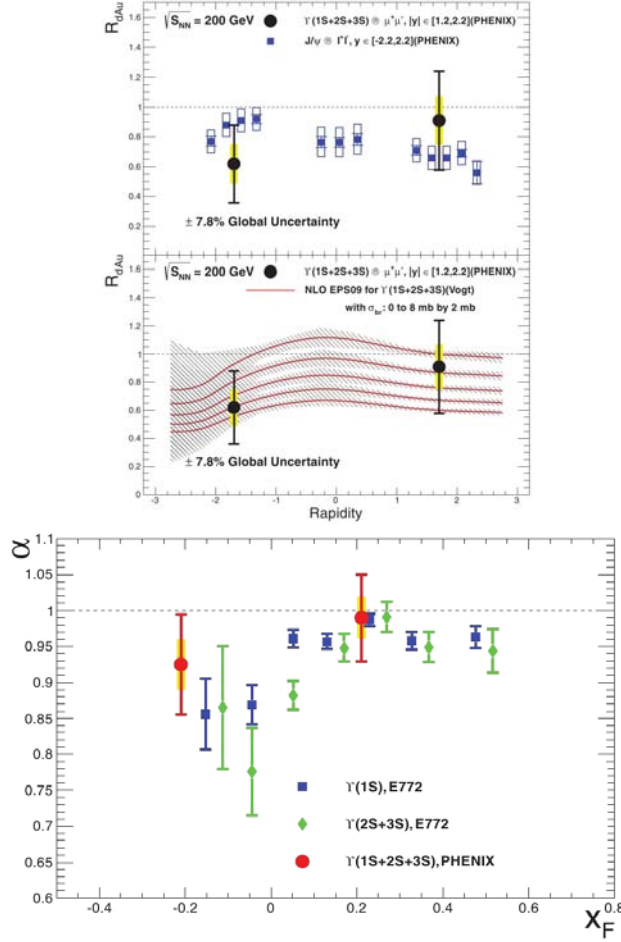


Figure 3.19: Top:  $\Upsilon R_{dAu}$  as a function of rapidity measured by the PHENIX Collaboration compared to  $J/\psi$  measurement and NLO EPS09 calculation for various cross section values. Bottom:  $\alpha$  vs  $x_F$  of  $\Upsilon$  states measured by E772 and PHENIX [93].

### 3.4 $\Upsilon$ production in heavy-ion collisions

As introduced in Sec. 2.4, the thermal suppression of quarkonium production in heavy-ion collisions due to Debye screening of the  $q\bar{q}$  potential was proposed as a clear signature of Quark-Gluon Plasma formation. The most important results obtained on the  $\Upsilon$  production are presented along

with theoretical predictions. The detailed analysis of the  $\Upsilon(1S)$  in Pb–Pb collisions at ALICE will be instead described in Chap. 8.

### 3.4.1 Introduction to theoretical models

Two models predicting the  $\Upsilon$  production in heavy-ion collisions are now introduced before to be compared to the experimental results.

#### Hydrodynamic formalism

The potential describing the interaction between the quark pair introduced by M. Strickland [94, 95, 96] to determine the impact of the Quark-Gluon Plasma phase on bottomonium states is composed of two parts. The short-range is computed at leading-order in the strong coupling constant using finite temperature quantum chromodynamics in the heavy quark limit [97, 98, 99, 100, 101], while for the long-range part a parametrization of the Cornell potential is used [102]. Bottomonium states and their decay widths are found integrating the potential over the space-time evolution of the Quark-Gluon Plasma using an hydrodynamic formalism (HYDRO) [103, 104, 105] which assumes finite local momentum-space anisotropy due to finite shear viscosity. This approach only includes the effects of the in-medium suppression of the states. It does not include any recombination effects expected to be small for bottomonium states. In addition, the state feed-down by higher mass bottomonia is considered, but no cold nuclear matter effects are implemented.

Usually two different initial temperature profiles in the spatial rapidity direction are used. One assumes a broad plateau containing a boost-invariant central rapidity region with half a Gaussian in the forward and backward directions, corresponding to a limited fragmentation. The second assumes a Gaussian profile which fits the low energy pion spectra. For each profile three possible ratios between the plasma shear viscosities  $\eta$  and the entropy density  $s$  are considered:  $4\pi\eta/s = \{1, 2, 3\}$ .

This model describes successfully the elliptic flow of charged particles measured by ALICE in Pb–Pb collisions at  $\sqrt{s_{NN}} = 2.76$  TeV [106, 107].

#### Rate equation approach

The model developed by A. Emerick et al. is based on a rate equation approach which accounts for both suppression and regeneration mechanisms along with hadronization phases of the evolving thermal medium [108, 109].

For these predictions, the spectral functions used as input for the equation corresponds to a strong binding scenario and the evolution of the medium is described with a fireball model tuned according to the LHC measurements [71, 110].

The number of bottomonium mesons at the QGP formation time is required as initial condition and the regeneration component needs the knowledge of the beauty quark cross section. Both information are evaluated from existing data.

Cold nuclear matter effects are taken into account by means of an overall absorption cross section ( $\sigma_{abs}$ ) which assumes to extreme values: 0 and 2 mb. It includes the effects of the nuclear modifications of parton distribution functions, of the absorption on passing-by nucleons and the Cronin effect. The cross section range can be interpreted as the uncertainty of the model related to the poor knowledge of cold nuclear effects.

The predictions separate the primordial  $R_{AA}$  to the effects due to the possible  $b\bar{b}$  regeneration (small, but not negligible in this model) and consider the feed-down by higher mass bottomonia assuming a 50% effect for the inclusive  $\Upsilon(1S)$  yield.

### 3.4.2 Experimental results

#### Measurements at RHIC: STAR and PHENIX

At RHIC energies, the  $\Upsilon$  meson is a clean probe of the QGP thanks to very small contribution to the enhancement due to  $b\bar{b}$  recombination.

The STAR Collaboration reported on the measurement of the  $\Upsilon(1S + 2S + 3S) \rightarrow e^+e^-$  production in Au–Au collisions at  $\sqrt{s_{NN}} = 200$  GeV [111]. Using the pp collisions as a baseline, they computed the nuclear modification factor  $R_{AA}$  as a function of the average number of participants. The results are shown on the left plot of Fig. 3.20 compared to the hydrodynamic model with two different inter-quark potentials: one based on the internal energy of the  $q\bar{q}$  pair and the other on the free energy [95]. On the right plot the  $R_{AA}$  is compared to the rate equation approach model [108].

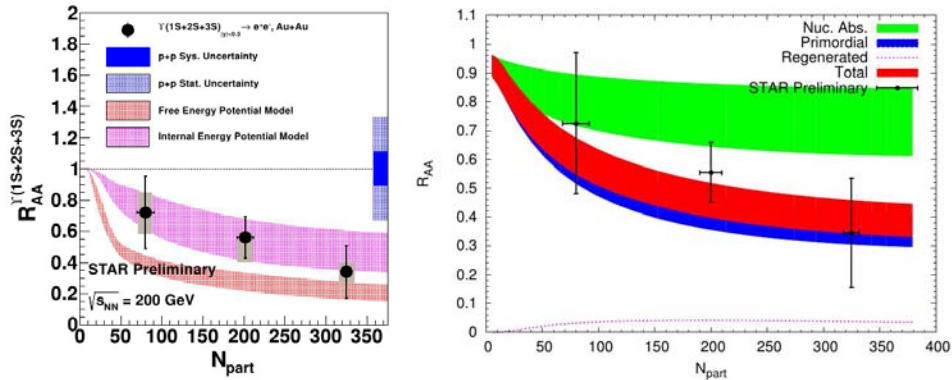


Figure 3.20:  $\Upsilon$   $R_{AA}$  as a function of the number of participants measured by STAR in Au–Au collisions and compared to the theoretical predictions introduced before [95, 108].

The results are consistent with the hydrodynamic model with internal energy potential and with the rate equation approach within the large uncertainties. No model can be discarded and more statistics is needed to reach a definitive conclusion.

Finally, the  $R_{AA}$  extracted by the PHENIX Collaboration from dielectron pairs [112] is in good agreement with data shown by STAR.

### Measurements at the LHC: CMS

CMS measured the suppression of the individual  $\Upsilon$  states in Pb–Pb collisions at  $\sqrt{s_{NN}} = 2.76$  TeV with respect to the yields in pp at the same center-of-mass energy. The centrality integrated  $R_{AA}$  (for  $|y| < 2.4$ ) are [113]:

$$R_{AA}^{\Upsilon(1S)} = 0.56 \pm 0.08 \pm 0.07$$

$$R_{AA}^{\Upsilon(2S)} = 0.12 \pm 0.04 \pm 0.02$$

$$R_{AA}^{\Upsilon(3S)} = 0.03 \pm 0.04 \pm 0.01 < 0.10 \text{ (CL = 95\%)}$$

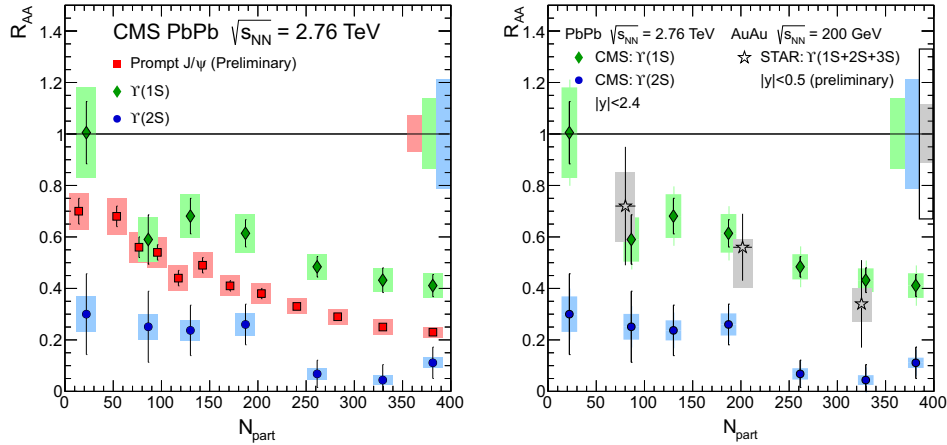


Figure 3.21: Comparison of the  $\Upsilon(1S)$  and  $\Upsilon(2S)$   $R_{AA}$  centrality dependence with prompt  $J/\psi$  measurements by CMS (left) and with the  $\Upsilon(1S + 2S + 3S)$  results by STAR (right) [113].

The nuclear modification factors for  $\Upsilon(1S)$  and  $\Upsilon(2S)$  as a function of the number of participants can be compared to the prompt  $J/\psi$  measurements by CMS and to those by STAR, as shown in Fig. 3.21. The results demonstrate a clear centrality dependence and a sequential quarkonium suppression of the states in Pb–Pb collisions at the LHC energies. For a proper comparison with the result obtained by STAR it is necessary to convert the CMS  $R_{AA}$  into a unique value for the three resonances:

$R_{AA}^{\Upsilon(1S+2S+3S)} \cong 0.44$ . The stronger suppression observed at the LHC suggests that the QGP temperature reached in the collisions is higher as well as the lifetime of the QGP is longer [113].

The CMS measurements are also compared in Fig. 3.22 to the model predictions previously introduced. The hydrodynamic model describes well the  $R_{AA}$  trend versus the centrality of the  $\Upsilon(1S)$  assuming as initial temperature rapidity profile a boost-invariant broad plateau and a plasma shear viscosity of  $4\pi\eta/s = 3$ . The rate equation model predicts quite well the  $\Upsilon(1S)$   $R_{AA}$  mostly in central collisions. According to this approach, one might conclude that the  $b\bar{b}$  regeneration is responsible of an enhancement of the  $\Upsilon(1S)$   $R_{AA}$  of an absolute value close to 0.1 (it corresponds to the difference between the primordial and the total  $R_{AA}$ ). For both models it is very difficult to make any conclusion on the agreement with the  $\Upsilon(2S)$  results.

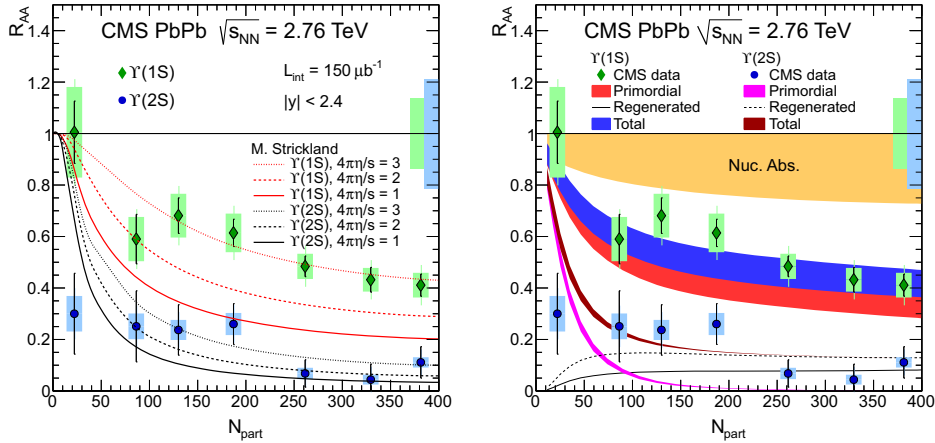


Figure 3.22: CMS  $\Upsilon(1S)$  and  $\Upsilon(2S)$  measurements compared to the hydrodynamic model (left) and to the rate equation approach (right) [113].

### 3.5 Summary of the results

At the end of this review on the  $\Upsilon$  production in different collision systems, energies and kinematic domains, it is worth to briefly summarize the most important results achieved.

- The  $\Upsilon$  production cross sections are determined for the three resonances in pp and  $p\bar{p}$  collisions at different energy scales, rapidities and  $p_T$  ranges. The agreement with theoretical predictions strictly depends on the model and on its calculation accuracy, but is not always satisfactory. The main results on  $\Upsilon(1S)$  polarization seems to

indicate an unpolarized production, with some contradictions within the experiments.

- Cold nuclear matter effects for  $\Upsilon$  mesons investigated in pA and dA collisions seem to be present mostly at backward rapidity and to be less important than those for the  $J/\psi$ . However, the results shown refer to old experiments at relatively low energies. Results from the LHC experiments are still to be published.
- Finally, the  $\Upsilon R_{AA}$  is extracted at different collision energies. The centrality dependence and the sequential suppression are well visible and, according to the theoretical prediction, the CNM effects alone cannot explain such a suppression pattern.

## Chapter 4

# ALICE at the LHC

The first part of this chapter briefly introduces the LHC accelerator. Then the ALICE experiment is described and lastly, an overview of the data taking procedure and of the data analysis framework is given.

### 4.1 The Large Hadron Collider

The Large Hadron Collider (LHC) at CERN<sup>1</sup> was built in the circular tunnel of 27 km length previously occupied by the Large Electron Positron collider (LEP). Having delivered the first proton-proton collisions on November 2009, it is now the most powerful accelerator ever constructed.

As all colliders, the LHC consists of acceleration cavities, bending magnets and two beam lines plus a huge set of beam optics and diagnostics instruments. The nominal field of 8.3 T and the collider radius of about 4.3 km lead to a nominal pp center-of-mass collision energy of 14 TeV [114].

Since the bending magnets have a minimum current at which they can operate, the resulting magnetic field corresponds to a minimal particle energy at which they can be injected into the collider. Pre-accelerators are therefore necessary.

In Fig. 4.1 the LHC is drawn as the big circle. The smaller one is the Super Proton Synchrotron (SPS) used as injector for the LHC and filled by the Proton Synchrotron (PS) small enough to fit on the CERN main site.

When the nominal or desired beam energy is reached, the beams collide in several interaction points (IP) where the four main experiments (ALICE, ATLAS, CMS and LHCb) are located. The beam intensity slowly decreases and after several hours the interaction rates become too low and a new fill is prepared. The collision rate  $R$  in a collider is proportional to the interaction

---

<sup>1</sup>The European Organization for Nuclear Research, known as CERN, is an international organization whose purpose is to operate the world's largest particle physics laboratory. Established in 1954, it is based in the northwest suburbs of Geneva on the Franco-Swiss border [114].

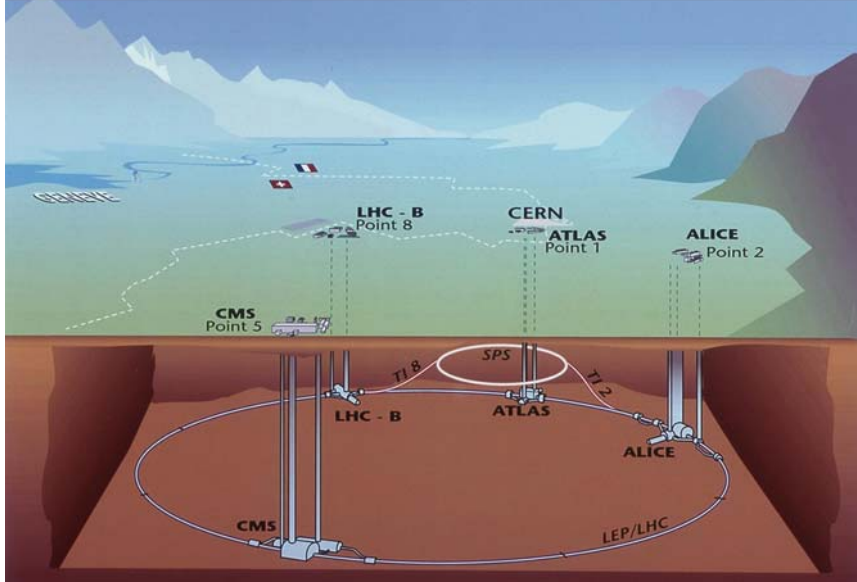


Figure 4.1: Schematic view of the LHC, the SPS and of the four main experiments (ALICE, ATLAS, CMS and LHCb).

cross section  $\sigma$  and a factor called *luminosity* ( $\mathcal{L}$ , usually in unit of  $\text{cm}^{-2}\text{s}^{-1}$ ):

$$R = \mathcal{L} \cdot \sigma \quad (4.1)$$

For technical reasons the beam is not continuous, but the particles are packed together in bunches. If two bunches containing  $n_1$  and  $n_2$  particles collide with frequency  $f$ , the luminosity is:

$$\mathcal{L} = f \frac{n_1 n_2}{4\pi\sigma_x\sigma_y} \quad (4.2)$$

where  $\sigma_x$  and  $\sigma_y$  characterize the Gaussian transverse beam profiles in the horizontal and vertical directions. To simplify the expression it is assumed that the bunches are identical in transverse profile, the profiles are independent of position along the bunch and the particle distribution are not altered during collisions [2].

During the first years of operation, the LHC delivered mainly pp collisions at  $\sqrt{s} = 0.9, 2.76$  TeV and for most of time at  $\sqrt{s} = 7$  and 8 TeV. An important part of the LHC program are annual Pb–Pb runs (so far two periods on 2010 and 2011 at  $\sqrt{s_{NN}} = 2.76$  TeV). Finally, at the beginning of 2013 asymmetric beams of protons and lead ions collided in LHC at an energy of  $\sqrt{s_{NN}} = 5.02$  TeV.

## 4.2 A Large Ion Collider Experiment

ALICE was designed to study the physics of the Quark-Gluon Plasma in an unprecedented energy regime. It is the only dedicated heavy-ion experiment at the LHC, sensitive to most of known observables. Its design was driven by the requirements of tracking and identifying particles in a wide momentum range (from less than 100 MeV/c up to about 100 GeV/c) and of reconstructing short-living particles such as open heavy-flavours and hyperons in a very high multiplicity environment, up to 8000 charged particles per rapidity unit at midrapidity [115].

A sketch of the ALICE setup is illustrated in Fig. 4.2. The experiment can be divided into three parts: the central barrel, the forward detectors and the Muon Spectrometer. They will be illustrated in more details in the following sections.

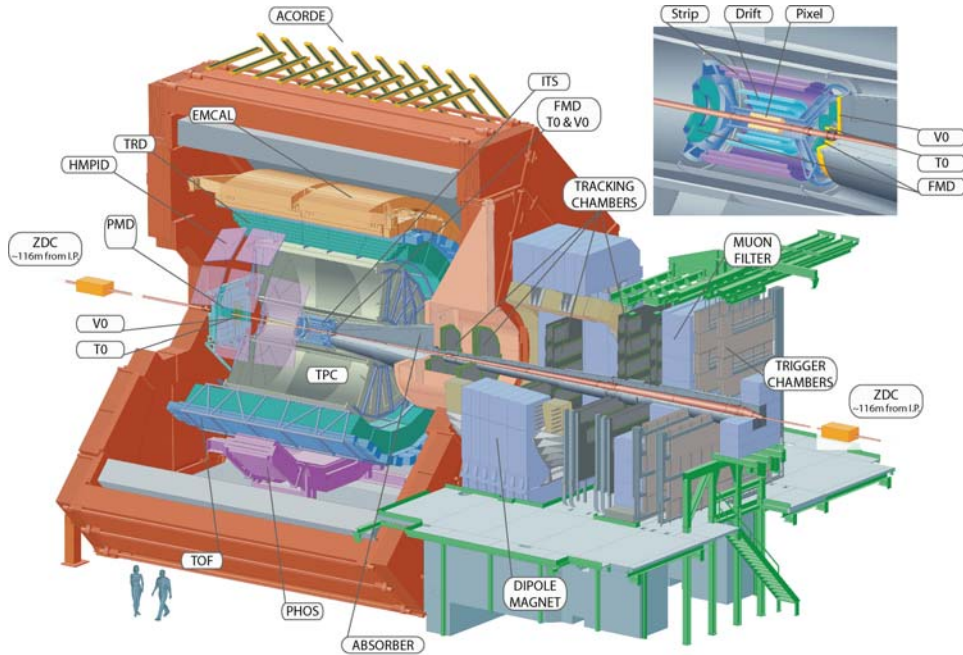


Figure 4.2: Schematic view of the ALICE experiment.

### 4.2.1 The ALICE coordinate system

A right-handed orthogonal Cartesian system was defined as the ALICE global coordinate system [116]. Its origin is the beam interaction point. The  $x$ -axis is perpendicular to the beam direction and points to the LHC ring center. The  $y$ -axis is perpendicular to the  $x$ -axis and to the beam direction at the IP, pointing upwards. Finally, the  $z$ -axis is parallel to the beam direction, with negative values in direction of the Muon Spectrometer.

Furthermore, the detector sides are named (as shown in Fig. 4.3):

- A and C for positive and negative  $z$ ;
- I and O inside and outside the accelerator ring;
- U and D upwards and downwards the experiment.

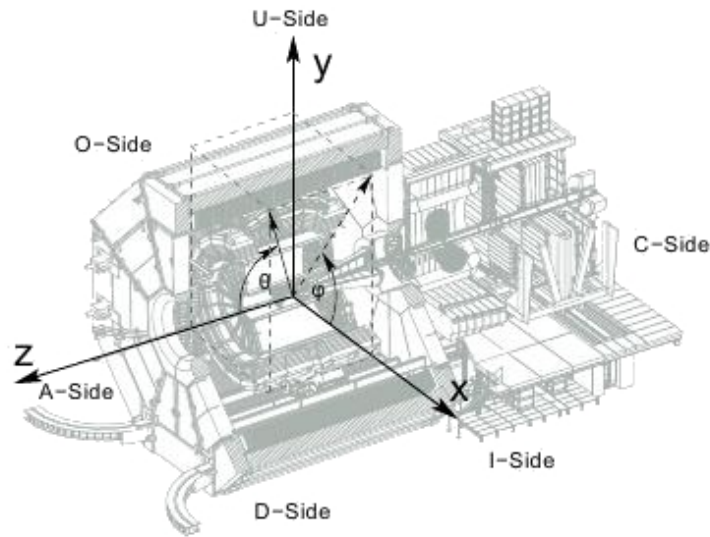


Figure 4.3: The ALICE coordinate system.

#### 4.2.2 Central barrel detectors

The ALICE central barrel is used for a broad variety of measurements such as vertex reconstruction and particle identification. What follows is a brief description of the different detectors.

##### Inner Tracking System

The Inner Tracking System (ITS) provides precise measurements of the primary vertex with a resolution better than  $100 \mu\text{m}$  in radial direction and the reconstruction of secondary vertices, for example from  $B$  and  $D$  decays. Moreover, it identifies tracks with  $p_T < 100 \text{ MeV}/c$  that do not reach the TPC and improves the momentum measurement for tracks reconstructed with the other detectors [117].

Being the closest to the interaction vertex and surrounding the beam pipe, the ITS is composed by six cylindrical layers of silicon detectors with a radius of 4 cm for the innermost and of 43 cm for the outermost covering an

acceptance of  $|\eta| < 1.98$ . Three different technologies are used: Silicon Pixel Detectors (SPD), Silicon Drift Detectors (SDD) and Silicon Strip Detectors (SSD), as illustrated in Fig. 4.4.

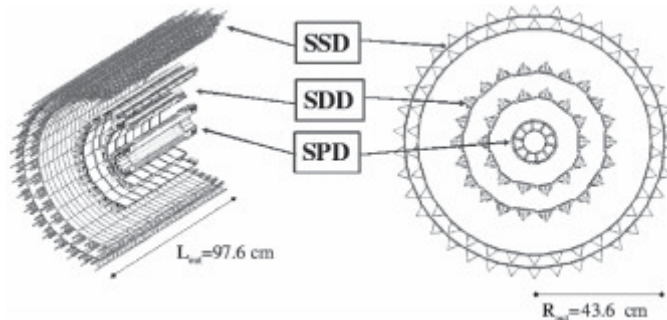


Figure 4.4: Layout of the ITS made of SPD, SDD and SSD.

Pixel and drift technologies are employed for the four innermost layers in order to achieve the impact parameter resolution and to cope with the high track densities expected in heavy-ion collisions. The SPD can run at high rate (about 1 kHz) to provide the vertex information for events triggered by the forward Muon Spectrometer.

Both SDD and SSD provide an analogue signal and can be used for particle identification via the specific energy loss of charged particles traversing the detector material.

### Time Projection Chamber

The main tracking detector of ALICE is a cylindrical Time Projection Chamber (TPC). With a total gas volume of about  $90 \text{ m}^3$  it is the largest TPC ever built (Fig. 4.5).

Its design provides vertex determination in the high-multiplicity environment expected in Pb–Pb collisions, charged-particle transverse momentum measurements from  $100 \text{ MeV}/c$  up to  $100 \text{ GeV}/c$  and good particle identification. The simultaneous detection of high and low momentum particles can be achieved with a low magnetic field ( $< 0.5 \text{ T}$ ) and a large detector volume which allows to measure a large segment of the tracks, thus increasing the sensitivity for the sagitta determination [118].

The TPC has an inner radius of  $85 \text{ cm}$  and an outer one of  $250 \text{ cm}$ , with a total length of about  $500 \text{ cm}$ . This leads to a  $88 \mu\text{s}$  drift time which is the limiting factor for the luminosity delivered by the LHC to ALICE in pp collisions<sup>2</sup>.

<sup>2</sup>As a consequence of the high TPC drift time, ALICE cannot cope with high interaction rates. With respect to the other LHC experiments, the luminosity in pp collisions is therefore reduced by displacing the proton beams at the IP or taking data in beam-satellite mode.

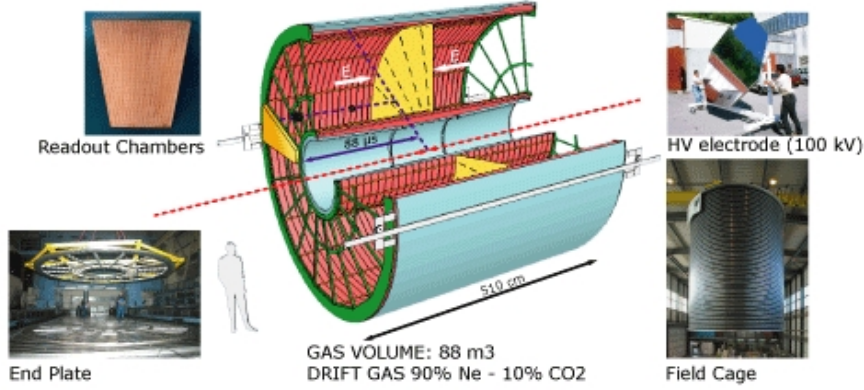


Figure 4.5: Schematic view of the TPC setup.

The study of soft hadronic observables requires a resolution of 1% for momenta between 100 MeV/c and 1 GeV/c, while the detection of hard probes requires a 10% resolution for tracks with  $p_T \sim 100$  GeV/c, achieved by using the TPC in combination with ITS and TRD. The resolution on the relative momentum between two particles, necessary to measure two-particle correlations, must be better than 5 MeV/c. Finally, the TPC can provide particle identification by  $dE/dx$  measurements from the low-momentum region up to few tens of GeV/c, in combination with TOF, TRD and ITS (Fig. 4.6).

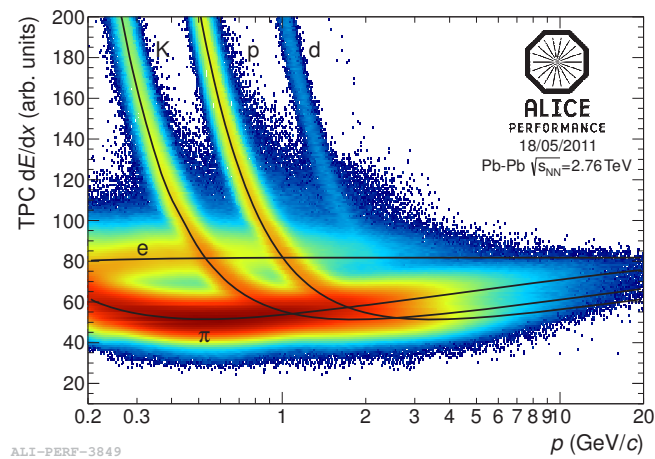


Figure 4.6: Specific energy loss in the TPC as a function of momentum with superimposed Bethe-Bloch lines for various particle species.

## Transition Radiation Detector

The Transition Radiation Detector (TRD) provides electron identification for momenta higher than 1 GeV/c where the pion rejection capability through energy loss measurement in the TPC is no longer sufficient. Its use, in conjunction with TPC and ITS, allows to measure the production of light and heavy vector meson resonances and, thanks to the determination of the impact parameter, of open charm and open beauty. A similar technique can be used to separate the promptly produced  $J/\psi$  mesons from those produced by the  $B$ -decays.

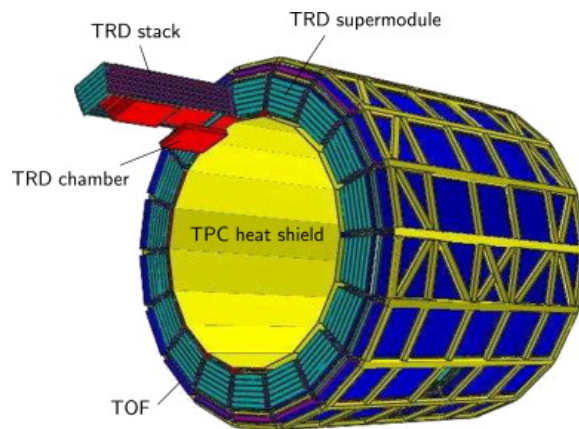


Figure 4.7: Illustration of the space frame holding the 18 TRD super modules, surrounded by the TOF detector.

The TRD detector fills the radial space between the TPC and the TOF. It consists of 18 sectors of 6 layers each with a 5-fold segmentation along the beam direction, for a total of 540 detector modules as shown in Fig. 4.7. Each module consists of a radiator of 4.8 cm thickness, a multi-wire proportional readout chamber and its front-end electronics. The TRD increases the ALICE pion rejection capabilities by a factor 100 for electrons with momentum above 3 GeV/c [119].

## Time Of Flight

The Time Of Flight (TOF) is the outermost detector having a full azimuthal coverage and a longitudinal acceptance of  $|\eta| < 0.9$ . It surrounds the TRD, as depicted in Fig. 4.7. Being segmented in 18 super modules in  $\phi$  and 5 in  $z$  direction, the TOF measures the particle time of flight with an overall resolution better than 80 ps. By the combination of this information with the particle momenta it is possible to determine their masses. The TOF provides particle identification in the intermediate momentum region: a separation of better than  $3\sigma$  can be achieved below 2.5 GeV/c for pions and kaons and below 4 GeV/c for kaons and protons [120].

The detector is made of Multi-gap Resistive Plate Chambers (MRPC). They are gaseous detectors with high and uniform electric field where ionization immediately starts the avalanches without any drift. They can operate at atmospheric pressure and with high gain due to the internal quenching capabilities of the resistive plates.

The TOF detector delivers trigger signals as well. It provides Level 0 (L0) triggers to select ultraperipheral collisions, minimum bias events in pp collisions and cosmic muons for the calibration of central detectors and cosmic ray physics.

### High Momentum Particle Identification Detector

The High Momentum Particle Identification Detector (HMPID) enhances the PID capability of ALICE by enabling the identification of particles beyond the momentum interval attainable through energy loss (in ITS and TPC) and time of flight measurements (in TOF). The detector is optimized to extend the range for  $\pi/K$  and  $K/p$  discrimination, on a track-by-track basis, up to 3 GeV/c and 5 GeV/c respectively [121].

The detector is designed as a single-arm array with a pseudorapidity acceptance of  $|\eta| < 0.6$  and an azimuthal coverage of about  $58^\circ$  which corresponds to 5% of the central barrel phase space. It is based on Ring Imaging Cherenkov counters and consists of seven modules of about  $1.5 \times 1.5 \text{ m}^2$  each (see Fig. 4.8).

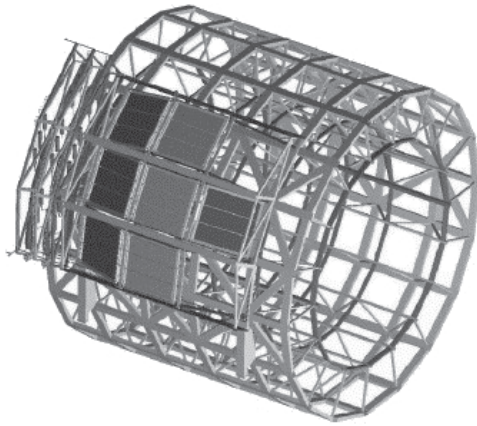


Figure 4.8: The seven HMPID modules on the TPC and TOF support.

### PHOton Spectrometer

The PHOton Spectrometer (PHOS) is a high-resolution electromagnetic spectrometer covering  $100^\circ$  in azimuth and  $|\eta| < 0.12$ , placed at the bottom of the ALICE setup at a distance of 460 cm from the interaction point.

It is divided into five independent modules of a segmented electromagnetic calorimeter and a Charged-Particle Veto (CPV) detector. Each calorimeter consists of 56 rows of 64 cells of  $\text{PbWO}_4$  crystals. Fig. 4.9 shows a 3D schematic view. The CPV is a Multi-Wire Proportional Chamber with a charged-particle detection efficiency better than 99%. The PHOS is designed to provide photon identification, as well as neutral meson identification, through the two-photons decay channel [122].

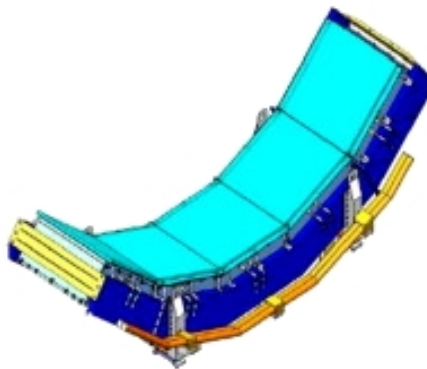


Figure 4.9: Schematic view of the PHOS.

### ElectroMagnetic Calorimeter

The ElectroMagnetic Calorimeter (EMCal) enhances the ALICE capabilities for high-energy jet measurements by improving jet energy resolution. It also increases the capabilities to measure high momentum photons and electrons. The EMCal is located 4.5 m away from the beam line with an azimuthal acceptance coverage of  $110^\circ$  and  $|\eta| < 0.7$ , limited by the PHOS and the HMPID (Fig. 4.10). The chosen technology is a layered Pb-scintillator sampling calorimeter with alternating layers of 1.44 mm of lead and 1.76 mm of scintillator [123].

### Magnet

The last component of the central barrel is the magnet: a large solenoid with a uniform field of 0.5 T. It eases considerably the track recognition thanks to the field strength that allows particle identification down to 100 MeV/c in  $p_T$ .

It is the same magnet used in the L3 experiment thanks to its large inner radius which can contain all the detectors described previously.

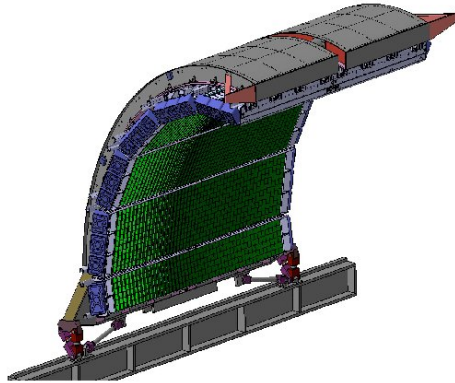


Figure 4.10: Layout of the EMCal.

### A COsmic Ray DEtector

The ALICE experimental program includes also a contribution to cosmic ray physics with the aim of studying high-energy cosmic air showers in the energy range  $10^{15}$  –  $10^{17}$  eV and to determine the nature of primary cosmic rays [124]. This purpose can be reached with the COsmic Ray DEtector (ACORDE) based on the ALICE tracking detectors plus an additional Cosmic Ray Trigger (CRT) made of scintillators located on top of the ALICE magnet as shown in Fig. 4.11.

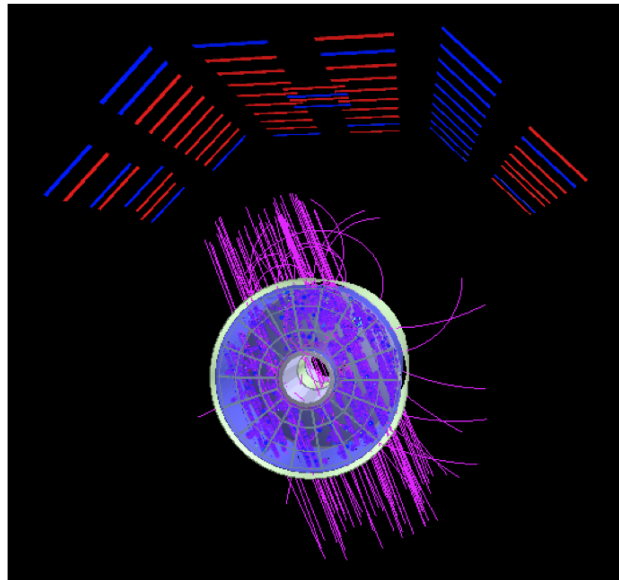


Figure 4.11: Cosmic rays detected by ACORDE (on the upper faces of the magnet).

### 4.2.3 Forward detectors

The main tasks of the ALICE forward detectors are the centrality determination of a AA collision and the multiplicity evaluation in pp, pA and AA collisions. A brief description of these detectors is now given.

#### Forward Multiplicity Detector

The Forward Multiplicity Detector (FMD) provides charged particle multiplicity information in the pseudorapidity range  $1.7 < \eta < 5.1$  (A-side) and  $-3.4 < \eta < -1.7$  (C-side). It consists of silicon strip detectors divided in seven disks perpendicular to the beam pipe and placed at distances between 42 and 225 cm from the interaction point [125]. In Fig. 4.12 a schematic view is presented.

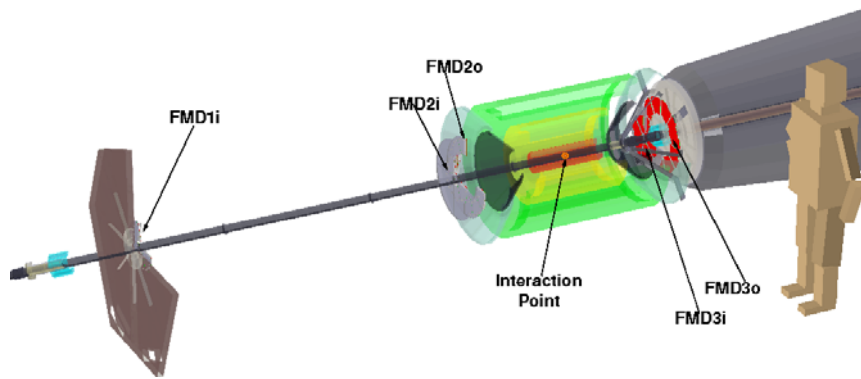


Figure 4.12: The Forward Multiplicity Detector.

#### Photon Multiplicity Detector

The Photon Multiplicity Detector (PMD) is a pre-shower detector measuring the multiplicity and spatial distribution of photons in the forward region ( $2.3 < \eta < 3.7$ ). Placed at about 360 cm from the interaction point, in A-side, its main goal is the estimate of the transverse electromagnetic energy and the reaction plane on an event-by-event basis for AA collisions analysis [126].

It consists of two identical planes of detectors, made of gas proportional counters with honeycomb structure and wire readout (Fig. 4.13), with a  $3X_0$  thick lead converter in between.

#### VZERO

The VZERO detector (V0) is made of two arrays of scintillator material, located at 340 cm (A-side) and 90 cm (C-side) from the interaction point.

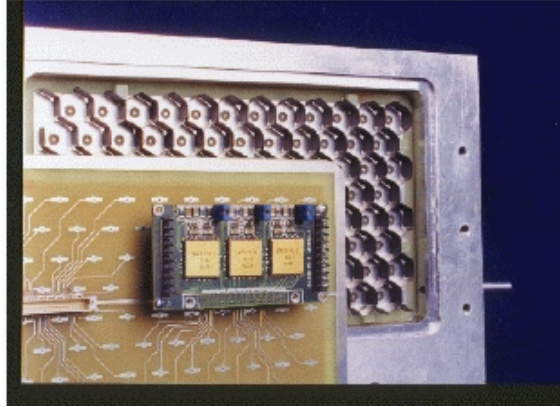


Figure 4.13: A PMD prototype tested at CERN.

The detectors are segmented into 64 elementary counters distributed in 8 rings, covering two pseudorapidity ranges:  $2.8 < \eta < 5.1$  and  $-3.8 < \eta < -1.7$ . The measurement of the time difference between the two subsystems allows to identify and reject the beam-gas events, thus providing a minimum bias trigger for the central barrel detectors and a validation signal for the Muon Trigger [125].

The V0 can also measure the charged particle multiplicity, acting as a centrality indicator for AA collision analysis.

The centrality is usually expressed as a percentage of the total nuclear interaction cross section  $\sigma$ . The centrality percentile  $c$  of an AA collision with an impact parameter  $b^3$  is defined by integrating the impact parameter distribution  $d\sigma/db$  as in the following formula:

$$c = \frac{\int_0^b \frac{d\sigma}{db'} db'}{\int_0^\infty \frac{d\sigma}{db'} db'} = \frac{1}{\sigma_{AA}} \int_0^b \frac{d\sigma}{db'} db' \quad (4.3)$$

With this definition, high values of centrality correspond to peripheral collisions. In ALICE, the centrality is defined as the percentile of the hadronic cross section corresponding to a charged particle multiplicity above a given threshold ( $N_{ch}^{thr}$ ) [127]:

$$c \cong \frac{1}{\sigma_{AA}} \int_{N_{ch}^{thr}}^\infty \frac{d\sigma}{dN'_{ch}} dN'_{ch} \quad (4.4)$$

Fig. 4.14 shows the distribution of VZERO amplitude (proportional to the multiplicity). It exhibits a peak corresponding to the most peripheral collisions (90%–100%) usually rejected in the analyses because contaminated by electromagnetic background and by missing events due to the trigger inefficiency.

<sup>3</sup>The impact parameter of a collision is defined as the distance between the centers of the two colliding nuclei in a plane transverse to the beam axis.

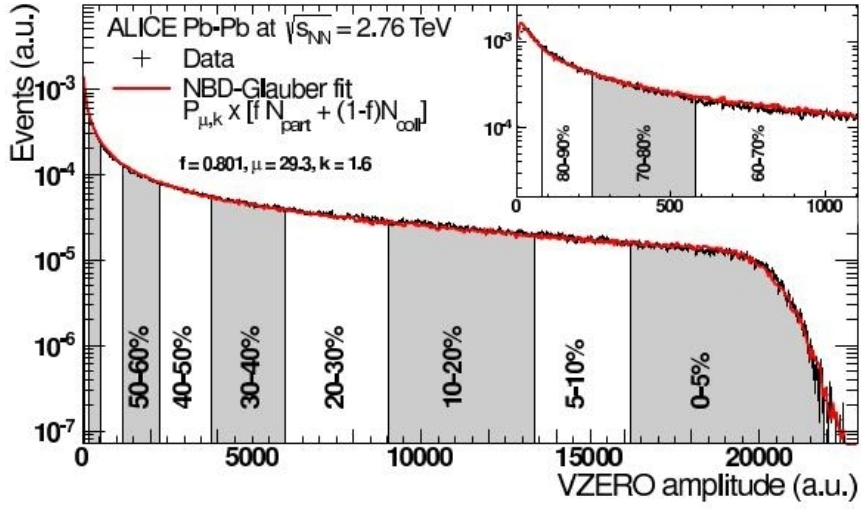


Figure 4.14: VZERO amplitude distribution fitted with a Glauber fit [128]. The centrality classes are indicated in the figure. The inset shows a zoom of the most peripheral region.

## T0

The T0 detector (Fig. 4.15) consists of two arrays of Cherenkov counters, with a time resolution better than 50 ps, asymmetrically placed at 375 cm (A-side) and 72.7 cm (C-side) from the interaction vertex, with a pseudorapidity coverage of  $4.61 < \eta < 4.92$  and  $-3.28 < \eta < -2.97$  respectively. It is designed to provide a start signal for the TOF detector, to measure the vertex position along the beam axis with a precision of  $\pm 1.5$  cm and to measure the particle multiplicity, generating a centrality trigger [125].



Figure 4.15: A view of the T0.

## Zero Degree Calorimeters

The Zero Degree Calorimeters (ZDC) provide a centrality estimate and trigger in Pb–Pb collisions by measuring the energy carried in the forward direction (at zero degrees with respect to the beam direction) by non-interacting nucleons (spectators) [129].

The detector consists of two pairs of quartz-fiber hadronic calorimeters (for neutrons and protons), placed on both sides of the interaction point, at 116 m from it. Being placed between the beam pipes (as shown in Fig. 4.16), the neutron calorimeter (ZN) has the most severe geometrical constraints: the transverse dimensions have to be smaller than 7 cm, requiring a very dense material (tungsten). The stringent space constraints do not hold for the proton calorimeter (ZP), which is made with a less dense material (lead). The ZN, segmented in four regions, can also provide an estimate of the reaction plane.

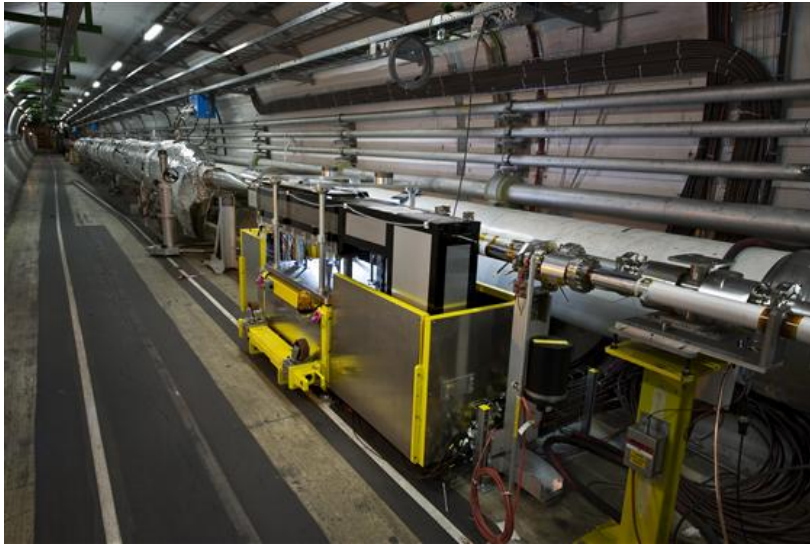


Figure 4.16: View of the ZDC apparatus close to the beam pipe.

The ZDC system presents also two electromagnetic calorimeters (ZEM), both placed at about 7 m from the IP (PMD side), which allow to resolve ambiguities in the determination of the centrality. The ZEM, made of lead and quartz fibers, are designed to measure the energy of particles, mostly photons generated from  $\pi^0$  decays, at forward rapidities ( $4.8 < \eta < 5.7$ ).

### 4.2.4 The Muon Spectrometer

The Muon Spectrometer in the pseudorapidity region  $-4 < \eta < -2.5$  allows studies of low-mass vector mesons and quarkonia (charmonium and bottomonium) in the dimuon channel and of open charm and open beauty

in the semi-leptonic decay channel. Due to its importance for this thesis, a more detailed description is provided in Chapter 5.

## 4.3 Online Control System

The Online Control System of ALICE [130] takes care of the data treatment during the data taking. The modules are now presented.

### 4.3.1 Detector Control System

During the data taking the shift crew must have the control of the status of the detectors, check errors that could happen and have the possibility to recover possible failures in order to maximize the efficiency during the acquisition. For these reasons, the ALICE Collaboration developed the Detector Control System (DCS), a remote control of all the detectors. Having to cope with a large variety of different subsystems and equipments, the DCS was designed to be flexible and modular, in order to give an easy environment to the sub-detector developers. The DCS is responsible of configuring, monitoring and controlling all the equipment of the experiment. It is also provided with a graphical user interface that shows the information from the detectors and allows the execution of commands [130].

### 4.3.2 Central Trigger Processor

The trigger signals from the detectors are collected and processed by the ALICE Central Trigger Processor (CTP) [131, 132]. It is designed to select events having different features and rates which can be downscaled to suit the physics requirements and restrictions imposed by the DAQ bandwidth. The aim of the ALICE trigger is to manage the detectors which are busy for different periods following a valid trigger and to perform trigger selection optimized for several different running conditions.

The fastest trigger signal, called Level 0 (L0), arrives  $1.2 \mu\text{s}$  after the collision. The L0 signals (24 L0 inputs) from the fastest detectors, such as the SPD, V0, T0 and the Muon Trigger, are treated with a three states logic (*asserted*, *not relevant* and *negated*) combined together with logic AND and OR in order to select a certain class of events.

The information of slower detectors is used to create a Level 1 trigger signal (L1) that is dispatched after  $6.5 \mu\text{s}$ . The ALICE trigger system is provided with a past-future protection circuit that looks for other events of requested types in a time windows before and after the collision under investigation: it should help the rejection of pile-up events and the good read out of the detectors.

The last level called Level 2 (L2), waits for the past-future protection and arrives after  $88 \mu\text{s}$ .

The CTP data are stored in the raw data stream and in dedicated scalers. In particular, there are scalers for all the inputs and for each trigger class that store the number of events passing each stage of the trigger (L0, L1, L2).

### 4.3.3 Data AcQusition System

The ALICE DAQ system was designed to cope with extremely challenging conditions: on one hand the large interaction rate in pp collisions with a relatively small event size and on the other hand the smaller collision rate with lead beams, but with a large amount of data, up to 1.25 GB/s sent to the storage. Its design was also driven by the requirement of sharing the resources between different groups (clusters) of detectors: these clusters are set up to study different observables that have different cross sections and, consequently, different trigger rates.

Once the CTP decides to acquire a particular event, the trigger signal is dispatched to the front-end read-out electronics (FERO) of the involved detectors. The data are then injected in the Detector Data Link (DDL<sup>4</sup>) and sent to a farm of computers, called Local Data Concentrators (LDC), that build the event fragments from the front-end electronics into sub-events. The sub-events are then shipped through an event building network to the Global Data Collectors (GDC) that take all the sub-events from the various LDC, build the whole event and eventually send it to the storage facilities [130].

### 4.3.4 High Level Trigger

Since the huge amount of data (up to 25 GB/s in central Pb–Pb collisions) cannot be treated by the DAQ and the storage facility (the bandwidth limit for sending data to the storage is about 1.25 GB/s), a selection of interesting events and a data compression is needed. The High Level Trigger [133] is designed to collect raw data from the LDC, to perform local pattern recognition, fast tracking and primary vertex localization, and to build up the global event. The trigger decision and the compressed data are sent back to the DAQ via the HLT DDL output. In order to fulfil these requirements the HLT consists in a farm of more than 1000 multi-processor computers. The HLT also has an online event display that allows visualizing the events and monitoring the goodness of the data taking.

### 4.3.5 Data Quality Monitoring

Due to the complexity of ALICE in terms of number of detectors and performance requirements, Data Quality Monitoring (DQM) [134] plays an

---

<sup>4</sup>The DDL is an ALICE-standard. In ALICE there are more than 450 optical DDL.

essential role in providing an online feedback on the data being recorded. It intends to provide operators with precise and complete information to quickly identify and overcome problems and, as a consequence, to ensure acquisition of high quality data. DQM typically involves the online gathering of data samples, their analyses by user-defined algorithms and the visualization of the monitoring results.

The final design of the DQM software framework of ALICE is AMORE (Automatic MONitoring Environment). This system is used to monitor the event data coming from the ALICE detectors allowing operators and experts to access a view of monitoring elements and to detect potential problems. Important features include the integration with the offline analysis and reconstruction framework, the interface with the electronic logbook that makes the monitoring results available everywhere through a web browser.

#### 4.3.6 Detector Algorithms

The ALICE detectors are regularly calibrated in order to achieve most accurate physics measurements. The ALICE online calibration framework is used to implement and run a set of Detector Algorithms (DA) provided by the detector teams [135]. Each DA grabs detector data (physics or calibration events) and produces results online. These results can be directly used (for example to configure the detector electronics or to give quality feedback to the DQM system) or shipped offline (to be processed and used in event reconstruction).

A DA consists of a specific detector code to analyse events and to produce results according to a given calibration task, using a support library to interact with the external components (read configuration, grab events, log messages, export results, deal with the control system commands). There are two types of DA: the monitoring DA, which subscribe to events on the fly and the LDC DA, which analyse at end of run a locally recorded data file [136].

### 4.4 ALICE offline framework

AliRoot, the ALICE offline framework, is the software used by the ALICE community for simulation, reconstruction, detector alignment, calibration, visualization and data analysis. What follows is a short overview of the most important features.

#### 4.4.1 AliRoot

The ALICE Offline Project started developing in 1998 the software of the experiment called AliRoot [137]. This framework is completely based on the Object Oriented paradigm and it is entirely written in C++ with

some makefiles for Fortran 90 to interface with GEANT. As described in Fig. 4.17, the AliRoot architecture is based on the ROOT framework [138] and it is designed to be extremely modular. The STEER module provides steering, run management, interface classes and base classes. The detector's code is divided into independent modules which provide the syntax for simulation and reconstruction. The analysis code is continuously developed and progressively added to the framework.

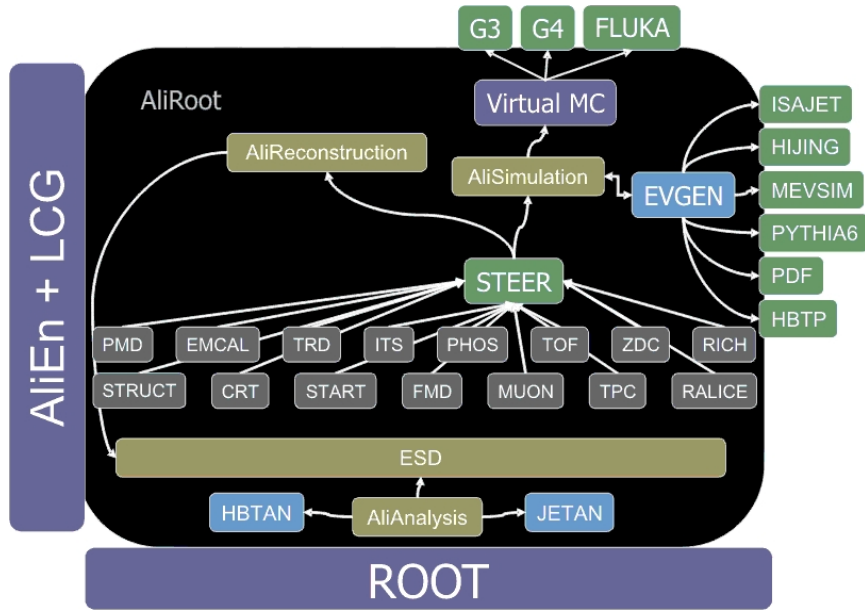


Figure 4.17: General scheme of the AliRoot architecture.

AliRoot is designed to easily interface with external Monte Carlo modules for the event generation and particle transport through the detector geometry.

### Simulation

The main simulation class is `AliSimulation` which provides the interface to event generators (such as PYTHIA [139, 140] or HIJING [141]) and to geometry builder (as detectors alignment and magnetic field). Also, users can force the particles to be produced and to decay in a particular acceptance region in order to speed up the processes and tune their kinematic parametrizations (basically  $y$  and  $p_T$  needed to get the phase space of the particles) in the cases they are known.

## Particle transport

In order to obtain the detector response for the simulated events, AliRoot provides different Monte Carlo packages: GEANT3 [142], GEANT4 [143] and FLUKA [144].

The geometry of ALICE detectors is built in these packages, including support structures, absorbers, shielding and beam pipe. The magnetic field of the solenoid and the warm dipole magnet can be described in the simulation as well.

Ideal geometry is used as a default, but it is possible to work with a more reliable apparatus condition by retrieving the Offline Conditions Data Base objects (OCDB) which include pedestals, noisy or dead channels, HV values... [145].

## Reconstruction

AliReconstruction class provides the interface to the configuration of the reconstruction phase (for both the real data and Monte Carlo simulations). The sequence is:

- reconstruction executed for each detector separately;
- primary vertex reconstruction;
- track reconstruction and particle identification;
- secondary vertices reconstruction.

The final output is an Event Summary Data (ESD), i.e. a `.root` file containing all the information relevant for physics analyses. During the production specific processes are possible such as the offline re-alignment of the tracking chambers. ESD could be further filtered for a more specific analysis and then stored in the Analysis Object Data (AOD) output files that are smaller in size and therefore give faster access for the users. The final stage of the filtering is the production of Muon Analysis Oriented Data (Muon AOD) which summarize all necessary information required for physics with the Muon Spectrometer.

### 4.4.2 The GRID

The amount of data produced by the ALICE apparatus is so enormous that the computing resources cannot be physically placed in a unique place, but they have to be distributed around the world. Such a distribution has to deal with very different kinds of tasks that should be timely performed and with a large number of different user. In addition, the resources are locally administrated by the computing centers afferent to the project and

could be implemented in large variety of different technologies. To answer all these issues the computing project called *Grid* was started [146].

The ALICE computing infrastructure, as those for the other LHC experiments, belongs to the program coordinated by the Worldwide LHC Computing Grid (WLCG). This infrastructure, based on the MONARC<sup>5</sup> [147] model, is hierarchical and its levels are called *Tiers*. The real data from the experiment are stored in the very large computing center at CERN, the *Tier 0*, then data are replicated in regional large computing centers, called *Tier 1* that also participate to the reconstruction and the storage of Monte Carlo data. The local computing centers, i.e. the resources of the participating institutes, are the *Tier 2*. Although with smaller data storage capabilities, they contribute with computing power for the user data analysis tasks and the Monte Carlo simulations. The lower levels of this infrastructure are the Tiers 3 and 4, local computing clusters of University departments and user's workstations.

The interconnections between all these different facilities are possible thanks to the Grid Middleware. ALICE developed a set of Middleware services called AliEn [148]. Through the AliEn User Interface (the MonALISA repository for ALICE [149, 150]), the user interacts with the Grid: after authentication, he can access and store files as in a Unix-like system, send his own tasks (jobs) for analysis or simulation purposes and monitor their execution.

## 4.5 ALICE upgrade program

The ALICE Collaboration is planning to upgrade the current detectors by enhancing its vertex reconstruction and low-momentum tracking capability and allowing data taking at higher rates [151].

The upgrade strategy is formulated under the assumption that, after the second long shutdown in 2018, the LHC will progressively increase its luminosity with reaching an interaction rate of about 50 kHz, i.e. instantaneous luminosities of  $\mathcal{L} = 6 \cdot 10^{27} \text{ cm}^{-2}\text{s}^{-1}$  in Pb–Pb collisions. The upgrade will include:

- a new ITS with high resolution and low material thickness which will improve by a factor 3 the resolution of the distance of closest approach between a track and the primary vertex [152];
- the replacement of the TPC readout multi-wire chambers with Gas Electron Multiplier (GEM) detectors;
- a development of the readout electronics for TPC, TRD, TOF, EMCAL and Muon Spectrometer in order to cope with a higher data taking rate;

---

<sup>5</sup>Models Of Networked Analysis at Regional Centres for the LHC experiments.

- new online systems (HLT, DAQ and CTP), to adapt for high rates and to increase the data mass storage to about 20 GB/s;
- a completion of the EMCal to nearly  $2\pi$  coverage (still under consideration).

Moreover, the installation of a Muon Forward Tracker (MFT, five planes of silicon pixel detector with very high granularity in the Muon Spectrometer acceptance) is approved. It should increase the secondary-vertex reconstruction capabilities for muon measurements and enhance the forward heavy-flavours program [153]. An installation of a Forward Calorimeter (FoCal) with a highly granular electromagnetic part is being discussed. It could allow additional jet and direct-photon measurements at forward rapidity enhancing the overall photon-jet physics of ALICE and enabling studies of gluon saturation [154].

## Chapter 5

# The forward Muon Spectrometer and its trigger system

In this chapter the Muon Spectrometer is described in details. A particular attention will be given to the Muon Trigger.

### 5.1 Physics with the Muon Spectrometer

The goal of the forward Muon Spectrometer [155] is the study of charmonium ( $J/\psi$  and  $\psi(2S)$ ) and bottomonium ( $\Upsilon$  resonances), low mass vector mesons ( $\rho$  and  $\phi$ ), open heavy-flavours ( $D$  and  $B$  families) and weak bosons ( $Z, W^\pm$ ), via their muonic decay channels in pp, pA and AA collisions at the LHC energies. The measurement can be achieved in a wide range of transverse momentum down to  $p_T = 0$  and in the rapidity range  $2.5 < y < 4$ <sup>1</sup>.

The energy domain covered by the LHC allows to probe the parton distribution functions of the nucleon and also their modifications in the nucleus in the case of pA and AA collisions, at very low values of momentum fraction (Bjorken- $x$ ). The capabilities to measure charm and beauty particles in the forward rapidity region using the ALICE Muon Spectrometer gives access to the regime down to  $x \sim 10^{-6}$  [156].

The design was essentially driven by two requirements: to perform quarkonia detection down to zero transverse momentum and to resolve the bottomonium states ( $\Upsilon(1S)$ ,  $\Upsilon(2S)$  and  $\Upsilon(3S)$ ) in the large background environment of central Pb–Pb collisions. The mass resolution required for the  $\Upsilon$  is about 100 MeV/ $c^2$  at 10 GeV/ $c^2$  [155].

---

<sup>1</sup>Despite the ALICE reference frame, in this thesis the results will be presented with a positive  $y$  notation keeping the  $\eta$  values signed.

## 5.2 The Muon Spectrometer setup

The Muon Spectrometer, as shown in Fig. 5.1, is composed of a system of absorbers, five stations of tracking detectors that, together with a warm dipole magnet, are used to track muons and to measure their momenta and two stations of trigger chambers shielded by a muon filter (or iron wall) [157, 158].

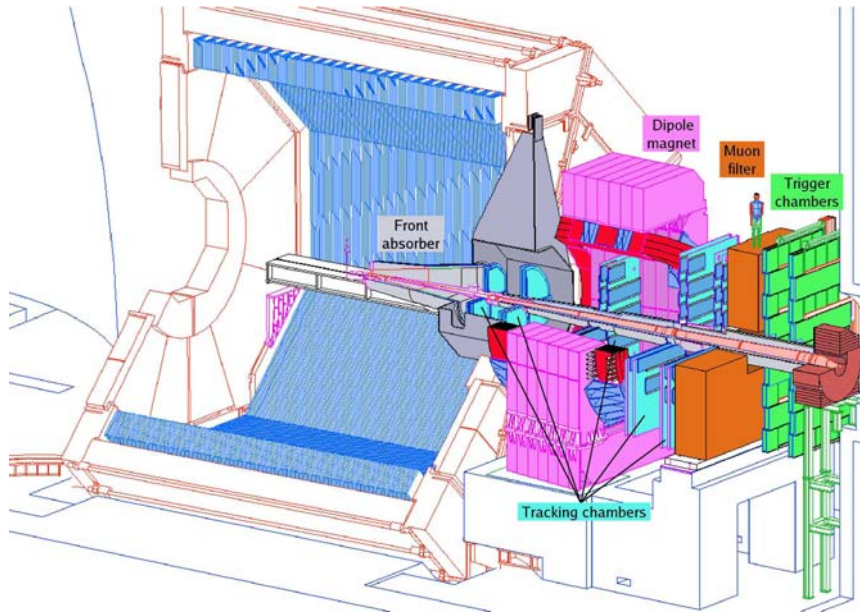


Figure 5.1: Layout of the ALICE forward Muon Spectrometer.

The Muon Spectrometer has a total length of 17 m and covers the polar angular range  $172^\circ < \theta < 178^\circ$  ( $-4.0 < \eta < -2.5$ ) with respect to the ALICE reference frame (see Sec. 4.2.1).

### 5.2.1 Front absorber

The front absorber is made out of carbon, concrete and steel with a conical geometry, for a total length of 4.13 m (corresponding to  $\sim 10$  radiation lengths), as shown in Fig. 5.2. Located at 90 cm from the IP, inside the L3 magnet, it is designed to limit multiple scattering and energy loss by traversing muons, but also to protect other ALICE detectors from secondary particles produced within the absorbing material [159]. For this reason, it is covered by a 10 mm layer of tungsten at the front end of the cone (close to ITS) and in the sector between  $10.5^\circ$  and  $12.5^\circ$  where it faces TPC. A tungsten cover of 100 mm thickness at the back end absorbs most of the low energetic electrons created inside the absorber. An additional ring of 100 mm of tungsten is added to the  $2^\circ$  cone to improve the shielding against

particles from the beam pipe. Finally, three layers of polyethylene are placed at the end of the absorber for stopping slow neutrons.

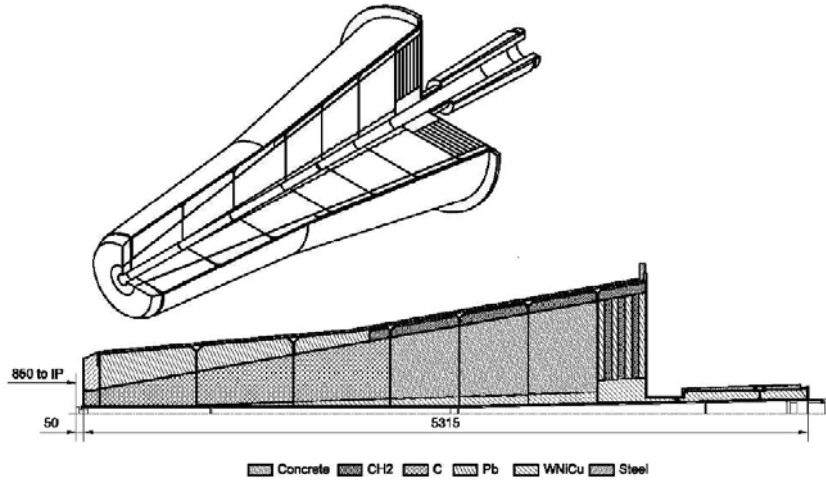


Figure 5.2: Design of the front absorber.

### 5.2.2 Muon filter

One more absorber is located between the Muon Tracking and the Muon Trigger, 14.5 m from the IP. It is a 120 cm thick wall made of cast iron, whose aim is to reduce the background on the Muon Trigger stations. It absorbs hadrons and low-momentum muons: the combined effect of the front absorber and the muon filter prevents muons with  $p < 4$  GeV/c from reaching the Muon Trigger chambers. The muon filter is shown in Fig. 5.3 along with the warm dipole magnet.

### 5.2.3 Dipole magnet

A warm dipole magnet is located at about 10 m away the IP. It houses the third Muon Tracking station and provides the bending power necessary to measure the transverse momenta of muons. It has a maximum central field of 0.7 T and an integral field of 3 T·m. The general concept of the magnet is based on a window-frame return yoke, fabricated from low-carbon steel sheets. Its overall dimensions are 5 m in length, 7 m in width and 9 m in height, with a total weight of about 890 tons [160]. The magnet is also used as a support for the front absorber and beam shield. An additional radial space of  $10 \div 15$  cm is provided to house the support frames of the Muon Tracking chambers inside the magnet. The dipole has an angular acceptance of  $171^\circ < \theta < 178^\circ$  and is designed to provide a horizontal magnetic field



Figure 5.3: View of the muon filter (left) and of the dipole magnet (right).

perpendicular to the beam axis. The field polarity can be reverted within a short time. A view of the warm dipole magnet is shown in Fig. 5.3.

#### 5.2.4 Beam shield

Small angle particles and secondary ones emerging from the beam pipe are stopped by the beam shield. It is an absorber made of high  $Z$  tungsten-lead mixture embedded in a 4 cm thick stainless steel envelope, which surrounds the beam pipe along the Muon Spectrometer. Its shape follows the  $178^\circ$  acceptance line up to a maximum radius of 30 cm and then it stays constant.

#### 5.2.5 Muon Tracking

##### Tracking chambers

The design of the Muon Tracking system was driven by the following requirements: working capability in a high multiplicity environment, good mass resolution in a large mass range up to  $\Upsilon$  resonances and area coverage of about  $100 \text{ m}^2$ . The high flux of particles was expected from past calculations to be up to 620 particles per central Pb–Pb collision [157] with a non-uniform distribution in  $\eta$  reaching values up to  $10^{-2} \text{ hit/cm}^2$  close to the beam pipe.

To achieve the expected mass resolution for the  $\Upsilon$ , a momentum resolution of  $\Delta p/p < 1\%$  is needed, which means a spatial resolution better than  $100 \mu\text{m}$  in the bending plane (perpendicular to the magnetic field). Less stringent criteria are required along the non-bending plane, where a resolution better than about 2 mm is enough for a good track finding.

In order to fulfil all these requirements, Multi-Wired Proportional Chambers (MWPC) were chosen with a high granularity cathode-pad read-out. The segmentation of the cathode pads is designed to keep the occupancy well below 5% for central Pb–Pb collisions: since the hit density decreases with the distance from the beam pipe, larger pads are used at larger radii, for a total number of about one million read-out channels. Each chamber has two cathode planes, which are both read out to provide two-dimensional hit information.

The multiple scattering in the Muon Tracking station materials could degrade the momentum resolution. Composite materials, such as carbon fibres, are used to minimize this effect. The thickness of each chamber corresponds to about  $0.03X_0$ .

The detector is composed by five stations of two planes each: two of them are placed before the dipole magnet inside the Front Absorber Support Structure (FASS) [161] at 5.4 and 6.4 m from the IP, one station is placed inside the dipole magnet at 9.8 m and the last two stations are placed just before the iron wall (at 12.9 and 14 m from the IP).

The design of the chambers was adapted to fit particular geometrical requirements: the first two stations are based on a quadrant structure (Fig. 5.4, left), while the other three have a slat design (Fig. 5.4, right). Quadrants and slats overlap to avoid dead zones on the detector.

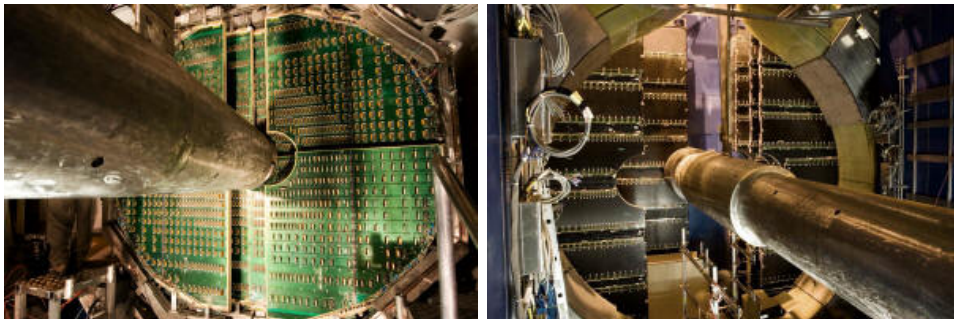


Figure 5.4: Tracking chambers with quadrant (left) and slat (right) layout.

The gas mixture, made of Ar (80%) and CO<sub>2</sub> (20%), maximizes the probability of ionization for charged particles and minimizes neutron interaction.

## Electronics

For all the stations, the front-end electronics is based on a 64 channel board (MANas NUmérique, MANU). On this board the signals of four 16-channels charge amplifier chips (Multiplexed ANalogic Signal processor, MANAS) are sent to 12-bits ADC and to a read-out chip (Muon Arm Read-out Chip, MARC) whose functionalities include the zero suppression. Thus,

the million of channels of the Muon Tracking system is treated by about 17000 MANU cards.

The Concentrator Read-Out ClUster (CROCUS) dispatches the trigger signal from the central trigger processor, performs the calibration of the MANU and gathers data through specific buses (Protocol for the ALICE Tracking CHamber, PATCH) sending them to the DAQ within  $240 \mu\text{s}$  after the trigger signal.

### Alignment

The alignment of the Muon Tracking chambers is strictly constrained by the above mentioned resolution in the  $\Upsilon$  mass region. Once installed, the chamber positions were measured with a precision of some tenths of millimetre [162].

Special runs without magnetic field are periodically carried out in order to improve the quality of the alignment: straight tracks are used in an offline realignment, performed using the Millepede algorithm [163], thus estimating the residual misalignment for each detection element. All these corrections are then implemented in the muon track reconstruction phase.

This position can be modified by the magnetic field as well as the heating of the electronics. In order to keep track of these displacements, an optical monitoring system was installed. The Geometry Monitoring System (GMS) is an array of about 460 optical sensors placed on the corners of each Muon Tracking chamber and in the ALICE cavern, as shown in Fig. 5.5.

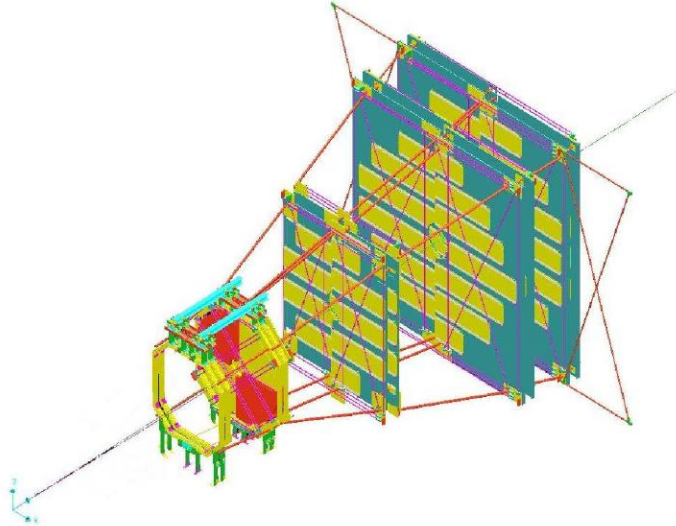


Figure 5.5: Geometry Monitoring System setup: the lines on this figure represent the optical lines.

This system monitors the relative position of two chambers of each station and between different stations, together with the flatness of the chambers and the absolute displacement of the entire Muon Spectrometer with respect to the ALICE cavern with a resolution of about  $20 \mu\text{m}$ .

### 5.2.6 Trigger system

The Muon Spectrometer is completed by the Muon Trigger, whose description is given in next section.

## 5.3 The Muon Trigger system

Simulations indicate that, at the level of Muon Trigger detector, in a central Pb–Pb collision several low-transverse momentum (soft) muons are expected from pion and kaon decays representing the main source of background, as shown in Fig. 5.6.

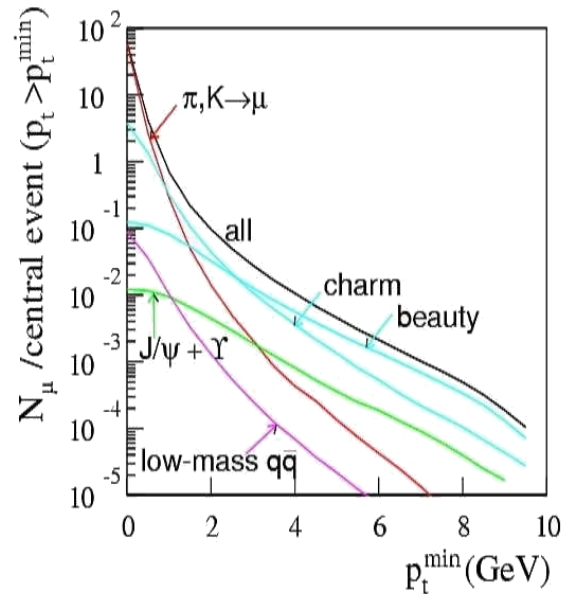


Figure 5.6: Simulation of average number of muons with  $p_T > p_T^{\text{min}}$  at forward rapidity in central Pb–Pb collisions as a function of  $p_T^{\text{min}}$ .

Furthermore, the expected Pb–Pb collision rate at the nominal luminosity is about 8 kHz, while the maximum trigger rate accepted by the acquisition system of ALICE is around 1 kHz. To reduce the probability of triggering on events without any high- $p_T$  muon, a hardware cut is applied on the transverse momentum. A rough estimate of the transverse momentum can be done with position sensitive detectors. These detectors have to

cover a large area and to give fast signals. For these reasons, Resistive Plate Chambers (RPC) were chosen for the ALICE Muon Trigger system.

### 5.3.1 Detector geometry

The trigger system is based on two large area (about  $5.5 \times 6.5 \text{ m}^2$ ) detector stations (MT1 and MT2) separated by 1 m and placed behind the muon filter at 16 and 17 m from the IP. Each station consists of two planes of 18 single-gap RPC. The presence of the beam shield affects the shape of the RPC: those closer the beam pipe are shorter or with a cut corner (Fig. 5.7).

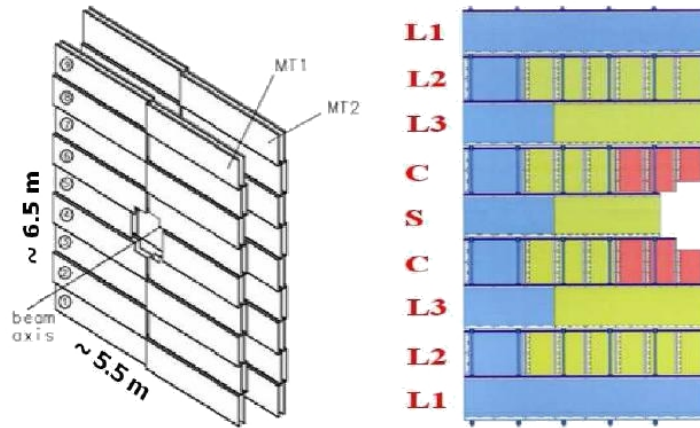


Figure 5.7: Layout of the ALICE Muon Trigger system. Different colours refer to the three strip widths, according to Tab. 5.1.

RPC signals are read out on both sides by orthogonal pick up strips, providing the spatial information. The  $y$  coordinate measures the bending deviation due to the dipole magnetic field and the read-out plane that provides this information is called *bending plane*, while  $x$  represents the *non-bending* coordinate. The strips dimensions are conditioned by two factors: the hit density and the required momentum resolution. The particle density is larger near the beam pipe and decreases with the distance. In order to ensure an occupancy as flat as possible through the plane surface, the pitch and the length of strips increase with the radius from the  $z$  axis. The  $x$  strips (horizontal) are the most conditioned by the requirement on the spatial resolution: they have widths ranging from about 1 cm (near the beam pipe) to 4 cm (in the most peripheral regions). For the non-bending direction the spatial requirements are less stringent and so  $y$  strips (vertical) have pitch of 2 cm (innermost part) and 4 cm (outermost part), as summarised in Tab. 5.1.

Station	Strip pitches (in mm)				
	Bending direction (horizontal strips)			Non-bending direction (vertical strips)	
MT1	10.6	21.2	42.4	21.2	42.5
MT2	11.3	22.6	45.2	22.6	45.2

Table 5.1: Strip pitches of the Muon Trigger.

The geometry of the system is projective: a straight track, i.e. an infinite momentum particle, coming from the IP crosses the same strips on all planes.

### 5.3.2 Resistive Plate Chambers

The Resistive Plate Chambers [164, 165] are gaseous detectors with parallel and resistive electrode plates. This type of detector was chosen for its characteristics:

- unlike the detectors with a cylindrical shape, the uniformity of the electric field entails faster discharges without fluctuations;
- the spatial resolution is of a few mm;
- the simple design and the not very expensive materials make this detector available for large area applications;
- it has a rate capability up to few hundreds of Hz/cm<sup>2</sup>.

For these characteristics, RPC are widely used in the LHC experiments for muon triggering purposes [166, 167].

#### Design

The layout scheme of the RPC of the ALICE Muon Trigger system is depicted in Fig. 5.8. The gas gap is the active part of the detector: two layers 2 mm thick of low resistivity Bakelite ( $3 \div 9 \cdot 10^9 \Omega\cdot\text{cm}$ ) are kept at a constant distance of 2 mm by insulating spacers distributed on a  $10 \times 10 \text{ cm}^2$  grid. A polycarbonate frame borders the gap ensuring the gas tightness. The gas mixture flushes through two inlets and two outlets directly fixed in the polycarbonate frame. After assembly, the inside surfaces of the gap were treated with a double deposition of linseed oil. This treatment ensures the smoothness of the inner surface of the Bakelite sheets and so the homogeneity of the electric field [168]. The external surface of the Bakelite plates are painted with graphite before the construction of the gap. The graphite electrodes are then connected to the HV and to the ground. The pick-up strips, made of Mylar with a deposition of 20  $\mu\text{m}$  of copper, are insulated from the graphite by PET foils 100  $\mu\text{m}$  thick [157, 158].

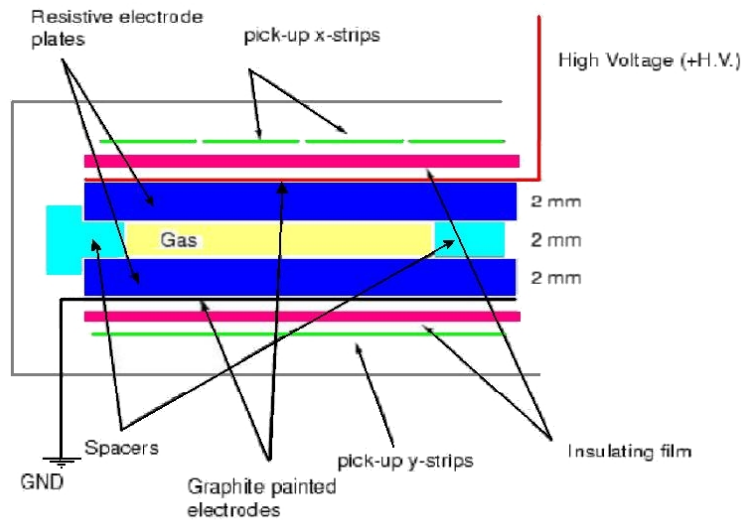


Figure 5.8: Cross section of a Resistive Plate Chamber.

### Gas mixture

As the first goal of ALICE is the study of heavy-ion collisions, the R&D of the RPC was focused on the requirements imposed by Pb–Pb data taking characterised by a high hit multiplicity. This led to the choice to equip the RPC with high-granularity read-out strips and a good spatial resolution is therefore needed. To achieve this result, the possibility of operating in streamer was explored, identifying the following gas mixture [169]:

$$50.5\% \text{ Ar} \quad 41.3\% \text{ C}_2\text{H}_2\text{F}_4 \quad 7.2\% \text{ i-C}_4\text{H}_{10} \quad 1\% \text{ SF}_6$$

The mixture permits the formation of the spark and prevents the degeneration of the discharge. The presence of strong electronegative gases, such as  $\text{SF}_6$ , helps the spatial localization of the spark capturing free electrons, but increases the presence of HF acid [170] that could attack the linseed oil and degrade the inner surfaces of the gap.

The constraints for the pp data taking are different. The expected multiplicity is smaller (and the requirement on the spatial resolution is less stringent), but the rates expected are much higher due to the higher luminosity and beam-gas background. These conditions, together with the long data taking time, make the detector lifetime issue more important. An intense R&D was carried out on the possibility of having the RPC operating in highly-saturated avalanche mode [171] with the same FEE foreseen for the streamer. The resulting gas mixture is:

$$89.7\% \text{ C}_2\text{H}_2\text{F}_4 \quad 10\% \text{ i-C}_4\text{H}_{10} \quad 0.3\% \text{ SF}_6$$

which provides a better lifetime of the detector without penalising the localising properties of the streamer mode.

In both operating modes a percentage of water vapour is added to the gas after the mixing. Flushing wet gas in the gap keeps constant the humidity of the Bakelite plates, preventing modifications in the resistivity and deformations of the surfaces. The relative humidity is about 37%.

After having considered the beam conditions and seen the detector behaviour in the first year of data taking, the Muon Trigger always operated in highly-saturated avalanche condition during pp, pPb and Pb–Pb collisions until the first long shutdown of the LHC (February 2013).

### High voltage

The adopted RPC can be operated in highly-saturated avalanche mode at a working voltage (independent for each chamber) ranging from 10000 to 10400 V [172].

Temperature ( $T$ ) and atmospheric pressure ( $p$ ) can affect the working point of the RPC. In order to operate in stable and constant conditions, a correction of the applied voltage is needed, according to the following equation, valid for small changes:

$$V_{app} = V_0 \cdot \frac{T}{T_0} \frac{p_0}{p} \quad (5.1)$$

where  $V_{app}$  and  $V_0$  are respectively the voltage really applied to RPC and the voltage set from the detector control system.  $T_0 = 20$  °C and  $p_0 = 970$  mbar are the reference values.

### 5.3.3 Trigger principle

The  $p_T$  cut, optimised by means of simulations [173], is implemented according to the method described below. Referring to Fig. 5.9, a muon produced at the IP is bent by the dipole magnetic field and crosses the Muon Trigger stations in  $(y_1, z_1)$  and  $(y_2, z_2)$ . The deviation  $\Delta y = y_2 - y_{2,\infty}$  represents the distance between the  $y$ -coordinate of the detected muon and the hypothetical crossing point of a straight track crossing the first station at the same coordinate  $y_1$  as the real muon.

For small deviations (i.e. less than 10°)  $\Delta y$  is, under certain approximations, proportional to the inverse of the transverse momentum at a given radial position  $R$  [157]:

$$\Delta y \cong \frac{eBL}{z_1} \cdot \frac{R}{p_T} \cdot (z_2 - z_1) \quad (5.2)$$

where  $z_1$  and  $z_2$  are the positions of the Muon Trigger stations,  $B$  is the magnetic field,  $L$  is the length of the dipole.

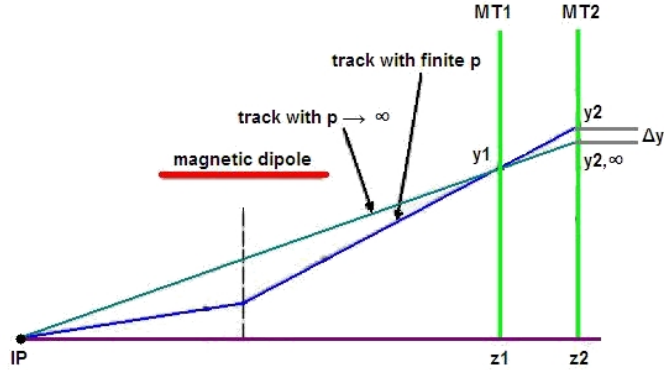


Figure 5.9: Schematic view of the trigger principle.

Therefore a cut on  $\Delta y$  will correspond very roughly on a cut on  $p_T$  (since the strip width increases with  $R$ ) with the possibility to distinguish positive from negative particles. The maximum value of  $\Delta y$  permitted for a given  $p_T$  threshold is determined through Monte Carlo simulations and then stored (in corresponding number of strips) in Look-Up Tables (LUT), to be compared to the measured deviation.

In the bending plane, when a muon fires at least one of the two planes in station MT1, signals of the particle are searched in MT2 within a maximum number of strips (called *road*). If three out of four planes counted a hit within the road, the track is processed and compared to the  $p_T$  deviations stored in the LUT. The maximum measurable deflection  $\Delta y$  (i.e. the largest road) is fixed, for practical reasons, to  $\pm 8$  strips.

For the  $x$ -coordinate, where there is no magnetic deflection of the track, more stringent requirements (typically  $\pm 1$  strip in the MT2) are applied by the trigger algorithm. It allows to select particles coming from the IP, but also to take into account the effect of the multiple scattering in the iron wall and any possible misalignment between the stations. The trigger is delivered if the track satisfies the requirement in both bending and non-bending planes [174].

The system is designed to cope with two different sets of  $p_T$  threshold in parallel (low- $p_T$  and high- $p_T$ ), stored in the LUT and tuned for specific physics channels. For each of them three trigger signal can be delivered: single muon, dimuon like-sign and dimuon unlike-sign trigger, for a total of a maximum of six inputs sent to the CTP.

### 5.3.4 Electronics

#### Front-end electronics

The design of the front-end electronics for the almost 21000 channels was driven by the requirements imposed by the streamer and highly-saturated avalanche operating modes, with the goal of a time resolution as accurate as possible.

The typical streamer signals (Fig 5.10) in a RPC could exhibit a double peak shape: the first peak is an avalanche precursor with an amplitude of about 20 mV/50  $\Omega$  synchronous with the particle crossing, while the second one is the signal generated by the streamer charge multiplication and characterized by a larger amplitude (about 120 mV/50  $\Omega$ ), but also by a time jitter up to 15 ns with respect to the precursor.

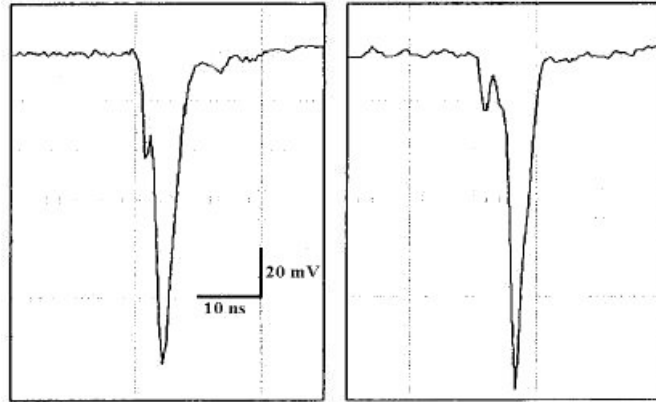


Figure 5.10: Example of two signals in a RPC running in streamer mode: the streamer signal is often delayed with respect of the small precursor up to 15 ns.

In order to improve the time response, a dual threshold discrimination technique (ADULT) [175] is adopted for the front-end electronics of the Muon Trigger system. With this technique a low threshold is used to discriminate the precursor and if a signal passes the high threshold the coincidence of the two is performed. A signal of 23 ns width is then delivered whose time reference is given by the low threshold signal. The two thresholds can be remotely dispatched and the values controlled via the DCS independently for each RPC side: this makes this FEE very flexible. This capability permits to run the RPC also in highly-saturated avalanche mode where the signal of a particle has a lower amplitude with respect to the streamer one. In this case there is only a small signal with similar characteristics of the precursor and the two thresholds are kept at the same value of 7 mV typically. The Muon Trigger works without signal amplifiers.

The system is equipped with diagnostic tools such as signal and trigger

scalars and a front-end test (FET): this test consists in injecting external signals from a pulse generator in the strips in order to check the integrity of the readout chain.

### Local boards

The trigger system is composed of 234 local boards (see the scheme in Fig. 5.11) that collect signals from corresponding regions of the four detection planes for both the read-out strip planes and deliver single muon trigger decisions. Each of them controls a set of 8 or 16 strips<sup>2</sup>. The local board treats the hit pattern, performing among others the so called *declustering*. This step aims at retrieving the most precise information on the actual track coordinates on the detection planes when at least two neighbour strips are fired. It consists in doubling the real bit patterns by inserting a virtual bit between two real bits (actually corresponding to strips). The new bit pattern is then filled according to the actual strips fired and the following procedure (see Tab. 5.2 as an example). When  $N = 1$  or  $N = 2$  ( $N$  denotes the number of neighbour strips fired) the center of the cluster is selected. Indeed, experimental measurements show that a cluster with  $N = 2$  most likely corresponds to a particle crossing the detector between two strips [176]. For  $N \geq 3$ , a reduction with a  $(2N - 5)$  algorithm is applied. This procedure is very powerful since it enhances the position resolution of the trigger improving in this way the  $p_T$  estimate.

Cluster size	$N = 1$	$N = 2$	$N = 3$	$N = 4$	$N = 5$
Initial cluster	0 0 <b>1</b> 0 0	0 0 <b>1 1</b> 0	0 <b>1 1 1</b> 0	0 <b>1 1 1 1</b>	<b>1 1 1 1 1</b>
After declustering	0000 <b>1</b> 0000	00000 <b>1</b> 000	0000 <b>1</b> 0000	0000 <b>11</b> 100	00 <b>1111</b> 100

Table 5.2: Illustrations of the declustering for bit patterns with a cluster size from  $N = 1$  to  $N = 5$ . More details on cluster size can be found in Chap. 6.

In events with more than one muon, the local board trigger decisions are collected and combined in order to provide also dimuon trigger signals [174].

### Electronic chain

The scheme of the electronics is shown in Fig. 5.12.

- The signals from the detector Front-End Electronics (FEE) are collected by the 234 local boards. Each of them sample the front-end signals of both the read-out planes at a frequency of 40 MHz corresponding to the LHC clock. The local board applies the trigger algorithm on the  $x$  and  $y$  bit patterns described previously.

<sup>2</sup>8 strips only in some particular cases in the non-bending plane.

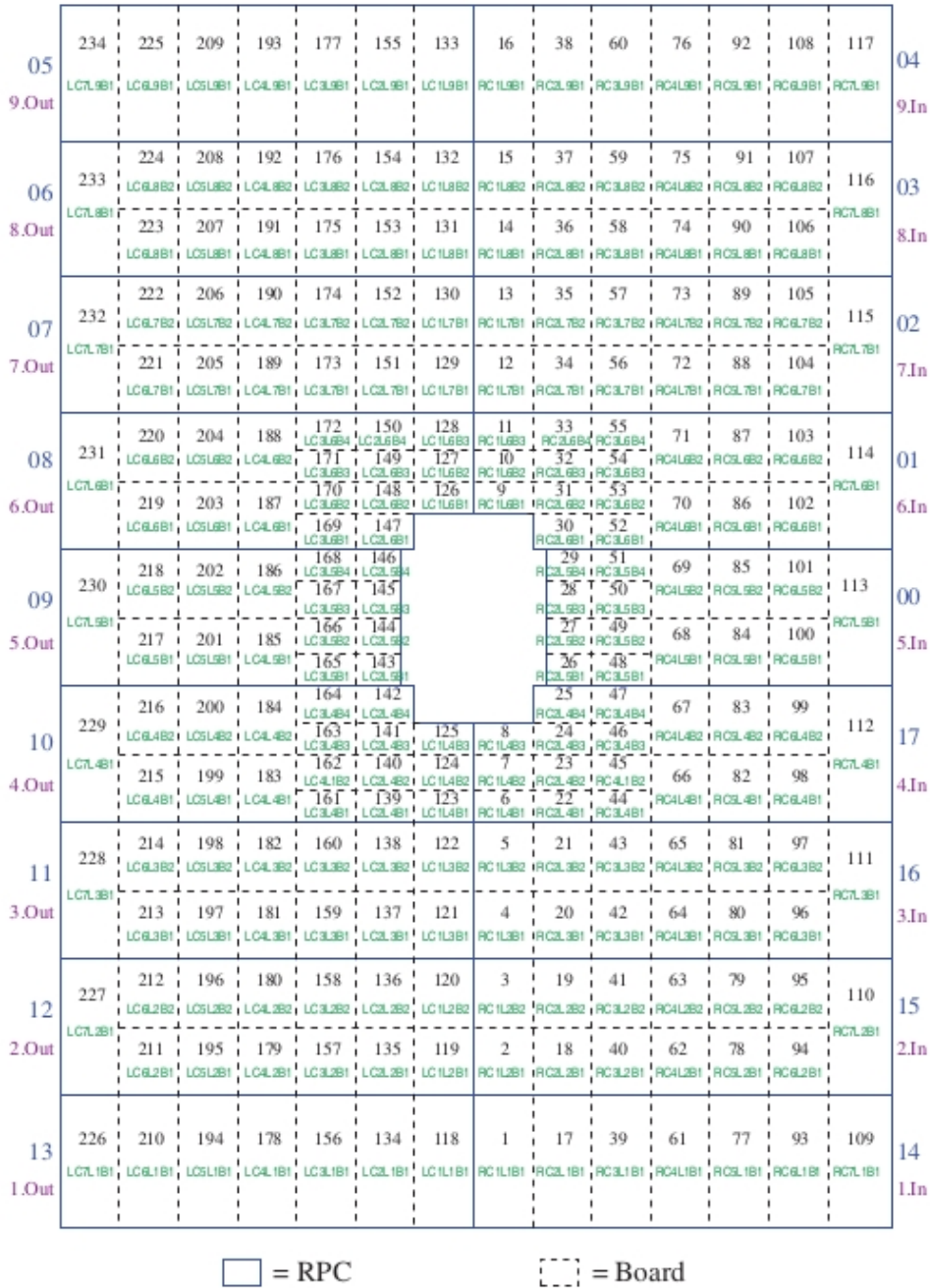


Figure 5.11: View of one of the Muon Trigger planes showing the 18 RPC and the 234 local boards with their numbering.

- The local boards are accommodated in 16 regional crates. Each regional crate is controlled by a regional board that collects the trigger decisions and sends the information coded in two 4-bit words (one per  $p_T$  threshold) to the last step of the trigger chain. The regional board also reads out the local DAQ memories and sends them to the acquisition board (the DARC) linked via optical fibres. It receives also the configurations through the JTAG links and dispatches them to the local boards through the VME bus.
- The trigger decisions from the 16 regional boards are gathered by the global board. This board is able to deliver the six different trigger signals mentioned above.

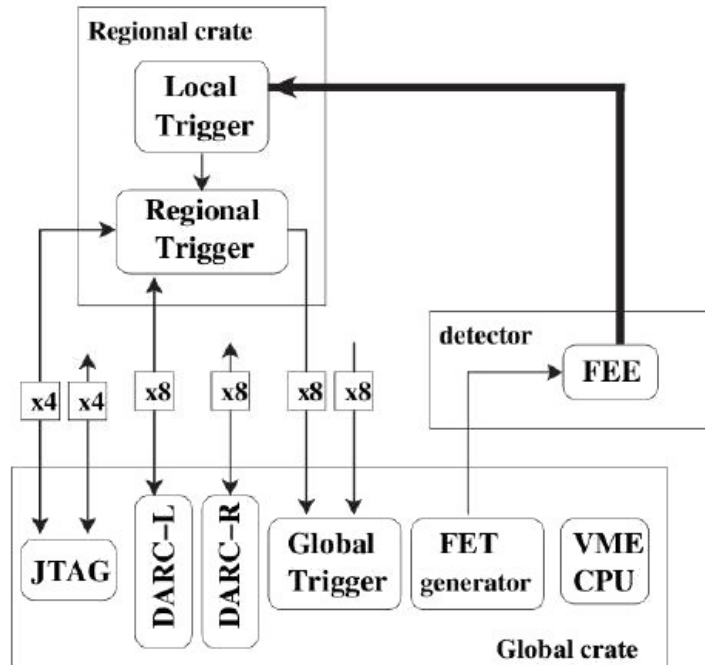


Figure 5.12: Schematic design of the Muon Trigger electronics.

The total latency of the L0 trigger signals of the Muon Trigger system is about 800 ns. The data read-out is performed by two DARC boards (DATA Read-out Card). This board takes care of receiving the L0 signals from the Central Trigger Processor (CTP, see Sec. 4.3.2), dispatching the order of data freezing to the local, regional and global boards and transferring the data, after the reception of the L2 trigger signals, to the ALICE DAQ system. These operations are completed in  $\sim 110 \mu\text{s}$  for the physics events (7 kB/event) and  $\sim 260 \mu\text{s}$  for software events (45 kB/event), also called calibration events.

## Chapter 6

# Cluster size of the Muon Trigger

In this chapter the cluster size will be studied in Pb–Pb collisions and the results will be presented for the different strip widths. Then, the simulation will be described and compared to the real data.

### 6.1 Cluster size: definition and dependences

Assuming a uniform distribution of the particle hits on the surface of the RPC, the spatial resolution  $\sigma$  is given by the formula:

$$\sigma = \frac{w}{\sqrt{12}} \quad (6.1)$$

where  $w$  is the strip width. Such a value can be modified by the RPC cluster size defined as the number of adjacent strips on which a signal above the discrimination threshold is induced when a particle passes through the detector. It depends on the following variables:

- strip width: narrower strips lead to a bigger cluster size;
- high voltage: an excessive high voltage favours the spark formation and thus the cluster size;
- discrimination threshold: the probability to have an high cluster size decreases increasing the threshold value;
- electrodes resistivity: a low resistivity facilitates the induction of signals on the strips;
- gas mixture: a poor quenching component in the gas mixture might be the responsible of an excessive cluster size;

- particle crossing angle: the higher is the angle with respect to the perpendicular direction to the detector surface and the higher is the probability to have a big cluster size.

The optimisation of all these variable involves a compromise between the cluster size, the spatial resolution and the detector efficiency. A properly working RPC will always count events with cluster size  $\sim 2$ : it happens when the particle impacts between two adjacent strips and in this case the spatial resolution will be better than Eq. 6.1 because the coordinate can be better estimated (with an analogical reading). On the other hand, an excessive cluster size might worsen the spatial resolution and the occupancy of the detector.

## 6.2 Estimate of the cluster size

### 6.2.1 Analysis conditions

The analysis of the Pb–Pb data is based on 94 runs collected during fall 2010 (LHC10h period) and on 134 runs collected during fall 2011 (LHC11h period). All these runs passed the standard quality assurance checks.

It was chosen to work with the ESD format instead of the raw data in order to be sure to consider only physical signals and not background noise. The useful information of the reconstructed tracks contained in the `AliESDMuonTrack` class are processed using the Grid facility and then stored in the ROOT `TTree` container for being analysed locally. ROOT designed the `TTree` class to store large quantities of same-class objects. Using a `TTree` its branch buffers are filled with leaf data and the buffers are written to disk only when it is full. The class is optimized to reduce disk space and to enhance the data access speed [138].

In both periods only minimum bias triggers are selected with a centrality percentage between 0% and 90% estimated through the V0 multiplicity (see Sec. 4.2.3) and each event is required to satisfy the physics selection [177] (see Sec. 8.1.2).

To select only muons produced in beam-beam collisions and to reject other particles, further cuts on each track are applied:

- all tracks reconstructed by the Muon Trigger have to match with a track reconstructed in the tracking system;
- track pseudorapidity value must lies in the interval  $-4 < \eta < -2.5$ ;
- $p \times DCA$  cut ensures that all tracks point to the interaction vertex (see Sec. 8.3.4 for more details);
- only tracks with a transverse radius coordinate at the end of the front absorber between 17.6 and 89.5 cm are selected.

The patterns of the strips hit by the selected tracks in the two directions of the four RPC planes are retrieved by the `GetTriggerPattern()` methods of the `AliESDMuonTrack` class, while the `LocalBoardNumber()` method of the `AliMUONVDigit` class gives the local board number crossed by the track. At this point, a last selection is made: if in the same local board there are two or more clusters the track is rejected because it is not possible to know which cluster the muon belongs to.

### 6.2.2 Cluster size distribution and average values

When the hit patterns are known, the dimension of the clusters is evaluated and used to obtain the cluster size distribution per detector element and strip width, as shown in the histogram of Fig. 6.1, as an example.

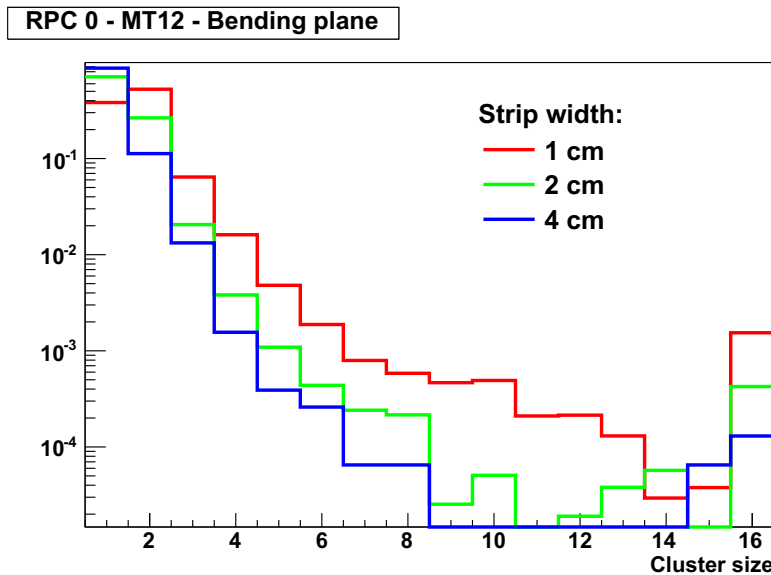


Figure 6.1: An example of cluster size distribution: the histogram refers to RPC 0, MT12, bending direction. Colours refer to the three strip widths.

From this distribution one can note that, even after all the cuts applied for selecting only physical muons, there are some tracks leading to a very large cluster size and, in particular, the situation with the whole local board hit (corresponding to 16 strips fired) exceeds the cases with a cluster size between 8 and 15. It could be due to electronic cross talk, showers or highly ionizing particles. However they are very rare events. Indeed, most of the tracks generate a cluster of a small number of strips, as reported in Tab. 6.1.

The average cluster size is then defined as the mean value of these histograms and the associated uncertainty is calculated assuming a Poissonian distribution of the clusters.

Cluster dimension	1 cm	2 cm	4 cm
= 1 strip	38.25%	70.81%	87.17%
≤ 2 strips	90.85%	97.30%	98.42%
≤ 3 strips	97.27%	99.36%	99.75%
= 16 strips	0.15%	0.04%	0.01%

Table 6.1: Percentage of tracks generating a cluster equal to 1, ≤ 2, ≤ 3 or equal to 16 strips for the three pitches. The numbers refer to the integrated statistics.

## 6.3 Cluster size in Pb–Pb collisions

### 6.3.1 Dependence on the geometry of the detector

The average cluster size values evaluated over the whole Muon Trigger are reported in Tab. 6.2. The dependence on the strip width introduced at the beginning of this chapter is evident.

Width	⟨Cluster size⟩
1 cm	$2.08 \pm 0.06$
2 cm	$1.46 \pm 0.02$
4 cm	$1.15 \pm 0.01$

Table 6.2: Average cluster size values for the three strip widths.

The average cluster size is shown as a function of the plane in the first two plots of Fig. 6.2 for the bending direction (left) and for the non-bending direction (right), distinguishing the three strip pitches. The cluster size, as expected, is independent from the plane and, therefore, from the distance from the interaction point. Moreover, comparing the two plots it is possible to note that the 2 cm and 4 cm strips have the same cluster size values in the  $x$ -side and the  $y$ -side [172].

The two plots in the middle of Fig. 6.2 show the average cluster size as a function of the RPC for plane MT11 (the others have the same behaviour) and for the different strip segmentation. Also in this case, it is possible to identify the different families of points corresponding to the different pitches. The mean values in the two directions are similar and close to those of the previous plots. The trends are not perfectly flat: for some chambers (as the RPC 6 in the bending plane) the cluster size for all the segmentations is higher than the one in other chambers. It can be justified by reminding that each RPC might have slightly different Bakelite resistivity, thickness or different electrodes distance which influence the formation of the signal

[178]. For the wider segmentation this phenomenon is less evident because the cluster size is always close to 1.

Finally, the average cluster size as a function of the local boards is reported in the two bottom plots. They include only boards belonging to the same RPC, in this case RPC 17 bending plane and RPC 4 non-bending plane of MT12 (see Fig. 5.11 for the numbering). For each family of points, the trend is almost flat and the average values are very close to the previous ones.

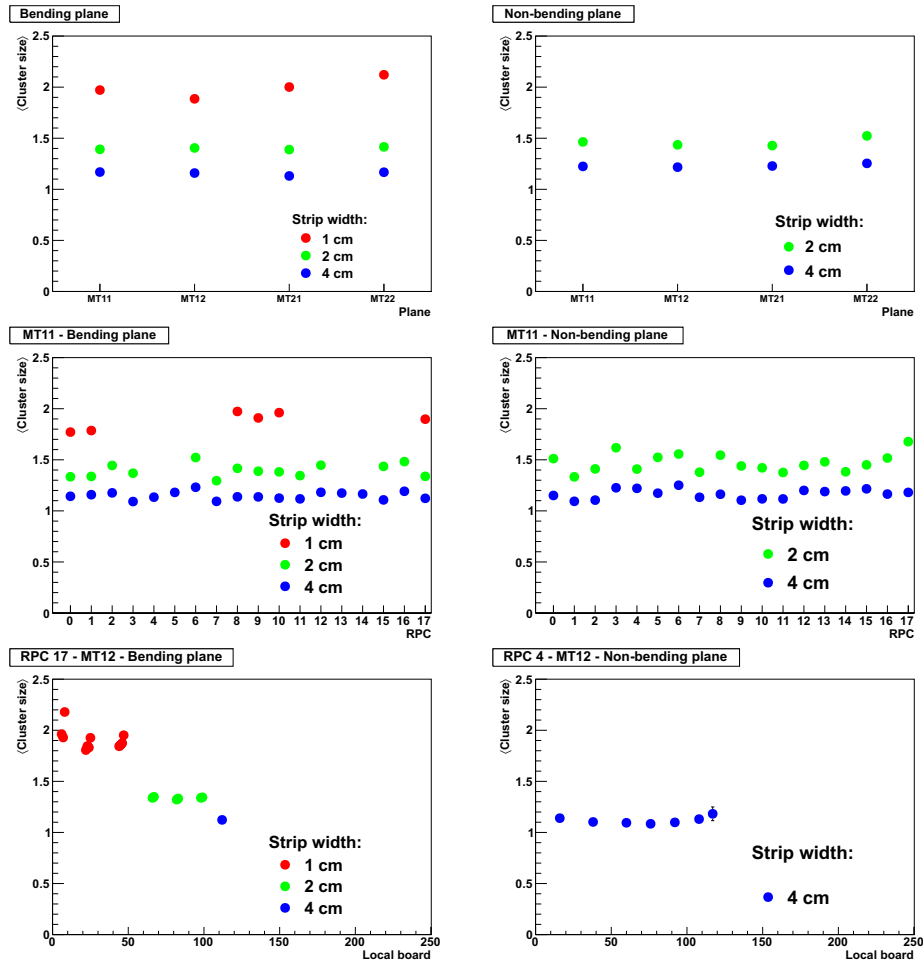


Figure 6.2: Average cluster size as a function of the plane (top plots), of the RPC (middle plots) for MT11 and of the local board for RPC 17 and 4 in MT12 (bottom plots). The colours reflect the different strip widths.

All these results are obtained integrating all the data collected during the two periods of Pb–Pb collisions. Because of the large statistics, the error bars for most of the points in the plots are too small to be visible.

### 6.3.2 Time dependence of the cluster size

The average cluster size integrated over all detector elements can be plotted as a function of the LHC fill number in order to have an idea of the time stability of the Muon Trigger. The *fill* is the period in which the accelerator is filled with the two beams according to a particular filling scheme. It lasts until the beam dump. If the stable beam condition is declared, then the experiments can proceed with runs of data taking. The number of the fills are progressive and automatically assigned by the accelerator procedure. LHC10h and LHC11h periods contain respectively 23 and 37 fills.

The plot in Fig. 6.3 (it refers to MT12 - bending plane, as an example) demonstrates a good stability of the average cluster size during the two periods of data taking in heavy-ion collisions. It is important to note that no substantial changes on the settings of the detector were made during the two phases of data taking.

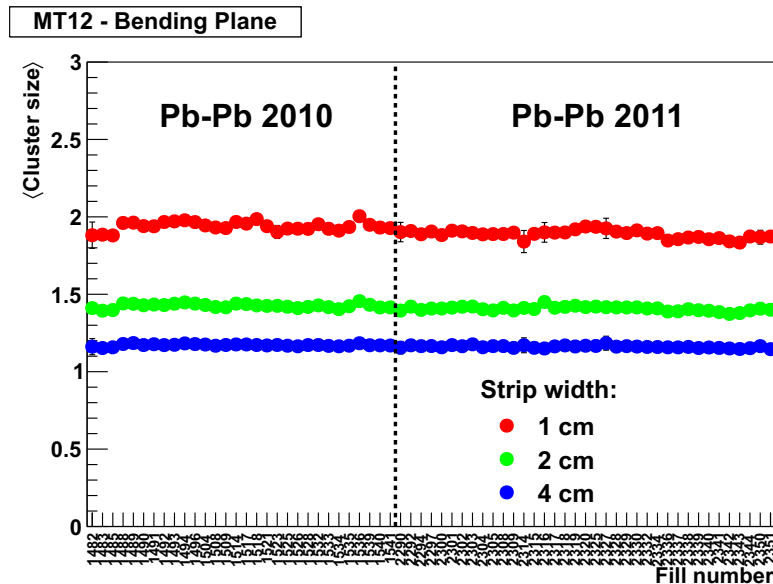


Figure 6.3: Average cluster size as a function of the fill for plane MT12,  $x$ -strips. The vertical dashed line separates the two years of data taking.

### 6.3.3 Comparison with results in pp collisions

The results shown so far arise from Pb–Pb collisions at a center-of-mass energy of 2.76 TeV. It is interesting to compare the cluster size of the Muon Trigger with another colliding system, i.e. pp collisions at  $\sqrt{s} = 7$  TeV, in the same detector conditions.

The results for the bending and non-bending directions as a function of the trigger planes are reported in Fig. 6.4. The plots show that the average

cluster size does not depend on the collision system and they also confirm the stability in time of the detector as the pp and Pb–Pb collisions were collected in different periods.

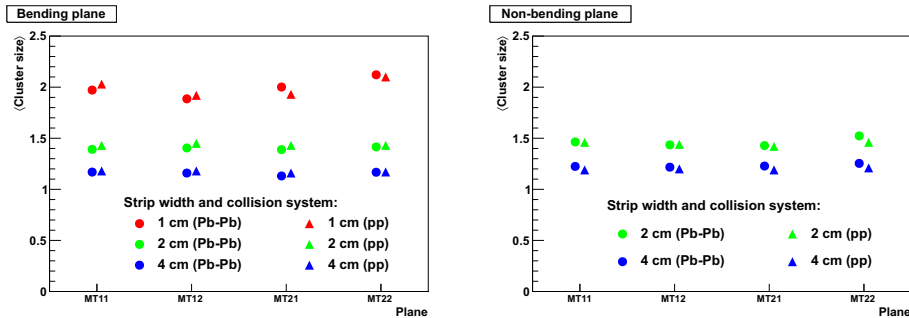


Figure 6.4: Comparison of the average cluster size measured in Pb–Pb collisions at  $\sqrt{s_{NN}} = 2.76$  TeV (circles) and in pp collisions at  $\sqrt{s} = 7$  TeV (triangles) and as a function of the plane in the bending (left) and non-bending direction (right).

## 6.4 Simulation of the cluster size

### 6.4.1 State of the art before 2012

The cluster size of the ALICE Muon Trigger RPC was already studied during the R&D phase in two test beam carried out at the CERN PS in 1999 and 2000, well before the beginning of the data taking. The cluster size of a RPC prototype working in streamer mode with a nominal high voltage of 9.2 kV was evaluated as a function of the applied voltage and of the particle crossing angle for two different strip segmentations of 1 and 2 cm. Three cathode strip chambers were employed to determine, with a resolution better than 1 mm, the particle trajectory in the RPC and the trigger signal was provided by a hodoscope equipped with seven scintillators and a start counter [179].

Analysing the measurements made it was possible to determine a probability distribution to fire the neighbouring strips as a function of the distance  $x_{strip}$  to the particle impact position on the RPC:

$$F_{prob}(x_{strip}; V, \theta) = \frac{1}{1 + c(V)} \left( \frac{a(V)}{a(V) + x_{strip}^b \cdot \cos \theta} + c(V) \right) \quad (6.2)$$

where  $\theta$  is the angle between the particle trajectory and the perpendicular to the RPC. The coefficients  $a$ ,  $b$  and  $c$  were determined from fits to the data. Their dependence on the high voltage applied to the RPC was written in

the following form, with  $V$  expressed in kV [179]:

$$\begin{aligned}
 a(V) &= 6.089 \times V - 52.70 \\
 b &= 2.966 \\
 c(V) &= 4.3 \cdot 10^{-4} \times V - 3.5 \cdot 10^{-3}
 \end{aligned}
 \tag{6.3}$$

Once defined the probability function, the simulation algorithm was developed in this way:

1. once a particle hits a strip, the distance to the closest edges of the left nearest neighbour strip (if it exists) is determined;
2. the probability to fire the neighbour strip is calculated knowing the RPC high voltage and the particle crossing angle;
3. this probability is then compared to a random number between 0 and 1, the same for all the strips;
4. if the random number is higher than the calculated probability, then the considered strip is not fired and the process is stopped to have a connected cluster, otherwise the strip is hit and the process is iterated to the next strip;
5. the same procedure is then applied for the right side strips (if they exist).

An ad hoc class named `AliMUONResponseTriggerV1` was created to reproduce the cluster size using the probability function described before.

The three plots in Fig. 6.5 (one for each strip segmentation) show the cluster size distribution normalized to the unity of RPC 0 in MT11, bending direction. The blue line refers to real data, while the green line represents a fast simulation employing the class. The average values are also reported.

It is evident that the simulation does not reproduce at all the measurements, basically for two reasons. First, the Muon Trigger always operated in a highly saturated avalanche mode with an applied high voltage around 10 kV (see Sec. 5.3.2 for more details), while the class was developed for an RPC working in a streamer condition and an HV equal to 9.2 kV. Moreover, in simulation the voltage cannot be modified and is equal for the 72 RPC, while the Muon Trigger permits to set an HV specific for each RPC.

For these reasons, the cluster size of the Muon Trigger has never been activated with the `AliMUONResponseTriggerV1` class in the official ALICE simulations.

#### 6.4.2 New simulation procedure

From the previous considerations it is clear that the existing code for the simulation of the cluster size needs to be modified to reproduce the results obtained in Pb–Pb and pp collisions.

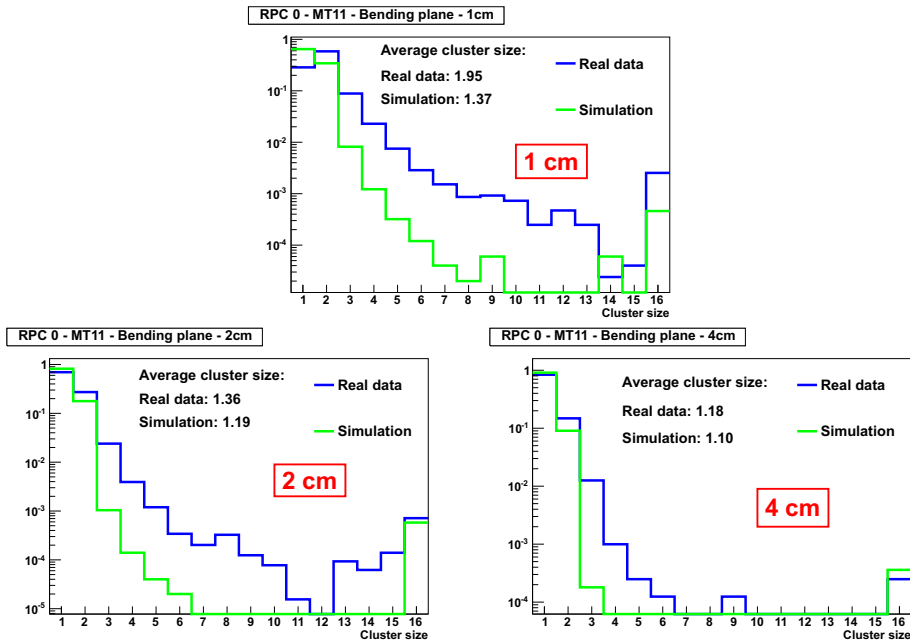


Figure 6.5: Comparison of the measured cluster size distribution in Pb–Pb collisions (blue line) and the simulated one with the original `AliMUONResponseTriggerV1` class (green line). The plots refer to the different strip widths of RPC 0, MT11, bending plane.

Being impossible to repeat the tests carried out at the CERN PS facility, the best way to proceed is to maintain the form of the probability function described in Eq. 6.2 and to improve it along with other parts of the class for reproducing the measured cluster size.

First of all, the coefficients  $b$  and  $c$  are modified to increase the simulated cluster size for an applied voltage around the nominal values. The old  $b$  parameter is splitted in 144 new  $b$  values (two for each RPC, i.e. one for each side) for taking into account each single chamber behaviour. The new values range between 1.72 and 2.97. Clearly this is not the most elegant way to proceed, but it is the only possibility to exploit the study done time ago. The  $c$  parameter is modified for ensuring a better agreement of the tails of the cluster size distributions: the new value is  $c(V) = 8.3 \cdot 10^{-4} \times V - 0.5 \cdot 10^{-3}$ .

After that, a new way to retrieve the high voltage information is adopted. In the modified version of `AliMUONResponseTriggerV1`, the value of each chamber is taken directly from the OCDB (see Sec. 4.4.1) and not written by hand in the class. Doing so, whether the settings will be changed for any reason, it will not be necessary to modify the code and the simulation will always reflect the real conditions of the detector. If it is impossible to retrieve the applied voltage for a particular run (it can happen for very old runs, where the high voltage values were not yet put in the OCDB) a default

value of 10.1 kV is set for all the 72 chambers.

Since AliRoot revision number 57334 (AliRoot version v5-03-35-AN) the new code is ready to be used and the official ALICE simulations which need the Muon Spectrometer, include the modified class. Seen the fact the measured cluster size is independent from the colliding system, the new procedure can be applied either in pp or Pb-Pb simulations.

### 6.4.3 Results with the new class

The real cluster size distributions are compared in Fig. 6.6 to a simulation produced with the new version of the `AliMUONResponseTriggerV1` class. They refer to the same RPC of Fig. 6.5.

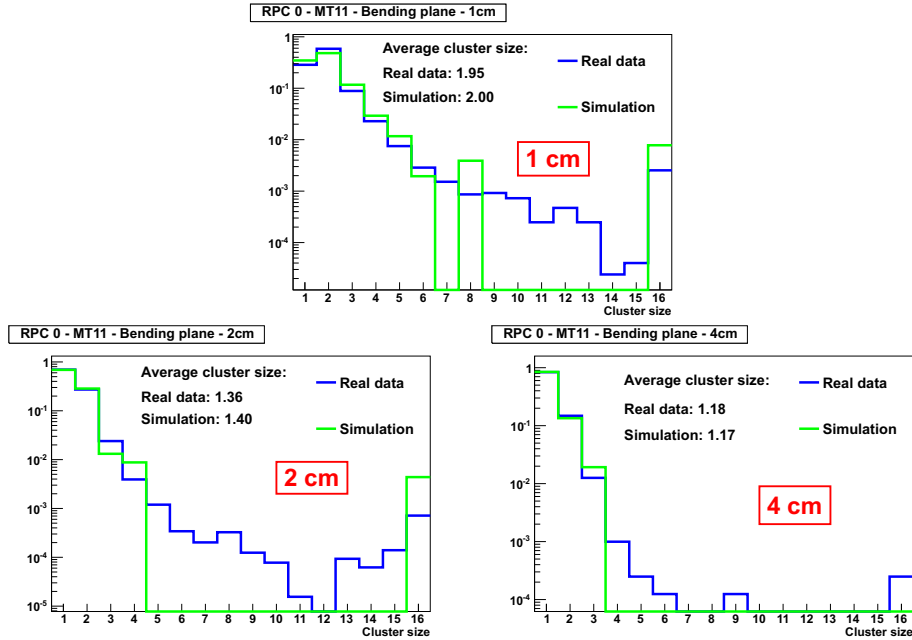


Figure 6.6: Comparison of the measured cluster size distribution in Pb-Pb collisions (blue line) and the simulated one with the improved class (green line). The plots refer to the different strip widths of RPC 0, MT11, bending plane.

It is evident that the distributions of the cluster size for the three strip dimensions are now better reproduced and the mean values reported in each plot are very close to the real ones. There are still some difficulties to reproduce the distribution of cluster with dimension between  $\sim 5$  and  $\sim 14$ , but they represent a very small fraction of the total clusters as seen before.

The comparison of the real and simulated average cluster size is shown in the two plots of Fig. 6.7 once again as a function of the local board for two different RPC. On the left plot, the RPC 17 of MT12 in the bending

plane is composed of three different kinds of strips and the agreement is satisfactory, but gets worse for smaller strips. The RPC 4 of the same plane (right) contains in the non-bending direction only the strip pitch of 4 cm: in this case the agreement between data and simulation is very good.

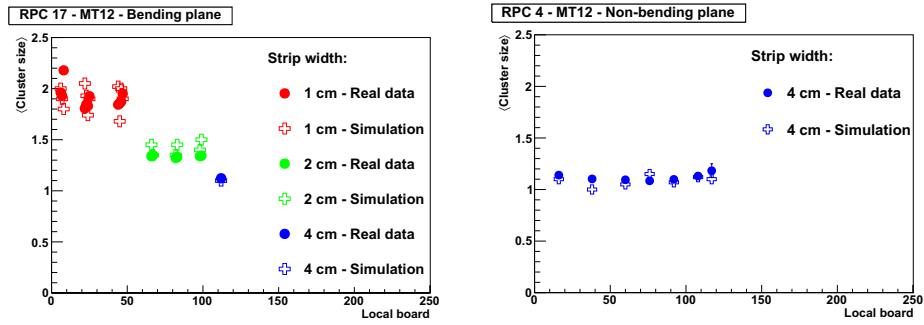


Figure 6.7: Measured cluster size (full points) compared to the simulated one with the new class (open symbols) as a function of the local board for the RPC 17 bending plane (left) and RPC 4 non-bending plane (right) of MT12. See the numbering in Fig. 5.11.

In general it is possible to note that it is more difficult to reproduce the cluster size for RPC with three segmentations. In fact in this case it is necessary to find a compromise between the small clusters characterizing the 4 cm strips and the bigger clusters of the 1 cm strips.

Important indirect effects of the new cluster size simulation on the Muon Trigger performance will be shown in Sec. 7.4.1.

## Chapter 7

# Muon Trigger performance in Pb–Pb collisions

This chapter is dedicated to the Muon Trigger performance during the first two runs of data taking in Pb–Pb collisions at  $\sqrt{s_{NN}} = 2.76$  TeV. The goal of this analysis is the monitoring of the detector stability during the time and the extraction of some useful information on the trigger behaviour. These numbers might be extrapolated to make some predictions in view of the coming data taking at higher luminosities and energies.

The results here presented and the cluster size measurements illustrated in the previous chapter are contained in the paper “Performance of the RPC-based ALICE Muon Trigger system at the LHC” by F. Bossù, M. Gagliardi and M. Marchisone, published on Journal of Instrumentation [172].

### 7.1 Muon Trigger configurations

First of all it is important to recall the possibility of the Muon Trigger to deliver at the same time trigger signals based on muon transverse momentum above two different thresholds, named *low- $p_T$*  and *high- $p_T$* . These thresholds are determined through simulations with muons of known  $p_T$  and correspond to an efficiency of 50% in rejecting muons with a transverse momentum (determined when they are produced) equal to the threshold itself [180].

Usually the two cuts are chosen considering the expected collision rate and the physics goal to achieve. For instance, with a *low- $p_T$*  threshold above  $\sim 1.5 \div 2$  GeV/ $c$ , the low-mass resonances like  $\rho$ ,  $\omega$  and  $\phi$  are almost fully suppressed. On the other hand, high-mass particles should be detected and reconstructed more easily.

The minimum and the maximum possible values of the thresholds are respectively 0.5 GeV/ $c$  and 4 GeV/ $c$ . The former corresponds to the maximum measurable deflection of  $\pm 8$  strips between the two trigger stations (see Sec. 5.3.3). The latter corresponds, instead, to tracks without any

measurable deflection with the detector resolution. These two values are called *all- $p_T$*  and *infinite- $p_T$* , they depend exclusively on the geometry of the Muon Trigger and therefore cannot be changed.

Thus, it is clear that all muons triggered by the Muon Trigger are automatically flagged as all- $p_T$  muons (whatever the two cuts are) and an high- $p_T$  muon is necessary a low- $p_T$  muon too.

The  $p_T$  cut values set during the two runs of Pb–Pb collisions are reported in Tab. 7.1. In the first period the low- $p_T$  cut was equal to all- $p_T$ , while the following year, seen the increased luminosity delivered by the accelerator, the thresholds were changed and the high- $p_T$  cut was put equal to the infinite- $p_T$ .

Threshold	2010 Pb–Pb collisions	2011 Pb–Pb collisions
low- $p_T$ cut	0.5 GeV/c = all- $p_T$	1 GeV/c
high- $p_T$ cut	1 GeV/c	4 GeV/c = infinite- $p_T$

Table 7.1: Muon Trigger  $p_T$  cuts adopted during the first two runs of Pb–Pb collisions.

## 7.2 Analysis conditions

The data sample, the applied cuts and the analysis procedure are the same already described in Sec. 6.2.1 for the cluster size.

In 2010 Pb–Pb collisions, no dedicated Muon Trigger was prepared in the ALICE configuration, due to the low luminosity ( $\mathcal{L}_{max} = 2 \cdot 10^{25}$  Hz/cm<sup>2</sup>). Nevertheless, the Muon Trigger information was always read out and used for offline analysis. The situation changed in 2011 with an higher luminosity ( $\mathcal{L}_{max} = 5 \cdot 10^{26}$  Hz/cm<sup>2</sup>, corresponding to a single muon trigger rate of about 500 Hz and to a dimuon trigger rate of about 200 Hz, both with a  $p_T$  threshold of 1 GeV/c). Ad hoc trigger classes including the different Muon Trigger signals were prepared, but in this analysis only minimum bias events are analysed for coherence with 2010 run. Moreover, it is better to present the multiplicities normalized by an unbiased number of events.

## 7.3 Multiplicities

In this part of analysis the time dependence of the muon and strip multiplicities for four centrality classes are shown: 0%–10%, 10%–20%, 20%–40% and 40%–80%. The cut at 80% is a consequence of the poorer V0 efficiency in peripheral collisions due to the limited particle multiplicity, mostly during the 2010 data taking.

### 7.3.1 Muon multiplicity

The average number of muons per minimum bias collision for different centrality bins are shown in Fig. 7.1 as a function of the fill number (i.e. of the time, see Sec. 6.3.2). Muons are required to match a reconstructed track in the Muon Tracking detector and to satisfy the all- $p_T$  condition in 2010 and 2011 years.

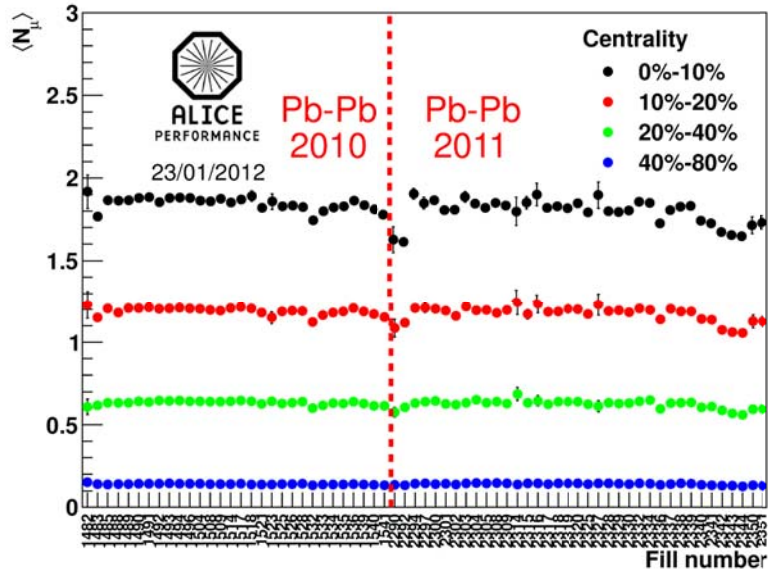


Figure 7.1: Single muon multiplicity as a function of the fill for four centrality classes. Vertical dashed red line separates the two years of data taking.

The average values are reported in the following Tab. 7.2. As expected, the muon multiplicity increases with the collision centrality, since so does the number of binary nucleon-nucleon collisions. The trend as a function of the time is quite flat, excluding the first fills of each period, where the collision rate is always very low, and the last 7 fills of 2011. This latter structure can be explained by changes in the number of active channels in the Muon Tracking system, affecting the muon reconstruction efficiency.

Centrality	0%–10%	10%–20%	20%–40%	40%–80%
$\langle N_\mu \rangle$	$1.83 \pm 0.16$	$1.18 \pm 0.10$	$0.62 \pm 0.07$	$0.14 \pm 0.01$

Table 7.2: Average number of detected muons per minimum bias collision as a function of the centrality.

### 7.3.2 Strip multiplicity

With the same selection criteria, it is possible to calculate the average number of hit strips per minimum bias event in the same centrality bins. This is shown in Fig. 7.2 as a function of fill number, for the first Muon Trigger plane in the bending direction. The other planes show the same features.

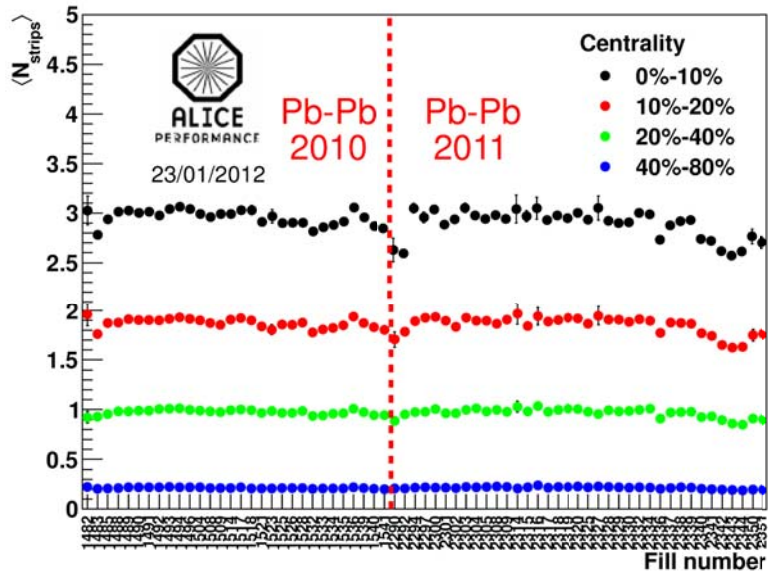


Figure 7.2: Strip multiplicity for MT11, bending plane as a function of the fill for four centrality classes. Vertical dashed red line separates the two years of data taking.

The average values are reported in Tab. 7.3. In the analysis the soft background is not included: only strips participating in tracks recognized by the algorithm are taken into account. This means that the difference with the average number of muons is mostly due to the cluster size (see Chap. 6).

Centrality	0%–10%	10%–20%	20%–40%	40%–80%
$\langle N_{strips} \rangle$	$2.93 \pm 0.39$	$1.86 \pm 0.24$	$0.97 \pm 0.12$	$0.21 \pm 0.02$

Table 7.3: Average number of hit strips as a function of centrality in the first Muon Trigger plane, bending direction.

Also in this case, the multiplicity of hit strips increases with centrality and the stability of the detector over the time is satisfactory.

## 7.4 Trigger response as a function of $p_T$

The only way to check with real data if there is a correspondence amongst the simulated cuts and the actually applied ones is to compute the ratio between the  $p_T$  distribution of the high- $p_T$  muons and the  $p_T$  distribution of the low- $p_T$  muons. The reconstructed  $p_T$  is measured by the Muon Tracking system. These ratios are shown in Fig. 7.3 for 2010 (left) and 2011 (right) Pb–Pb collisions.

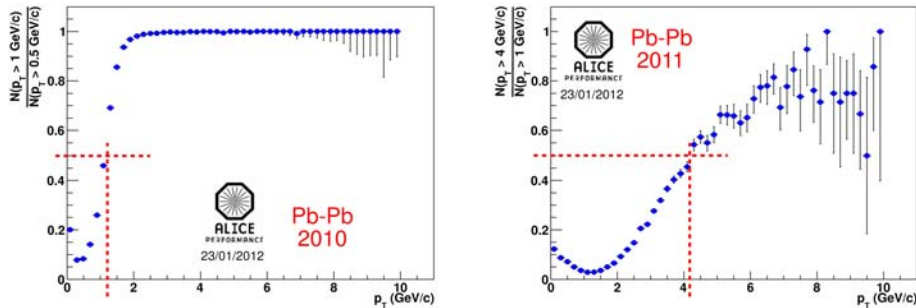


Figure 7.3: Number of muons satisfying the high- $p_T$  condition divided by the number of muons satisfying the low- $p_T$  condition, as a function of the  $p_T$ . Left plot refers to Pb–Pb 2010 collisions, while the right one to 2011 collisions. Vertical dashed red lines indicate the  $p_T$  at which the two curves reach the value of 0.5.

The theoretical shape of these plots should be a step function equal to 0 below the high- $p_T$  cut and equal to 1 above this threshold. In reality a plateau with saturation value close to unity is seen only at large  $p_T$  values. The behaviour of the ratios at very low  $p_T$  can be attributed to the fact that low- $p_T$  muons passing through the muon filter placed between the two subdetectors can be affected by multiple scattering effects. Being their trajectory deviated, the  $p_T$  estimate based on the muon position in the trigger chambers is thus modified.

As expected, the transverse momenta corresponding to a ratio equal to 50% are close to the requested values of 1 GeV/c and 4 GeV/c for 2010 and 2011 respectively. The closeness of the actual and the envisaged cut-off confirms the validity of the Muon Trigger based method for performing  $p_T$  cuts.

### 7.4.1 Effects of the cluster size

Before the implementation of the new cluster size described in Sec. 6.4.2, the high- $p_T$  over low- $p_T$  ratios were not well reproduced in simulations. As demonstrated in the plots of Fig. 7.4 provided by D. Stocco, a  $p_T$  shift was

systematically observed with respect to real data, especially when high- $p_T$  values were set as thresholds (as for 2011 Pb–Pb collisions).

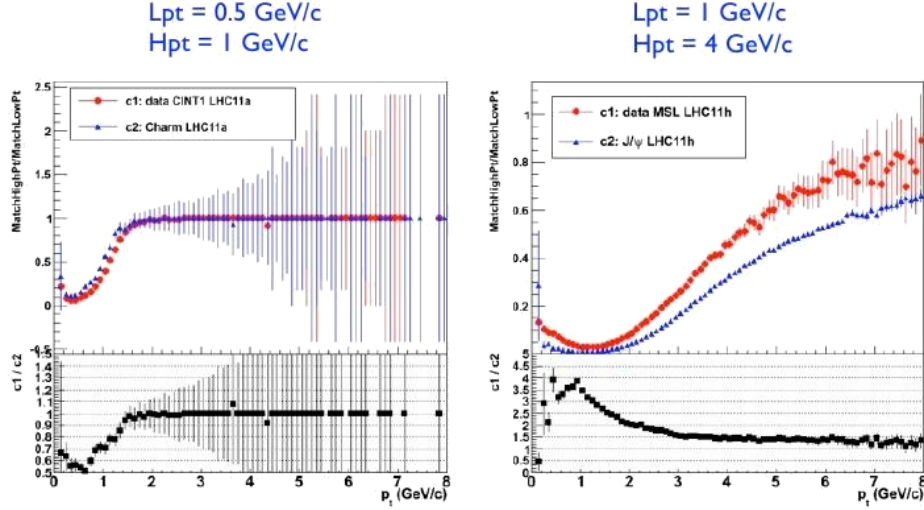


Figure 7.4: Comparison between data (red points) and simulations (blue points) of the Muon Trigger response as a function of  $p_T$  for two sets of  $p_T$  cuts. Black points in the low panels represent the ratios of the two sets of points.

This was a very old problem spotted in 2010 and never solved, which affected, for instance, the study of the  $J/\psi$  polarization. A deep investigation was made within the ALICE muon community, excluding progressively many possible reasons such as misalignment effects, wrong reproduction of the Muon Trigger geometry or of the muon filter material, biases in the look-up tables...

At the end of this intensive study, a bad description of the magnetic permeability of the muon filter and the missing Muon Trigger cluster size effects were found as responsible of this discrepancy between simulations and real data. The former problem was solved by delivering a different mapping of the magnetic field after new simulations, while the latter is significantly improved by the new cluster size parametrization. Fig. 7.5 shows how the slope determination of a track, and thus of the  $p_T$ , can be influenced by the cluster size.

The following plots in Fig. 7.6, always provided by D. Stocco, demonstrates that the issue is now solved. The remaining discrepancy is small and is taken into account in the systematic uncertainties of any affected analysis.

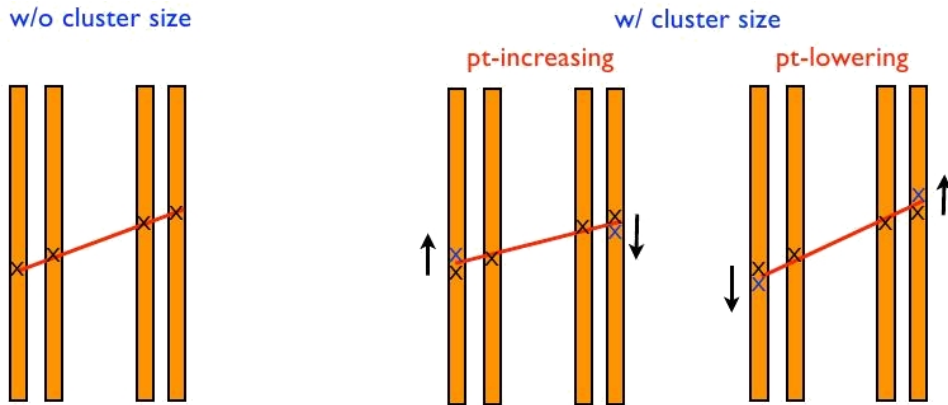


Figure 7.5: Sketch of the possible effects of the cluster size in determining the track transverse momentum in the Muon Trigger. Orange rectangles represent the four trigger planes, the red lines a track and the black and blue crosses the hit strips.

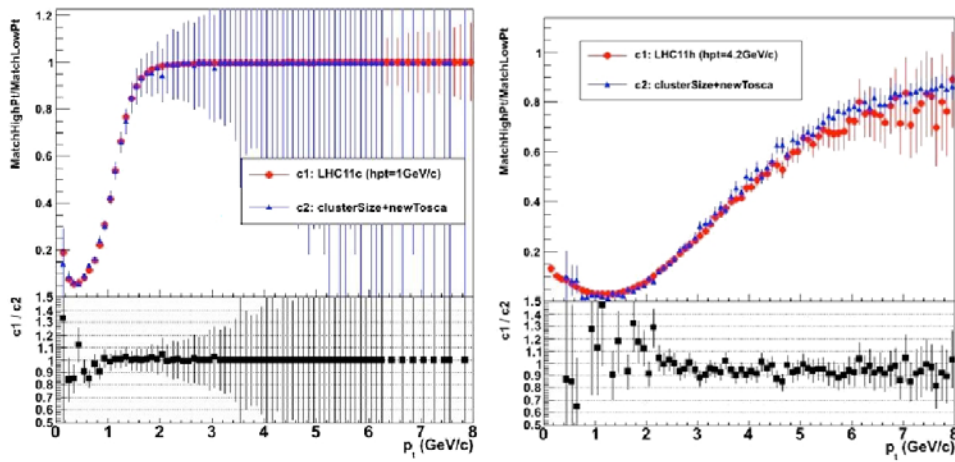


Figure 7.6: Comparison between data (red points) and simulations (blue points) of the Muon Trigger efficiency as a function of  $p_T$  for two sets of  $p_T$  cuts. Black points in the low panels represent the ratios of the two sets of points.

## 7.5 Global triggers

The ratios between the number of events containing at least one triggered muon and all the minimum bias events are reproduced in Fig. 7.7 as a function of the centrality for different trigger thresholds.

In the 2010 data taking the low- $p_T$  threshold was equal to all- $p_T$ , while the high- $p_T$  cut was set at 1 GeV/c. The selectivity is lower in the most central classes, where, as shown in Fig. 7.1, muon production is enhanced by the large number of nucleon-nucleon collisions.

The same feature can be observed in the bottom left plot of Fig. 7.7 (2011 period) where the low- $p_T$  cut is 1 GeV/c. The global trigger percentage for the most central and most peripheral bins are reported in Tab. 7.4. The agreement between these two ratios with the same cut (in red) is evident. The small (1.5%) difference seen between the 2010 and 2011 selectivity in the most central collisions can be ascribed to slight variations in the fraction of unavailable channels or small changes in the RPC efficiency, affecting the overall trigger efficiency.

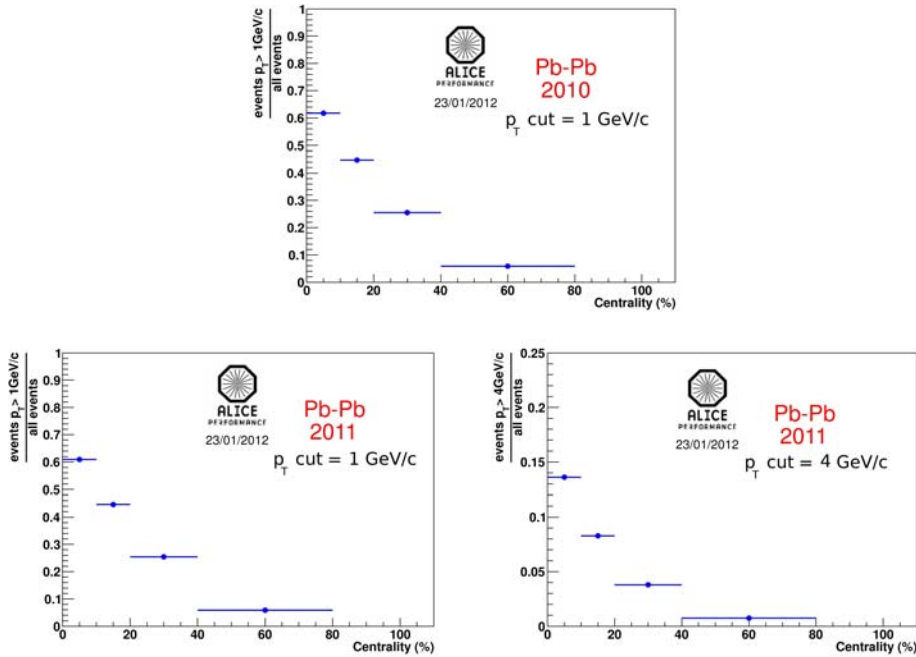


Figure 7.7: Global trigger fraction relative to minimum bias collisions (trigger selectivity) as a function of the centrality for 2010 period (top plot, with high- $p_T$  threshold equal to 1 GeV/c) and for 2011 period (bottom plots, with low- $p_T$  threshold equal to 1 GeV/c on the left and high- $p_T$  threshold equal to 4 GeV/c on the right). Horizontal bars indicate the bin widths.

Finally, the bottom right plot contains the global trigger percentage as

a function of the centrality for the high- $p_T$  cut of 2011 period at 4 GeV/c. The trend is very similar to those in the previous plots, but in this case the absolute values are smaller: only in the 14% of the central minimum bias events at least one muon satisfies the trigger condition and this number becomes smaller than 1% in the peripheral collisions.

Centrality	2010	2011	2011
	$p_T > 1$ GeV/c	$p_T > 1$ GeV/c	$p_T > 4$ GeV/c
0%–10%	$(61.82 \pm 0.09)\%$	$(60.91 \pm 0.10)\%$	$(13.61 \pm 0.05)\%$
40%–80%	$(5.81 \pm 0.02)\%$	$(5.88 \pm 0.02)\%$	$(0.73 \pm 0.01)\%$

Table 7.4: Trigger selectivity for two extreme centrality ranges and different cuts.

## 7.6 Trigger-tracking matching probability

As already described here and in Sec. 6.2.1, tracks used for studying the cluster size and the Muon Trigger performance so far illustrated are required to be detected by both the Muon Spectrometer subsystems. This is made for rejecting the possible light hadrons such as  $\pi$  or  $K$  not stopped by the front absorber or there produced.

In order to quantify this component, the fraction of the tracks detected by the two detectors (so called matched tracks) with respect to the total amount of tracks reconstructed in the Muon Tracking is studied. The trend as a function of  $p_T$  is illustrated in the two plots of Fig. 7.8 (one for each year of data taking). In order to be able to compare them, the  $p_T$  threshold in both cases is the all- $p_T$  (0.5 GeV/c).

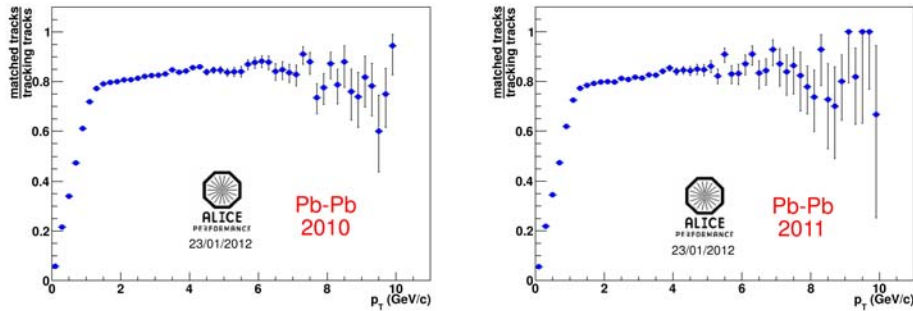


Figure 7.8: Ratios between the number of matched tracks and the number of tracks detected by the Muon Tracking as a function of the transverse momentum. Left plot refers to 2010, while the right one to 2011 period.

The same trend in both plots is a further confirmation of the stability of the detector. Another important point is the saturation value ( $\sim 0.85$ , common to 2010 and 2011) of the plateau which does not reach the value of 100% even at very high values of  $p_T$ .

According to Pb–Pb collision simulations performed with the HIJING event generator and shown in Fig. 7.9 (top plots), the fraction of unmatched tracks is largely accounted for by the contamination of hadrons in the sample of reconstructed tracks. The top left plot shows the composition of the reconstructed tracks in the Muon Tracking as a function of their transverse momentum without asking the matching with the Muon Trigger tracks. The hadron fraction in the top right plot around 15% confirms what is seen in real data.

The same simulation is presented in the bottom plots with the trigger-tracking matching. The fraction of accepted hadrons after this cut is drastically reduced to a few percent.

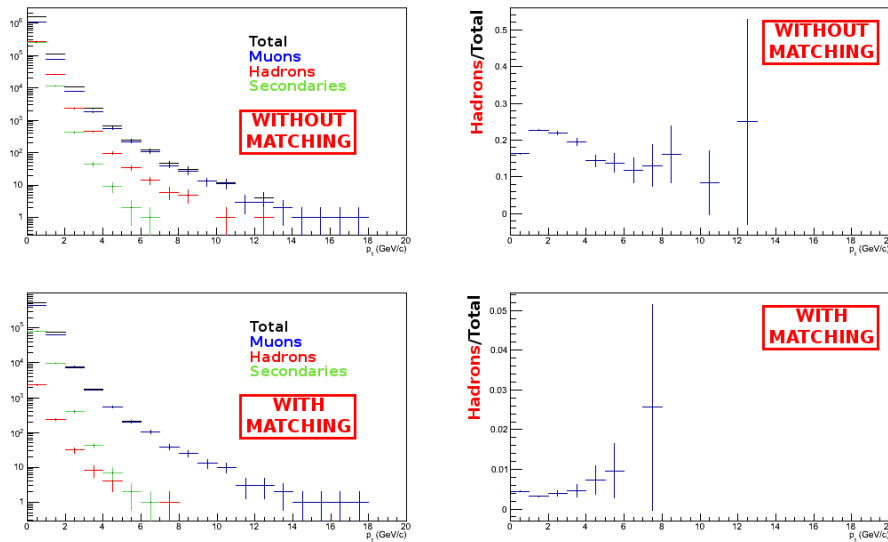


Figure 7.9: Top: composition of reconstructed tracks by the Muon Tracking (left) and fraction of hadrons (right), both without matching. Bottom: same plots including the matching cut.

Other effects like trigger and matching inefficiencies and tracks from beam-gas interactions play a marginal role in determining the value of the ratio.

## Chapter 8

# Analysis of $\Upsilon$ production in Pb–Pb collisions

In this chapter the analysis of  $\Upsilon$  production at forward rapidity in Pb–Pb collisions at  $\sqrt{s_{NN}} = 2.76$  TeV is described in detail. The aim is to investigate the effects of the hot and dense medium by studying the nuclear modification factor. For a summary of the results obtained by the other experiments, see Sec. 3.4.

### 8.1 $\Upsilon$ analysis framework

#### 8.1.1 The Correction Framework

Among the possible analysis procedures, the Correction Framework classes (CORRFW) [181] of AliRoot are used for obtaining the results shown in this chapter. They were developed with the initial purpose of assisting the ALICE users in deriving the corrections for acceptance and efficiency. The classes can be grouped into two categories:

- container classes to store real and simulated data in  $N$ -dimensional grids and to derive the correction maps for the observed data;
- selection classes to give the general selections common to several analyses.

#### Container classes

The container classes are used to store counts over  $N$ -dimensional grids while looping on real or simulated events. The classes directly or indirectly involved in the analysis are reported below, together with a brief description. Additional information can be found in the header and implementation files [182]. All these classes inherit from `TNamed` class in ROOT.

- **AliCFFFrame** is the base class of the framework. It defines the dimension of the grid corresponding to the number of variables, the number of bins and the bin width in each dimension.
- **AliCFGridSparse**, based on ROOT **THnSparse** class, makes an efficient use of memory for multi-dimensional histograms. This class allows to perform basic operations such as addition, multiplication, division, scaling, integration, projection (or slice) of the conventional **TH1**, **TH2** or **TH3** histograms. In particular, the projection creates a 1-dimensional histogram corresponding to a variable (**ivar**), as well as 2 or 3-dimensional histograms to get the correlation between the variables by using the methods:
 

```
TH1D* Project(Int_t ivar) const;
TH2D* Project(Int_t ivar1, Int_t ivar2) const;
TH3D* Project(Int_t ivar1, Int_t ivar2, Int_t ivar3) const;
```
- **AliCFContainer** fills the  $N$ -dimensional grids. Any analysis step can be configured for either real or simulated data. The filling of the grid with the array variable **var**, at step **istep** (i.e. real or Monte Carlo data) is performed by calling the function:
 

```
void Fill(const Double_t *var, Int_t istep);
```

 The correction factor between two different steps can thus be derived by dividing the contents of the two corresponding grids, to be then applied to the appropriate set of observed data.

### Selection classes

A set of classes handling general selections at event or particle level are prepared. Those used in this analysis are:

- **AliCFParticleGenCuts** for non-kinematic basic selections on generated particles as, for example, particle type, decay mode, charge...
- **AliCFTrackKineCuts** for kinematic selections on both generated and reconstructed tracks as, momentum range, rapidity, angular distribution...

#### 8.1.2 Dedicated classes for $\Upsilon$ analysis

**AliCFMuonResUpsilon** is the Correction Framework based class developed and used for the analysis of  $\Upsilon$  particle here described.

The class, which inherits from **AliAnalysisTaskSE**, can store information into the  $N$ -dimensional histogram from real data (first step) and simulated data (second step) filling an **AliCFContainer** object. It has the capability to read either ESD or AOD format, stored in the local path or on remote storage connected with Grid thanks to the AliEn interface.

In addition, the `AliPhysicsSelection` class is used in order to select event candidates which must satisfy all the following requirements [177]:

- have the correct event type (tagged as *physics* during data taking);
- have the interaction trigger, i.e. trigger on bunch crossings;
- fulfil the on-line trigger condition (hardware trigger);
- not be flagged as beam-empty or beam-gas event by either VZERO-A or VZERO-C;
- for pp collisions, not be flagged as beam-gas by the correlation of SPD clusters and tracklets;
- for Pb–Pb runs, not be identified as debunched events by the ZDC timing cut.

The class must be explicitly used for the ESD analysis, while it is not necessary working with the AOD since the physics selection was already done during their production.

An additional macro is required to configure the `AliCFContainer` variables (together with their number of bins and bin width) and the selection cuts. The list of variables stored in the container and used in this analysis is the following.

- On event:
  - centrality of the collision (from VZERO multiplicity);
  - event trigger type;
  - physics selection flag (for ESD only);
  - number of muon tracks.
- On single muon:
  - energy ( $E$ );
  - sign of the charge;
  - trigger-tracking matching flag;
  - pseudorapidity ( $\eta$ );
  - $R_{ABS}$  (track radial position at the end of the front absorber);
  - momentum components ( $p_x, p_y, p_z$ );
  - transverse momentum  $p_T = \sqrt{p_x^2 + p_y^2}$ ;
  - $p \times DCA$  (see Sec. 8.3.4).
- On generated  $\Upsilon$ :

- rapidity;
- transverse momentum.
- On reconstructed opposite sign dimuon:
  - mass
 
$$= \sqrt{(E_1 + E_2)^2 - [(p_{1,x} + p_{2,x})^2 + (p_{1,y} + p_{2,y})^2 + (p_{1,z} + p_{2,z})^2]};$$
  - rapidity =  $\frac{1}{2} \cdot \ln \left( \frac{(E_1 + E_2) + (p_{1,z} + p_{2,z})}{(E_1 + E_2) - (p_{1,z} + p_{2,z})} \right);$
  - transverse momentum =  $\sqrt{(p_{1,x} + p_{2,x})^2 + (p_{1,y} + p_{2,y})^2}.$

## 8.2 Data processing

The analysis is based on 134 runs collected in three weeks during fall 2011 (LHC11h data). All the runs passed the standard quality assurance checks. The GRID infrastructure described in Sec. 4.4.2 is used to process the raw data collected by ALICE in order to reduce the number and the size of files by selecting only relevant information.

### 8.2.1 Pass1

The first available ESD are produced with the standard re-alignment process (Pass1) which takes advantage of the specific sets of data previously collected in absence of magnetic field in the Muon Tracking. First, tracks are reconstructed and their positions with respect to the clusters formed by the pads hit by incoming particles are estimated. The track parameters are then tuned in order to minimize the position differences observed between tracks and clusters.

With those settings, the position of the  $\Upsilon(1S)$  peak is shifted by  $\sim 1\%$  towards higher mass with respect to the nominal value from [2] and the meson resolution is poor ( $217 \pm 54$  MeV/ $c^2$ ) as shown in Fig. 8.1 top left plot (see Sec. 8.3 and Sec. 8.4 for the details on data sample and fit procedure).

Before to continue with the signal extraction, raw data need to be further treated to improve the quality suitable for  $\Upsilon$  analysis.

### 8.2.2 Pass2

The second ESD production (Pass2) is made with a much more efficient alignment procedure, first initiated for 2011 pp data. The new method takes now advantage of data collected with and without magnetic field. The new procedure can make good use of a large data sample and it is less affected by possible modifications of chamber positions due to the magnetic field.

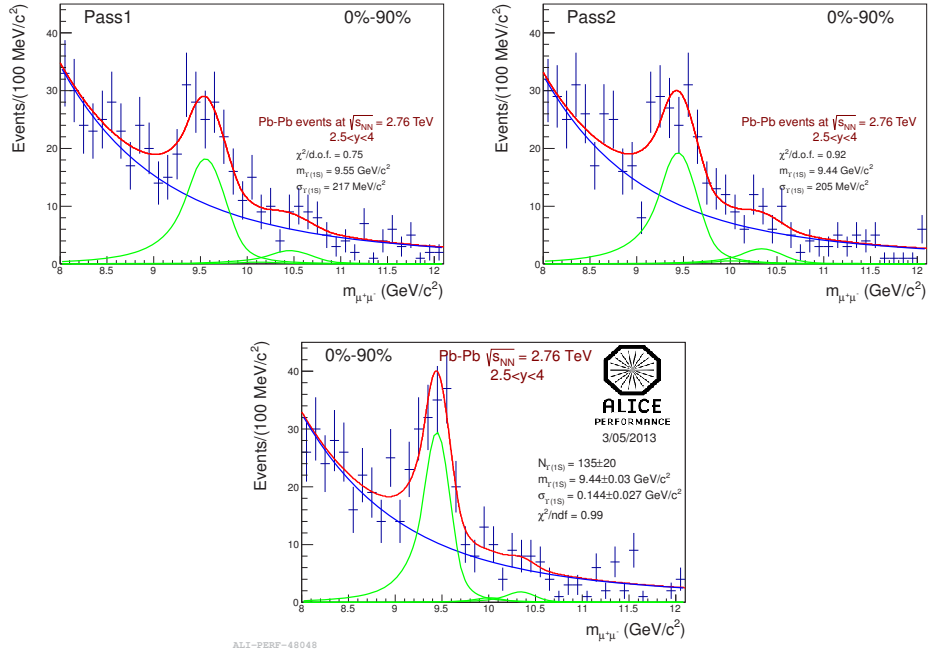


Figure 8.1: Improvement of the mass position and resolution with the different alignment processes used to treat the data.

From Pass1 to Pass2 the position becomes compatible with the nominal  $\Upsilon(1S)$  mass and an improvement of about 5% of the width ( $205 \pm 42$  MeV/ $c^2$ ) is observed (Fig. 8.1 top right), but it is still far from the envisaged resolution of 100 MeV/ $c^2$ .

### 8.2.3 Pass2 after refit

In the last processing (called *refit*) always performed at ESD level, the effects of some abnormal pad clusters of the Muon Tracking are better handled.

Each side of a tracking chamber is supposed to provide one spatial coordinate of the track. Accordingly, pads of the bending plane are sized to provide accurate vertical positions and vice versa. Therefore, if the charge of an incoming particle is not collected by one of the two planes of a chamber due to a malfunction, the resulting resolution on the position will be poor in the non-supported direction.

This issue does not affect the first two stations as pad dimensions are rather small in both directions.

To solve the problem for the other three stations, an ad hoc resolution value is assigned to the cathode clusters in the lacking direction. 10 cm are set instead of 2 mm, so that in the reconstruction algorithm they basically

are not taken into account and the data quality is improved as demonstrated in the bottom plot of Fig. 8.1, where the final mass resolution achieved is  $144 \pm 27 \text{ MeV}/c^2$ . The difference with the envisaged resolution of about  $100 \text{ MeV}/c^2$  is still due to the residual misalignment of the tracking chambers.

## 8.3 Data selection

The analysis is performed with the v5-34-01 ROOT version and the v5-03-58-AN AliRoot version on the official Muon AOD (AOD119) produced after the refit of the Pass2.

### 8.3.1 Triggers

The minimum bias trigger (MB) is defined as the coincidence of signal in both sides of V0 detector synchronized with the passage of two colliding Pb bunches. This trigger provides an high efficiency ( $> 95\%$ ) for hadronic interactions. To improve the purity an additional threshold on the energy deposited in the ZDC is used to reject the contribution from electromagnetic processes.

During the data taking this trigger was considerably down-scaled to open the bandwidth for more rare triggers as for the unlike sign dimuon low- $p_T$  trigger (also called CMUL) used in this analysis and characterized by a  $p_T$  threshold of  $1 \text{ GeV}/c$  (see Sec. 5.3.3 and Tab. 7.1).

### 8.3.2 Centrality

Events are selected according to their degree of collision centrality by means of the V0 signal amplitude fitted using the Glauber model [128] (see Sec. 4.2.3). This model allows as well to extract other related variables such as the average number of binary collisions  $\langle N_{coll} \rangle$ , of participating nucleons  $\langle N_{part} \rangle$  and the nuclear overlap function  $\langle T_{AA} \rangle$ . The latter is equal to the average number of binary collisions divided by the nucleon-nucleon inelastic cross section [128] and represents the effective nucleon luminosity in the collision process [127].

In order to ensure a fully efficient MB trigger, the data sample is cut between 0% and 90%. Indeed, in this range the contribution of the electromagnetic background is negligible and Monte Carlo simulations demonstrate that more than 99% of the events expected to satisfy the trigger conditions actually lead to a positive decision. On the other hand, the efficiency loss in the very peripheral collisions is related to the low particle multiplicity [127].

In this analysis the statistics is further divided into two bins: 0%–20% (central collisions) and 20%–90% (semi-peripheral collisions). The related numerical values are given in Tab. 8.1.

Centrality	$\langle N_{coll} \rangle$	$\langle N_{part} \rangle$	$\langle T_{AA} \rangle$ (mb $^{-1}$ )
0%–90%	402 $\pm$ 41	125 $\pm$ 2	6.27 $\pm$ 0.21
0%–20%	1211 $\pm$ 131	308 $\pm$ 4	18.92 $\pm$ 0.63
20%–90%	170 $\pm$ 16	72 $\pm$ 2	2.67 $\pm$ 0.10

Table 8.1: Average number of binary collisions, participants and nuclear overlap function for the centrality classes considered in the analysis [127].

### 8.3.3 Number of minimum bias events

A data sample of  $17.3 \cdot 10^6$  Pb–Pb collisions triggered with the unlike-sign dimuon low- $p_T$  condition and satisfying all the above requirements is collected.

Taking advantage of the small part of the DAQ bandwidth kept open for MB triggers, it is possible to scale the number of available CMUL events to the equivalent MB events. The scaling factor for this normalization is called  $F_{norm}$  and is defined as the number of MB events ( $N_{MB}$ ) in the statistics divided by the number of events fulfilling MB and unlike sign dimuon low- $p_T$  trigger conditions together ( $N_{CMUL \in MB}$ ):

$$F_{norm} = \frac{N_{MB}}{N_{CMUL \in MB}} \quad (8.1)$$

A run-by-run study is done in order to estimate it. As shown in Fig. 8.2, the points are fitted with a zero-order polynomial function which provides the central value and the statistical uncertainty.

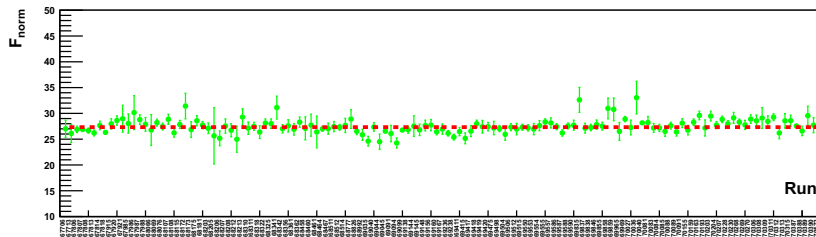


Figure 8.2:  $F_{norm}$  as a function of the run number. Points are fitted with a constant function (dashed red line).

Then, from the root mean square (RMS) of the distribution of the 134 values, the systematic uncertainty is extracted, assuming the following formula:

$$RMS^2 = (stat.)^2 + (syst.)^2 \quad (8.2)$$

The result is  $F_{norm} = 27.50 \pm 0.01 \pm 0.99$ .

Since the number of MB events does not depend on the centrality of the Pb–Pb collision (if expressed in percentage of the nuclear cross section), the number of MB events in a selected centrality interval scales with the width of the range. The corresponding numerical values are given in Tab. 8.2 with the statistical and systematic uncertainties arising from the  $F_{norm}$ .

Centrality	$N_{MB}$ in $10^6$
0%–90%	$476.15 \pm 0.17 \pm 17.14$
0%–20%	$105.81 \pm 0.04 \pm 3.81$
20%–90%	$370.34 \pm 0.13 \pm 13.33$

Table 8.2: Number of Pb–Pb minimum bias events.

Assuming a nuclear Pb–Pb cross section of  $7.7 \pm 0.1_{-0.5}^{+0.6}$  b [127], the data sample corresponds to an integrated luminosity of:

$$\mathcal{L}_{int} = 68.8 \pm 0.9(\text{stat.}) \pm 2.5(\text{syst. } F_{norm})_{-4.5}^{+5.5}(\text{syst. } \sigma_{Pb-Pb}) \mu\text{b}^{-1}.$$

### 8.3.4 Track selection

The high background environment of Pb–Pb collisions reduces the signal significance. Its improvement is achieved by means of different selection cuts on single muons.

- All tracks reconstructed by the Muon Tracking have to match with a track segment in the trigger chambers. Because of the thick iron wall located upstream of the Muon Trigger, this selection rejects efficiently light hadrons escaping from the front absorber. Indeed some hadrons coming from the interaction point are sufficiently energetic to reach the Muon Spectrometer or can also be produced in the front absorber itself by hadronic interaction. This cut rejects as well a part of the low-momentum muons coming mainly from  $\pi$  and  $K$  decays.
- Only tracks with pseudorapidity in the interval  $-4 < \eta < -2.5$  are considered. This selection is efficient to reject particles induced by beam-gas interactions.
- Tracks with a transverse radius coordinate at the end of the absorber ( $R_{ABS}$ ) between 17.6 cm and 89.5 cm are selected<sup>1</sup>. A part of the tracks outgoing from the beam pipe are thus rejected.
- Tracks have to point to the interaction vertex. This requirement can be achieved by introducing a cut on their value of  $p \times DCA$ . This

---

<sup>1</sup>These values are tuned after Monte Carlo simulations.

quantity is defined as the product of the momentum and the distance of closest approach (i.e. the distance to the primary vertex of the track extrapolated in the vertex transverse plane). This additional selection, widely used in the single muon analyses, is expected to have negligible effects and to remove the last fake tracks contaminating the muon sample.

- Transverse momentum of the tracks is required to be strictly larger than 2 GeV/c. It is verified that this selection does not modify the signal counts, but reduces significantly the background. This fact can be understood considering that muons from  $\Upsilon(1S)$  have usually a large  $p_T$  because of the large mass of the meson. On the other hand, background muons have lower transverse momentum as they come from light hadron decays.

## 8.4 Signal extraction

$\Upsilon$  candidates are formed by combining pairs of opposite sign tracks. In addition to the cuts on single muons just described, only dimuons with a reconstructed rapidity in the range  $2.5 < y < 4$  are selected.

Tab. 8.3 contains a summary of the cuts applied on events, single muons and reconstructed dimuons leading to the invariant mass spectrum shown in Fig. 8.3. The peaks of the  $J/\psi$  and  $\Upsilon$  are now visible.

	Type of cut	Value
Event	physics selection	Applied
	trigger type	CMUL (dimuon low- $p_T$ )
	centrality	0%-90%
Single muon	trigger-tracking matching	Required
	pseudorapidity	$-4 < \eta < -2.5$
	$R_{ABS}$	$17.6 < R_{ABS} < 89.5$ cm
	$p \times DCA$	Applied
	transverse momentum	$p_T > 2$ GeV/c
Dimuon	rapidity	$2.5 < y < 4$

Table 8.3: Summary of the selections.

### 8.4.1 Fit procedure

The distribution in Fig. 8.3 is then fitted by the following functions.

- The  $\Upsilon$  states are described by the sum of three extended Crystal Ball functions consisting of a Gaussian core with two power-law tails (one

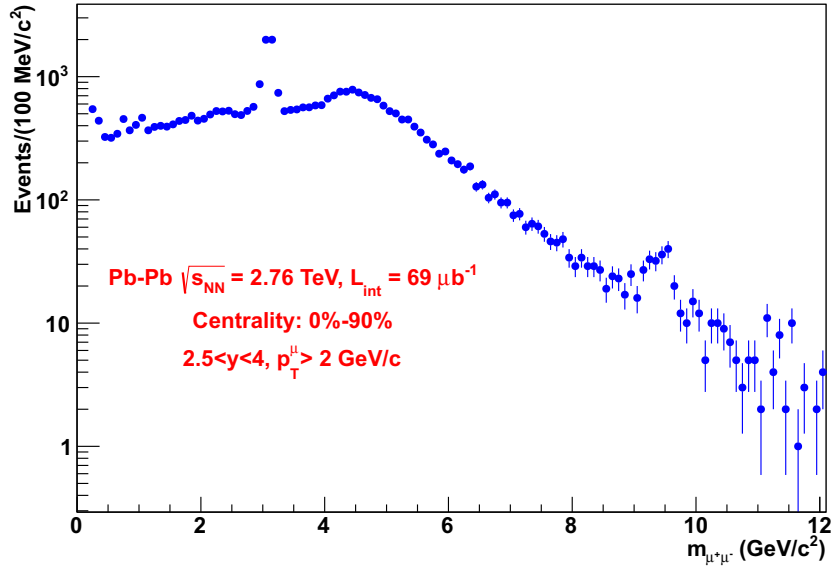


Figure 8.3: Dimuon invariant mass distribution after having applied the selection cuts.

for low masses and the other for high masses). They are an extension of the Crystal Ball function named after the Crystal Ball Collaboration [183]. The extended Crystal Ball function has seven parameters: the amplitude, the position ( $m$ ), the width ( $\sigma$ ) and two parameters for each tail. This function minimizes the  $\chi^2$  fit of realistic Monte Carlo simulations described in details in Sec. 8.5.1. See Eq. A.1 and Eq. A.2 for further details.

- The underlying continuum is described by a sum of two exponential functions (also called double exponential). It has four parameters: one amplitude and one argument for each of the two exponentials (see Eq. A.3).

In this analysis the amplitude of the three extended Crystal Ball are left free as well as the position and the width of the  $\Upsilon(1S)$ . Due to the low statistics above  $9 \text{ GeV}/c^2$ , the widths and the positions of the  $\Upsilon(2S)$  and  $\Upsilon(3S)$  are constrained as follows:

- the masses take into account the possible shift in the fit of the  $\Upsilon(1S)$  position:

$$m_{\Upsilon(2S)} = m_{\Upsilon(2S)}^{PDG} + \left( m_{\Upsilon(1S)} - m_{\Upsilon(1S)}^{PDG} \right) \cdot \frac{m_{\Upsilon(2S)}^{PDG}}{m_{\Upsilon(1S)}^{PDG}} \quad (8.3)$$

$$m_{\Upsilon(3S)} = m_{\Upsilon(3S)}^{PDG} + \left( m_{\Upsilon(1S)} - m_{\Upsilon(1S)}^{PDG} \right) \cdot \frac{m_{\Upsilon(3S)}^{PDG}}{m_{\Upsilon(1S)}^{PDG}} \quad (8.4)$$

where  $m_{\Upsilon(nS)}^{PDG}$  is the mass of the resonance taken from [2];

- the widths of  $\Upsilon(2S)$  and  $\Upsilon(3S)$  are forced to scale with their masses:

$$\sigma_{\Upsilon(2S)} = \sigma_{\Upsilon(1S)} \cdot \frac{m_{\Upsilon(2S)}^{PDG}}{m_{\Upsilon(1S)}^{PDG}} \quad (8.5)$$

$$\sigma_{\Upsilon(3S)} = \sigma_{\Upsilon(1S)} \cdot \frac{m_{\Upsilon(3S)}^{PDG}}{m_{\Upsilon(1S)}^{PDG}} \quad (8.6)$$

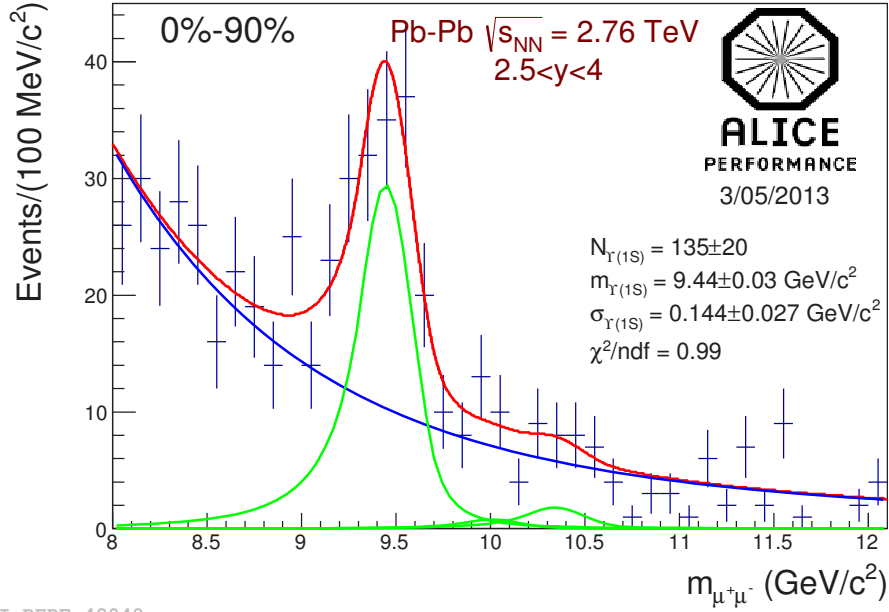
The four tail parameters of each resonance are fixed according to the results from realistic Monte Carlo simulations shown in Sec. 8.5.1. The tails of the three  $\Upsilon$  states are assumed to be described by the same set of parameters.

Finally, all parameters of the background function are left free. Thus, the overall fit function has 9 free parameters amongst the 25 considered.

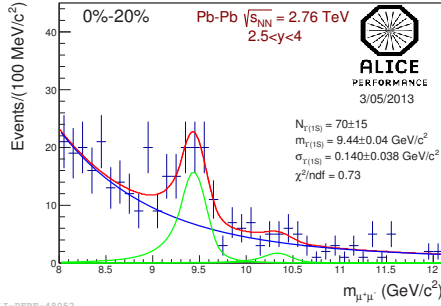
#### 8.4.2 Fit results

The fit procedure is applied to the invariant mass distribution integrated on centrality and rapidity between 5 and 16.5 GeV/c<sup>2</sup> (Fig. 8.4, top), i.e. in more than 110 bins of 100 MeV/c<sup>2</sup> each. The fit gives a mass of  $9.44 \pm 0.03$  GeV/c<sup>2</sup> for the  $\Upsilon(1S)$ . This result is in good agreement with the PDG value (9.460 GeV/c<sup>2</sup>) [2]. The  $\Upsilon(1S)$  width is  $144 \pm 27$  MeV/c<sup>2</sup>, the signal-over-background ratio ( $S/B$ ) is larger than 1 and the significance  $\left( \frac{S}{\sqrt{S+B}} \right)$  is around 8. Both are evaluated at  $3\sigma$  and are reported in Tab. 8.4. This large value of significance clearly ensures that the structure observed in the invariant mass range between 9 and 10 GeV/c<sup>2</sup> is not a statistical fluctuation.

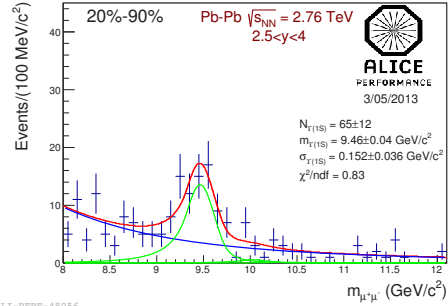
The number of extracted  $\Upsilon(2S)$  and  $\Upsilon(3S)$  is respectively  $4 \pm 27$  and  $9 \pm 28$ . A raw estimate of the upper limit of the ratios  $\frac{N_{\Upsilon(2S)}}{N_{\Upsilon(1S)}}$  and  $\frac{N_{\Upsilon(3S)}}{N_{\Upsilon(1S)}}$  can be done using the statistical uncertainties only and assuming the same  $A \times \varepsilon$  value for the three resonances. The results are  $\frac{N_{\Upsilon(2S)}}{N_{\Upsilon(1S)}} < 1.27$  and  $\frac{N_{\Upsilon(3S)}}{N_{\Upsilon(1S)}} < 1.44$  (both evaluated at a confidence level of 99.73%) to be compared to the LHCb results obtained in pp collision at  $\sqrt{s} = 7$  TeV:  $\sim 0.25$  and  $\sim 0.12$  [83]. Since the number of  $\Upsilon(2S)$  and  $\Upsilon(3S)$  are compatible with zero and it is impossible to give with the present statistics a reasonable upper limit on the production ratios, this analysis henceforth will be focused only on the ground bottomonium state.



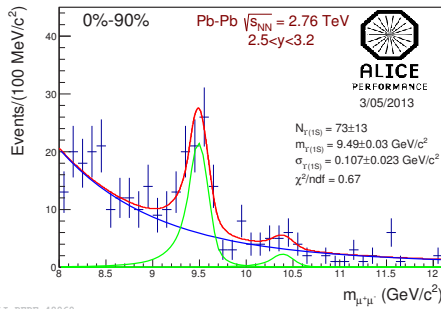
ALI-PERF-48048



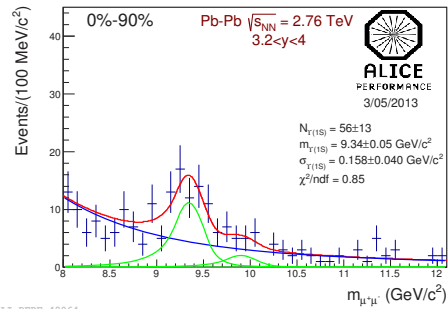
ALI-PERF-48052



ALI-PERF-48056



ALI-PERF-48060



ALI-PERF-48064

Figure 8.4: Fit procedure applied in different centrality classes and rapidity ranges. The global function is represented by a red line. The green lines represent the three extended Crystal Ball, while the blue line describes the underlying continuum.

Centrality	Rapidity	$m_{\Upsilon(1S)}$ (GeV/c <sup>2</sup> )	$\sigma_{\Upsilon(1S)}$ (MeV/c <sup>2</sup> )	$S/B$	$\frac{S}{\sqrt{S+B}}$
0%–90%	2.5 – 4	9.44 ± 0.03	144 ± 27	1.3 ± 0.2	8.1 ± 1.3
0%–20%	2.5 – 4	9.44 ± 0.04	140 ± 38	1.1 ± 0.2	5.6 ± 1.2
20%–90%		9.46 ± 0.04	152 ± 36	1.8 ± 0.4	6.0 ± 1.4
0%–90%	2.5 – 3.2	9.49 ± 0.03	107 ± 23	1.6 ± 0.3	6.3 ± 1.4
	3.2 – 4	9.34 ± 0.05	158 ± 40	1.1 ± 0.2	5.1 ± 1.2

Table 8.4: Mass position, width, signal-over-background ratio and significance of the  $\Upsilon(1S)$  state from fits. Values are shown for the different centrality classes and the different rapidity ranges considered in the analysis.

The available statistics can be divided into two more centrality classes where the signal has still a good significance. Tab. 8.4 shows that in 0%–20% and 20%–90% the  $S/B$  is larger than 1 and the significance is larger than five. The same happens dividing the dimuons in the rapidity intervals  $2.5 < y < 3.2$  and  $3.2 < y < 4$ .

For the distributions in the two centrality classes, the width of the  $\Upsilon(1S)$  varies between  $140 \pm 38$  and  $152 \pm 36$  MeV/c<sup>2</sup>, compatible within uncertainties. In the two considered rapidity bins, a more important difference is observed as the kinematic regions are not the same.

Finally, it is important to note that all fits presented in Fig. 8.4 exhibit a  $\chi^2$  per degree of freedom smaller than unity.

### 8.4.3 Systematic uncertainties

The constraints mentioned before to fit the invariant mass distribution lead to possible systematic uncertainties that are now investigated.

No systematic error can be associated to the sharp  $p_T$  cut at 2 GeV/c on single tracks. Indeed, the available statistics prevents from ranging the cut value enough to obtain a number of  $\Upsilon(1S)$  statistically different. It becomes therefore difficult to disentangle the statistical contribution from the systematic one.

In order to test a large number of fit conditions, an automatic procedure is applied. Nevertheless, the goodness of the results and the  $\chi^2$  per degree of freedom  $< 1.5$  is always checked.

A weighted mean of the results of each tested fit allows to determine the central value (Eq. 8.7) and the statistical uncertainty (Eq. 8.8):

$$\langle n^{\Upsilon(1S)} \rangle = \frac{\sum_{i=1}^N \frac{n_i^{\Upsilon(1S)}}{\sigma_i^2}}{\sum_{i=1}^N \frac{1}{\sigma_i^2}} \quad (8.7)$$

$$stat. = \sqrt{\frac{1}{\sum_{i=1}^N \frac{1}{\sigma_i^2}}} \quad (8.8)$$

where  $n_i^{\Upsilon(1S)}$  is the number of  $\Upsilon(1S)$  got from each fit  $i$ ,  $\sigma_i$  is the associated uncertainty and  $N$  is the total number of tests for each possible source of systematics. The applied weight (the inverse of the variance) limits the influence of fits leading to large uncertainties.

For a given source, the overall systematic uncertainty is estimated by a root mean square (Eq. 8.9):

$$syst. = \sqrt{\frac{\sum_{i=1}^N \left( n_i^{\Upsilon(1S)} - \langle n^{\Upsilon(1S)} \rangle \right)^2}{N}} \quad (8.9)$$

## Background description

In place of a double exponential, another function is used to describe the underlying background: a double power-law defined as a sum of two power-law functions with four parameters, one amplitude and one argument for each power-law (Eq. A.4). All of them are let free during the fit.

For each function the fit is applied in different invariant mass regions. The lower and the upper bounds of the fit are independently modified in the range 5–8  $\text{GeV}/c^2$  and 12–18  $\text{GeV}/c^2$ . Fig. 8.5 shows the number of  $\Upsilon(1S)$  obtained from the fits applied in the different ranges to the integrated statistics. The abscissa refers to the upper limit, while colours refer to the lower limit considered. The left plot shows results for the double exponential, while the right one refers to the double power-law function.

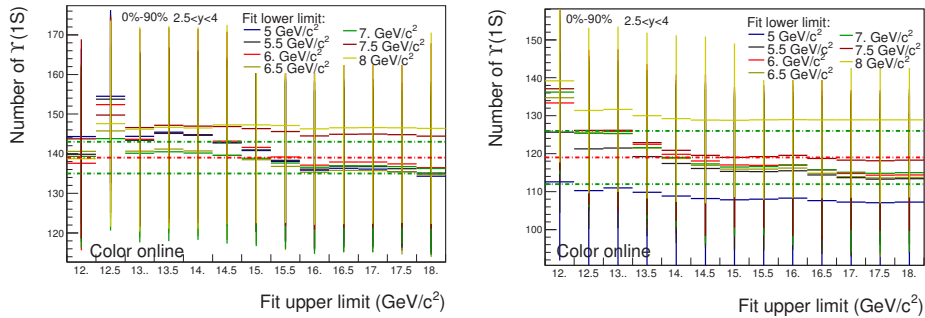


Figure 8.5: Number of  $\Upsilon(1S)$  obtained fitting the integrated mass distribution with a double exponential (left) or with a double power-law function (right) in different fit ranges.

In the second case the number of  $\Upsilon(1S)$  is systematically smaller and the uncertainties are more important.

Tab. 8.5 shows the combined results of the study in all bins. The relative statistical uncertainty on the number of  $\Upsilon(1S)$  is about 20%, while the relative systematic uncertainty ranges over 4% and 7% depending on the considered bin.

<b>Background description summary</b>		
<b>Centrality</b>	<b>Rapidity</b>	<b>Number of <math>\Upsilon(1S)</math></b>
0%–90%	2.5 – 4	$130 \pm 21(16\%) \pm 6(5\%)$
0%–20%	2.5 – 4	$63 \pm 15(24\%) \pm 3(5\%)$
20%–90%		$68 \pm 13(19\%) \pm 4(6\%)$
0%–90%	2.5 – 3.2	$70 \pm 14(20\%) \pm 3(4\%)$
	3.2 – 4	$56 \pm 13(23\%) \pm 4(7\%)$

Table 8.5: Summary of the study on systematic uncertainties induced by the background function choice.

### Mass position of $\Upsilon(2S)$ and $\Upsilon(3S)$

The positions of the extended Crystal Ball used to describe the  $\Upsilon(2S)$  and the  $\Upsilon(3S)$  distributions are kept fixed, thus leading to a potential source of systematic uncertainty. In order to estimate it, both positions are independently shifted by various values between  $\pm 0.05$  GeV/ $c^2$ , corresponding to  $\pm 0.5\%$  of the mass of the state. This choice is driven by Eq. 8.3 and 8.4. As the uncertainties on the masses of  $\Upsilon$  mesons are of the order of 0.2%, the chosen shift value of  $\pm 0.5\%$  seems reasonable.

Fig. 8.6 shows the number of  $\Upsilon(1S)$  obtained for different  $\Upsilon(2S)$  positions ( $x$ -axis) and  $\Upsilon(3S)$  positions (coloured lines). It refers to full statistics. Tab. 8.6 summarizes the results for all the bins.

<b>Mass position summary</b>		
<b>Centrality</b>	<b>Rapidity</b>	<b>Number of <math>\Upsilon(1S)</math></b>
0%–90%	2.5 – 4	$134 \pm 19(14\%) \pm 0.4(0.3\%)$
0%–20%	2.5 – 4	$70 \pm 15(21\%) \pm 0.7(1\%)$
20%–90%		$65 \pm 12(18\%) \pm 0.2(0.3\%)$
0%–90%	2.5 – 3.2	$74 \pm 13(18\%) \pm 0.8(1\%)$
	3.2 – 4	$59 \pm 13(22\%) \pm 3(5\%)$

Table 8.6: Summary of the study on systematic errors induced by the choice of the  $\Upsilon(2S)$  and  $\Upsilon(3S)$  mass position.

Central values and the statistical uncertainties are close to the numbers

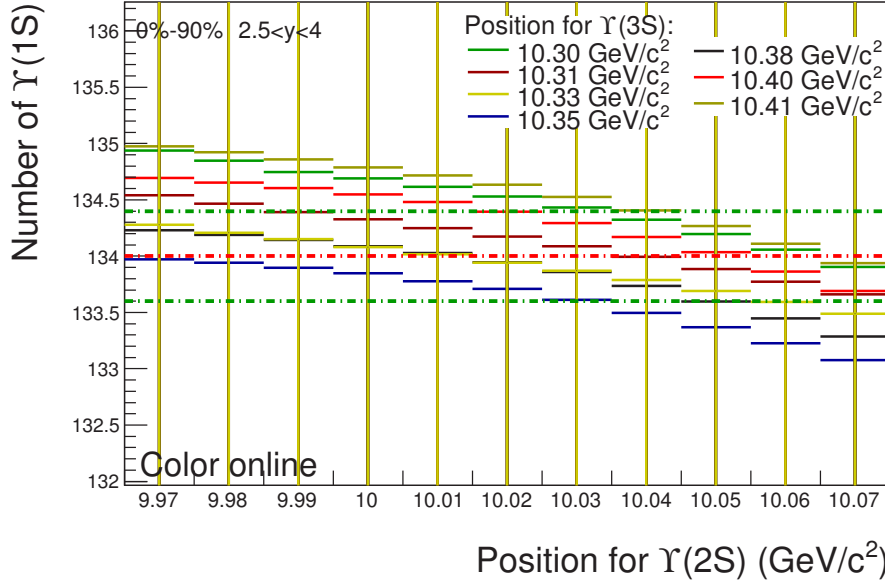


Figure 8.6: Number of  $\Upsilon(1S)$  obtained from fits applied with different  $\Upsilon(2S)$  and  $\Upsilon(3S)$  mass positions.

provided by the standard fit procedure, while systematics are of the order of 1% except for one bin.

### Signal width of $\Upsilon(2S)$ and $\Upsilon(3S)$

In order to estimate the uncertainty due to  $\sigma$  of  $\Upsilon(2S)$  and  $\Upsilon(3S)$ , the widths are independently scaled by various factors in the ranges 0.6–1.4.

Fig. 8.7 shows the number of  $\Upsilon(1S)$  for different width values fitting the invariant mass integrated on centrality and rapidity. The colours indicate the width of the  $\Upsilon(3S)$ , while the abscissa the  $\sigma$  of the  $2S$  state. Tab. 8.7 summarizes this study.

Signal width summary		
Centrality	Rapidity	Number of $\Upsilon(1S)$
0%–90%	2.5 – 4	$134 \pm 19(14\%) \pm 0.4(0.3\%)$
0%–20%	2.5 – 4	$70 \pm 15(21\%) \pm 0.4(0.6\%)$
20%–90%		$65 \pm 12(18\%) \pm 0.2(0.3\%)$
0%–90%	2.5 – 3.2	$73 \pm 13(18\%) \pm 0.3(0.4\%)$
	3.2 – 4	$56 \pm 12(21\%) \pm 0.7(1\%)$

Table 8.7: Summary of the study on systematic uncertainties induced by the choice of the  $\Upsilon(2S)$  and  $\Upsilon(3S)$  widths.

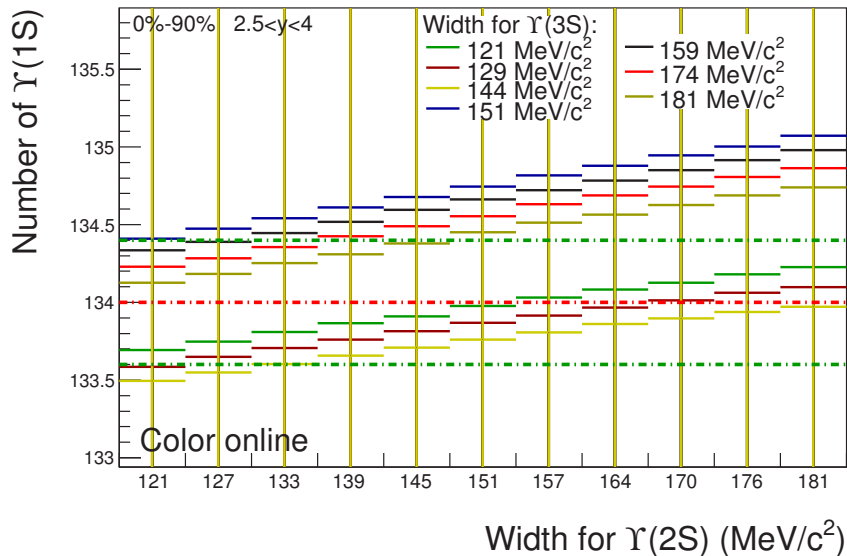


Figure 8.7: Number of  $\Upsilon(1S)$  obtained from fits applied with different  $\Upsilon(2S)$  and  $\Upsilon(3S)$  widths.

The conclusions are very similar to what observed studying the mass positions. The systematic uncertainties are negligible and the central values do not vary a lot with respect to the nominal fit procedure. The statistical uncertainties remain the same.

### Tail parameters

This study is done in two steps. First, the same set of parameters is still supposed to describe the tails of all the resonances. The four tail parameters of each function are multiplied independently by a scaling factor between 0.75 and 1.25.

Fig. 8.8 (top) shows in red all the function shapes used, the nominal shape is represented in green and the two extra parametrizations for the second step in blue. In this figure shapes are normalized to unity, while position and width are those observed fitting the data.

The principle of the second step, instead, is meant to use different sets for the three resonances in the same fit. The sets are chosen amongst those considered above: the default and the two extremes.

The final results are illustrated in Fig. 8.8 (bottom). Tab. 8.8 summarizes the results obtained in step 1 and step 2 together. No important changes in the central values and systematic uncertainties are observed with respect to the nominal fit procedure. The systematic uncertainties ranges between 1% and 4% depending on the considered bin. This source provides the second more important contribution to the overall systematic uncer-

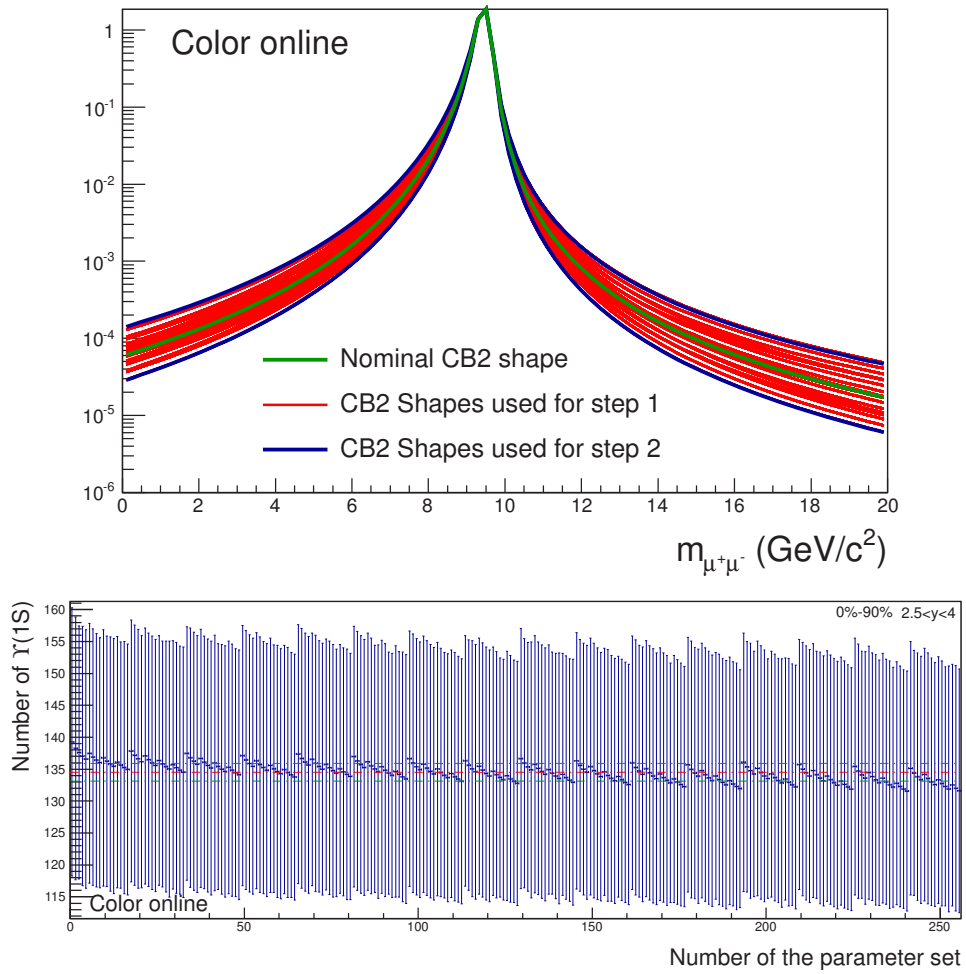


Figure 8.8: Top: shapes used to evaluate systematic uncertainties related to the choice of the tail parameters (see text for more details). Bottom: number of  $\Upsilon(1S)$  obtained from fits. The value given in abscissa refers to a particular set of parameters.

tainty on signal extraction.

Tail parameters summary		
Centrality	Rapidity	Number of $\Upsilon(1S)$
0%–90%	2.5 – 4	$135 \pm 20(15\%) \pm 2(1\%)$
0%–20%	2.5 – 4	$70 \pm 15(21\%) \pm 2(3\%)$
20%–90%		$65 \pm 12(18\%) \pm 1(2\%)$
0%–90%	2.5 – 3.2	$73 \pm 13(18\%) \pm 2(3\%)$
	3.2 – 4	$56 \pm 13(23\%) \pm 2(4\%)$

Table 8.8: Summary of the study on systematic errors induced by the choice of the tail parameters.

### $p \times DCA$ cut

In order to estimate the effects of the  $p \times DCA$  cut on the signal extraction, the selection is now applied more or less selectively. Fig. 8.9 shows the number of  $\Upsilon(1S)$  obtained after cuts between  $4\sigma$  (the tightest selection) and  $9\sigma$  (the widest one). The default cut is at  $6\sigma$ . Tab. 8.9 gives the results for the different bins of the analysis. It is clear that this selection has almost no effect on signal extraction.

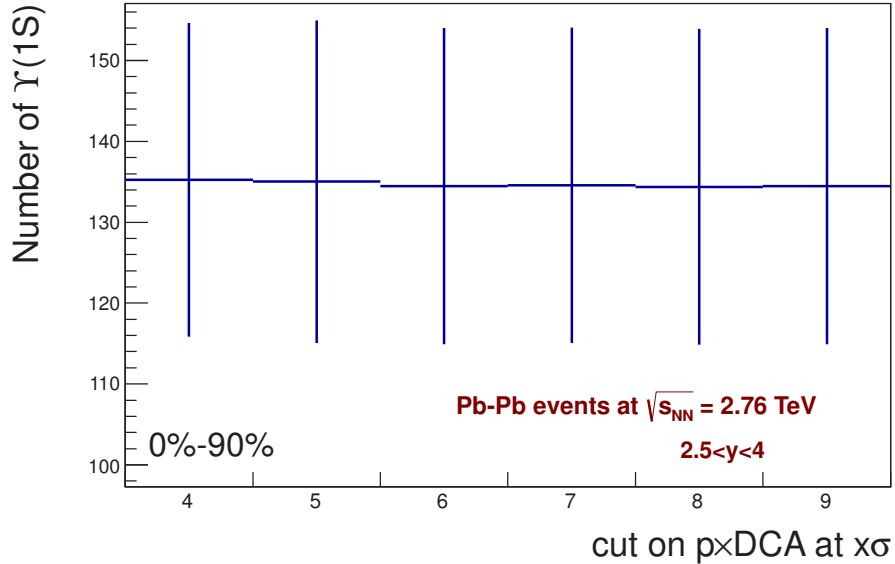


Figure 8.9: Number of  $\Upsilon(1S)$  at various  $\sigma$  of  $p \times DCA$  cut.

<i>p</i> × <i>DCA</i> cut summary		
Centrality	Rapidity	Number of $\Upsilon(1S)$
0%–90%	2.5 – 4	$135 \pm 20(15\%) \pm 0.3(0.2\%)$
0%–20%	2.5 – 4	$70 \pm 15(21\%) \pm 0.2(0.3\%)$
20%–90%		$65 \pm 12(18\%) \pm 0.2(0.3\%)$
0%–90%	2.5 – 3.2	$72 \pm 13(18\%) \pm 0.1(0.1\%)$
	3.2 – 4	$57 \pm 13(23\%) \pm 0.4(0.7\%)$

Table 8.9: Summary of the study on systematic errors induced by the choice of the *p* × *DCA* cut.

### Signal extraction summary

Tab. 8.10 gives the final values of signal extraction. Central values and statistical uncertainties obtained in the different studies described above are averaged by a weighted mean. Systematics uncertainties from each source are summed in quadrature. Overall statistical errors range from 15% to 23%, while the systematics are between 5% and 11%. The choice of the background function and the fit range represents the dominant source of systematic uncertainties followed by the set of parameters describing the extended Crystal Ball tails.

Signal extraction summary		
Centrality	Rapidity	Number of $\Upsilon(1S)$
0%–90%	2.5 – 4	$134 \pm 20(15\%) \pm 7(5\%)$
0%–20%	2.5 – 4	$69 \pm 15(22\%) \pm 4(6\%)$
20%–90%		$66 \pm 12(18\%) \pm 4(6\%)$
0%–90%	2.5 – 3.2	$72 \pm 13(18\%) \pm 4(5\%)$
	3.2 – 4	$57 \pm 13(23\%) \pm 6(11\%)$

Table 8.10: Overall results from signal extraction. The first uncertainty is statistical and the second one is systematic.

## 8.5 MC simulation

### 8.5.1 Embedding production

The embedding Monte Carlo technique provides the most realistic background conditions necessary to well reproduce central Pb–Pb collisions where the high particle multiplicity environment could alter the track reconstruction efficiency. In this analysis it consists in simulating one  $\Upsilon(1S)$  and

embedding the detector response into a real event. The signal and background embedding is performed at the SDigits (Summable Digit) level. The raw data of a real event is first converted into SDigits, then the  $\Upsilon(1S)$  is generated and forced to decay into dimuons transported through the detector. After that, the charged deposited by the muons are merged with the background SDigits. Finally, the resulting merged SDigits are processed by the normal reconstruction chain allowing to reproduce a highly realistic detector response.  $\Upsilon(1S)$  are generated with a fast generator (`AliGenParam`) according to real kinematic distributions. In addition, the particle transport is made by a realistic estimate of the Muon Spectrometer setup provided by GEANT3 [142] using a description of the real alignment of the tracking chambers and the detector dead areas.

The simulation is performed on a run-by-run basis, thus taking into account the time dependence of the detector characteristics. The variations of the available statistics for each of the 134 runs are also taken into account. One  $\Upsilon(1S)$  per event is generated in about 40% of the MB events of each run at the position of the real primary vertex. The statistics amounts to a total number of  $\sim 3 \cdot 10^6$  mesons.

### Acceptance and efficiency correction factor

The embedding simulation allows to compute an unbiased correction factor for acceptance and efficiency ( $A \times \varepsilon$ ) in centrality and rapidity bins. This factor is defined in order to take into account the different kinematic behaviours of the  $\Upsilon(1S)$ , the detector efficiency and the analysis cuts.

The  $A \times \varepsilon$  for a given bin is first estimated run-by-run and then weighted by the number of unlike sign dimuon trigger events in each run. This is necessary because the number of mesons generated scales with the number of MB, while the CMUL trigger is considered in the rest of the analysis. The resulting values are further integrated over the full data taking period, thus providing the overall factor. Fig. 8.10 shows the  $A \times \varepsilon$  as a function of the runs integrated on centrality and rapidity. A drop due to a decrease of the tracking efficiency at the end of the data taking period is observed in the last twenty runs.

The  $A \times \varepsilon$  is shown as a function of the centrality in Fig. 8.11 top. Since the number of generated  $\Upsilon(1S)$  depends only on the run-by-run available statistics and does not reflect the actual centrality dependence of the meson production, the values are given weighted by the average number of binary nucleon-nucleon collisions corresponding to each centrality class. The integrated  $A \times \varepsilon$  is  $21.93 \pm 0.13\%$  (dashed red line in the plot). From peripheral to central collisions the reconstruction efficiency factor decreases from  $23.07 \pm 0.13\%$  (80%–90%) to  $21.28 \pm 0.13\%$  (0%–10%) leading to a relative efficiency loss of 7%.

The same factor as a function of the rapidity is shown in Fig. 8.11 on

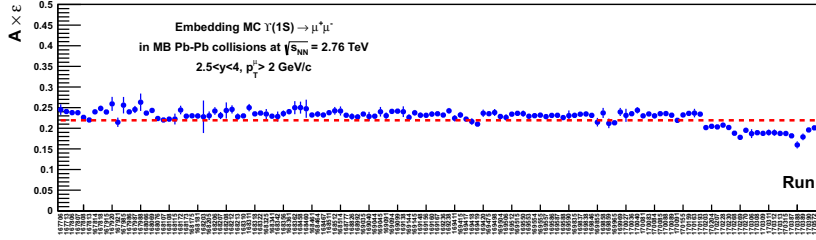


Figure 8.10: Run-by-run  $A \times \varepsilon$  factor integrated on centrality and rapidity. Dashed red line indicates the integrated value.

bottom left. The  $A \times \varepsilon$  maximum is reached at the center of the detector and decreases at the edges.

Finally, on bottom right, the  $A \times \varepsilon$  trend as a function of the  $p_T$  (not used in this analysis) shows that it is really possible to measure  $\Upsilon(1S)$  down to zero transverse momentum.

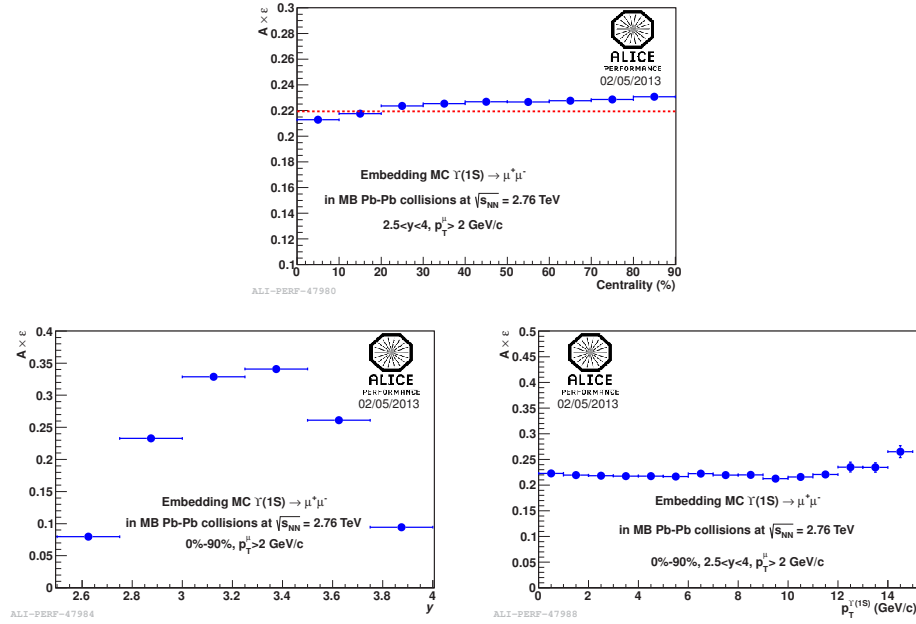


Figure 8.11:  $A \times \varepsilon$  factor as a function of the centrality (top), of the rapidity (bottom left) and of the  $p_T$  (bottom right).

Tab. 8.11 summarizes the  $A \times \varepsilon$  values for each rapidity and centrality bin considered in this analysis.

Centrality	Rapidity	$A \times \varepsilon$ (%)
0%–90%	2.5 – 4	$21.93 \pm 0.13$
0%–20%	2.5 – 4	$21.58 \pm 0.13$
20%–90%		$22.63 \pm 0.13$
0%–90%	2.5 – 3.2	$19.34 \pm 0.06$
	3.2 – 4	$25.68 \pm 0.08$

Table 8.11:  $A \times \varepsilon$  values in the various bins.

### Signal line shape

With the embedding production it is also possible to obtain the expected invariant mass distribution of  $\Upsilon(1S)$ . The combinatorial background is fully removed by selecting only muons coming from simulated bottomonium states (top left plot of Fig. 8.12). Due to the muon multiple scattering in the front absorber and the residual misalignment of the tracking chambers, the shape of the reconstructed dimuons deviates from a Gaussian distribution as shown in the top right distribution. A Crystal Ball function allows to describe the left tail, but it fails to describe the right tail (bottom left plot). The use of an extended Crystal Ball function is therefore necessary to better reproduce the distribution as bottom right plot in Fig. 8.12 demonstrates.

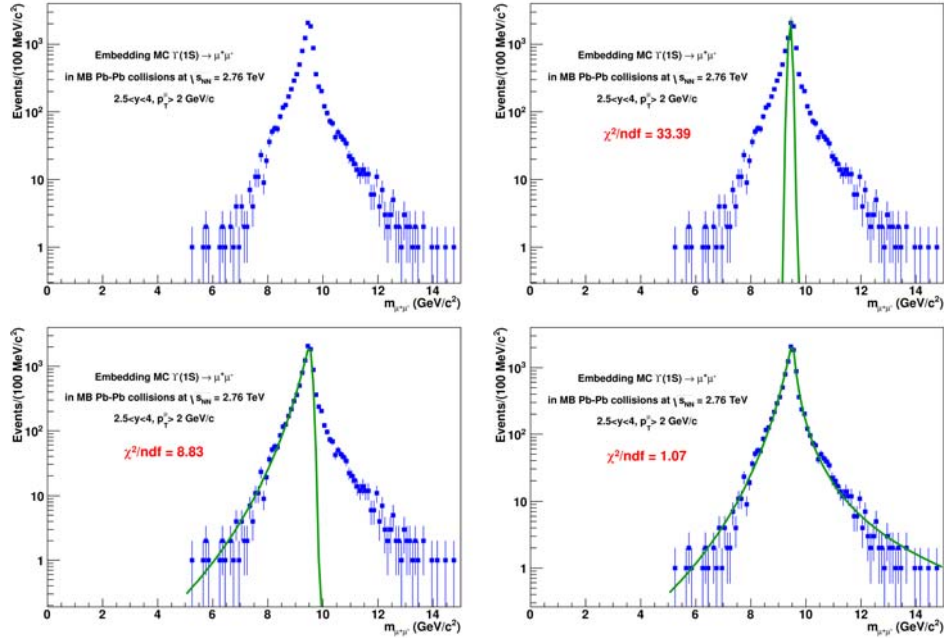


Figure 8.12: From top left to bottom right, integrated signal distribution from embedding production, distribution fitted with a Gaussian function, with a Crystal Ball and with an extend Crystal Ball.

The extended Crystal Ball function is also used to fit the distributions in centrality and rapidity bins. Fig. 8.13 shows how its parameters vary as a function of the centrality (on the left) and of the rapidity (on the right). In the first case they are rather stable, while in the second plot the width increases with the rapidity.

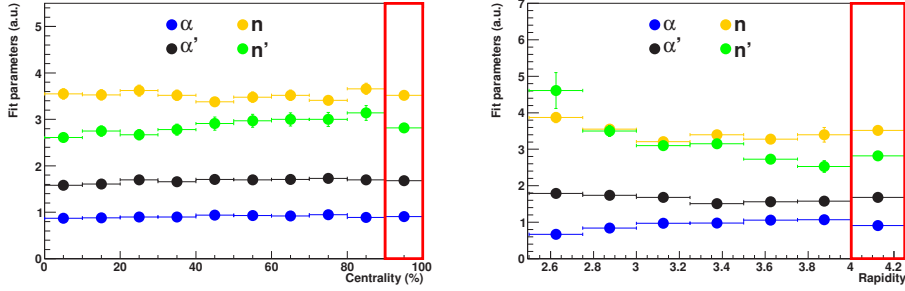


Figure 8.13: Extended Crystal Ball parameters (see Eq. A.2) as a function of centrality (left) and rapidity (right). Values from the integrated distribution are shown in the red boxes.

Tab. 8.12 gives the values for each bin considered in this analysis. The tail parameters obtained for  $\Upsilon(1S)$  are supposed to describe the other two resonances as well. This assumption is taken into account during the evaluation of the systematic uncertainties (Sec. 8.4.3).

Centrality	Rapidity	$\alpha$	$n$	$\alpha'$	$n'$
0%–90%	2.5 – 4	$0.91 \pm 0.01$	$3.54 \pm 0.04$	$1.69 \pm 0.01$	$2.72 \pm 0.04$
0%–20%	2.5 – 4	$0.87 \pm 0.01$	$3.55 \pm 0.08$	$1.60 \pm 0.02$	$2.56 \pm 0.07$
20%–90%		$0.92 \pm 0.01$	$3.52 \pm 0.04$	$1.71 \pm 0.01$	$2.80 \pm 0.05$
0%–90%	2.5 – 3.2	$0.87 \pm 0.01$	$3.43 \pm 0.06$	$1.74 \pm 0.02$	$3.28 \pm 0.08$
	3.2 – 4	$0.99 \pm 0.01$	$3.45 \pm 0.05$	$1.57 \pm 0.02$	$2.70 \pm 0.05$

Table 8.12: Values of the low-end tail parameters ( $\alpha$ ,  $n$ ) and of the high-end tail parameters ( $\alpha'$ ,  $n'$ ) of the extended Crystal Ball function.

## 8.5.2 Systematic uncertainties on MC parametrizations

The estimate of the  $A \times \varepsilon$  factor might depend on the  $\Upsilon(1S)$   $p_T$  and  $y$  distributions used as input in the Monte Carlo simulation. In order to evaluate the sensitivity of the results on this initial choice, several tests are performed on a run-by-run basis and, for simplicity, without the centrality dependence. Pure  $\Upsilon(1S)$  samples generated with different  $p_T$  and  $y$  parametrizations (Fig. 8.14) are then forced to decay into two muons. The

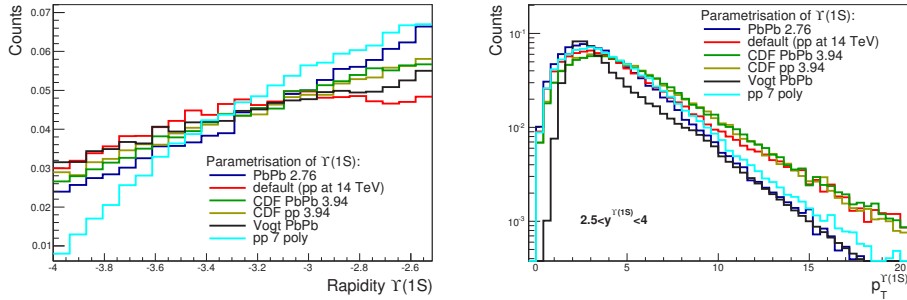


Figure 8.14: Rapidity (left) and  $p_T$  (right) parametrizations of the generated  $\Upsilon(1S)$  used to evaluate the systematic uncertainties on  $A \times \varepsilon$ . The distributions are normalized to the unity.

particles are then transported in the same realistic detector setup used for the embedding simulation. The number of generated  $\Upsilon(1S)$  is chosen to scale with the number of CMUL. Finally, the  $A \times \varepsilon$  factor is integrated over the whole data taking period. What follows is the list of the considered  $p_T$  and  $y$  parametrizations available in the AliRoot `AliGenMUONlib` class.

- **PbPb 2.76**: it is the standard parametrization used in the embedding simulation. It is obtained by interpolating the available RHIC and LHC data to Pb–Pb collisions at  $\sqrt{s_{NN}} = 2.76$  TeV, including the EKS98 parametrization for the shadowing [184].
- **default**: this parametrization corresponds to pp collisions at  $\sqrt{s} = 14$  TeV. It is scaled from CDF data at  $\sqrt{s} = 2$  TeV.
- **CDF PbPb 3.94**: it is very similar to the previous one, but it includes the EKS98 parametrization for the shadowing.
- **CDF pp 3.94**: it is obtained by rescaling CDF data in pp collisions at  $\sqrt{s} = 3.94$  TeV by means of LO QCD method.
- **Vogt PbPb**: the parametrization corresponds to Pb–Pb collisions at  $\sqrt{s_{NN}} = 5.5$  TeV.
- **pp 7 poly**: it is supposed to describe pp collisions at  $\sqrt{s} = 7$  TeV. It is obtained from the fit to CDF and the LHC data [184].

The maximum spread observed amongst the values is around 1% (see Tab. 8.13). To be as safer as possible and to include nuclear matter effects a systematic uncertainty of 4% (or 5% and 7% in the two rapidity bins) associated to the  $A \times \varepsilon$  is chosen. In any case, it is dominated by systematic uncertainty on the pp reference cross section (described in Sec. 8.7).

Parametrizations	$A \times \varepsilon$ (%)
PbPb 2.76	$23.42 \pm 0.06$
default	$24.05 \pm 0.06$
CDF PbPb 3.94	$23.03 \pm 0.06$
CDF pp 3.94	$22.94 \pm 0.06$
Vogt PbPb	$23.22 \pm 0.06$
pp 7 poly	$24.04 \pm 0.06$

Table 8.13:  $A \times \varepsilon$  values for the different  $p_T$  and  $y$  parametrizations.

## 8.6 Systematic uncertainties on detector response

It is also necessary to consider the uncertainties related to the ability of simulations in reproducing the actual detector efficiency. The following values are obtained by data driven methods which do not allow to study the centrality dependence.

### Muon Tracking efficiency

The tracking efficiency for muons and dimuons is compared to simulations based on realistic  $p_T$  and  $y$  parametrizations. The difference between the efficiencies from real data and Monte Carlo gives the estimate of the systematic uncertainty. The overall value is around 8% (independent on centrality), while it ranges between 7% and 9% as a function of the rapidity.

An additional uncertainty of 2% due to the malfunctioning of a few detector elements has to be taken into account too. This is not fully uncorrelated to the previous one and therefore has to be added bin-by-bin.

### Muon Trigger efficiency

Real data are used to evaluate the Muon Trigger efficiency map for different trigger configurations or different event characteristics, such as centrality or particle  $p_T$ . The same efficiency is then evaluated in simulations with the same trigger configurations. The spread observed between the two results is 2%, which represents another source of uncertainty supposed to be centrality independent and uncorrelated in rapidity.

### Matching efficiency

For large mass resonances as  $J/\psi$  and  $\Upsilon$ , the systematic uncertainty on matching efficiency between the tracks reconstructed in the Muon Tracking and those reconstructed by the Muon Trigger is about 1% for single muons.

It arises from the difference observed in data and simulation when applying different  $\chi^2$  cuts on the matching between  $2\sigma$  and  $6\sigma$ .

### Final values

Finally, a last overall uncertainty of less than 1% should be taken into account for the dependence on the centrality, not considered in the previous studies, but this effect is largely dominated by the systematic on the tracking efficiency. The values is estimated by comparing the efficiency obtained with the embedding Monte Carlo simulation and real data.

The final results are summarized in Tab. 8.14.

Source	Centrality	Rapidity
Tracking	10%	9%–11%
Trigger	2%	2%
Matching	1%	1%

Table 8.14: Systematic uncertainties on Muon Tracking, Muon Trigger and matching efficiency.

In the  $p_T$  range covered by the Muon Spectrometer, the  $\Upsilon(1S)$  is supposed to be not polarized in Pb–Pb collisions. CMS and CDF demonstrated that this is true for pp [87] and  $p\bar{p}$  collisions [76]. For this reason no related uncertainties are assigned to the  $A \times \varepsilon$  factor.

## 8.7 pp reference cross section

In order to normalize the  $\Upsilon(1S)$  production in Pb–Pb collisions at  $\sqrt{s_{NN}} = 2.76$  TeV at forward rapidity, a reference cross section in pp collisions at the same center-of-mass energy and in the same kinematic region is needed<sup>2</sup>. Data collected by ALICE during the pp runs at  $\sqrt{s} = 2.76$  TeV do not allow to extract any useful information in the  $\Upsilon$  mass region. An alternative strategy is thus adopted.

A few  $\Upsilon(1S)$  cross section measurements in pp collisions at TeV energies exist and most of them refer to central rapidities. Based on these data, the midrapidity differential cross section of  $\Upsilon(1S)$  in pp collisions at  $\sqrt{s} = 2.76$  TeV is estimated by means of an interpolation procedure described in Sec. 8.7.1. The obtained value is then extrapolated at forward rapidity using different rapidity shapes predicted with an event generator and validated according to their ability in reproducing the available data (Sec. 8.7.2).

<sup>2</sup>The results presented in this section are a summary of the work carried out by F. Bossù and M. Gagliardi (from a private communication).

### 8.7.1 Interpolation of the $\Upsilon(1S)$ cross section at midrapidity

The measurements used for the interpolation of the  $\Upsilon(1S)$  cross section at midrapidity are summarized in Tab. 8.15 [70, 76, 79, 89].

Experiment	$\sqrt{s}$ (TeV)	$BR \cdot d\sigma^{\Upsilon(1S)}/dy$ (nb)	Rapidity
CDF	1.8	$0.680 \pm 0.015 \pm 0.056$	$ y  < 0.4$
DØ	1.96	$0.628 \pm 0.016 \pm 0.063 \pm 0.038$	$ y  < 0.6$
CMS	2.76	$0.921 \pm 0.128 \pm 0.157 \pm 0.055$	$ y  < 1.2$
CMS	7	$2.025^{+0.284}_{-0.263}$	$ y  < 0.4$

Table 8.15: Experimental results used for the interpolation of the  $\Upsilon(1S)$  cross section at midrapidity.

The data are fitted with power-law and a logarithmic function (Fig. 8.15) and the fit parameters obtained are used to determine  $BR \cdot d\sigma^{\Upsilon(1S)}/dy$  at midrapidity at  $\sqrt{s} = 2.76$  TeV. The statistical, systematic and luminosity uncertainties of each measurement are summed in quadrature in order to be used. When the CMS point at  $\sqrt{s} = 2.76$  TeV is removed from the fit, the results change by less than 0.5%. Other functional forms tested lead to a less satisfactory description.

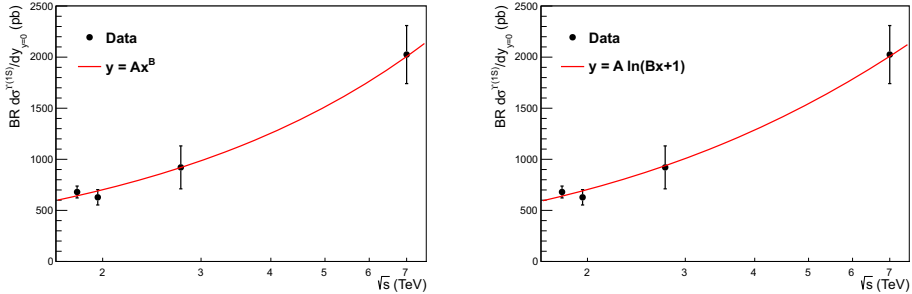


Figure 8.15: Energy dependence of the  $\Upsilon(1S)$  cross section at midrapidity, with overlaid power-law (left) and logarithmic (right) fit functions.

Besides the purely phenomenological fit, a second option is considered for the interpolation. Models such as the Color Evaporation Model [50] predict that the quarkonium cross section is proportional to the bare quark pair production cross section (Eq. 8.10) calculated in pQCD approach:

$$\frac{d\sigma^{\Upsilon(1S)}}{dy}(y, \sqrt{s}) = \alpha \cdot \frac{d\sigma^{b\bar{b}}}{dy}(y, \sqrt{s}) \quad (8.10)$$

The available FONLL predictions [185] for the beauty cross section used for the interpolation provide a central value and an uncertainty band, obtained

by varying calculation parameters<sup>3</sup>. Three energy dependence curves are therefore defined, corresponding to the central value and to the lower and upper edge of the uncertainty band. For each of the three curves, the  $\alpha$  parameter is determined by fitting the ratio of data contained in Tab. 8.15 and FONLL predictions with a constant function. As shown in Fig. 8.16, the model provides a good description of the data and can be used for the interpolation at  $\sqrt{s} = 2.76$  TeV.

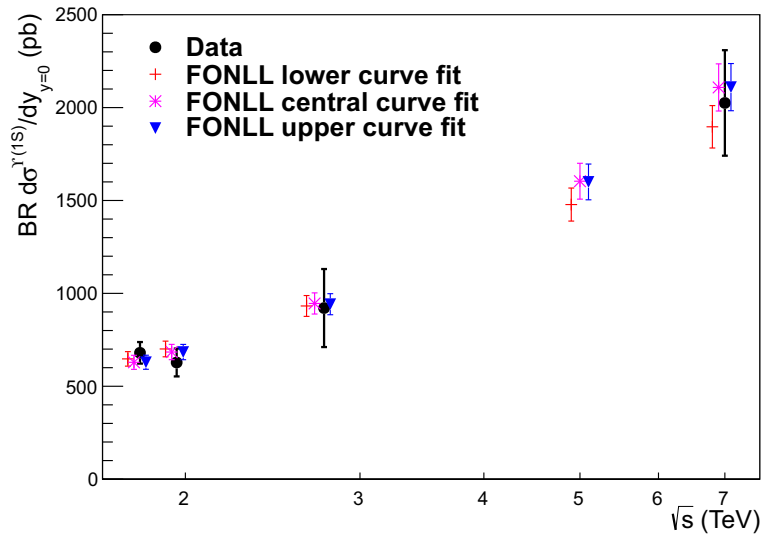


Figure 8.16: Energy dependence of the  $\Upsilon(1S)$  cross section at midrapidity, with overlaid FONLL predictions rescaled by the  $\alpha$  parameter. The points corresponding to different predictions at the same energy are slightly shifted horizontally for visibility.

The results obtained from the fit with the two functional forms and with the three FONLL curves are summarized in Tab. 8.16. They are compatible within uncertainties among each other, and with the CMS result of Tab. 8.15.

The five estimates are averaged in order to obtain the final result of  $BR \cdot \frac{d\sigma^{\Upsilon(1S)}}{dy}(y = 0, \sqrt{s} = 2.76 \text{ TeV}) = 0.935 \pm 0.082 \text{ nb}$ .

## 8.7.2 Extrapolation to forward rapidity

The CMS Collaboration showed that PYTHIA 6.4 [140] is able to reproduce the  $\Upsilon(1S)$  rapidity and  $p_T$  distributions in pp collisions at  $\sqrt{s} = 7$  TeV

<sup>3</sup>The FONLL (Fixed Order plus Next-to-Leading Logarithms) is a code for calculating double-differential, single inclusive heavy-quark production cross sections in pp, p $\bar{p}$  and (electro)photoproduction.

Fit type	$BR \cdot d\sigma^{\Upsilon(1S)}/dy$ (nb)
Power-law	$0.920 \pm 0.057$
Logarithmic	$0.937 \pm 0.057$
FONLL lower	$0.932 \pm 0.056$
FONLL central	$0.946 \pm 0.057$
FONLL upper	$0.941 \pm 0.057$

Table 8.16: Interpolated  $\Upsilon(1S)$  cross section at midrapidity obtained with the power-law, logarithmic and FONLL fits.

[89]. Taking advantage of this fact, the strategy to obtain the reference in the Muon Spectrometer acceptance can be summarized as follows:

- test PYTHIA 6.4  $\Upsilon(1S)$  production with different settings against data at 7 TeV from the LHC experiments;
- use the successful settings to make PYTHIA 6.4 productions at  $\sqrt{s} = 2.76$  TeV;
- normalize the generated rapidity distribution at 2.76 TeV to the mid-rapidity value estimated in Sec. 8.7.1;
- combine the predictions obtained with the different settings in the rapidity bins used in the analysis.

### Test at 7 TeV

The bottomonium production is made with PYTHIA 6.4 using the Color Singlet Model (CSM) [44] and the non-relativistic QCD (NRQCD) which allows to produce all the resonances taking into account the feed-down from higher masses [186].

In order to test the ability of PYTHIA 6.4 in reproducing the rapidity distribution at  $\sqrt{s} = 7$  TeV, different parton distribution functions (PDF) available in the framework and different tunings are tested<sup>4</sup>. For each simulation  $80 \cdot 10^3$  bottomonium events are generated in the rapidity range  $0 < y < 5.5$ .

The  $\Upsilon(1S)$  measurements in pp collisions at  $\sqrt{s} = 7$  TeV by CMS [89] and LHCb [83] (confirmed by ALICE, as reported in Sec. 3.2.2) are chosen to test the PYTHIA 6.4 predictions in the widest possible rapidity range. The procedure for this test is:

- the rapidity distributions of the generated  $\Upsilon$  are rebinned in the same binning of the experimental data;

<sup>4</sup>The PDF considered for this test are CTEQ5L [187], CTEQ6l and CTEQ6ll [188].

- the ratio between the data and the simulation is fitted with a zero-order polynomial function;
- the  $\chi^2$  of the fit is used as a measure of how compatible the generated distributions are with the measured ones.

A choice of  $\chi^2/\text{ndf} < 1.5$  is adopted as the limit for accepting the fit. In Fig. 8.17, the simulated rapidity distributions that passed the test are multiplied by the normalization parameter obtained from the fit and then plotted together with the experimental points for a visual comparison.

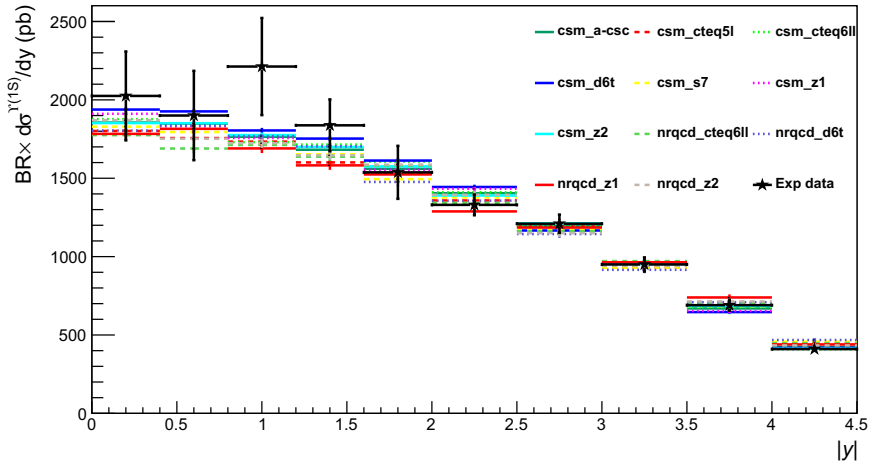


Figure 8.17:  $d\sigma^{\Upsilon(1S)}/dy$  obtained with PYTHIA 6.4 productions and measured by CMS and LHCb experiments in pp collisions at  $\sqrt{s} = 7$  TeV.

### Cross section at 2.76 TeV at forward rapidity

The extrapolation from midrapidity to forward rapidity is performed by combining the results obtained simulating bottomonium states at  $\sqrt{s} = 2.76$  TeV with the settings that passed the test at 7 TeV. The rapidity distributions are normalized to the midrapidity cross section evaluated in Sec. 8.7.1. The cross section in the Muon Spectrometer acceptance is computed in the same rapidity bins used in this analysis.

In Tab. 8.17 the combined results at forward rapidity are reported multiplied by the branching ratio. The value is the average of those obtained with the various  $\Upsilon$  productions. The statistical uncertainty, not reported in the table, is less than 1% and it is related to the number of bottomonium particles generated. The first systematic uncertainty is associated to the extrapolation from midrapidity to forward rapidity and is evaluated as the difference between the average and the maximum and minimum values

of the predictions obtained with the various settings, thus leading to an asymmetric component. The second uncertainty (*norm.* in the table) is instead related to the normalization to the midrapidity point. The former is considered uncorrelated versus rapidity, while the latter is correlated.

Rapidity	$BR \cdot d\sigma^{\Upsilon(1S)}/dy$ (nb) value $\pm$ extrap. $\pm$ norm.
2.5 – 4	$0.310^{+0.047(15\%)}_{-0.030(10\%)} \pm 0.027(9\%)$
2.5 – 3.2	$0.427^{+0.040(9\%)}_{-0.030(7\%)} \pm 0.037(9\%)$
3.2 – 4	$0.208^{+0.052(25\%)}_{-0.030(14\%)} \pm 0.017(9\%)$

Table 8.17: Combined results for  $BR \cdot d\sigma^{\Upsilon(1S)}/dy$  in pp collisions at  $\sqrt{s} = 2.76$  TeV at forward rapidity.

Fig. 8.18 shows the obtained values along with the CMS measurements, as comparison.

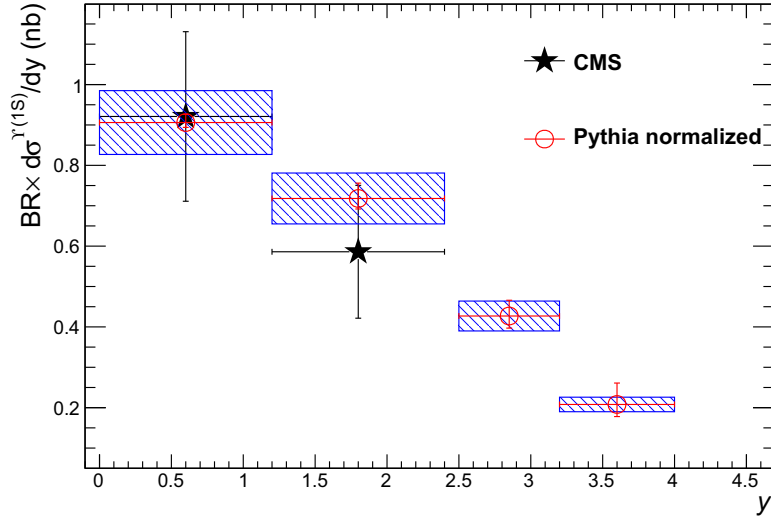


Figure 8.18: Final cross section values plotted with CMS data points at midrapidity. The error bars represent the extrapolation uncertainty, while the boxes represent the normalization one.

## 8.8 Summary of the uncertainties

In Tab. 8.18 a summary of the statistical uncertainties is given. The signal extraction represents the most important source.

Source	Centrality	Rapidity
$N_{MB}$	0.04%	0.04%
Signal extraction <sup>5</sup>	18%–22%	18%–23%
$A \times \varepsilon$	0.6%	0.3%
pp normalization	< 1%	< 1%
Total	18%–22%	18%–23%

Table 8.18: Summary of the statistical uncertainties.

All the systematic uncertainties are shown in Tab. 8.19, distinguishing the uncorrelated (U) and the correlated (C) sources. The cross section gives the highest contribution.

Source		Centrality		Rapidity	
$T_{AA}$		3%–4%	U	3%	C
$N_{MB}$		4%	C	4%	C
Signal extraction	bkg. description	5%–6%	U	4%–7%	U
	mass position	0.3%–1%	U	1%–5%	U
	signal width	0.3%–0.6%	U	0.4%–1%	U
	tail parameters	2%–3%	U	3%–4%	U
	$p \times DCA$ cut	0.3%	U	0.1%–0.7%	U
	total	5%–6%	U	5%–11%	U
$p_T$ and $y$ MC parametrizations		4%	C	5%–7%	U
Detector response	tracking eff.	10%	C	9%–11%	U
	trigger eff.	2%	C	2%	U
	matching eff.	1%	C	1%	U
	total	10%	C	9%–11%	U
pp reference	normalization	9%	C	9%	C
	extrapolation	+15% –10%	C	+9% –7% +25% –14%	U

Table 8.19: Summary of the systematic uncertainties.

The systematic uncertainty on the number of MB events is considered correlated even for the centrality dependence. In fact it arises from the  $F_{norm}$  factor which is centrality independent.

<sup>5</sup>It is 15% for the integrated statistics.

## 8.9 Nuclear modification factor

In this section the nuclear modification ( $R_{AA}$ ) factor values are presented.

### 8.9.1 Method

#### Yield

The yield of  $\Upsilon(1S)$  per unit of rapidity is defined as:

$$\frac{dY_{\Upsilon(1S)}}{dy} = \frac{N_{\Upsilon(1S)}}{BR \cdot N_{MB} \cdot (A \times \varepsilon) \cdot \Delta y} \quad (8.11)$$

- $N_{\Upsilon(1S)}$  is the number of  $\Upsilon(1S)$  obtained in Sec. 8.4. It depends on the considered centrality or rapidity bin.
- $BR$  is the  $\Upsilon(1S) \rightarrow \mu^+ \mu^-$  branching ratio ( $2.48 \pm 0.05\%$ ) [2]. In what follows, its small uncertainty is neglected.
- $N_{MB}$  is the number of minimum bias Pb–Pb events. It can be obtained from the number of collected CMUL triggers for each centrality class as described in Sec. 8.3.1. Values do not depend on rapidity.
- $A \times \varepsilon$  is the acceptance and efficiency correction factor described in Sec. 8.5.1. It depends on the considered centrality and rapidity bin.
- $\Delta y$  is the rapidity bin width. It is 1.5 if integrated, while it is 0.7 for  $2.5 < y < 3.2$  and 0.8 for  $3.2 < y < 4$  ranges.

The differential yield values are given in Tab. 8.20. The statistical and systematic uncertainties are obtained by summing in quadrature the contribution of each source of Eq. 8.11.

Centrality	Rapidity	Differential yield in $10^{-5}$ value $\pm$ stat. $\pm$ uncorr. $\pm$ corr.
0%–90%	2.5 – 4	$3.44 \pm 0.51(15\%) \pm 0.18(5\%) \pm 0.40(12\%)$
0%–20%	2.5 – 4	$8.07 \pm 1.76(22\%) \pm 0.48(6\%) \pm 0.93(12\%)$
20%–90%		$2.11 \pm 0.40(19\%) \pm 0.12(6\%) \pm 0.24(12\%)$
0%–90%	2.5 – 3.2	$4.53 \pm 0.82(18\%) \pm 0.57(13\%) \pm 0.16(4\%)$
	3.2 – 4	$2.35 \pm 0.53(23\%) \pm 0.38(16\%) \pm 0.08(4\%)$

Table 8.20:  $\Upsilon(1S)$  yields per unit of rapidity.

## Normalization

The nuclear modification factor presented in Eq. 8.12 allows to estimate the relative production of the  $\Upsilon(1S)$  in Pb–Pb collisions with respect to that in pp at the same center-of-mass energy. It is obtained by normalizing the  $\Upsilon(1S)$  Pb–Pb yield per unit of rapidity (Eq. 8.11) to the average nuclear overlap function ( $\langle T_{AA} \rangle$ ) of the considered centrality class (Sec. 8.3.2) and the pp  $y$ -differential cross section presented in Sec. 8.7:

$$R_{AA} = \frac{\frac{dY_{\Upsilon(1S)}}{dy}}{\langle T_{AA} \rangle \cdot \frac{d\sigma_{pp}}{dy}} \quad (8.12)$$

The yield depends on rapidity and centrality, while the nuclear overlap function depends only on centrality and the reference cross section only on rapidity. It is thus possible to obtain the  $R_{AA}$  in the centrality and rapidity bins considered so far.

## 8.9.2 Results

### Centrality dependence

The inclusive  $\Upsilon(1S)$   $R_{AA}$  measured by ALICE at  $\sqrt{s_{NN}} = 2.76$  TeV in the range  $2.5 < y < 4$  and  $p_T > 0$  is shown in Fig. 8.19 as a function of  $\langle N_{part} \rangle$ . The statistical uncertainties (bars) are of the same order than the correlated uncertainties (empty boxes) and dominate the uncorrelated systematics (filled boxes).

Values reported in Tab. 8.21 indicate a clear  $\Upsilon(1S)$  suppression which increases with the centrality of the collisions.

Centrality	$\langle N_{part} \rangle$	$R_{AA}$ value $\pm$ stat. $\pm$ uncorr. $\pm$ corr.
0%–90%	125	$0.438 \pm 0.065(15\%) \pm 0.027(6\%)_{-0.076(17\%)}^{+0.092(21\%)}$
0%–20%	308	$0.341 \pm 0.075(22\%) \pm 0.023(7\%)_{-0.059(17\%)}^{+0.072(21\%)}$
20%–90%	72	$0.634 \pm 0.120(19\%) \pm 0.044(7\%)_{-0.111(17\%)}^{+0.133(21\%)}$

Table 8.21:  $R_{AA}$  numerical values as a function of the centrality (average number of participants is also reported).

### Rapidity dependence

The  $\Upsilon(1S)$   $R_{AA}$  integrated on centrality (0%–90%) measured by ALICE at  $\sqrt{s_{NN}} = 2.76$  TeV is shown in Fig. 8.20 and reported in Tab. 8.22 for two rapidity bins ( $2.5 < y < 3.2$  and  $3.2 < y < 4$ ) and for  $p_T > 0$ .

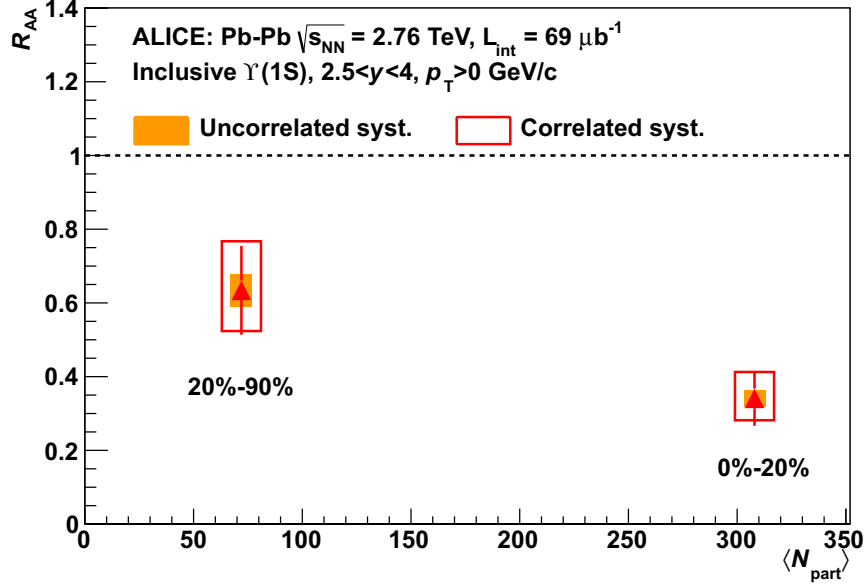


Figure 8.19:  $\Upsilon(1S)$  inclusive  $R_{AA}$  as a function of the average number of participants.

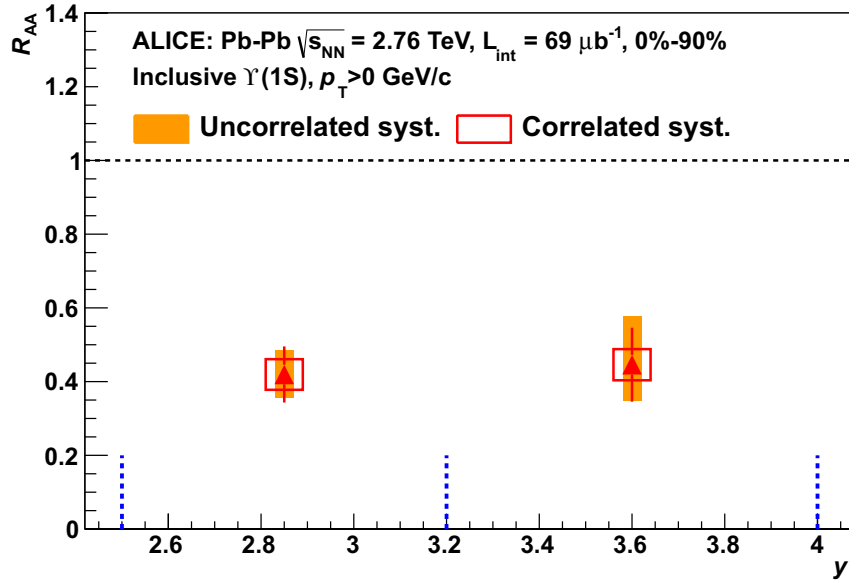


Figure 8.20:  $\Upsilon(1S)$  inclusive  $R_{AA}$  as a function of the rapidity. Vertical dashed blue lines represent the rapidity bin widths.

In the first bin the statistical uncertainty (bars) dominates the others, while in the second bin the uncorrelated systematics (filled boxes) gives the highest contribution. In both cases the correlated uncertainties represent the smallest component. No clear rapidity dependence is observed within the errors.

Rapidity	$R_{AA}$	
	value $\pm$ stat. $\pm$ uncorr. $\pm$ corr.	
2.5 – 3.2	$0.419 \pm 0.076(18\%)$	$^{+0.066(16\%)}_{-0.061(15\%)} \pm 0.042(10\%)$
3.2 – 4	$0.446 \pm 0.100(23\%)$	$^{+0.133(30\%)}_{-0.097(22\%)} \pm 0.043(10\%)$

Table 8.22:  $R_{AA}$  numerical values as a function of rapidity.

## 8.10 Central-to-peripheral ratio

The central-to-peripheral ratio ( $R_{CP}$ ) is defined as the ratio between the  $R_{AA}$  as a function of the centrality and its most peripheral value. Since the reference pp cross section does not depend on centrality, it does not participate into the ratio and most of the systematic uncertainties are cancelled out.

In this particular case, having only two  $R_{AA}$  points, the  $R_{CP}$  can be written as:

$$R_{CP} = \frac{\left[ \frac{N_{\Upsilon}}{N_{MB} \cdot T_{AA} \cdot A \times \varepsilon} \right]_{0\% - 20\%}}{\left[ \frac{N_{\Upsilon}}{N_{MB} \cdot T_{AA} \cdot A \times \varepsilon} \right]_{20\% - 90\%}} = 0.538 \pm 0.156(29\%) \pm 0.086(17\%) \quad (8.13)$$

where the first uncertainty is statistical and the second one is systematic.

In conclusion, it is possible to affirm that a clear suppression of the  $\Upsilon(1S)$  production is observed in Pb–Pb collisions with respect to pp ones. The suppression increases with the collision centrality, while it is rather independent on rapidity.

## Chapter 9

# Discussion and comparison of the results

The results shown in the previous chapter are now compared to the  $J/\psi$  production at forward rapidity measured by ALICE, to the  $\Upsilon$  measurements made by CMS and finally to theoretical models.

### 9.1 Comparison to the $J/\psi$ $R_{AA}$ measured at forward rapidity by ALICE

The observed inclusive  $\Upsilon(1S)$   $R_{AA}$  is compared to the ALICE inclusive  $J/\psi$  measurements in the same kinematic window [68]. In Fig. 9.1 the results are shown as a function of the average number of participating nucleons. Considering the large uncertainties on the  $\Upsilon(1S)$  values, the suppression is similar for the two mesons.

Fig. 9.2 presents the  $\Upsilon(1S)$  and  $J/\psi$   $R_{AA}$  as a function of the rapidity. Both results are integrated over the 0%–90% centrality range. No different behaviour is observed at very forward rapidity values.

The comparison of the data with theory suggests an important contribution of  $J/\psi$  regeneration in Pb–Pb collisions at  $\sqrt{s_{NN}} = 2.76$  TeV for the most central collisions at low- $p_T$  [68, 189], while for the  $\Upsilon(1S)$  it is expected to be much less important. Moreover, heavier bottomonium states contribute with their decays to the inclusive  $\Upsilon(1S)$  yield and their dissociation affects the measured suppression [113]. This feed-down contribution to the  $\Upsilon(1S)$  is measured to be about 50% [75, 190], although in a different kinematic range.

Due to the interplay of all these mechanisms, it is difficult to provide a definitive interpretation of the similarity between the two patterns.

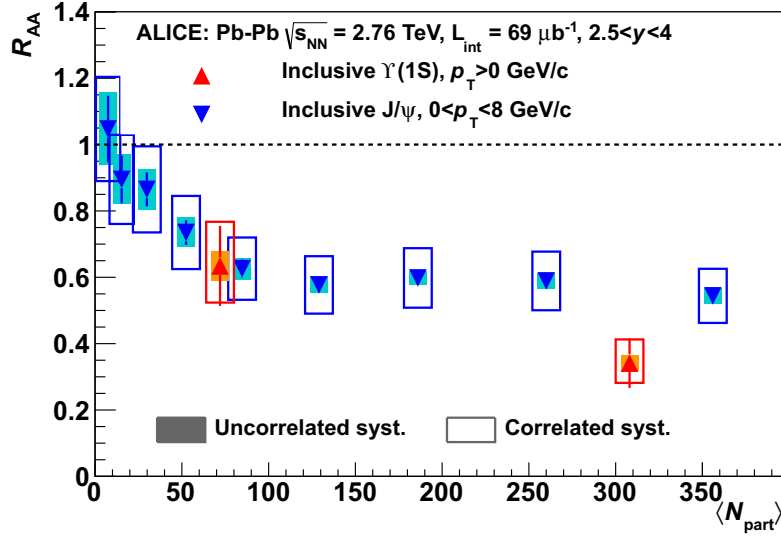


Figure 9.1: Comparison of ALICE  $\Upsilon(1S)$  and  $J/\psi$  inclusive  $R_{AA}$  in the same kinematic window as a function of the average number of participants.

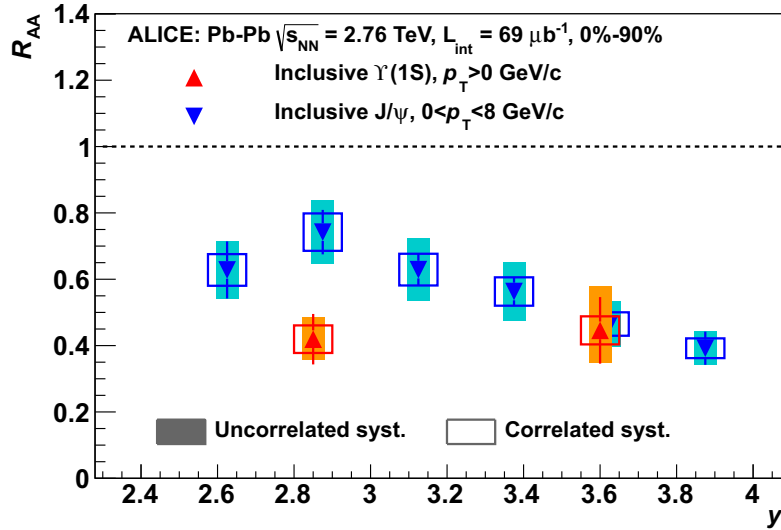


Figure 9.2: Comparison of ALICE  $\Upsilon(1S)$  and  $J/\psi$  inclusive  $R_{AA}$  in the same kinematic window as a function of the rapidity.

## 9.2 Comparison to the CMS results

The ALICE inclusive  $\Upsilon(1S)$   $R_{AA}$  measured in the  $2.5 < y < 4$  rapidity range is compared to the CMS results obtained in  $|y| < 2.4$  [113]. It is important to underline that both experiments are able to measure  $\Upsilon(1S)$  down to  $p_T = 0$ .

The comparison of  $R_{AA}$  as a function of the average number of participating nucleons is shown in Fig. 9.3 on the left side. The suppression at forward rapidity measured by ALICE is similar to the results obtained at midrapidity by CMS.

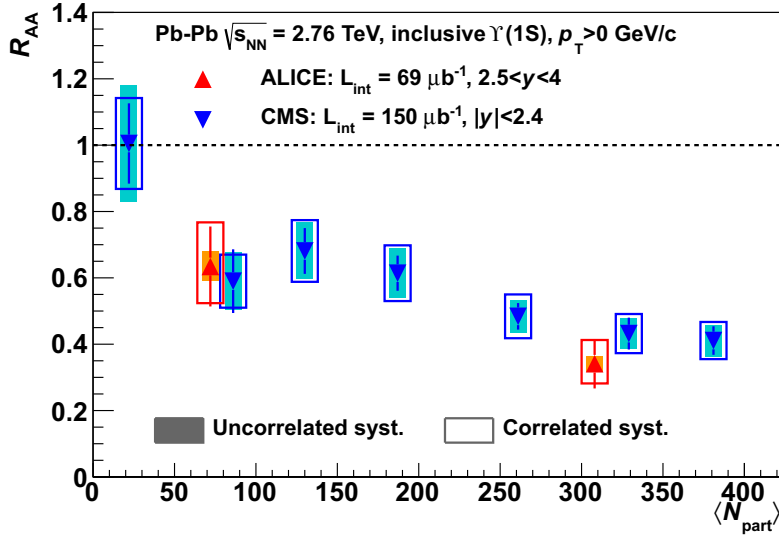


Figure 9.3: Comparison of ALICE and CMS  $\Upsilon(1S)$  inclusive  $R_{AA}$  as a function of the average number of participants.

The ALICE and CMS results as a function of rapidity are compared in Fig. 9.4. CMS data are integrated on the 0%–100% centrality range, while ALICE data are integrated on the 0%–90%. The  $\Upsilon(1S)$  suppression does not differ in this wide rapidity range.

For a better understanding of these results, it might be useful to have a look to the comparison of the inclusive  $J/\psi$   $R_{AA}$  measured by the two experiments [70, 189]. This is done in Fig. 9.5 as a function of the number of participants. On top of the different rapidities, it has to be pointed out that the  $p_T$  ranges are not the same: in both plots CMS quotes the results in the interval  $6.5 < p_T < 30$  GeV/c, while ALICE between 0 and 8 GeV/c on the left side and restricts the measurements between 5 and 8 GeV/c on the right side. In the first case, in a very different kinematic domain, CMS shows a suppression stronger than ALICE, with hints of a flat trend

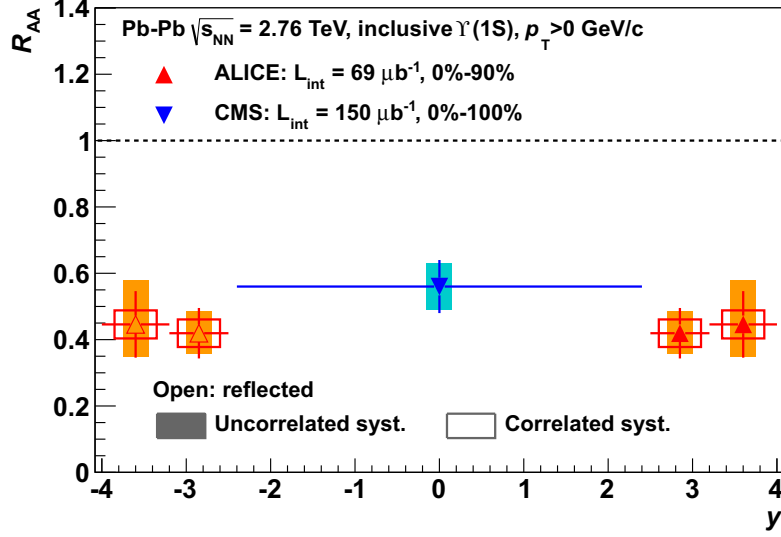


Figure 9.4: Comparison of ALICE and CMS  $\Upsilon(1S)$  inclusive  $R_{AA}$  as a function of the rapidity.

in central collisions. It is worth to recall that at forward rapidity models predict an important regeneration component at low- $p_T$ , up to  $\sim 4$  GeV/c (see Fig. 2.12) [71]. In a closer  $p_T$  range, as in the right plot, the two measurements are quite similar, as it happens for the  $\Upsilon(1S)$ .

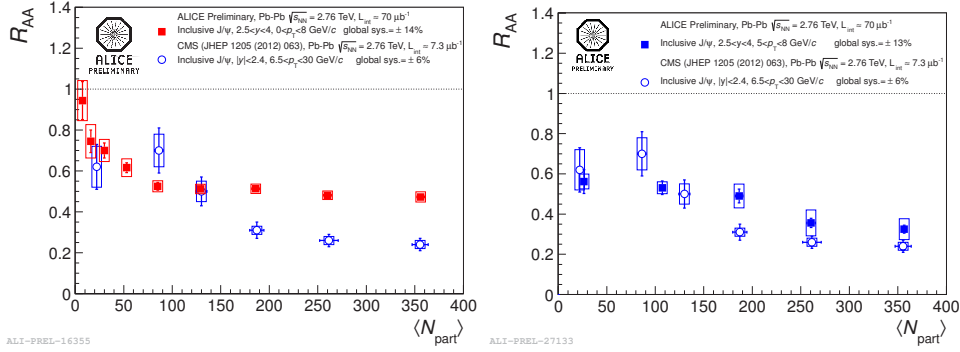


Figure 9.5: Comparison of CMS [70] and ALICE [189]  $J/\psi$   $R_{AA}$  as a function of the centrality of the collisions. The ALICE measurement in the left plot goes down to  $p_T = 0$ , while in the right plot is between 5 and 8 GeV/c.

## 9.3 Comparison to theoretical predictions

### Hydrodynamic formalism

The observed inclusive  $\Upsilon(1S)$   $R_{AA}$  values as a function of centrality and rapidity are now compared in Fig. 9.6 and 9.7 to the theoretical predictions made by M. Strickland based on a hydrodynamic formalism [94] already introduced in Sec. 3.4.1. Considering the calculated values for boost-invariant plateau with limited fragmentation, the experimental data shows a reasonable agreement with the minimum value of shear viscosity ( $4\pi\eta/s = 1$ ). It has to be noted that at midrapidity, instead, the CMS point seems to indicate a bigger value of viscosity.

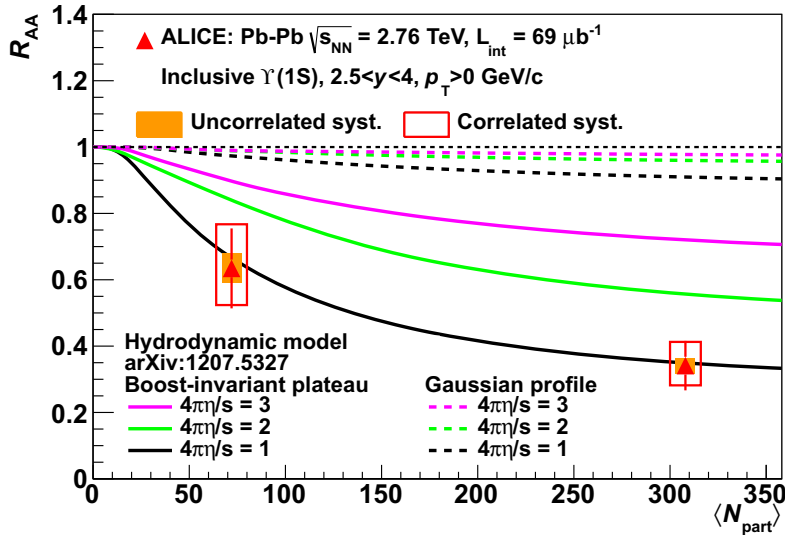


Figure 9.6: Comparison of ALICE  $\Upsilon(1S)$  inclusive  $R_{AA}$  with theoretical predictions by M. Strickland [94] as a function of the average number of participants.

### Rate equation approach

The results on the nuclear modification factor can be also compared to the theoretical predictions by A. Emerick et al. [108] described in Sec. 3.4.1 based on a rate equation approach (Fig. 9.8 and 9.9). The ALICE data are reasonably reproduced, although the model slightly underestimates the suppression in more central collisions. It could be interpreted as an observed  $\Upsilon(1S)$  regeneration smaller than the predictions. The model tends to indicate that the directly produced  $\Upsilon(1S)$  are not significantly suppressed and the observed  $R_{AA}$  is compatible with the suppression of higher mass

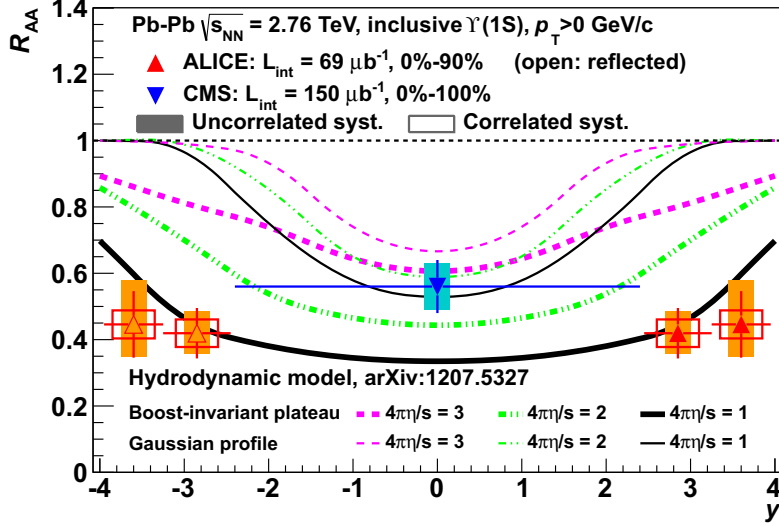


Figure 9.7: Comparison of ALICE  $\Upsilon(1S)$  inclusive  $R_{AA}$  with theoretical predictions by M. Strickland [94] as a function of rapidity with the CMS measurement.

states. The same model describes the CMS data as well [108].

For the moment no model can be discharged. More statistics is needed and the analysis of the 2013 pPb and Pbp data will help to understand the effective contribution of the cold nuclear matter on the observed suppression.

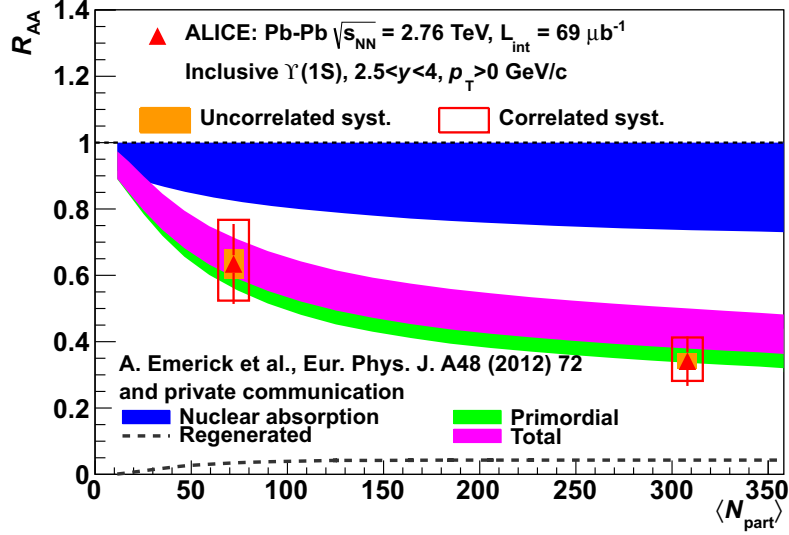


Figure 9.8: Comparison of ALICE  $\Upsilon(1S)$  inclusive  $R_{AA}$  with theoretical predictions by A. Emerick et al. [108] as a function of the average number of participants.

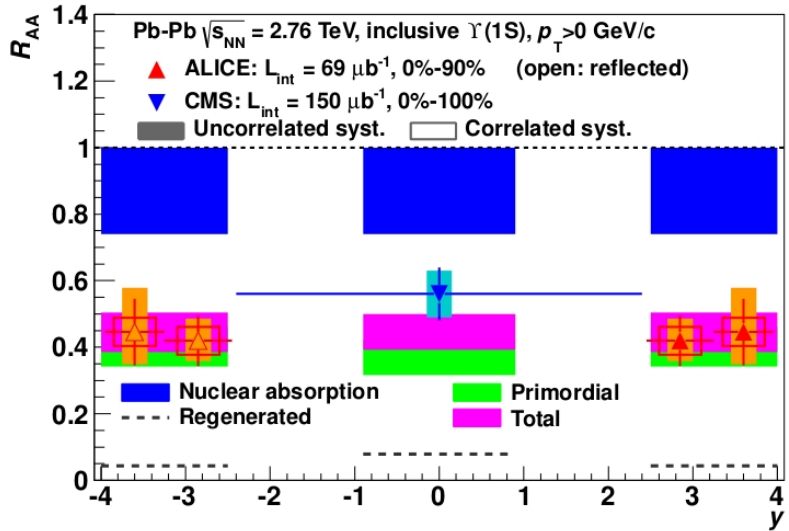


Figure 9.9: Comparison of ALICE  $\Upsilon(1S)$  inclusive  $R_{AA}$  with theoretical predictions by A. Emerick et al. [108] as a function of rapidity.

## Chapter 10

# Conclusions and outlook

In this thesis the data collected by the ALICE forward Muon Spectrometer in Pb–Pb collisions at  $\sqrt{s_{NN}} = 2.76$  TeV have been analysed in order to study the Muon Trigger cluster size, other related performance and the  $\Upsilon$  production.

### 10.1 Muon Trigger cluster size

The cluster size of the Muon Trigger has been measured in both the bending and the non-bending directions for the different strip pitches. The average value strongly depends on the strip widths: it ranges from 1.1 for the strips of 4 cm to 2.1 for those of 1 cm. The cluster size is found to be on average independent to the detection plane, while little dependences can be appreciated between different RPC: they can be explained considering the small intrinsic differences of each chamber. The flat time dependence of the cluster size and the same values measured in Pb–Pb and pp collisions indicate a satisfying performance of the Muon Trigger apparatus throughout the first years of data taking.

The old `AliMUONResponseTriggerV1` class never used in official simulations has been modified in order to reproduce the actual cluster size and a new and most efficient procedure for retrieving the high voltage of each RPC is now implemented. The results are satisfactory, but there is still room for improvement. Thanks to the new code, the Muon Trigger response is now better reproduced in Monte Carlo productions.

### 10.2 Muon Trigger performance

Analysing the performance of the Muon Trigger in Pb–Pb collisions at  $\sqrt{s_{NN}} = 2.76$  TeV of 2010 and 2011 data taking, it is possible to conclude that the detector shows a stable behaviour during the time, the RPC are operating with a high level of performance, the trigger decision algorithm is

efficient and selective and finally the Muon Trigger is efficient in rejecting hadrons and low  $p_T$  muons detected by the Muon Tracking. It actually acts as a muon identifier.

### 10.3 $\Upsilon$ production

The inclusive  $\Upsilon(1S)$  nuclear modification factor has been measured in the  $2.5 < y < 4$  rapidity range down to  $p_T = 0$ . The integrated  $R_{AA}$  value is  $0.438 \pm 0.065 \pm 0.027^{+0.092}_{-0.076}$  implying a significant suppression. Considering the 50% of feed-down from higher mass states measured by CDF [75] and the recent observations of the strong  $\Upsilon(2S)$  and  $\Upsilon(3S)$  suppression made by CMS[113], most of the observed suppression could be due to the heavier  $b\bar{b}$  bound states. Moreover, hints of an increasing suppression from the semi-peripheral to the central collisions are observed, while no significant dependence of the nuclear modification factor on rapidity is highlighted.

The  $R_{AA}$  as a function of both rapidity and centrality is similar to the measurements done for the  $J/\psi$  by ALICE in the same kinematic window. This observation can be interpreted taking into account the high regeneration of  $J/\psi$  expected at the LHC energies and the  $\Upsilon$  feed-down.

The comparison with the CMS results at midrapidity highlights an unexpected rather small rapidity suppression dependence over a large range.

Finally, theoretical predictions based on an anisotropic hydrodynamic formalism [94] and rate equation approach including a small regeneration and cold nuclear matter effects [108] describe reasonably well the data.

A better understanding of the  $\Upsilon$  production in heavy-ion collisions would require a precise estimate of the feed-down contribution from higher mass states and the measurement of the  $R_{AA}$  of the other bottomonium mesons ( $\Upsilon(2S)$  and  $\Upsilon(3S)$ ) in the kinematic window reachable with the ALICE Muon Spectrometer. In order to achieve this second purpose, a substantially larger integrated luminosity and a better mass resolution are needed.

The ongoing ALICE analysis of the 2013 pPb and PbPb data taking will allow to evaluate the cold nuclear matter component in the observed suppression.

# Appendix A

## Fitting functions

### A.1 Crystal Ball function

The Crystal Ball function consists of a Gaussian core portion and a power-law tail at low mass defined by the parameters  $\alpha$  and  $n$  for reproducing the non Gaussian fluctuation due to energy loss and multiple scattering effects:

$$f(x; N, \mu, \sigma, \alpha, n) = N \cdot \begin{cases} e^{-\frac{(x-\mu)^2}{2\cdot\sigma^2}} & \text{if } \frac{x-\mu}{\sigma} > -\alpha \\ A \cdot (B - \frac{x-\mu}{\sigma})^{-n} & \text{if } \frac{x-\mu}{\sigma} \leq -\alpha \end{cases} \quad (\text{A.1})$$

where:

$$A = \left(\frac{n}{|\alpha|}\right)^n \cdot e^{-\frac{|\alpha|^2}{2}} \quad B = \frac{n}{|\alpha|} - |\alpha|$$

### A.2 Extended Crystal Ball function

The signal shape in  $\Upsilon$  simulations can not be fully reproduced by the Crystal Ball function described above, as shown in Fig. 8.12. For this reason a new function is defined including a second power-law tail in the high mass region:

$$f(x; N, \mu, \sigma, \alpha, n, \alpha', n') = N \cdot \begin{cases} e^{-\frac{(x-\mu)^2}{2\cdot\sigma^2}} & \text{if } -\alpha \leq \frac{x-\mu}{\sigma} < \alpha' \\ A \cdot (B - \frac{x-\mu}{\sigma})^{-n} & \text{if } \frac{x-\mu}{\sigma} < -\alpha \\ C \cdot (D + \frac{x-\mu}{\sigma})^{-n'} & \text{if } \frac{x-\mu}{\sigma} \geq \alpha' \end{cases} \quad (\text{A.2})$$

where:

$$A = \left(\frac{n}{|\alpha|}\right)^n \cdot e^{-\frac{|\alpha|^2}{2}} \quad B = \frac{n}{|\alpha|} - |\alpha|$$

$$C = \left(\frac{n'}{|\alpha'|}\right)^{n'} \cdot e^{-\frac{|\alpha'|^2}{2}} \quad D = \frac{n'}{|\alpha'|} - |\alpha'|$$

Fig. A.1 shows some extended Crystal Ball functions obtained using the different sets of parameters reported in Tab. 8.12.

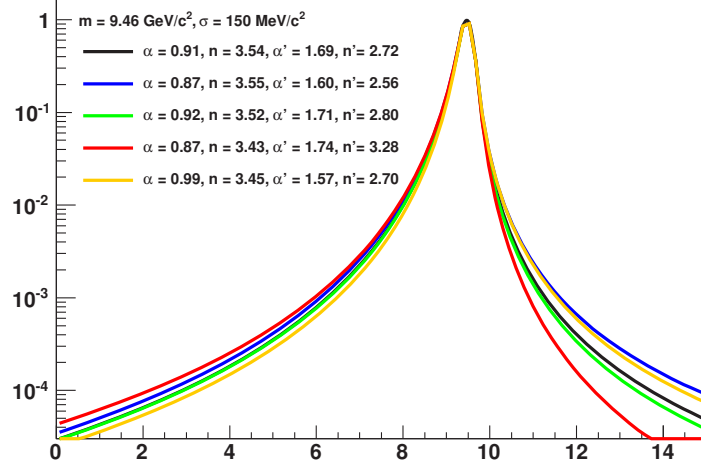


Figure A.1: Extended Crystal Ball shapes normalized to unity for different power-law parameters.

While with a Gaussian function an integral between  $\pm 3\sigma$  is enough to include almost the 100% of the signal, with an extended Crystal Ball the range has to be extended to  $\pm 25\sigma$  as shown in Tab. A.1 and in Fig. A.2

$\sigma$	Gaussian function	Extended Crystal Ball function
1	68.27%	53.91%
3	<b>99.73%</b>	86.79%
5	100%	93.85%
9	100%	97.82%
13	100%	98.94%
17	100%	99.40%
21	100%	99.62%
25	100%	<b>99.74%</b>

Table A.1: Percentage of the integral at  $\pm n\sigma$  for a Gaussian function and an extended Crystal Ball.

Assuming  $m = 9.46 \text{ GeV}/c^2$  and  $\sigma = 150 \text{ MeV}/c^2$  (values very close to the fit results reported in Sec. 8.4.2), the range at  $\pm 25\sigma$  would correspond to  $\sim 5.7 - 13.2 \text{ GeV}/c^2$ .

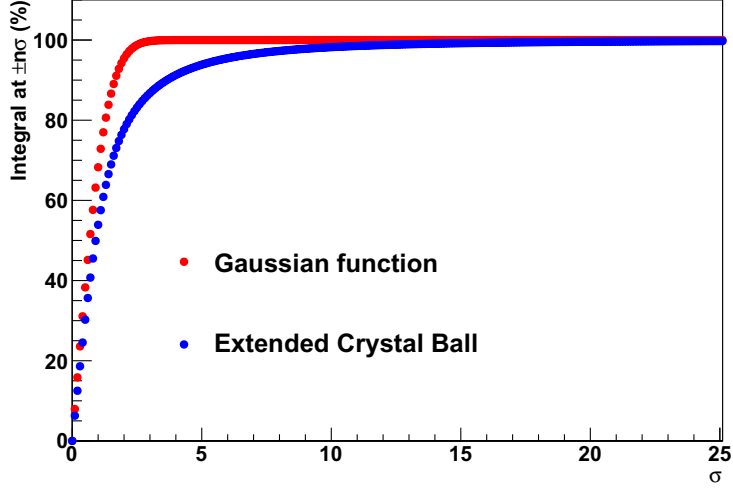


Figure A.2: Percentage of the integral at  $\pm n\sigma$  vs  $\sigma$  for a Gaussian function (in red) and an Extended Crystal Ball (in blue).

### A.3 Double exponential function

The function chosen for fitting the underlying continuum is a double exponential, i.e. a sum of two exponential functions:

$$f(x; \alpha, \beta, \gamma, \delta) = \alpha \cdot e^{\beta \cdot x} + \gamma \cdot e^{\delta \cdot x} \quad (\text{A.3})$$

### A.4 Double power-law function

A sum of two power-law functions is used to extract the systematic uncertainty affecting the signal extraction. It is defined as:

$$f(x; \alpha, \beta, \gamma, \delta) = \alpha \cdot x^{\beta} + \gamma \cdot x^{\delta} \quad (\text{A.4})$$

# Résumé

## Étude du plasma de quarks et gluons via la production à l'avant de bottomonium dans l'expérience ALICE au LHC

Les collisions d'ions lourds ultrarelativistes ont pour objectif principal l'étude des propriétés de la matière nucléaire soumise à températures et densités d'énergie extrêmes. La chromodynamique quantique (QCD) prédit, dans ces conditions, l'existence d'une nouvelle phase de la matière dans laquelle les constituants des hadrons sont déconfinés en un plasma de quarks et gluons (QGP). Les saveurs lourdes (charme et beauté) sont produites lors de processus durs aux premiers instants des collisions, avant de traverser le milieu. Par conséquent, la mesure des quarkonia (mésons  $c\bar{c}$  et  $b\bar{b}$ ) est particulièrement intéressante pour l'étude du QGP : leur dissociation, due notamment à l'écrantage de couleur, est sensible à la température initiale du système.

Les mesures effectuées au SPS et RHIC ont permis de mettre en évidence plusieurs caractéristiques du milieu produit, mais ont aussi laissé plusieurs questions sans réponse. Avec une énergie 14 fois supérieure à celle du RHIC, l'accélérateur LHC (Large Hadron Collider) au CERN, entré en fonctionnement fin 2009, a ouvert une nouvelle ère pour l'étude des propriétés du QGP.

ALICE (A Large Ion Collider Experiment) est une des quatre grandes expériences fonctionnant auprès du LHC et dont le but principal est l'étude du plasma de quarks et gluons produit dans les collisions d'ions plomb à une énergie de 2.76 TeV par nucléon. Elle enregistre aussi des collisions pp afin de fournir la référence indispensable pour l'étude des collisions noyau-noyau et proton-noyau et de tester les calculs perturbatifs de QCD dans la région des faibles valeurs de la variable d'échelle  $x$  de Bjorken.

Les quarkonia, ainsi que les saveurs lourdes ouvertes et les mesons légers, sont mesurés dans ALICE suivant leur mode de désintégration muonique avec le spectromètre à muons situé à petit angle polaire ( $2^\circ < \vartheta < 9^\circ$ ). Il est constitué d'un ensemble d'absorbeurs, d'un dipôle chaud, de cinq stations de trajectographie (Muon Tracking) et de deux stations de déclenchement

(Muon Trigger).

Le travail présenté dans cette thèse a été réalisé de 2011 à 2013 pendant les premières années de prise de données dans l'expérience ALICE. Après une introduction à la physique des ions lourds à hautes énergies et une description du setup expérimental, une étude des performances du Muon Trigger en Pb–Pb est proposée. En particulier, la stabilité dans le temps du détecteur et son efficacité de fonctionnement sont contrôlées. Le *cluster size*, correspondant au nombre moyen de voies adjacentes touchées par particule détectée, est étudié en fonction des différentes variables. Les valeurs expérimentales sont comparées à des simulations afin de fournir une paramétrisation de cet effet.

Finalement, la production du méson  $\Upsilon$  en collisions Pb–Pb est analysée en détail et comparée à celle en collisions pp à la même énergie. Les résultats obtenus sont comparés aux mesures du  $J/\psi$  par ALICE, aux mesures par CMS et à des prédictions de modèles théoriques.

**Mots clés :** plasma de quarks et gluons, quarkonium, LHC, expérience ALICE, spectromètre à muons, système de déclenchement, cluster size, suppression du  $\Upsilon$ .

# Abstract

## Probing the Quark-Gluon Plasma from bottomonium production at forward rapidity with ALICE at the LHC

The main goal of ultrarelativistic heavy-ion collisions is the study of the properties of the matter at very high temperatures and energy densities. Quantum chromodynamics (QCD) predicts in these conditions the existence of a new phase of the matter whose components are deconfined in a Quark-Gluon Plasma (QGP). Heavy quarks (charm e bottom) are produced in the first stages of the collisions, before to interact with the medium. Therefore, the measurement of the quarkonia ( $c\bar{c}$  and  $b\bar{b}$  mesons) is of particular interest for the study of the QGP: their dissociation mainly due to the colour screening is sensible to the initial temperature of the medium.

Previous measurements at the SPS and RHIC allowed to understand some characteristics of the system produced, but they also opened many questions. With an energy 14 times higher than RHIC, the LHC (Large Hadron Collider) at CERN opened a new era for the study of the QGP properties.

ALICE (A Large Ion Collider Experiment) is the LHC experiment fully dedicated to the study of the Quark-Gluon Plasma produced in Pb–Pb collisions at an energy of 2.76 TeV per nucleon. The experiment also participates to the proton-proton data taking in order to obtain the fundamental reference for the study of ion-ion and proton-ion collisions and for testing the predictions at very small Bjorken- $x$  values of the perturbative QCD.

Quarkonia,  $D$  and  $B$  mesons and light vector mesons are measured at forward rapidity by a Muon Spectrometer exploiting their (di)muonic decay. This detector is composed of a front absorber, a dipole magnet, five stations of tracking (Muon Tracking) and two stations of trigger (Muon Trigger).

The work presented in this thesis has been carried out from 2011 to 2013 during the first period of data taking of ALICE. After a detailed introduction of the heavy-ion physics and a description of the experimental setup, the performance of the Muon Trigger in Pb–Pb collisions are shown. A particular attention is devoted to the stability of the detector during the time

and to the trigger effectiveness. Moreover, the cluster size, corresponding to the number of adjacent strips hit by a particle, is studied as a function of different variables. The experimental results will be compared to simulations in order to obtain a good parametrization of this phenomenon.

Finally, the  $\Upsilon$  production in Pb–Pb collisions is carefully analysed and compared to that in pp collisions at the same energy. The results are then compared to the  $J/\psi$  measurements obtained by ALICE, to the CMS results and to some theoretical predictions.

**Keywords:** Quark-Gluon Plasma, quarkonium, LHC, ALICE experiment, Muon Spectrometer, trigger, cluster size,  $\Upsilon$  suppression.

# List of Figures

1.1	The fundamental particles predicted by the Standard Model.	2
1.2	Summary of $\alpha_s$ measurements as a function of the energy scale $Q$ [2]. . . . .	2
1.3	QCD phase diagram as predicted by lattice QCD calculations and with experimental points, adapted from [9, 10]. . . . .	4
1.4	Space-time evolution of an heavy-ion collision [19]. . . . .	6
1.5	Energy densities and temperatures expressed in units of $T_c$ for different collision energies [20]. . . . .	7
2.1	Charmonium decay modes with spectroscopy notation [43]. . . . .	11
2.2	The LO QCD processes for quarkonium production. . . . .	12
2.3	Comparison between CDF $J/\psi$ measurements (full circles) and CSM (dotted lines), CEM (dashed and dashed dotted lines) and NRQCD (solid line) predictions [45]. . . . .	13
2.4	Prompt polarization of $J/\psi$ (left) and $\psi(2S)$ (right) as a function of $p_T$ measured by CDF experiment compared to NRQCD predictions [54]. . . . .	14
2.5	Scale evolution of the ratios $R_G^A(x, Q^2)$ for a Pb nucleus and different values of $Q^2$ [59]. . . . .	17
2.6	Hadron yields in dAu collisions at $\sqrt{s_{NN}} = 200$ GeV normalized to pp collisions. Dashed line is the $R_{dAu}$ of inclusive charged hadrons [62]. . . . .	17
2.7	The $J/\psi$ and Drell-Yan cross section ratio vs the path length in nucleus ( $L$ ) divided by the normal nuclear absorption pattern for several collision systems [65]. . . . .	19
2.8	$J/\psi$ suppression pattern in In-In (circles) and Pb-Pb (triangles) from NA60 experiment [66]. . . . .	20
2.9	$J/\psi$ $R_{AA}$ at forward and midrapidity in Au–Au collisions measured by PHENIX as a function of the number of participants [67]. . . . .	20
2.10	Inclusive $J/\psi$ $R_{AA}$ measured by ALICE and PHENIX (left) and by CMS and PHENIX (right) [68, 70]. . . . .	21
2.11	Inclusive $J/\psi$ $R_{AA}$ measured by ALICE vs rapidity (left) and vs $p_T$ (right, with CMS points). . . . .	22

2.12	Inclusive $J/\psi$ $R_{AA}$ vs $p_T$ for two centrality bins. . . . .	22
3.1	Measured dimuon production cross sections as a function of the dimuon invariant mass. The peak of the $\Upsilon$ resonances is well visible at around $9.5 \text{ GeV}/c^2$ [72]. . . . .	23
3.2	Bottomonium decay modes with spectroscopy notation [43]. . . . .	25
3.3	Schema of the helicity frame. . . . .	26
3.4	$\Upsilon(1S)$ cross section as a function of the transverse momentum compared to LO NRQCD, CSM, CEM (left) and to NLO and NNLO CSM (right) [44, 78]. . . . .	27
3.5	Normalized differential cross sections for $\Upsilon(1S)$ production in different rapidity bins compared with theory predictions (left) and with CDF results (right) [76, 80]. . . . .	27
3.6	Left: polarization parameter $\alpha$ measured by DØ and CDF for $\Upsilon(1S)$ production compared with LO NRQCD. Right: polarization parameter $\alpha$ measured by DØ for $\Upsilon(2S)$ production [77]. . . . .	28
3.7	Collision energy dependence of the $\Upsilon$ cross section [81]. . . . .	29
3.8	Differential cross sections multiplied by the dimuon branching ratio as a function of $p_T$ (left) and $y$ (right) in pp collisions at 7 TeV [83]. . . . .	29
3.9	Differential $\Upsilon(1S)$ cross section times the dimuon branching ratio as a function of $p_T$ compared to NLO and NNLO CSM (left) and NLO NRQCD and CEM (right) [83]. . . . .	30
3.10	Differential cross sections multiplied by the dimuon branching ratio as a function of $p_T$ (left) and $y$ (right) in pp collisions at 8 TeV [84]. . . . .	30
3.11	Dimuon invariant mass distribution with fit functions (see text for more details). . . . .	31
3.12	$\Upsilon$ differential cross sections multiplied by the dimuon branching ratio as a function of $p_T$ (left) and rapidity (right) measured by ALICE and LHCb. . . . .	32
3.13	Double-differential cross sections of the $\Upsilon$ states as a function of $p_T$ (top plots and bottom left plot) and $y$ differential cross section (bottom right plot) compared to different theoretical predictions [86] (see text for more details). . . . .	33
3.14	Double-differential $\Upsilon$ cross sections vs $p_T$ in two bins of rapidity (top) and differential $\Upsilon$ cross sections vs rapidity (bottom) [88]. . . . .	34

3.15	Double-differential $\Upsilon(1S)$ cross sections in two rapidity bins. The solid band indicates the variation of the result due to spin-alignment uncertainty. In the lower panels NNLO CSM prediction of direct production and inclusive prediction from CEM are presented as the ratio to the data along with cross section measurements under four possible spin-alignment scenarios [88]. . . . .	35
3.16	Left: ratio of yields per nucleon vs A for $\Upsilon(1S)$ and $\Upsilon(2S + 3S)$ . Right: $\alpha$ dependence on $x_F$ [90]. . . . .	36
3.17	Left: Drell-Yan $\Upsilon$ cross section divided by the mass number A. Right: ratio $BR_{\mu\mu} \cdot \sigma_{\Upsilon}/\sigma_{DY}$ (full circles) and the cross section per nucleon $BR_{\mu\mu} \cdot \sigma_{\Upsilon}/A$ (open circles), always as a function of A [91]. . . . .	37
3.18	$\Upsilon$ cross section at midrapidity compared with the NLO CEM model prediction. The raw yield vs rapidity is shown by the red histogram [92]. . . . .	38
3.19	Top: $\Upsilon R_{dAu}$ as a function of rapidity measured by the PHENIX Collaboration compared to $J/\psi$ measurement and NLO EPS09 calculation for various cross section values. Bottom: $\alpha$ vs $x_F$ of $\Upsilon$ states measured by E772 and PHENIX [93]. . . . .	39
3.20	$\Upsilon R_{AA}$ as a function of the number of participants measured by STAR in Au–Au collisions and compared to the theoretical predictions introduced before [95, 108]. . . . .	41
3.21	Comparison of the $\Upsilon(1S)$ and $\Upsilon(2S)$ $R_{AA}$ centrality dependence with prompt $J/\psi$ measurements by CMS (left) and with the $\Upsilon(1S + 2S + 3S)$ results by STAR (right) [113]. . . . .	42
3.22	CMS $\Upsilon(1S)$ and $\Upsilon(2S)$ measurements compared to the hydrodynamic model (left) and to the rate equation approach (right) [113]. . . . .	43
4.1	Schematic view of the LHC, the SPS and of the four main experiments (ALICE, ATLAS, CMS and LHCb). . . . .	46
4.2	Schematic view of the ALICE experiment. . . . .	47
4.3	The ALICE coordinate system. . . . .	48
4.4	Layout of the ITS made of SPD, SDD and SSD. . . . .	49
4.5	Schematic view of the TPC setup. . . . .	50
4.6	Specific energy loss in the TPC as a function of momentum with superimposed Bethe-Bloch lines for various particle species. . . . .	50
4.7	Illustration of the space frame holding the 18 TRD super modules, surrounded by the TOF detector. . . . .	51
4.8	The seven HMPID modules on the TPC and TOF support. . . . .	52
4.9	Schematic view of the PHOS. . . . .	53

4.10	Layout of the EMCal. . . . .	54
4.11	Cosmic rays detected by ACORDE (on the upper faces of the magnet). . . . .	54
4.12	The Forward Multiplicity Detector. . . . .	55
4.13	A PMD prototype tested at CERN. . . . .	56
4.14	VZERO amplitude distribution fitted with a Glauber fit [128]. The centrality classes are indicated in the figure. The inset shows a zoom of the most peripheral region. . . . .	57
4.15	A view of the T0. . . . .	57
4.16	View of the ZDC apparatus close to the beam pipe. . . . .	58
4.17	General scheme of the AliRoot architecture. . . . .	62
5.1	Layout of the ALICE forward Muon Spectrometer. . . . .	67
5.2	Design of the front absorber. . . . .	68
5.3	View of the muon filter (left) and of the dipole magnet (right). . . . .	69
5.4	Tracking chambers with quadrant (left) and slat (right) layout. . . . .	70
5.5	Geometry Monitoring System setup: the lines on this figure represent the optical lines. . . . .	71
5.6	Simulation of average number of muons with $p_T > p_T^{min}$ at forward rapidity in central Pb–Pb collisions as a function of $p_T^{min}$ . . . . .	72
5.7	Layout of the ALICE Muon Trigger system. Different colours refer to the three strip widths, according to Tab. 5.1. . . . .	73
5.8	Cross section of a Resistive Plate Chamber. . . . .	75
5.9	Schematic view of the trigger principle. . . . .	77
5.10	Example of two signals in a RPC running in streamer mode: the streamer signal is often delayed with respect of the small precursor up to 15 ns. . . . .	78
5.11	View of one of the Muon Trigger planes showing the 18 RPC and the 234 local boards with their numbering. . . . .	80
5.12	Schematic design of the Muon Trigger electronics. . . . .	81
6.1	An example of cluster size distribution: the histogram refers to RPC 0, MT12, bending direction. Colours refer to the three strip widths. . . . .	84
6.2	Average cluster size as a function of the plane (top plots), of the RPC (middle plots) for MT11 and of the local board for RPC 17 and 4 in MT12 (bottom plots). The colours reflect the different strip widths. . . . .	86
6.3	Average cluster size as a function of the fill for plane MT12, $x$ -strips. The vertical dashed line separates the two years of data taking. . . . .	87

6.4	Comparison of the average cluster size measured in Pb–Pb collisions at $\sqrt{s_{NN}} = 2.76$ TeV (circles) and in pp collisions at $\sqrt{s} = 7$ TeV (triangles) and as a function of the plane in the bending (left) and non-bending direction (right). . . . .	88
6.5	Comparison of the measured cluster size distribution in Pb–Pb collisions (blue line) and the simulated one with the original <code>AliMUONResponseTriggerV1</code> class (green line). The plots refer to the different strip widths of RPC 0, MT11, bending plane. . . . .	90
6.6	Comparison of the measured cluster size distribution in Pb–Pb collisions (blue line) and the simulated one with the improved class (green line). The plots refer to the different strip widths of RPC 0, MT11, bending plane. . . . .	91
6.7	Measured cluster size (full points) compared to the simulated one with the new class (open symbols) as a function of the local board for the RPC 17 bending plane (left) and RPC 4 non-bending plane (right) of MT12. See the numbering in Fig. 5.11. . . . .	92
7.1	Single muon multiplicity as a function of the fill for four centrality classes. Vertical dashed red line separates the two years of data taking. . . . .	95
7.2	Strip multiplicity for MT11, bending plane as a function of the fill for four centrality classes. Vertical dashed red line separates the two years of data taking. . . . .	96
7.3	Number of muons satisfying the high- $p_T$ condition divided by the number of muons satisfying the low- $p_T$ condition, as a function of the $p_T$ . Left plot refers to Pb–Pb 2010 collisions, while the right one to 2011 collisions. Vertical dashed red lines indicate the $p_T$ at which the two curves reach the value of 0.5. . . . .	97
7.4	Comparison between data (red points) and simulations (blue points) of the Muon Trigger response as a function of $p_T$ for two sets of $p_T$ cuts. Black points in the low panels represent the ratios of the two sets of points. . . . .	98
7.5	Sketch of the possible effects of the cluster size in determining the track transverse momentum in the Muon Trigger. Orange rectangles represent the four trigger planes, the red lines a track and the black and blue crosses the hit strips. . . . .	99
7.6	Comparison between data (red points) and simulations (blue points) of the Muon Trigger efficiency as a function of $p_T$ for two sets of $p_T$ cuts. Black points in the low panels represent the ratios of the two sets of points. . . . .	99

7.7	Global trigger fraction relative to minimum bias collisions (trigger selectivity) as a function of the centrality for 2010 period (top plot, with high- $p_T$ threshold equal to 1 GeV/c) and for 2011 period (bottom plots, with low- $p_T$ threshold equal to 1 GeV/c on the left and high- $p_T$ threshold equal to 4 GeV/c on the right). Horizontal bars indicate the bin widths.	100
7.8	Ratios between the number of matched tracks and the number of tracks detected by the Muon Tracking as a function of the transverse momentum. Left plot refers to 2010, while the right one to 2011 period.	101
7.9	Top: composition of reconstructed tracks by the Muon Tracking (left) and fraction of hadrons (right), both without matching. Bottom: same plots including the matching cut.	102
8.1	Improvement of the mass position and resolution with the different alignment processes used to treat the data.	107
8.2	$F_{norm}$ as a function of the run number. Points are fitted with a constant function (dashed red line).	109
8.3	Dimuon invariant mass distribution after having applied the selection cuts.	112
8.4	Fit procedure applied in different centrality classes and rapidity ranges. The global function is represented by a red line. The green lines represent the three extended Crystal Ball, while the blue line describes the underlying continuum.	114
8.5	Number of $\Upsilon(1S)$ obtained fitting the integrated mass distribution with a double exponential (left) or with a double power-law function (right) in different fit ranges.	116
8.6	Number of $\Upsilon(1S)$ obtained from fits applied with different $\Upsilon(2S)$ and $\Upsilon(3S)$ mass positions.	118
8.7	Number of $\Upsilon(1S)$ obtained from fits applied with different $\Upsilon(2S)$ and $\Upsilon(3S)$ widths.	119
8.8	Top: shapes used to evaluate systematic uncertainties related to the choice of the tail parameters (see text for more details). Bottom: number of $\Upsilon(1S)$ obtained from fits. The value given in abscissa refers to a particular set of parameters.	120
8.9	Number of $\Upsilon(1S)$ at various $\sigma$ of $p \times DCA$ cut.	121
8.10	Run-by-run $A \times \varepsilon$ factor integrated on centrality and rapidity. Dashed red line indicates the integrated value.	124
8.11	$A \times \varepsilon$ factor as a function of the centrality (top), of the rapidity (bottom left) and of the $p_T$ (bottom right).	124
8.12	From top left to bottom right, integrated signal distribution from embedding production, distribution fitted with a Gaussian function, with a Crystal Ball and with an extend Crystal Ball.	125

8.13	Extended Crystal Ball parameters (see Eq. A.2) as a function of centrality (left) and rapidity (right). Values from the integrated distribution are shown in the red boxes. . . . .	126
8.14	Rapidity (left) and $p_T$ (right) parametrizations of the generated $\Upsilon(1S)$ used to evaluate the systematic uncertainties on $A \times \varepsilon$ . The distributions are normalized to the unity. . . . .	127
8.15	Energy dependence of the $\Upsilon(1S)$ cross section at midrapidity, with overlaid power-law (left) and logarithmic (right) fit functions. . . . .	130
8.16	Energy dependence of the $\Upsilon(1S)$ cross section at midrapidity, with overlaid FONLL predictions rescaled by the $\alpha$ parameter. The points corresponding to different predictions at the same energy are slightly shifted horizontally for visibility. . .	131
8.17	$d\sigma^{\Upsilon(1S)}/dy$ obtained with PYTHIA 6.4 productions and measured by CMS and LHCb experiments in pp collisions at $\sqrt{s} = 7$ TeV. . . . .	133
8.18	Final cross section values plotted with CMS data points at midrapidity. The error bars represent the extrapolation uncertainty, while the boxes represent the normalization one. . .	134
8.19	$\Upsilon(1S)$ inclusive $R_{AA}$ as a function of the average number of participants. . . . .	138
8.20	$\Upsilon(1S)$ inclusive $R_{AA}$ as a function of the rapidity. Vertical dashed blue lines represent the rapidity bin widths. . . . .	138
9.1	Comparison of ALICE $\Upsilon(1S)$ and $J/\psi$ inclusive $R_{AA}$ in the same kinematic window as a function of the average number of participants. . . . .	141
9.2	Comparison of ALICE $\Upsilon(1S)$ and $J/\psi$ inclusive $R_{AA}$ in the same kinematic window as a function of the rapidity. . . . .	141
9.3	Comparison of ALICE and CMS $\Upsilon(1S)$ inclusive $R_{AA}$ as a function of the average number of participants. . . . .	142
9.4	Comparison of ALICE and CMS $\Upsilon(1S)$ inclusive $R_{AA}$ as a function of the rapidity. . . . .	143
9.5	Comparison of CMS [70] and ALICE [189] $J/\psi$ $R_{AA}$ as a function of the centrality of the collisions. The ALICE measurement in the left plot goes down to $p_T = 0$ , while in the right plot is between 5 and 8 GeV/c. . . . .	143
9.6	Comparison of ALICE $\Upsilon(1S)$ inclusive $R_{AA}$ with theoretical predictions by M. Strickland [94] as a function of the average number of participants. . . . .	144
9.7	Comparison of ALICE $\Upsilon(1S)$ inclusive $R_{AA}$ with theoretical predictions by M. Strickland [94] as a function of rapidity with the CMS measurement. . . . .	145

9.8	Comparison of ALICE $\Upsilon(1S)$ inclusive $R_{AA}$ with theoretical predictions by A. Emerick et al. [108] as a function of the average number of participants. . . . .	146
9.9	Comparison of ALICE $\Upsilon(1S)$ inclusive $R_{AA}$ with theoretical predictions by A. Emerick et al. [108] as a function of rapidity.	146
A.1	Extended Crystal Ball shapes normalized to unity for different power-law parameters. . . . .	150
A.2	Percentage of the integral at $\pm n\sigma$ vs $\sigma$ for a Gaussian function (in red) and an Extended Crystal Ball (in blue). . . . .	151

# List of Tables

2.1	Quarkonium binding energies ( $\Delta E$ ), quark distance ( $r_0$ ) and dissociation temperatures in units of $T_c = 173$ MeV [58]. . . .	15
2.2	Number of heavy quark pairs produced in central heavy-ion collisions at different energies. . . . .	16
3.1	Summary of the most important characteristics of the three $\Upsilon$ states. The percentages near the decay modes are the branching ratios [2]. . . . .	24
5.1	Strip pitches of the Muon Trigger. . . . .	74
5.2	Illustrations of the declustering for bit patterns with a cluster size from $N = 1$ to $N = 5$ . More details on cluster size can be found in Chap. 6. . . . .	79
6.1	Percentage of tracks generating a cluster equal to 1, $\leq 2$ , $\leq 3$ or equal to 16 strips for the three pitches. The numbers refer to the integrated statistics. . . . .	85
6.2	Average cluster size values for the three strip widths. . . . .	85
7.1	Muon Trigger $p_T$ cuts adopted during the first two runs of Pb–Pb collisions. . . . .	94
7.2	Average number of detected muons per minimum bias collision as a function of the centrality. . . . .	95
7.3	Average number of hit strips as a function of centrality in the first Muon Trigger plane, bending direction. . . . .	96
7.4	Trigger selectivity for two extreme centrality ranges and different cuts. . . . .	101
8.1	Average number of binary collisions, participants and nuclear overlap function for the centrality classes considered in the analysis [127]. . . . .	109
8.2	Number of Pb–Pb minimum bias events. . . . .	110
8.3	Summary of the selections. . . . .	111

8.4	Mass position, width, signal-over-background ratio and significance of the $\Upsilon(1S)$ state from fits. Values are shown for the different centrality classes and the different rapidity ranges considered in the analysis. . . . .	115
8.5	Summary of the study on systematic uncertainties induced by the background function choice. . . . .	117
8.6	Summary of the study on systematic errors induced by the choice of the $\Upsilon(2S)$ and $\Upsilon(3S)$ mass position. . . . .	117
8.7	Summary of the study on systematic uncertainties induced by the choice of the $\Upsilon(2S)$ and $\Upsilon(3S)$ widths. . . . .	118
8.8	Summary of the study on systematic errors induced by the choice of the tail parameters. . . . .	121
8.9	Summary of the study on systematic errors induced by the choice of the $p \times DCA$ cut. . . . .	122
8.10	Overall results from signal extraction. The first uncertainty is statistical and the second one is systematic. . . . .	122
8.11	$A \times \varepsilon$ values in the various bins. . . . .	125
8.12	Values of the low-end tail parameters ( $\alpha, n$ ) and of the high-end tail parameters ( $\alpha', n'$ ) of the extended Crystal Ball function. . . . .	126
8.13	$A \times \varepsilon$ values for the different $p_T$ and $y$ parametrizations. . . . .	128
8.14	Systematic uncertainties on Muon Tracking, Muon Trigger and matching efficiency. . . . .	129
8.15	Experimental results used for the interpolation of the $\Upsilon(1S)$ cross section at midrapidity. . . . .	130
8.16	Interpolated $\Upsilon(1S)$ cross section at midrapidity obtained with the power-law, logarithmic and FONLL fits. . . . .	132
8.17	Combined results for $BR \cdot d\sigma^{\Upsilon(1S)}/dy$ in pp collisions at $\sqrt{s} = 2.76$ TeV at forward rapidity. . . . .	134
8.18	Summary of the statistical uncertainties. . . . .	135
8.19	Summary of the systematic uncertainties. . . . .	135
8.20	$\Upsilon(1S)$ yields per unit of rapidity. . . . .	136
8.21	$R_{AA}$ numerical values as a function of the centrality (average number of participants is also reported). . . . .	137
8.22	$R_{AA}$ numerical values as a function of rapidity. . . . .	139
A.1	Percentage of the integral at $\pm n\sigma$ for a Gaussian function and an extended Crystal Ball. . . . .	150

# Bibliography

- [1] M. E. Peskin et al. *An Introduction to Quantum Field Theory*. Addison-Wesley Publishing Company, 1995.
- [2] J. Beringer et al. Review of Particle Physics. *Phys. Rev. D*, 86, Jul 2012.
- [3] A. Pich. Aspects of Quantum Chromodynamics. *arXiv:hep-ph/0001118*, Jan 2000.
- [4] E. V. Shuryak. Quark-gluon plasma and hadronic production of leptons, photons and psions. *Phys. Lett. B*, 78(1):150–153, 1978.
- [5] E. V. Shuryak. Quantum chromodynamics and the theory of superdense matter. *Phys. Rep.*, 61(2):71–158, May 1980.
- [6] A. Chodos et al. New extended model of hadrons. *Phys. Rev. D*, (9):3471–3495, June 1974.
- [7] T. Hatsuda et al. QCD phenomenology based on a chiral effective Lagrangian. *Phys. Rep.*, 247(5–6):221–367, Oct 1994.
- [8] Z. Fodor et al. Critical point of QCD at finite  $T$  and  $\mu$ , lattice results for physical quark masses. *JHEP*, 2004(04), 2004.
- [9] M. Stephanov. QCD phase diagram: an overview. *Proceedings of Science*, LAT2006(024), 2006.
- [10] S. Hands. The Phase Diagram of QCD. *Contemp. Phys.*, 42:209–225, 2001.
- [11] F. Becattini et al. Energy and system size dependence of chemical freeze-out in relativistic nuclear collisions. *Phys. Rev. C*, 73, Apr 2006.
- [12] J. Cleymans et al. Centrality dependence of thermal parameters deduced from hadron multiplicities in Au+Au collisions at  $\sqrt{s_{NN}} = 130$  GeV. *Phys. Rev. C*, 71, May 2005.
- [13] P. Petreczky. QCD at non-zero temperature: Bulk properties and heavy quarks. *Mod. Phys. Lett. A*, 25(37):3081–3092, 2010.

- [14] Y. Aoki et al. The QCD transition temperature: Results with physical masses in the continuum limit. *Phys. Lett. B*, 643(1):46–54, 2006.
- [15] Y. Aoki et al. The QCD transition temperature: Results with physical masses in the continuum limit II. *JHEP*, 0906(088), 2009.
- [16] P. Petreczky. Recent progress in lattice QCD at finite temperature. *arXiv:0906.0502*, Jun 2009.
- [17] D. J. Fixsen et al. Calibrator Design for the COBE Far Infrared Absolute Spectrophotometer (FIRAS). *The Astrophysical Journal*, 512(2), 1999.
- [18] L. P. Csernai et al. Neutron stars, hybrid stars and the equation of state. *Nucl. Phys. A*, 540(3–4):630–645, 1992.
- [19] H. Satz. The SPS heavy ion programme. *Phys. Rep.*, 403–404:33–50, 2004.
- [20] H. Satz. Colour deconfinement and quarkonium binding. *J. Phys. G*, 32(R25), 2006.
- [21] K. Aamodt et al. Two-pion Bose-Einstein correlations in central Pb–Pb collisions at  $\sqrt{s_{NN}} = 2.76$  TeV. *Phys. Lett. B*, 696(4):328–337, 2011.
- [22] P. V. Ruuskanen. Transverse Hydrodynamics with a First Order Phase Transition in Very High Energy Nuclear Collisions. *Acta Physica Polonica B*, 18(6), 1987.
- [23] M. Gyulassy et al. Jet quenching and monojet rates in ultrarelativistic nucleus-nucleus collisions. *Nucl. Phys. A*, 590(1–2):511–514, Jul 1995.
- [24] The PHENIX Collaboration. Dense-Medium Modifications to Jet-Induced Hadron Pair Distributions in Au+Au Collisions at  $\sqrt{s_{NN}} = 200$  GeV. *Phys. Rev. Lett.*, 97, Aug 2006.
- [25] R. Baier et al. Induced gluon radiation in a QCD medium. *Phys. Lett. B*, 345(3):277–286, Feb 1995.
- [26] The STAR Collaboration. Distributions of Charged Hadrons Associated with High Transverse Momentum Particles in pp and Au+Au Collisions at  $\sqrt{s_{NN}} = 200$  GeV. *Phys. Rev. Lett.*, 95, Oct 2005.
- [27] R. Hagedorn. *Rivista Nuovo Cimento*, 6, 1983.
- [28] U. Heinz et al. Search for collective flow in relativistic heavy-ion collisions using transverse momentum spectra of emitted hadrons. *Nucl. Phys. A*, 525:523–526, Apr 1991.

- [29] U. Heinz. Concepts of Heavy-Ion Physics. *arXiv:hep-ph/0407360*, Jul 2004.
- [30] S. Voloshin et al. Flow Study in Relativistic Nuclear Collisions by Fourier Expansion of Azimuthal Particle Distributions. *arXiv:hep-ph/9407282*, Jul 1994.
- [31] The STAR Collaboration. System size and energy dependence of near-side dihadron correlations. *Phys. Rev. C*, 85, Jan 2012.
- [32] V. Koch. Aspects of Chiral Symmetry. *International Journal of Modern Physics E*, 06(02):203–249, 1997.
- [33] R. Arnaldi et al. First Measurement of the  $\rho$  Spectral Function in High-Energy Nuclear Collisions. *Phys. Rev. Lett.*, 96, Apr 2006.
- [34] J. J. Aubert et al. Experimental Observation of a Heavy Particle J. *Phys. Rev. Lett.*, 33:1404–1406, Dec 1974.
- [35] J. Augustin et al. Discovery of a Narrow Resonance in  $e^+e^-$  Annihilation. *Phys. Rev. Lett.*, 33:1406–1408, Dec 1974.
- [36] C. Bacci et al. Preliminary Result of Frascati (ADONE) on the Nature of a New 3.1-GeV Particle Produced in  $e^+e^-$  Annihilation. *Phys. Rev. Lett.*, 33:1408–1410, Dec 1974.
- [37] G. S. Abrams et al. Observation in  $e^+e^-$  Annihilation of a Narrow State at 1865 MeV/c<sup>2</sup> Decaying to  $K\pi$  and  $K\pi\pi\pi$ . *Phys. Rev. Lett.*, 37:255–259, Aug 1976.
- [38] G. S. Abrams et al. Observation of a Narrow Charged State at 1876 MeV/c<sup>2</sup> Decaying to an Exotic Combination of  $K\pi\pi$ . *Phys. Rev. Lett.*, 37:569–571, Sep 1976.
- [39] J. Bronstein et al. Observation of a Narrow Antibaryon State at 2.26 GeV/c<sup>2</sup>. *Phys. Rev. Lett.*, 37:882–885, Oct 1976.
- [40] C. Bebek et al. Evidence for New-Flavor Production at the  $\Upsilon(4S)$ . *Phys. Rev. Lett.*, 46:84–87, Jan 1981.
- [41] M. Basile et al. Evidence for a new particle with naked beauty and for its associated production in high-energy (pp) interactions. *Lettere al Nuovo Cimento*, 31(4):97–111, 1981.
- [42] G. Aad et al. Observation of a New  $\chi_b$  State in Radiative Transitions to  $\Upsilon(1S)$  and  $\Upsilon(2S)$  at ATLAS. *Phys. Rev. Lett.*, 108, Apr 2012.
- [43] J. M. Richard. An introduction to the quark model. *arXiv:1205.4326*, May 2012.

- [44] N. Brambilla et al. Heavy Quarkonium Physics. *CERN Yellow Reports*, May 2005.
- [45] A. Andronic et al. Heavy quarkonium: progress, puzzles, and opportunities. *EPJ C*, 71(2):1–178, 2011.
- [46] C. Chao-Hsi. Hadronic production of  $J/\psi$  associated with a gluon. *Nucl. Phys. B*, 172:425–434, 1980.
- [47] G. A. Schuler. Quarkonium production and decays. *arXiv:hep-ph/9403387*, Mar 1994.
- [48] F. Abe et al. Inclusive  $J/\psi$ ,  $\psi(2S)$ , and  $b$ -quark production in  $p\bar{p}$  collisions at  $\sqrt{s} = 1.8$  TeV. *Phys. Rev. Lett.*, 69:3704–3708, Dec 1992.
- [49] E. Braaten et al. Gluon fragmentation into heavy quarkonium. *Phys. Rev. Lett.*, 71:1673–1676, Sep 1993.
- [50] M. Gluck et al. Gluon contribution to hadronic  $J/\psi$  production. *Phys. Rev. D*, 17:2324–2331, May 1978.
- [51] H. Fritzsch. Producing heavy quark flavors in hadronic collisions – A test of quantum chromodynamics. *Phys. Lett. B*, 67(2):217–221, 1977.
- [52] J. F. Amundson et al. Colorless states in perturbative QCD: Charmonium and rapidity gaps. *Phys. Lett. B*, 372(1–2):127–132, 1996.
- [53] W. E. Caswell et al. Effective lagrangians for bound state problems in QED, QCD, and other field theories. *Phys. Lett. B*, 167(4):437–442, 1986.
- [54] A. Abulencia et al. Polarizations of  $J/\psi$  and  $\psi(2S)$  Mesons Produced in  $p\bar{p}$  Collisions at  $\sqrt{s} = 1.96$  TeV. *Phys. Rev. Lett.*, 99:132001, Sep 2007.
- [55] H. S. Chung et al. Cornell Potential Parameters for  $S$ -wave Heavy Quarkonia. *arXiv:0803.3116*, Mar 2008.
- [56] T. Matsui et al.  $J/\psi$  suppression by quark-gluon plasma formation. *Phys. Lett. B*, 178(4):416–422, Oct 1986.
- [57] H. Satz. Quarkonium Binding and Dissociation: The Spectral Analysis of the QGP. *Nucl. Phys. A*, 783(1–4):249–260, Feb 2007.
- [58] H. Satz. Charm and Beauty in a Hot Environment. *arXiv:hep-ph/0602245*, Jan 2006.
- [59] K. J. Eskola et al. EPS09 – A new generation of NLO and LO nuclear parton distribution functions. *JHEP*, 2009(04), 2009.

- [60] M. Malek. Low- $x$  QCD at the LHC with the ALICE detector. *arXiv:0911.1458*, Nov 2009.
- [61] R. Vogt.  $x_F$  dependence of  $\psi$  and Drell-Yan production. *Phys. Rev. C*, 61, Feb 2000.
- [62] J. Adams et al. Pion, kaon, proton and anti-proton transverse momentum distributions from p+p and d+Au collisions at  $\sqrt{s_{NN}} = 200$  GeV. *Phys. Lett. B*, 616(1-2):8–16, 2005.
- [63] C. Lourenco et al. Energy dependence of  $J/\psi$  absorption in proton-nucleus collisions. *JHEP*, 2009(02), 2009.
- [64] R. Vogt. Shadowing and absorption effects on  $J/\psi$  production in dA collisions. *Phys. Rev. C*, 71, May 2005.
- [65] B. Alessandro et al. A new measurement of  $J/\psi$  suppression in Pb–Pb collisions at 158 GeV per nucleon. *EPJ C*, 39:335–345, 2005.
- [66] R. Arnaldi et al.  $J/\psi$  production in pA and AA collisions at fixed target experiments. *Nucl. Phys. A*, 830(1–4):345c–352c, 2009.
- [67] A. Adare et al.  $J/\psi$  Production versus Centrality, Transverse Momentum and Rapidity in Au+Au Collisions at  $\sqrt{s_{NN}} = 200$  GeV. *Phys. Rev. Lett.*, 98, Jun 2007.
- [68] B. Abelev et al. Centrality, rapidity and transverse momentum dependence of  $J/\psi$  suppression in Pb–Pb collisions at  $\sqrt{s_{NN}} = 2.76$  TeV. *arXiv:1311.0214*, Nov 2013.
- [69] G. Aad et al. Measurement of the centrality dependence of  $J/\psi$  yields and observation of  $Z$  production in lead–lead collisions with the ATLAS detector at the LHC. *Phys. Lett. B*, 697:294–312, 2011.
- [70] The CMS Collaboration. Suppression of non-prompt  $J/\psi$ , prompt  $J/\psi$ , and  $\Upsilon(1S)$  in PbPb collisions at  $\sqrt{s_{NN}} = 2.76$  TeV. *JHEP*, 1205, 2012.
- [71] R. Rapp et al. Medium modifications and production of charmonia at LHC. *Nucl. Phys. A*, 859(1):114–125, 2011.
- [72] J. A. Appel et al. Observation of a Dimuon Resonance at 9.5 GeV in 400-GeV Proton-Nucleus Collisions. *Phys. Rev. Lett.*, 39:252–255, Aug 1977.
- [73] J. A. Appel et al. Observation of Structure in the  $\Upsilon$  Region. *Phys. Rev. Lett.*, 39:1240–1242, Nov 1977.

- [74] B. Brown et al. Evidence for the  $\Upsilon''$  and a Search for New Narrow Resonances. *Phys. Rev. Lett.*, 42:486–489, Feb 1979.
- [75] T. Affolder et al. Production of  $\Upsilon(1S)$  Mesons from  $\chi_b$  Decays in  $p\bar{p}$  Collisions at  $\sqrt{s} = 1.8$  TeV. *Phys. Rev. Lett.*, 84:2094–2099, Mar 2000.
- [76] D. Acosta.  $\Upsilon$  Production and Polarization in  $p\bar{p}$  Collisions at  $\sqrt{s} = 1.8$  TeV. *Phys. Rev. Lett.*, 88:161802, Apr 2002.
- [77] V. M. Abazov. Measurement of the Polarization of the  $\Upsilon(1S)$  and  $\Upsilon(2S)$  States in  $p\bar{p}$  Collisions at  $\sqrt{s} = 1.96$  TeV. *Phys. Rev. Lett.*, 101:182004, Oct 2008.
- [78] J.P. Lansberg. On the mechanisms of heavy-quarkonium hadroproduction. *EPJ C*, (60):693–703, 2009.
- [79] V. M. Abazov et al. Measurement of Inclusive Differential Cross Sections for  $\Upsilon(1S)$  Production in  $p\bar{p}$  Collisions at  $\sqrt{s} = 1.96$  TeV. *Phys. Rev. Lett.*, 94, Jun 2005.
- [80] E. L. Berger et al. Upsilon Transverse Momentum at Hadron Colliders. *International Journal of Modern Physics A*, 20(16):3753–3755, 2005.
- [81] C. L. da Silva. Quarkonia measurement in p+p and d+Au collisions at  $\sqrt{s} = 200$  GeV by PHENIX Detector. *Nucl. Phys. A*, 830(1–4):227c–230c, 2009.
- [82] P. Djawotho et al.  $\Upsilon$  cross section in p+p collisions at STAR. *J. Phys. G*, 34(8), 2007.
- [83] R. Aaij et al. Measurement of  $\Upsilon$  production in pp collisions at  $\sqrt{s} = 7$  TeV. *EPJ C*, 72:2025, Apr 2012.
- [84] R. Aaij et al. Production of  $J/\psi$  and  $\Upsilon$  mesons in pp collisions at  $\sqrt{s} = 8$  TeV. *JHEP*, 2013(6), 2013.
- [85] M. Marchisone. Quarkonium production in hadron collisions at forward rapidity with ALICE at the LHC. *Proceedings of Science*, EPS-HEP 2013(185).
- [86] S. Chatrchyan et al. Measurement of the  $\Upsilon(1S)$ ,  $\Upsilon(2S)$  and  $\Upsilon(3S)$  cross sections in pp collisions at  $\sqrt{s} = 7$  TeV. *Phys. Lett. B*, 727(1–3), 2013.
- [87] The CMS Collaboration. Measurement of the  $\Upsilon(1S)$ ,  $\Upsilon(2S)$ , and  $\Upsilon(3S)$  Polarizations in pp Collisions at  $\sqrt{s} = 7$  TeV. *Phys. Rev. Lett.*, 110:081802, Feb 2013.

- [88] G. Aad et al. Measurement of  $\Upsilon$  production in 7 TeV pp collisions at ATLAS. *Phys. Rev. D*, 87(1–2):9–27, Mar 2013.
- [89] The CMS Collaboration. Upsilon production cross section in pp collisions at  $\sqrt{s} = 7$  TeV. *Phys. Rev. D*, 83:112004, Jun 2011.
- [90] M. R. Adams et al. Nuclear dependence of the production of  $\Upsilon$  resonances at 800 GeV. *Phys. Rev. Lett.*, 66:2285–2288, May 1991.
- [91] B. Alessandro et al. Bottomonium and Drell-Yan production in pA collisions at 450 GeV. *Physics Letters B*, 635(5–6):260–269, 2006.
- [92] H. Liu.  $\Upsilon$  production in d+Au collisions at STAR. *Nucl. Phys. A*, 830(1–4):235c–238c, 2009.
- [93] A. Adare et al.  $\Upsilon(1S+2S+3S)$  production in d+Au and p+p collisions at  $\sqrt{s_{NN}} = 200$  GeV and cold-nuclear-matter effects. *Phys. Rev. C*, 87, Apr 2013.
- [94] M. Strickland. Thermal  $\Upsilon(1S)$  and  $\chi_{b1}$  suppression at  $\sqrt{s_{NN}} = 2.76$  TeV Pb–Pb collisions at the LHC. *Phys. Rev. Lett.*, 107:132301, Sep 2011.
- [95] D. Bazow et al. Thermal bottomonium suppression at RHIC and LHC. *Nucl. Phys. A*, 879:25–58, 2012.
- [96] M. Strickland. Thermal Bottomonium Suppression. *arXiv:1207.5327*, Jul 2012.
- [97] M. Laine et al. Real-time static potential in hot QCD. *JHEP*, 0703:54, 2007.
- [98] A. Dumitru et al. The heavy-quark potential in an anisotropic plasma. *Phys. Lett. B*, 662(1):37–42, 2008.
- [99] N. Brambilla et al. Static quark-antiquark pairs at finite temperature. *Phys. Rev. D*, 78:014017, Jul 2008.
- [100] Y. Burnier et al. Quarkonium dissociation in the presence of a small momentum space anisotropy. *Phys. Lett. B*, 678(1):86–89, 2009.
- [101] A. Dumitru et al. Imaginary part of the static gluon propagator in an anisotropic (viscous) QCD plasma. *Phys. Rev. D*, 79:114003, Jun 2009.
- [102] F. Karsch et al. Color screening and deconfinement for bound states of heavy quarks. *Zeitschrift für Physik C Particles and Fields*, 37(4):617–622, 1988.

- [103] W. Florkowski et al. Non-boost-invariant motion of dissipative and highly anisotropic fluid. *J. Phys. G*, 38(1):015104, 2011.
- [104] M. Martinez et al. Dissipative dynamics of highly anisotropic systems. *Nucl. Phys. A*, 848(1–2):183–197, 2010.
- [105] M. Martinez et al. Non-boost-invariant anisotropic dynamics. *Nucl. Phys. A*, 856(1):68–87, 2011.
- [106] K. Aamodt et al. Elliptic Flow of Charged Particles in Pb–Pb Collisions at  $\sqrt{s_{NN}} = 2.76$  TeV. *Phys. Rev. Lett.*, 105:252302, Dec 2010.
- [107] C. Gale et al. Anisotropic flow in collisions at the LHC. *Phys. Lett. B*, 702(1):59–63, 2011.
- [108] A. Emerick et al. Bottomonia in the Quark-Gluon Plasma and their Production at RHIC and LHC. *EPJ A*, 48:72, 2012.
- [109] L. Grandchamp et al. Bottomonium production at  $\sqrt{s_{NN}} = 200$  GeV and  $\sqrt{s_{NN}} = 5.5$  TeV. *Phys. Rev. C*, 73:064906, 2006.
- [110] R. Rapp et al. Charmonium in medium: From correlators to experiment. *Phys. Rev. C*, 82:064905, 2010.
- [111] A. Kesich. Measurements of  $\Upsilon$  Production and Nuclear Modification Factor at STAR. *J. Phys.*, 389(1), 2012.
- [112] S. Whitaker. Upsilon Measurements by the PHENIX Collaboration. *arXiv:1207.6649*, Oct 2012.
- [113] S. Chatrchyan et al. Observation of sequential Upsilon suppression in PbPb collisions. *Phys. Rev. Lett.*, 109:222301, Aug 2012.
- [114] <http://public.web.cern.ch/public>.
- [115] The ALICE Collaboration. The ALICE experiment at the CERN LHC. *JINST*, 3(08), 2008.
- [116] L. Betev et al. Definition of the ALICE coordinate system and basic rules for sub-detector components numbering. *ALICE-INT*, 2003-038, 2003.
- [117] The ALICE Collaboration. ITS Technical Design Report. *CERN-LHCC*, 99–12, 1999.
- [118] The ALICE Collaboration. TPC Technical Design Report. *CERN-LHCC*, 2000–001, 2000.
- [119] The ALICE Collaboration. TRD Technical Design Report. *CERN-LHCC*, 2001–021, 2001.

- [120] The ALICE Collaboration.  
TOF Technical Design Report. *CERN-LHCC*, 2000–012, 2000.
- [121] The ALICE Collaboration.  
HMPID Technical Design Report. *CERN-LHCC*, 98–19, 1998.
- [122] The ALICE Collaboration.  
PHOS Technical Design Report. *CERN-LHCC*, 99–4, 1999.
- [123] The ALICE Collaboration.  
EMCAL Technical Design Report. *CERN-LHCC*, 2006–014, 2006.
- [124] A. Fernandez et al. ACORDE a Cosmic Ray Detector for ALICE. *Nucl. Instrum. Meth. A*, 572:102–103, 2007.
- [125] The ALICE Collaboration. Forward Detectors: FMD, T0 and V0 Technical Design Report. *CERN-LHCC*, 2004–25, 2004.
- [126] The ALICE Collaboration.  
PMD Technical Design Report. *CERN-LHCC*, 99–32, 1999.
- [127] B. Abelev et al. Centrality determination of Pb–Pb collisions at  $\sqrt{s_{NN}} = 2.76$  TeV with ALICE. *Phys. Rev. C*, 88, Oct 2013.
- [128] P. Shukla. Glauber model for heavy ion collisions from low energies to high energies. *arXiv:0112039*, Dec 2001.
- [129] The ALICE Collaboration.  
ZDC Technical Design Report. *CERN-LHCC*, 99–5, 1999.
- [130] The ALICE Collaboration. Trigger, Data Acquisition, High-Level Trigger and Control System Technical Design Report. *CERN-LHCC*, 2003–062, 2003.
- [131] D. Evans et al. The ALICE central trigger processor. *CERN-LHCC*, 2005–038, 2005.
- [132] A. Bhasin et al. Recent developments on the ALICE central trigger processor. *CERN*, 2007–001, 2007.
- [133] T. Alt et al. The ALICE high level trigger. *J. Phys. G*, 30:S1097–S1100, 2004.
- [134] A. Telesca et al. The ALICE Data Quality Monitoring System. *Real Time Conference (RT)*, 2010 17th IEEE-NPSS, May 2010.
- [135] F. Carena et al. Online processing in the ALICE DAQ, the Detector Algorithms. *J. Phys.*, 219:022004, 2010.

- [136] F. Carena et al. Experiences and evolutions of the ALICE DAQ Detector Algorithms framework. *J. Phys.*, 396:012012, 2012.
- [137] <http://aliweb.cern.ch/Offline>.
- [138] <http://root.cern.ch>.
- [139] H.-U. Bengtsson et al. The Lund Monte Carlo for hadronic processes – PYTHIA version 4.8. *Comp. Phys. Comm.*, 46(1):43–82, 1987.
- [140] S. Mrenna et al. PYTHIA 6.4 Physics and Manual. *JHEP*, 0605:026, 2006.
- [141] M. Gyulassy et al. HIJING 1.0: A Monte Carlo program for parton and particle production in high energy hadronic and nuclear collisions. *Comp. Phys. Comm.*, 83(2–3):307–331, 1994.
- [142] M. Goossens et al. GEANT: Detector Description and Simulation Tool. *CERN program library long write-up*, W5013, 1994.
- [143] S. Agostinelli et al. Geant4 - a simulation toolkit. *Nucl. Instrum. Meth. A*, 506(3):250–303, 2003.
- [144] G. Battistoni et al. Applications of FLUKA Monte Carlo code for nuclear and accelerator physics. *Nucl. Instrum. Meth. B*, 269(24):2850–2856, 2011.
- [145] <http://aliceinfo.cern.ch/Offline/Activities/ConditionDB.html>.
- [146] I. Foster et al. *Morgan Kaufmann Publishers*, 1999.
- [147] <http://monarc.web.cern.ch/MONARC>.
- [148] <http://alien2.cern.ch>.
- [149] <http://monalisa.cern.ch/monalisa.html>.
- [150] <http://alimonitor.cern.ch>.
- [151] K. Safarik. Long-term plans of the ALICE Collaboration. *Open Symposium – European Strategy Preparatory Group*, Krakow 2012.
- [152] L. Musa. Upgrade of the Inner Tracking System Conceptual Design Report. *CERN-LHCC*, 2012-013, 2012.
- [153] The ALICE MFT Collaboration. Letter of Intent: A Muon Forward Tracker for the ALICE Experiment.
- [154] The ALICE FoCal Collaboration. Letter of Intent: A Forward Calorimeter (FoCal) for the ALICE experiment.

- [155] The ALICE Collaboration. The forward muon spectrometer. Addendum to the ALICE Technical Proposal. *CERN-LHCC*, 96–32, 1996.
- [156] D. Das. Performance and First Physics Results of the ALICE Muon Spectrometer. *Nucl. Phys. A*, 862–863:223–230, 2011.
- [157] The ALICE Collaboration. ALICE dimuon forward spectrometer: Technical Design Report. *CERN-LHCC*, 99–22, 1999.
- [158] The ALICE Collaboration. ALICE dimuon forward spectrometer: addendum to the Technical Design Report. *CERN-LHCC*, 2000–46, 2000.
- [159] S. Grigoryan. Contribution of Secondary  $\pi/K$  Mesons, Produced in the Absorber, into the Dimuon Background in Pb–Pb Collisions. *ALICE Internal Note*, 2002–06, 2002.
- [160] D. Swoboda. ALICE Muon Arm Dipole Magnet. *ALICE Internal Note*, 1999–06, 1999.
- [161] The ALICE Collaboration. Technical Specification for the manufacturing of the Front Absorber Support Structure. *ALI-DIS-SPC*, 0024, 1999.
- [162] A. Behrens et al. Positioning strategy, metrology and survey in ALICE. *EDMS*, 884850, 2007.
- [163] V. Blobel. Software alignment for tracking detectors. *Nucl. Instrum. Meth. A*, 566(1):5–13, 2006.
- [164] R. Cardarelli et al. Development of resistive plate counters. *Nuclear Instrum. Meth.*, 187(2–3):377–380, 1981.
- [165] R. Cardarelli et al. Progress in resistive plate counters. *Nucl. Instrum. Meth. A*, 263(1):20–25, 1988.
- [166] G. Aielli et al. The RPC first level muon trigger in the barrel of the ATLAS experiment. *Nucl. Phys. B*, 158:11–15, 2006.
- [167] Z. Aftab et al. Production and the quality control for the CMS endcap RPC. *Nucl. Phys. B*, 158:16–20, 2006.
- [168] F. Poggio. Beam and ageing tests of Resistive Plate Chambers for the ALICE Muon Spectrometer. *Ph.D. Thesis*, 2005.
- [169] R. Arnaldi et al. A low-resistivity RPC for the ALICE dimuon arm. *Nucl. Instrum. Meth. A*, 451(2):462–473, 2000.

- [170] R. Arnaldi et al. Aging tests and chemical analysis of Resistive Plate Chambers for the trigger of the ALICE dimuon arm. *Nucl. Instrum. Meth. A*, 533(1–2):112–115, 2004.
- [171] R. Arnaldi et al. Beam and ageing tests with a highly-saturated avalanche gas mixture for the ALICE pp data taking. *Nucl. Phys. B*, 158:149–153, 2006.
- [172] F. Bossù et al. Performance of the RPC-based ALICE muon trigger system at the LHC. *JINST*, 7(12):T12002, 2012.
- [173] P. Dupieux et al. Description and Optimization of the ALICE dimuon trigger. *ALICE Internal note*, Aug 1998.
- [174] G. Blanchard et al. The local trigger electronics of the ALICE dimuon trigger. *ALICE-EN*, 2003–010, 2003.
- [175] R. Arnaldi et al. A dual threshold technique to improve the time resolution of resistive plate chambers in streamer mode. *Nucl. Instrum. Meth. A*, 457(1–2):117–125, Jan 2001.
- [176] O. Roig. Étude du système de déclenchement du spectromètre dimuons de l’expérience ALICE au CERN-LHC. *Ph.D. Thesis*, 1999.
- [177] <https://twiki.cern.ch/twiki/bin/viewauth/ALICE/PWG1EvSelDocumentation>. Link accessible only by the ALICE members.
- [178] M. Marchisone. Study of the ALICE muon trigger performance during the first p-p runs at 7 TeV. *Master thesis*, 2010.
- [179] R. Arnaldi et al. Spatial resolution of RPC in streamer mode. *Nucl. Instrum. Meth. A*, 490(1–2):51–57, 2002.
- [180] A. Blanc et al. The trigger system of the ALICE muon spectrometer at the LHC. *Nucl. Instrum. Meth. A*, 604(1–2):301, 2009.
- [181] <http://aliceinfo.cern.ch/Offline/Activities/Analysis/CORRFW.html>.
- [182] <https://aliceinfo.cern.ch/static/aliroot-new/html/roothtml/ClassIndex.html>.
- [183] J. E. Gaiser. Charmonium Spectroscopy from Radiative Decays of the  $J/\psi$  and  $\psi'$  – Appendix F. *Ph.D. Thesis*, Aug 1982.
- [184] F. Bossù et al. Phenomenological extrapolation of the inclusive  $J/\psi$  cross section to proton-proton collisions at 2.76 TeV and 5.5 TeV. *arXiv:1103.2394*, Apr 2011.

- [185] M. Cacciari et al. Theoretical predictions for charm and bottom production at the LHC. *JHEP*, 1210:137, 2012.
- [186] G. T. Bodwin et al. Rigorous QCD analysis of inclusive annihilation and production of heavy quarkonium. *Phys. Rev. D*, 51:1125–1171, Feb 1995.
- [187] H. L. Lai. Global QCD Analysis of Parton Structure of the Nucleon: CTEQ5 Parton Distributions. *EPJ C*, 12:375, 2000.
- [188] H. L. Lai. New Generation of Parton Distributions with Uncertainties from Global QCD Analysis. *JHEP*, 0207:012, 2002.
- [189] E. Scapparini. ALICE results on quarkonia. *arXiv:1211.1623*, Nov 2012.
- [190] R. Aaij et al. Measurement of the fraction of  $\Upsilon(1S)$  originating from  $\chi_b(1P)$  decays in pp collisions at  $\sqrt{s} = 7$  TeV. *JHEP*, 11:031, 2012.

# Thanks! Merci! Grazie!

In conclusion of my Ph.D. I want to thank my Italian supervisor Ermanno Vercellin for having allowed to continue my research activity within the ALICE experiment and for having introduced me Pascal Dupieux, my French supervisor.

I thank a lot Pascal for having accepted to follow me in this co-tutorship thesis and for having helped me since the early beginning of the work. A special thanks goes to Xavier Lopez for his advice and his encouragements during the analysis of the  $\Upsilon$  and the writing of the thesis.

Thanks Pascal and Xavier for your continue support, for the useful advice and for having read very carefully all my posters, my slides, my proceedings and the thesis.

And finally, thanks to the two referee Imad Laktineh and Giuseppe Iaselli and to Roberta Araldi for having accepted to be part of the jury.

Après les remerciements officiels, je renouvelle ma gratitude à Pascal pour tout ce que il a fait pour moi. Merci Pascal, surtout pour ton aide au cours de mon travail et pour avoir si bien expliqué le fonctionnement du muon trigger. Merci pour m'avoir permis de connaître et d'apprécier les magnifiques paysages autour Clermont-Ferrand, pour les balades ensemble en VTT et pour les discussions sur le rugby.



Puy de Dôme.

Je remercie encore une fois Xavier pour ses conseils et son amitié. Je remercie toutes les personnes du groupe ALICE du LPC pour leur sympathie et disponibilité.

Un grazie va anche a chi mi ha seguito dall'Italia, quindi non solo ad Ermanno, ma anche ad Enrico Scomparin ed a Roberta Araldi per la loro disponibilità e per i preziosissimi consigli. Il mio ringraziamento va esteso

anche a tutto il gruppo di Torino che mi ha accolto all'inizio del 2010 quando ho incominciato la tesi specialistica.

Infine un enorme grazie va alla mia famiglia che mi è sempre stata vicina in questi anni ed a tutti i miei amici, soprattutto coloro i quali, nonostante la distanza, non mi hanno mai fatto mancare il loro sostegno.

Thanks everybody! Merci à tous! Grazie a tutti!